

FORZAMIENTO DE FLUJOS AGEOSTRÓFICOS.
MAR DE ALBORÁN Y PLATAFORMA
DE MALLORCA-CABRERA

Memoria para la obtención
del título de doctor en Ciencias Físicas de:

Álvaro Viúdez Lomba

VOLUMEN I: TEXTO

Universitat de les Illes Balears
Junio de 1994

Forzamiento de flujos ageostróficos. Mar
de Alborán y plataforma de
Mallorca-Cabrera.

Memoria para la obtención del
título de Doctor en Ciencias Físicas de:
Álvaro Viúdez Lomba

Director:
Dr. Joaquín Tintoré Subirana

VOLUMEN I: TEXTO

Universitat de les Illes Balears
Junio de 1994

A mis padres,
por su generosidad.

Prólogo

El contenido básico de la presente memoria de tesis doctoral, dirigida por el Dr. Joaquín Tintoré, está formado por un conjunto de artículos de Oceanografía Física elaborados desde 1991 en colaboración con otros investigadores.

El primer capítulo sitúa e introduce, desde la perspectiva general de la Oceanografía Física, los diversos trabajos que forman esta tesis.

El segundo capítulo, cuyo principal autor es el Dr. Francisco E. Werner, es básicamente un estudio numérico de la circulación en la plataforma insular de Mallorca-Cabrera en el que se considera la topografía real y la influencia de diversos tipos de forzamiento.

El tercer capítulo es la descripción, basada en datos experimentales provenientes de una campaña oceanográfica realizada en 1991, de un nuevo estado de la circulación en la cuenca Este del Mar de Alborán.

El siguiente artículo es el análisis dinámico de la estructura tridimensional de la circulación en el Mar de Alborán realizado a partir de los datos experimentales obtenidos en una campaña oceanográfica llevada a cabo por la UIB y el *Institut de Ciències del Mar de Barcelona* (CSIC) en 1992, bajo la dirección del Dr. Jordi Font. En este trabajo se obtuvo, por primera vez a partir de datos experimentales hidrográficos, la velocidad vertical quasigeostrófica asociada a un campo de densidad tridimensional mediante la resolución numérica de la ecuación Omega quasigeostrófica.

Constituye el quinto capítulo la asimilación de los anteriores datos en un modelo numérico que resuelve las ecuaciones primitivas de Navier-Stokes con el propósito de diagnosticar los campos de densidad y de velocidad mutuamente equilibrados. Este trabajo fue realizado en estrecha colaboración con el Dr. Robert L. Haney, profesor en el *Naval Postgraduate School* y autor del modelo numérico. Representa la primera vez que se aplica con éxito un modelo de ecuaciones primitivas para calcular velocidades verticales a partir de datos hidrográficos experimentales.

El siguiente y último artículo es un estudio analítico sobre la naturaleza de la ecuación Omega generalizada. En este trabajo se introduce una interpretación nueva y compacta de esta ecuación.

Finalmente, en el último capítulo, presentamos las conclusiones principales de esta tesis doctoral.

Agradecimientos

Quisiera agradecer al director de esta tesis doctoral **Joaquín Tintoré** de la *Universitat de les Illes Balears* (UIB) por todas las ideas fructíferas, comentarios acertados, ayuda, interés y constante dedicación que han llevado a término la realización de este trabajo.

Estoy profundamente agradecido a **Robert L. Haney** del *Naval Postgraduate School* (NPS) por haberme acogido y tratado con una enorme hospitalidad durante mis visitas al NPS. Sus brillantes ideas y acertados comentarios han contribuido a la realización de gran parte de esta tesis.

A **Francisco E. Werner** (*University of North Carolina*) por todas sus enseñanzas sobre aspectos numéricos relacionados con el Método de los Elementos Finitos.

Existe también una serie de personas que han intervenido de una forma u otra en la elaboración de este trabajo, y aunque muchas de sus contribuciones han sido escuetamente agradecidas en la brevedad de los *acknowledgments* de cada artículo, creo poder disponer aquí de un mayor espacio para agradecerles su ayuda de una forma más específica.

Jordi Font, del *Institut de Ciències del Mar de Barcelona* (ICMB, CSIC), fue una persona imprescindible en la organización y realización de las campañas oceanográficas realizadas en el Mar de Alborán en 1990 (AL90) y 1992 (AL92). **Mario Manríquez** (ICMB) realizó gran parte de la adquisición y tratamiento de los datos de CTD a bordo del B.O. García del Cid durante AL90, AL92, y en la campaña oceanográfica llevada a cabo en la plataforma de Mallorca-Cabrera en 1992 (MA92); fue un profesional competente derrochando siempre simpatía y buen humor. **Jordi Salat** (ICMB) realizó también una gran parte del tratamiento de los datos en AL90 y AL92; estuvo siempre disponible para solucionar cualquier problema por grande y difícil que fuera. **Arturo Castellón** y **Elisa G. Górriz** (ICMB) trabajaron intensamente sobre todo en la adquisición de datos del complicado perfilador acústico Doppler en AL90 y AL92. **Maribel Lloret** y **Josep Sánchez** (ICMB) por su trabajo realizado en AL92 a bordo del B.O. García del Cid. **Ramiro Varela** (Instituto de Estudios Avanzados de Blanes) y **Mercedes Masó** (ICMB) proporcionaron los datos de las concentraciones de nutrientes y clorofila tomados en AL90.

Damià Gomis (UIB) aportó ideas y comentarios muy útiles relacionados con la interpolación de datos. Aportó asimismo las subrutinas para el cálculo de interpolaciones según el método de las correcciones sucesivas. Gracias a **Alberto Álvarez** (UIB), que desinteresadamente se prestó voluntario para transportar un nuevo CTD al B.O. García del Cid, pudimos llevar a feliz término la campaña AL92. Le estoy profundamente agradecido por ésta, y por todas las innumerables ayudas prestadas, pequeñas y grandes, que durante los últimos tres años han favorecido de una forma u otra este trabajo.

A **Jean-Michel Pinot** (UIB) por su colaboración también desinteresada en la campaña AL92. Le estoy agradecido por sus detallados comentarios relacionados con el análisis de datos, y especialmente por haber encontrado un error en el código de uno de mis programas. **Climent Ramis** (UIB) aportó útiles comentarios acerca del régimen de brisas en la isla de Mallorca. Le estoy también agradecido por haber corregido y comentado el artículo sobre la ecuación Omega generalizada. **Sergio Alonso** (UIB) clarificó también ciertos aspectos del régimen atmosférico en Mallorca. **Cristina Reus** (UIB) trabajó de forma incansable para proporcionarnos los innumerables medios informáticos necesarios para poder realizar este trabajo en el incipiente Laboratorio de Visualización (VISLAB). **María Garcies** (UIB) realizó un considerable número de gráficas útiles para la elaboración de uno de los artículos (Viúdez et al. 1994a). La espléndida figura de la distribución de estaciones (Fig. 1) de este artículo es obra suya.

Bob Hale (NPS) ayudó en la implementación del modelo de ecuaciones primitivas en el CRAY-YMP. **Russ Schwanz**, **Donna Burych**, **Mike McCann** y **Matthew Koebbe** (todos en el NPS) fueron una imprescindible ayuda en el uso con los ordenadores. **Wayne Wright** (NASA) fue un colaborador esencial en la adquisición de los datos AXBT. **Paul E. La Violette** (MSURC) fue también esencial en la adquisición de los datos AXBT y en el procesamiento de las imágenes de satélite de la campaña AL90. Sus comentarios fueron muy útiles para la elaboración del artículo sobre AL90. Agradezco también especialmente a **Bob Arnone** por el procesamiento de imágenes de satélite y por sus comentarios al artículo sobre AL90. A **Dong-Ping Wang** (*University of New York at Stony Brook*) también por revisar y comentar sabiamente este trabajo. **Andrew Folkard** y **Peter Davies** (*The University of Dundee*) aportaron interesantes ideas sobre la variabilidad temporal de la temperatura de la superficie del mar a partir de las imágenes de satélite correspondientes a la campaña AL90.

Estoy profundamente agradecido al **Servicio Aéreo de Rescate** (SAR), Escuadrón 801, con base en Palma de Mallorca por cumplir brillantísimamente con la misión de lanzar las sondas AXBT en AL90. **José Luis López-Jurado** (Centro Oceanográfico de Palma, IEO) compartió generosamente el CTD del IEO en AL92; él y **Francisco Arredondo** (INCIMA S.A.) nos proporcionaron también de forma desinteresada los datos de correntímetros y de viento empleados en el artículo sobre la circulación en la plataforma de Mallorca-Cabrera; sus comentarios fueron muy útiles para la elaboración de este artículo. Le estoy también agradecido por haber sido el responsable de la campaña MA92. **José Luis Casanovas** (Universidad de Valladolid) nos proporcionó las imágenes de satélite utilizadas en AL92. A **Julio Gil** (Centro Oceanográfico de Santander, IEO) por haberme proporcionado datos y valiosa información sobre el Mar de Alborán. Nuestros colegas **Joan J. Fornós**, **Lluís Pomar** y **Mauricio Ruíz** (*Departament de Ciències de la*

Terra, UIB) nos ayudaron con su experiencia y equipo en la digitalización de la batimetría de la plataforma de Mallorca-Cabrera. Roy Walters y Peggy Sullivan (USGS, Tacoma, WA) nos proporcionaron el programa de interpolación y generación de mallas de elementos finitos TRIGRID.

Esta tesis es parte de la contribución de la UIB al proyecto **Euromodel**, financiado por el programa de la C.E. MAST (MAS2-CT93-0066) y por la **Comisión Interministerial de Ciencia y Tecnología**, CICYT, MAR91-1492-CE y AMB93-1046-CE.

Este trabajo ha sido realizado gracias a una beca de cuatro años —desde 1991 hasta 1994— del Plan de Formación del Personal Investigador (PFPI) del Ministerio de Educación y Ciencia de España.

Índice

1	Introducción	1
1.1	El océano: sistema físico	2
1.2	Escalas y órdenes de aproximación. Movimiento geostrofico y ageostrofico	3
1.3	Las aguas costeras	4
1.4	El océano profundo	6
1.4.1	La velocidad vertical quasigeostrofica	8
1.4.2	Asimilación dinámica	10
1.4.3	La ecuación Omega generalizada	11
1.5	Trabajo para un futuro próximo	12
2	An Exploratory Numerical Study of the Currents off the Southern Coast of Mallorca Including the Cabrera Island Complex	19
2.1	Introduction	21
2.2	The study area and the mesh	22
2.3	Governing equations	23
2.4	Results	25
2.4.1	The Steady State Circulation	25
2.4.2	Sea Breeze Conditions	26
2.4.3	Storm Conditions	29
2.5	Concluding remarks and suggestions	29
3	Time and Space Variability in the Eastern Alboran Sea From March to May 1990	39
3.1	Introduction	41
3.2	Data	42
3.3	Results	43
3.3.1	Large scale structures	43
3.3.2	The eastward jet in the southern Alboran	44
3.3.3	Northward jet in the northeastern Alboran	45
3.3.4	Current meter results	45
3.3.5	Geostrophic computations	46

3.4	Discussion	46
4	Three-Dimensional Structure of the Two Anticyclonic Gyres in the Alboran Sea	55
4.1	Introduction	57
4.2	Data	58
4.3	Observations	58
4.4	Potential Vorticity	62
4.5	Vertical velocity from QG theory	66
4.6	Discussion	69
4.7	Appendix: Derivation of the Omega equation for $N^2(x, y, z)$.	72
5	Diagnosis of Mesoscale Ageostrophic Motion through Density Dynamical Assimilation: Application to the Alboran Sea	83
5.1	Introduction	85
5.2	The data	86
5.3	The models of vertical motion	87
5.4	Data assimilation	89
	5.4.1 Density field preprocessing	89
	5.4.2 The development of ageostrophic motion	90
	5.4.3 Weight function	92
5.5	Results and discussion	94
6	About the Nature of the Generalized Omega Equation	107
6.1	Introduction	109
6.2	Previous formulations of the generalized ω -equation	109
6.3	The rate of change of differential ageostrophic vertical vorticity	111
6.4	Conclusions	114
6.5	Appendix A: Derivation of (6.12) from (6.1)	116
6.6	Appendix B: Derivation of (6.12) from (6.2)	118
6.7	Appendix C: Equations for the differential ageostrophic vertical stretching and shearing deformation	119
7	Conclusiones	125

En las playas de todos los mundos, se reúnen los niños. El cielo infinito se encalma sobre sus cabezas; el agua, impaciente, se alborota. En las playas de todos los mundos, los niños se reúnen, gritando y bailando.

Hacen casitas de arena y juegan con las conchas vacías. Su barco es una hoja seca que botan, sonriendo, en la vasta profundidad. Los niños juegan en las playas de todos los mundos.

No saben nadar; no saben echar la red. Mientras el pescador de perlas se sumerge por ellas, y el mercader navega en sus navíos, los niños cogen piedrecitas y vuelven a tirarlas. Ni buscan tesoros ocultos, ni saben echar la red.

El mar se alza, en una carcajada, y brilla pálida la playa sonriente. Olas asesinas cantan a los niños baladas sin sentido, igual que una madre que meciera a su hijo en la cuna. El mar juega con los niños, y, pálida, luce la sonrisa de la playa.

En las playas de todos los mundos, se reúnen los niños. Rueda la tempestad por el cielo sin caminos, los barcos naufragan en el mar sin rutas, anda suelta la muerte, y los niños juegan. En las playas de todos los mundos, se reúnen, en una gran fiesta, todos los niños.

Rabindranath Tagore
(*Gitanjali*).

Capítulo 1

Introducción

1.1 El océano: sistema físico

La Filosofía de la Ciencia acostumbra a clasificar todo proceso de conocimiento científico en dos tipos de métodos: el método deductivo y el inductivo. El método deductivo consiste esencialmente en la explicación de fenómenos particulares a partir de leyes generales, mientras que el método inductivo parte de un comportamiento común observado en un conjunto de realidades particulares para elevar dicho comportamiento a la categoría de ley general. En ambos casos es evidente la necesidad de la observación, de la medida, tanto para verificar la validez de una ley general como para reunir un conjunto de observaciones a partir de las cuales poder inferir un comportamiento común. Si esta necesidad es evidente en todas las ramas de la Ciencia, probablemente lo sea de una forma más acentuada en el estudio de sistemas complejos cuyas leyes de gobierno provienen de diferentes ramas de la Física. Este es el caso del océano como sistema físico.

Las ecuaciones básicas que gobiernan los procesos oceánicos se rigen por los principios físicos de conservación de la cantidad de movimiento, de conservación de la masa, salinidad y flujo de calor, y una ecuación de estado. La ecuación del momento del océano es la correspondiente ley de Newton de la dinámica clásica; la ley que obedece el campo de temperatura (o en su caso el campo de densidad potencial) es la ecuación termodinámica de conservación y transferencia de calor; la ecuación de estado del agua de mar es una función empírica no lineal de la temperatura y salinidad. Y si bien las propiedades termodinámicas del agua de mar completan a las propiedades dinámicas y caracterizan el medio físico marino, no menos importantes son las propiedades ópticas y radiativas, las propiedades eléctricas y las propiedades acústicas (e.g. Apel 1987). Las propiedades ópticas y radiativas tienen especial importancia en las observaciones remotas. Existe un creciente uso de la teledetección (sensores remotos en el rango visual, infrarrojo, microondas, etc.) para adquirir medidas sinópticas de la temperatura, rugosidad, altimetría, etc., de la capa superficial del océano. Las propiedades acústicas se utilizan para obtener medidas de la velocidad del fluido mediante el efecto Doppler, o medidas de la velocidad del sonido en el agua de mar para obtener, mediante la inversión de la ecuación de ondas acústicas, valores horizontalmente integrados del campo de densidad. Incluso la salinidad, cuyo concepto resulta evidente y cuya influencia es clave en la ecuación de estado, se refiere a la concentración de iones en el agua de mar y su valor se obtiene por medio de la medida de una propiedad eléctrica del fluido: la conductividad. Por último, la circulación marina afecta en primer grado a la distribución de variables químicas y biológicas como la concentración de elementos y compuestos químicos, concentración de clorofila, turbidez, etc. En muchos casos estas propiedades se comportan como agentes inertes, y como tales pueden ser utilizados como trazadores pasivos del movimiento. En otros casos, como en

zonas de altas concentraciones de clorofila en la capa fótica, son indicadores de movimientos verticales o afloramientos marinos.

1.2 Escalas y órdenes de aproximación. Movimiento geostrófico y ageostrófico

La gran variedad de fenómenos que tienen lugar en el océano provoca que su estudio se divida primeramente según criterios de escalas temporales y espaciales, y según criterios de órdenes de magnitud. En este sentido, la oceanografía física estudia todo un rango de fenómenos que se extienden desde las pequeñas escalas temporales de la turbulencia hasta las grandes escalas del orden del periodo de las glaciaciones, pasando por las escalas inercial, estacional, interanual, etc. Y abarca desde las pequeñas escalas espaciales características de la difusión turbulenta hasta las mayores escalas, lo que se denomina el Océano Mundial, pasando por las escalas propias de los estuarios, aguas costeras y mares regionales.

Uno de los conceptos fundamentales en la dinámica de fluidos geofísicos es el concepto de "gran escala". Un fenómeno se considera de gran escala cuando está influenciado de forma significativa por la rotación de la Tierra (e.g. Pedlosky 1987, p. 2). Por tanto si un fenómeno ha de ser considerado de gran escala no sólo depende de su tamaño. Una medida fundamental de la importancia de la rotación sobre un fenómeno particular es el número de Rossby (cociente entre la aceleración relativa y la aceleración de Coriolis de un fluido). Cuando la aceleración relativa es pequeña comparada con la aceleración de Coriolis, el número de Rossby es menor que uno, y el flujo se considera de gran escala. A primer orden de aproximación en las ecuaciones de la dinámica de geofluidos, cuando el número de Rossby es del orden de 0.1 o menor, el gradiente horizontal de presión está aproximadamente en equilibrio con la aceleración horizontal de Coriolis (aproximación o equilibrio geostrófico) y el gradiente vertical de presión sólo depende de la densidad (aproximación hidrostática). La velocidad geostrófica es de divergencia horizontal nula, y como consecuencia el movimiento del océano, en primera aproximación, es horizontal. Conviene recordar que el orden de magnitud de la velocidad horizontal en los frentes oceánicos más intensos es de 1 m s^{-1} , mientras que el orden de magnitud de la velocidad vertical no excede de $100 \times 10^{-5} \text{ m s}^{-1}$, es decir tres órdenes de magnitud inferior.

Sin embargo se ha puesto recientemente de manifiesto la importancia del movimiento ageostrófico (i.e. cuyo gradiente horizontal de presión no está en equilibrio con la aceleración horizontal de Coriolis) en general en fenómenos oceánicos de mesoescala (remolinos, frentes, meandros y filamentos). Los movimientos verticales en remolinos y frentes oceánicos de mesoescala, y sus

consecuencias biológicas (transporte de fitoplacton a través de la termoclina y crecimiento de fitoplacton en la zona fótica) han sido el tema de varios estudios recientes [Woods et al. 1977, Woods et al. 1986, Leach 1987, Woods 1988, Pollard y Regier (1990, 1992)]. Regiones de afloramiento y subducción de agua con valores máximos de $10\text{-}40\text{ m d}^{-1}$ caracterizan el movimiento vertical en los filamentos de la denominada Zona de Transición Costera (Haidvogel et al. 1991, Walstad et al. 1991, Dewey et al. 1991, Washburn et al. 1991). En la Corriente del Golfo se pueden producir importantes desviaciones de la geostrofia ($\sim 20\text{ cm s}^{-1}$) debido a efectos de curvatura (Johns et al. 1989, Kontoyiannis y Watts 1990). Recientemente y también en la Corriente del Golfo se ha estudiado la circulación transversal (*cross-stream circulation*) y se han obtenido movimientos verticales del orden de $10\text{-}100\text{ m d}^{-1}$ (Chew et al. 1985, Bower y Rossby 1989, Bower 1991, Samuelson 1991, Onken 1992, Lindstrom y Watts 1994).

Actualmente, a causa del pequeño orden de magnitud de las velocidades verticales, las medidas directas fiables de la velocidad vertical son extremadamente difíciles de conseguir. Tan sólo medidas lagrangianas obtenidas con sofisticadas boyas isopícnas están últimamente siendo utilizadas para estimar velocidades verticales. Esto ha provocado el desarrollo de un notable esfuerzo teórico y numérico enfocado a la obtención de velocidades verticales —y velocidades ageostróficas en general— mediante métodos indirectos [e.g. Leach 1987, Tintoré et al. 1991, Pollard and Regier 1992, Viúdez et al. (1994a, 1994b), Lindstrom y Watts 1994]. Una parte considerable de esta tesis está también dedicada a ello.

A la hora de abordar de forma genérica el estudio del movimiento ageostrófico resulta necesario conocer sus causas. Y aunque las causas del movimiento ageostrófico son múltiples, éstas actúan de forma diferente en dos regiones de estudio de la Oceanografía Física: las aguas costeras y el océano profundo.

1.3 Las aguas costeras

La primera característica de las aguas costeras es su escasa profundidad —normalmente menor de 200 m — comparada con las profundidades del orden de 4000 m en el océano profundo. El límite de la plataforma continental está frecuentemente caracterizado por un aumento abrupto de la pendiente del fondo: el talud continental. La presencia del fondo a relativamente escasa profundidad juega un papel mucho mayor sobre el movimiento del agua que en aguas más profundas. Las corrientes cerca del fondo son a menudo bastante intensas (provocando el transporte de sedimentos) y el rozamiento con el fondo, que es normalmente despreciable en el océano, actúa de forma significativa sobre su dinámica. La presencia de la costa actúa como una

compresión lateral sobre el movimiento del agua, tendiendo a desviar las corrientes de forma que fluyan paralelas a ella. Impidiendo el flujo de agua, la costa causa una inclinación de la superficie y ésta, a su vez, reacciona y modifica los movimientos del agua.

El flujo de agua dulce proveniente de tierra produce un descenso de la salinidad, y por tanto de la densidad de las aguas costeras. Sin embargo esto no se cumple en las plataformas que poseen una descarga de agua dulce despreciable —caso de la plataforma de Mallorca— debido al escaso caudal de los ríos.

Las anteriores características de las aguas costeras conducen a algunas consecuencias físicas importantes. En primer lugar, las mareas y corrientes de marea se modifican considerablemente en relación con sus propiedades en el océano profundo. Sus amplitudes se ven normalmente aumentadas, a veces por un gran factor cuando se produce resonancia entre un periodo de marea y el periodo de oscilación natural de un volumen de agua costera (e.g. Neumann y Pierson, 1966). Normalmente las corrientes de marea tienden a ser más rápidas en la plataforma y, por tanto, el rozamiento del fondo tiene una mayor influencia sobre ellas.

Las ondas de superficie son un fenómeno común en los océanos y mares, y en algunos aspectos sus propiedades son similares en todos los sitios. Sin embargo cuando las ondas penetran en aguas poco profundas la proximidad del fondo induce sobre ellas cambios considerables, en muchos casos su rotura, disipándose en la orilla la mayor parte de su energía. La liberación de la energía de las ondas produce, en algunas zonas, el movimiento de grandes cantidades de material de playa y ejerce fuerzas considerables sobre estructuras naturales y artificiales.

La presencia de la costa y del fondo afecta también a las corrientes generadas por el viento. En algunas áreas esto da lugar a *storm surges*, mientras que en otras puede producir otros efectos, como afloramiento o generación de flujos costeros.

Las zonas costeras no pueden, sin embargo, ser consideradas de forma aislada de los mares adyacentes. En algunos casos, corrientes que fluyen a lo largo del talud continental cambian su dirección y tienen una gran influencia sobre la dinámica costera, provocando la intrusión de diferentes masas de aguas en la plataforma.

La dinámica de corrientes en la plataforma sur de Mallorca obedece —dado el escaso caudal de los ríos y las débiles componentes de las ondas de marea— a causas de tipo campo remoto —influencia de los mares adyacentes— y al forzamiento debido al viento. Bajo esta perspectiva se realiza el estudio numérico de la circulación en la plataforma sur de Mallorca-Cabrera titulado *An exploratory numerical study of the currents off the southern coast of Mallorca including the Cabrera island complex* (Werner, Viúdez y Tintoré 1993). El objetivo de dicho trabajo es determinar la variabili-

dad espacial y temporal de la circulación en la plataforma considerando la topografía real y bajo la influencia de diferentes tipos de forzamiento. En particular, estudiamos la influencia local de dos condiciones atmosféricas — brisa y temporal— y el efecto producido por condiciones de frontera de tipo campo remoto. En este sentido constituye el primer trabajo realizado hasta la fecha sobre este dominio.

1.4 El océano profundo

La circulación en el océano profundo obedece a otras causas. Los factores responsables de la circulación de gran escala del océano mundial son de un carácter termohidrodinámico. La cizalladura del viento en la superficie produce una simple desviación del transporte, que juega un papel secundario en el transporte general de masas de agua, siendo los procesos de intercambio de calor, y posiblemente de salinidad, mucho más importantes. Estos factores provocan la diferenciación de las masas de agua y, por tanto, la existencia de frentes de densidad. Una característica importante de los frentes de densidad estacionarios es que se alcanza el equilibrio, en la dirección perpendicular al frente, entre el gradiente de presión y la fuerza de Coriolis. Este balance —el ya mencionado equilibrio geostrófico— es el responsable de la corriente de gravedad perpendicular al frente. Sin embargo a escalas más pequeñas no se alcanza el equilibrio geostrófico y surge una circulación secundaria ageostrófica. Esta circulación secundaria inducida por fuerzas no lineales parece ser responsable de la alta actividad biológica presente frecuentemente en frentes oceánicos. El movimiento ageostrófico debe ser especialmente intenso en aquellas zonas del océano profundo en donde exista un alta variabilidad espacial y temporal asociada a intensos frentes de densidad. Una de las regiones del Océano Mundial que posee estas características de forma idónea es, sin lugar a dudas, el Mar de Alborán, la cuenca más occidental del Mar Mediterráneo.

El Mar Mediterráneo es un mar semicerrado cuya circulación de gran escala está principalmente determinada por el exceso de evaporación en relación con la precipitación y descarga de agua dulce de los ríos. Como consecuencia se produce un flujo de dos capas en el Estrecho de Gibraltar que compensa el déficit de agua y de salinidad, con agua atlántica entrando en el Mediterráneo por la capa superior y agua mediterránea saliendo al Atlántico por la capa inferior. El Mar de Alborán es la primera cuenca que recibe esta agua atlántica y en donde coexisten, debido a los factores termohidrodinámicos expuestos, dos masas de agua muy diferentes. La consecuencia directa de la coexistencia de estas masas de agua es la formación de intensos frentes de densidad. En concreto, la permanencia de un giro anticiclónico en la cuenca Oeste —Giro Oeste de Alborán—, la existencia de un frente en forma de onda asociado

al flujo de agua atlántica desplazándose desde Gibraltar y penetrando en el Mediterráneo, la variabilidad de otro giro anticiclónico en la cuenca Este —Giro Este de Alborán—, la variabilidad de un intenso frente de densidad que separa aguas mediterráneas de aguas atlánticas en el límite Este del Mar de Alborán —el Frente Almería-Orán— y el origen de la Corriente Argelina han sido —y continúan siendo— objetivo de importantes proyectos internacionales de investigación (e.g. ¿Dónde va? 1984, La Violette 1990) y tema de un número abundante de artículos (e.g. Seco 1959, Cano y de Castillejo 1972, Lanoix 1974, Cheney 1978, Cheney y Doblar 1982, Gascard y Richez 1985, La Violette 1986, Parrilla y Kinder 1987, Tintoré et al. 1988 Heburn y La Violette 1990, Perkins et al. 1990, Arnone et al. 1990, Tintoré et al. 1991, Speich 1992, Viúdez et al. 1994a)

Con el objetivo genérico de obtener datos experimentales en la cuenca Este del Mar de Alborán, y en particular con el ánimo de adquirir medidas de la circulación asociada al Frente Almería-Orán, se organizó una campaña oceanográfica en la primavera de 1990. En dicha campaña de observación se obtuvieron perfiles de conductividad, temperatura y presión (CTD) en cincuenta y cinco estaciones hidrográficas. También se obtuvieron medidas de la velocidad de la corriente proporcionadas por un correntímetro Doppler y por correntímetros mecánicos convencionales, imágenes térmicas de satélites NOAA, datos de nutrientes (fosfatos y silicatos) y concentración de clorofila en estaciones. A pesar de que las malas condiciones atmosféricas impidieron la completa realización del plan original de campaña, el análisis detallado de estos datos permitió caracterizar un nuevo estado de la circulación en la cuenca Este del Mar de Alborán, detectar movimientos ageostróficos, y relacionar la circulación presente con las anomalías en las distribuciones de nutrientes y clorofila. Estos temas forman el contenido del segundo artículo de esta tesis, titulado *Time and space variability in the eastern Alboran Sea from March to May 1990* (Viúdez y Tintoré 1994a).

Aunque en este capítulo se analizan casos aislados de movimiento ageostrófico, el incompleto muestreo realizado sobre la zona no permitió aplicar ningún método para obtener el campo de la velocidad vertical. En particular, el diagnóstico de velocidades verticales quasigeostróficas (QG), ampliamente utilizado en Meteorología Dinámica, requiere un muestreo adecuado para poder interpolar, a partir de los datos originales en las estaciones, datos de densidad en puntos de una malla regular. El cálculo de velocidades verticales debía estar ligado por tanto a una nueva adquisición de datos, a la obtención de datos hidrográficos con una resolución de mesoscala, y a ser posible a un muestreo que abarcara todo el Mar de Alborán. Esta nueva adquisición de datos se realizó dos años más tarde, en el otoño de 1992.

1.4.1 La velocidad vertical quasigeostrófica

Henry Stommel (1989) en un artículo histórico-crítico sobre la Oceanografía Física comentaba, por una parte, que ésta es interesante debido a lo mucho que hay por conocer y que hay una gran variedad de actividad, observacional y teórica, en la cual uno puede sumergirse. Por otra parte señalaba que la fuente de nuevas ideas en oceanografía proviene de nuevas observaciones: hay más descubrimientos que predicciones y la mayoría de las teorías tratan sobre observaciones que ya han sido hechas.

Nuestro grupo de investigación planificó una campaña de observación que se llevó a cabo a cabo en septiembre-octubre de 1992 con el objetivo de realizar 134 estaciones hidrográficas y obtener datos con un perfilador acústico Doppler sobre una malla regular con la resolución necesaria (30×18 km) para captar fenómenos de mesoescala. No sin dificultades —entre las que se incluyen una rotura del instrumento CTD y cuatro arribadas forzosas a puerto en busca de refugio ante las adversas condiciones meteorológicas— obtuvimos después de 20 días de campaña un conjunto de datos en todo el Mar de Alborán que bien puede considerarse como el más completo de los realizados hasta la fecha.

El análisis de estos datos permitió caracterizar el estado de la circulación en la capa superior del Mar de Alborán, durante el periodo de la campaña, como una estructura formada por un frente en forma de onda acoplado con dos sistemas giro anticiclónico mayor-remolino ciclónico menor. Aunque la existencia del Giro Oeste de Alborán era ya conocida, y aunque se tenían indicios superficiales por medio de imágenes térmicas de satélite del Giro Este de Alborán, la coexistencia de los dos giros anticiclónicos (uno en cada cuenca de Alborán) y su estructura tridimensional era desconocida.

Estos datos permitieron aplicar la teoría quasigeostrófica —el siguiente orden de aproximación al equilibrio geostrófico— y calcular el campo tridimensional de velocidades verticales QG mediante la resolución numérica de la denominada ecuación Omega QG, cuyo uso se había prácticamente restringido a la dinámica de la atmósfera. El forzamiento de esta ecuación se expresaba en términos de la advección diferencial de vorticidad y del Laplaciano de la advección de densidad. Hoskins et al. (1978) habían propuesto una nueva formulación de esta ecuación expresando los dos términos de forzamiento anteriores como un sólo término: la divergencia del recién introducido vector \mathbf{Q} . De esta forma se evitaba la cancelación y duplicación de los dos términos de forzamiento de la anterior formulación. Después de los trabajos pioneros de Leach (1987) y Tintoré et al. (1991) enfocados a la resolución de la ecuación Omega QG a partir de datos hidrológicos, Pollard y Regier (1992) habían sido los primeros en invertir una versión bidimensional de esta ecuación en un frente oceánico. Nuestro trabajo es el primero en el cual se resuelve la ecuación Omega QG en tres dimensiones a partir de datos

hidrográficos. Aplicamos asimismo el teorema de la conservación de vorticidad potencial de Ertel para obtener un orden de magnitud de la velocidad vertical. Ambos métodos diagnosticaron velocidades verticales del orden de $10\text{-}20 \times 10^{-5} \text{ m s}^{-1}$ a pesar de que los errores numéricos, debido a errores experimentales en los datos de densidad, en los términos derivados que intervienen en la ecuación Omega eran del orden del 30%. Estos resultados y otras importantes consecuencias de la estructura de ambos giros se presentan en el artículo que constituye la cuarta parte de esta tesis: *Three-dimensional structure of the two anticyclonic gyres in the Alboran Sea* (Viúdez, Tintoré y Haney 1994a).

Sin embargo, y aún teniendo en cuenta que el cálculo del campo de velocidad vertical QG en el océano es ya de por sí algo novedoso, la descripción QG no está completa si no se conoce el campo de velocidad horizontal QG. De nuevo varios trabajos en Meteorología Dinámica habían expuesto dos metodologías alternativas para obtener las velocidades horizontales QG a partir de las correspondientes velocidades verticales QG (Keyser et al. 1992, Xu and Keyser 1993). Debido a que la velocidad QG es de divergencia nula ambos métodos se basan en la descomposición del campo de velocidad horizontal en una parte no divergente y en una parte irrotacional, es decir en el teorema de Helmholtz (e.g. Dutton 1976, p. 149). Sin embargo esta descomposición es única sólo cuando las condiciones de frontera son periódicas (Lynch 1987, 1989), razón por la cual Keyser et al. (1992) aplican su metodología a datos sintéticos, generados de forma analítica, correspondientes a estados idealizados de fenómenos atmosféricos.

Evidentemente las condiciones de frontera en el Mar de Alborán, con el fuerte condicionante del Estrecho de Gibraltar en el límite Oeste, distan mucho de ser condiciones de frontera periódicas. Ante este panorama se presentaba una opción alternativa tan atractiva como arriesgada: cabía la posibilidad de intentar la asimilación dinámica de los datos hidrológicos en un modelo que resolviese las ecuaciones primitivas de Navier-Stokes, es decir, inicializar un modelo de ecuaciones primitivas con los datos hidrológicos experimentales y realizar una integración del modelo hasta que la evolución del estado del sistema sea la correspondiente a la evolución de gran escala.

Esta posibilidad resultaba atractiva porque, en caso de llevarse a cabo con éxito, obtendríamos un campo de velocidad ajustado según la dinámica de las ecuaciones primitivas con el campo de densidad. Consecuentemente el campo de velocidades resultante sería el campo de velocidades total, y no el correspondiente a la aproximación QG.

Pero por otra parte no dejaba de ser una alternativa dificultosa. En primer lugar porque los modelos de ecuaciones primitivas suelen diagnosticar la velocidad vertical a partir de la ecuación de continuidad, es decir a partir de la divergencia de la velocidad horizontal. Esta divergencia es nula a primer orden de aproximación, y por tanto el cálculo de la velocidad vertical

es extremadamente susceptible al error y ruido numérico. En segundo lugar el modelo debía ser inicializado con los datos hidrológicos —y por tanto con las velocidades geostróficas— e ir adquiriendo un estado ajustado durante un proceso de asimilación en el cual se desarrollan las velocidades ageostróficas. Como consecuencia, el proceso de asimilación implicaba variaciones de segundo orden en el campo de velocidades, es decir aceleraciones, y las consecuencias que estas aceleraciones tendrían en el proceso de inicialización dinámica gobernado por ecuaciones no lineales (en especial la aparición de ondas inerciales de segundo orden) podría provocar velocidades verticales de una amplitud superior a las velocidades verticales correspondientes a la evolución de gran escala del sistema. Esta es la razón principal por la cual el diagnóstico de movimiento ageostrófico —y en especial del campo de velocidades verticales— mediante la asimilación dinámica de datos hidrográficos no se había realizado hasta la fecha.

1.4.2 Asimilación dinámica

El objetivo de la asimilación de datos es la obtención de información sobre ciertas variables a partir de la información que ya se posee sobre otras variables y a partir de una dinámica común. En nuestro caso conocíamos el campo de densidad —y por tanto las velocidades geostróficas— y teníamos el objetivo de conocer el campo de velocidad total. El modelo numérico empleado fue el diseñado por el profesor Robert L. Haney (Haney 1974, 1985). Una forma de verificar el comportamiento del modelo era mediante la comparación de las velocidades verticales QG, las cuales ya habían sido calculadas, con las velocidades verticales diagnosticadas por el modelo numérico. Si ambas distribuciones eran parecidas, la parte irrotacional de la velocidad horizontal diagnosticada por el modelo debía ser correcta, y como el modelo no separa entre parte irrotacional y parte no-divergente, tampoco habría serias razones para dudar de la validez de la parte ageostrófica no-divergente, y por tanto de la validez de la velocidad horizontal total.

Cuando se aplica el proceso de la asimilación dinámica con un propósito de diagnóstico se deben tener en cuenta dos conceptos básicos. En un primer lugar está el concepto de la variable temporal. Por una parte ésta es sólo un parámetro iterativo únicamente necesario para que el sistema alcance un estado ajustado, pero por otra parte tiene su propio significado físico pues interviene en las derivadas temporales de las ecuaciones primitivas (de aquí que una mejor denominación para esta variable pueda ser la de *pseudotiempo*). Y en un segundo lugar es preciso tener en cuenta que, debido a que no se deben considerar efectos diabáticos ni de rozamiento en las ecuaciones primitivas, la integración numérica puede desarrollarse en ambos sentidos del eje *pseudotemporal*.

Estos dos últimos conceptos son el punto de partida clave para poder

entender el método empleado para eliminar el efecto directo de las ondas inerciales, generadas durante el proceso de asimilación, sobre el campo de velocidades verticales. La implementación numérica de dicho método consiste en la aplicación de una función de peso, que se basa en el filtro digital desarrollado por Lynch y Huang (1992), sobre las variables generadas por integraciones *hacia adelante* y *hacia atrás* del modelo numérico. El resultado final fue la obtención de un campo de velocidad vertical muy similar al proporcionado por la teoría quasigeostrófica. El proceso completo de esta asimilación dinámica es el tema del cuarto artículo de esta tesis, titulado *Diagnosis of mesoscale ageostrophic motion through density dynamical assimilation: application to the Alboran Sea* (Viúdez, Haney y Tintoré 1994b).

La conclusión de fondo del anterior trabajo de asimilación fue la viabilidad de utilizar la asimilación dinámica en datos de densidad con una resolución de mesoescala para diagnosticar el campo de velocidad ageostrófica. Dicha conclusión se basaba en la similitud existente entre los campos de velocidad vertical proporcionados por el modelo de ecuaciones primitivas y por la teoría QG. Sin embargo ambas distribuciones, si bien eran similares, no eran idénticas, y el paso siguiente fue investigar el origen de estas diferencias.

Existían trabajos aplicados a la atmósfera (e.g. Pauley y Nieman 1992) cuyo objetivo principal era justamente dicha comparación: velocidades verticales quasigeostróficas y no-quasigeostróficas. El análisis de Pauley y Nieman (1992) se basaba en la ecuación Omega generalizada expresada en términos de la advección diferencial de vorticidad y del Laplaciano de la advección de densidad. Sin embargo nosotros habíamos seguido la interpretación de la ecuación Omega QG en términos de la divergencia del vector \mathbf{Q} . Deberíamos por lo tanto, a partir de los valores de velocidad y densidad proporcionados por el modelo numérico, calcular todos los términos de una ecuación Omega generalizada formulada en términos de un vector \mathbf{Q} generalizado y en la cual no existiera cancelación o duplicación de términos. Y esta ecuación no había sido todavía formulada.

1.4.3 La ecuación Omega generalizada

Varios trabajos recientes en Meteorología Dinámica habían extendido la ecuación Omega más allá de los límites quasigeostróficos, y como consecuencia se habían formulado ecuaciones Omega generalizadas y vectores \mathbf{Q} generalizados (Davies-Jones 1991, Pauley y Nieman 1992, Xu 1992). La ecuación Omega generalizada se obtiene normalmente por la combinación de la ecuación termodinámica, la ecuación de vorticidad y la ecuación hidrostática con el objetivo de cancelar la variación temporal de vorticidad. Debido a que el uso de la ecuación termodinámica sólo puede cancelar la parte geostrófica de la derivada material de vorticidad relativa diferencial, la formulación natural de la ecuación Omega generalizada debe ser la expresión de la derivada material

de la parte ageostrófica de esta magnitud. Sin embargo esta interpretación estaba oculta en las anteriores formulaciones de esta ecuación. El siguiente artículo *About the nature of the generalized Omega equation* (Viúdez y Tintoré 1994b), que forma la última parte de esta tesis, tiene el objetivo de introducir la anterior interpretación de la ecuación Omega generalizada formulándola como una expresión para la derivada material de la vorticidad relativa ageostrófica diferencial. La ecuación resultante establece que, para fluidos no viscosos, isoentrópicos, bajo las aproximaciones hidrostática, de Boussinesq y en el plano f , la variación de vorticidad relativa ageostrófica diferencial en un elemento de fluido está en equilibrio con la divergencia de sólo un campo vectorial. Esta ecuación Omega generalizada es la correspondiente generalización de la ecuación Omega quasigeostrófica formulada en términos de la divergencia del vector Q , y por tanto es una expresión adecuada para ser empleada en estudios comparativos de la velocidad vertical diagnosticada por las ecuaciones primitivas y la teoría QG usando la formulación del vector Q .

1.5 Trabajo para un futuro próximo

Aunque el conjunto de trabajos que forman esta tesis doctoral se completa con el último artículo, la línea de investigación iniciada continúa su curso. Y si bien es cierto que el próximo paso parece ser el uso de la ecuación Omega generalizada, formulada en términos del vector Q , para explicar las diferencias halladas en la aplicación de la ecuación Omega quasigeostrófica, también es cierto que existen numerosas bifurcaciones en todo el proceso anterior al final de las cuales pueden estar esperando resultados relevantes para la Oceanografía Física. Concretamente, ¿cuál es la causa de la formación y colapso de los giros anticiclónicos del Mar de Alborán?, ¿cuál es la importancia de la circulación ageostrófica en la estabilidad de estos giros?, ¿qué influencia tiene la circulación profunda de Agua Mediterránea?, ¿cómo es la circulación real en la plataforma de Mallorca-Cabrera? Estas y otras cuestiones podrán ser esclarecidas con el futuro análisis de los datos de agua profunda adquiridos en el Mar de Alborán, con los datos hidrológicos tomados en una reciente campaña realizada en la plataforma de Mallorca-Cabrera, con las posibles contribuciones de futuras campañas oceanográficas, y con la asimilación de estos datos en modelos numéricos.

REFERENCIAS

- Apel, J. R., 1987: Principles of Ocean Physics. *International Geophysics Series*, **38**, Academic Press, 634 pp.
- Arnone, R. A., D. A. Wiesenburg and K. D. Saunders, 1990: The origin and characteristics of the Algerian Current. *J. Geophys. Res.*, **95** (C2), 1587-1598.
- Bower, A. S., and T. Rossby, 1989: Evidence of cross-frontal exchange process in Gulf Stream meanders based on isopycnal RAFOS float data. *J. Phys. Oceanogr.*, **19**, 1177-1190.
- Bower, A. S., 1991: A simple kinematic mechanism for mixing fluid parcels across a meandering jet. *J. Phys. Oceanogr.*, **21**, 173-180.
- Cano, N. and F. F. de Castillejo, 1972: Contribución al conocimiento del Mar de Alborán III. Variaciones del remolino anticiclónico. *Bol. Inst. Esp. Oceanogr.*, **157**, 3-7 plus 18 Figs.
- Cheney, R. E., 1978: Recent observations of the Alboran Sea frontal system. *J. Geophys. Res.*, **83**, 4593-4597.
- Cheney, R. E., and R. A. Doblár, 1982: Structure and variability of the Alboran Sea frontal system. *J. Geophys. Res.*, **87**, 585-594.
- Chew, F., J. M. Bane, and D. A. Brooks, 1985: On vertical motion, divergence, and the thermal wind balance in cold-dome meanders: a diagnostic study. *J. Geophys. Res.*, **90**, 3173-3183.
- Davies-Jones, R., 1991: The frontogenetical forcing of secondary circulations. Part I: the duality and generalization of the Q-vector. *J. Atmos. Sci.*, **48**, 497-509.
- Dewey, R. K., J. N. Moum, C. A. Paulson, D. R. Caldwell, and S. D. Pierce, 1991: Structure and dynamics of a coastal filament. *J. Geophys. Res.*, **96**, 14885-14907.
- Dutton, J. A., 1976: The ceaseless wind. An introduction to the theory of atmospheric motion. *McGraw-Hill*, 579 pp.

- Donde Va? Group, 1984: ¿Donde Va? An oceanographic experiment in the Alboran Sea. The oceanographic report. *Eos Trans. AGU*, **65**, (36), 682-683.
- Gascard, J. C., and C. Richez, 1985: Water masses and circulation in the western Alboran Sea and in the strait of Gibraltar, *Progress in Oceanography*, **15**, 157-216.
- Keyser, D., B. D. Schmidt, and D. G. Duffy, 1992: Quasigeostrophic diagnosis of three-dimensional ageostrophic circulations in an idealized baroclinic disturbance. *Mon. Wea. Rev.*, **120**, 698-730.
- Haidvogel, D. B., A. Beckmann, and K. S. Hedström, 1991: Dynamical simulations of filament formation and evolution in the Coastal Transition Zone. *J. Geophys. Res.*, **96**, 15017-15040.
- Haney, R. L., 1974: A numerical study of the response of an idealized ocean to large-scale surface heat and momentum flux. *J. Phys. Oceanogr.*, **4**, 145-167.
- Haney, R. L., 1985: Midlatitude sea surface temperature anomalies: a numerical hindcast. *J. Phys. Oceanogr.*, **15**, 787-799.
- Heburn, G. W., and P. E. La Violette, 1990: Variations in the structure of the anticyclonic gyres found in the Alboran Sea, *J. Geophys. Res.*, **95**(C2), 1599-1613.
- Hoskins, B. J., I. Draghici, and H.C. Davies, 1978: A new look at the w -equation. *Quart. J. R. Met. Soc.*, **104**, 31-38.
- Johns, E., D. R. Watts, and H. T. Rossby, 1989: A test of geostrophy in the Gulf Stream. *J. Geophys. Res.*, **94**, 3211-3222.
- Kontoyiannis, H., and D. R. Watts, 1990: Ageostrophy and pressure work in the Gulf Stream at 73° W. *J. Geophys. Res.*, **95**, 22209-22228.
- La Violette, P. E., 1986: Short term measurements of surface currents associated with the Alboran Sea during ¿Donde Va? *J. Phys. Oceanogr.*, **16**, 262-279.
- La Violette, P. E., 1990: The Western Mediterranean Circulation Experiment

- (WMCE): Introduction. *J. Geophys. Res.*, **95** (C2), 1511-1514.
- Lanoix, F., 1974: Projet Alboran, Etude hydrologique et dynamique de la Mer d'Alboran. Tech. Rep. 66, NATO, Brussels. 39 pp. plus 32 figs.
- Leach, H., 1987: The diagnosis of synoptic-scale vertical motion in the seasonal thermocline. *Deep-Sea Res.*, **34**, 2005-2017.
- Lindstrom, S. S., and D. R. Watts, 1994: Vertical motion in the Gulf Stream near 68° W. *J. Phys. Oceanogr.* (submitted).
- Lynch, P., and X-Y. Huang, 1992: Initialization of the HIRLAM model using a digital filter. *Mon. Wea. Rev.*, **120**, 1019-1034.
- Neumann, G., and W. J. Pierson, Jr., 1966: Principles of Physical Oceanography. *Prentice-Hall International, INC.*, London, 545 pp.
- Onken, R., 1992: Mesoscale upwelling and density finestructure in the seasonal thermocline—A dynamical model. *J. Phys. Oceanogr.*, **22**, 1257-1273.
- Parrilla, G. and T. H. Kinder, 1987: The physical oceanography of the Alboran Sea. *NORDA Rep.*, **184**, 26 pp.
- Pauley, P. M., and S. J. Nieman, 1992: A comparison of quasigeostrophic and nonquasigeostrophic vertical motions for a model-simulated rapidly intensifying marine extratropical cyclone. *Mon. Wea. Rev.*, **120**, 1108-1134.
- Pedlosky, J., 1987: Geophysical Fluid Dynamics. *Springer-Verlag*, 2nd edition, 710 pp.
- Perkins, H., T. Kinder, and P. E. La Violette, 1990: The atlantic inflow in the Western Alboran Sea. *J. Phys. Oceanogr.*, **20**, 242-263.
- Pollard, R. T., and L. Regier, 1990: Large variations in potential vorticity at small spatial scales in the upper ocean. *Nature*, **348**, 227-229.
- Pollard, R. T., and L. Regier, 1992: Vorticity and vertical circulation at an ocean front. *J. Phys. Oceanogr.*, **22**, 609-625.

- Samuelson, R. M., 1991: Fluid exchange across a meandering jet. *J. Phys. Oceanogr.*, **22**, 431-440.
- Seco, E., 1959: La capa de velocidad cero en el mar de Alborán. *Rev. Ceincas.*, **XXV**, 765-779.
- Speich, S., 1992: Étude du forçage de la circulation océanique par les détroits: cas de la mer d'Alboran. *Doctoral dissertation, Université Paris VI*. 245 pp.
- Stommel, H., 1989: Why we are oceanographers. *Oceanography*, **2**, no 2, 48-54.
- Tintoré, J., P. E. La Violette, I. Blade, and A. Cruzado, 1988: A study of an intense density front in the eastern Alboran Sea: The Almería-Oran Front. *J. Phys. Oceanogr.*, **18**, 1384-1397.
- Tintoré, J., D. Gomis, S. Alonso, and G. Parrilla, 1991: Mesoscale dynamics and vertical motion in the Alboran Sea. *J. Phys. Oceanogr.*, **21**, 811-823.
- Viúdez A., and J. Tintoré, 1994a: Time and space variability in the eastern Alboran Sea from March to May 1990. *J. Geophys. Res.*, (accepted).
- Viúdez, A., J. Tintoré, and R. L. Haney, 1994a: Three-dimensional structure of the two anticyclonic gyres in the Alboran Sea, *J. Phys. Oceanogr.*, (accepted).
- Viúdez, A., R. L. Haney, and J. Tintoré, 1994b: Diagnosis of mesoscale ageostrophic motion through dynamical density assimilation: application to the Alborán Sea. *J. Phys. Oceanogr.*, (submitted).
- Viúdez, A., and J. Tintoré, 1994b: About the nature of the generalized Omega equation. *J. Phys. Oceanogr.*, (submitted).
- Walstad, L. J., J. S. Allen, P. M. Kosro, and A. Huyer, 1991: Dynamics of the Coastal Transition Zone through data assimilation studies. *J. Geophys. Res.*, **96**, 14959-14977.
- Washburn, L., D. C. Kadko, B. H. Jones, T. Hayward, P. M. Kosro, T. P. Stanton, S. Ramp, and T. Cowles, 1991: Water mass subduction and the transport of phytoplankton in a coastal upwelling system. *J. Geophys.*

Res., **96**, 14927-14945.

Werner, F. E., A. Viúdez, and J. Tintoré, 1993: An exploratory numerical study of the currents off the southern coast of Mallorca including the Cabrera Island complex. *J. Mar. Systems*, **4**, 45-66.

Woods, J. D., 1988: Mesoscale upwelling and primary production. *Toward a theory of biological physical interactions in the World Ocean*, B. J. Rothschild, Ed., D. Reidal, 650 pp.

Woods, J. D., R. L. Wiley, and M. G. Briscoe, 1977: Vertical circulations at fronts in the upper ocean. *Deep-Sea Res. (Suppl:A Voyage to Discovery)*, **24**, 253-275.

Woods, J. D., R. Onken, and J. Fischer, 1986: Thermohaline intrusions created isopycnally at oceanic fronts are inclined to isopycnals. *Nature*, **322**, 446-449.

Xu, Q., 1992: Ageostrophic pseudovorticity and geostrophic C-vector Forcing —A new look at the \mathbf{Q} vector in three dimensions. *J. Atmos. Sci.*, **49**, 981-990.

Xu, Q., and D. Keyser, 1993: Barotropic and baroclinic ageostrophic winds and completeness of solution for the Psi equations. *J. Atmos. Sci.*, **50**, 588-596.

Grande es lo breve, y si queremos ser y parecer más grandes, unamos sólo con amor, no cantidad. El mar no es más que gotas unidas, ni el amor que murmullos unidos, ni tú cosmos que cosmillos unidos. Lo más bello es el átomo último, el sólo indivisible, y que por serlo no es ya más pequeño. Unidad de unidades es lo uno; ¡y qué viento más plácido levantan esas nubes menudas al cenit; qué dulce luz es esa suma roja única.

Juan Ramón Jiménez
(*Espacio*).

Capítulo 2

An Exploratory Numerical Study of the Currents off the Southern Coast of Mallorca Including the Cabrera Island Complex

Francisco E. Werner¹
Alvaro Viúdez²
Joaquín Tintoré²

J. of Marine Systems, 4, 45-66, 1993.

¹Skidaway Institute of Oceanography, P.O. Box 13687, Savannah, GA 31416, USA

²Grup de Fluids Geofísics, Departament de Física, Universitat de les Illes Balears,
Palma 07071, SPAIN

Abstract

Exploratory results obtained from a 3-D numerical model of the continental shelf circulation off the southern coast of the Island of Mallorca are described. The responses to idealized wind forcings (sea breezes and storms) and prescribed inflow through the open boundaries are considered. The model results identify circulation patterns consistent with features inferred from existing biological and geological studies and suggest specific future experimental studies.

2.1 Introduction

In this paper we examine the flow on the southern continental shelf of the Island of Mallorca under idealized forcing and realistic geometry. Our aim is to present, with the help of a numerical model, a first rough picture of some of the region's patterns of shelf circulation and to provide a background for future field efforts. Thus far, all knowledge concerning the dynamics of the shelf circulation is largely anecdotal and/or inferred from biogeochemical and paleological studies (*e.g.*, Guillén, 1987; Mateu, 1989).

The Balearic Islands are located in the western Mediterranean (Figure 1) approximately 200 Km east of the Iberian Peninsula. The three largest islands of the set are Mallorca, Menorca and Ibiza, and are separated from the Iberian Peninsula by the Balearic (or Catalán) Sea. Mallorca and Menorca, the two northernmost islands, share a common shelf; Ibiza, the southernmost island, is separated from Mallorca and Menorca by the Mallorca Channel that can reach depths in excess of 800 m. The shelf break is at roughly 200 m.

As indicated above there is very little known about the dynamics of the currents of the Balearic Islands. By contrast, certain aspects of the large scale dynamics of the neighboring Balearic Sea and Algerian Basin have been studied. Font et al. (1988) described two large permanent density fronts in the Balearic Sea: one located over the continental slope (the Catalán front) off the Spanish mainland, and a second one located over the northwest Balearic Island slope (the Balearic front). Satellite thermal imagery has provided additional information on the strength and variability of these fronts (La Violette et al. (1990); and López et al. 1992). The southern shelf of the Balearic Islands is influenced by the dynamics of the Algerian basin (Perkins and Pistek, 1990; and Millot, 1991) where the unstable nature of the Algerian current generates long-lived anticyclonic eddies. The presence of older offshore eddies can deflect the Atlantic waters of the Algerian current seaward, reaching at times the vicinity of the Balearic Islands. We know of no studies on the interaction of the currents in the Balearic Sea and Algerian Basin and the shelf waters of the Balearic Islands.

Locally, during summer months, there are persistent sea breeze conditions in Mallorca. In July and August, the weather is often almost identical from one day to the next. In the vicinity of the Bahía de Palma, and along the southern coast of Mallorca the breeze blows from the south-west (Ramis et al. 1990). Storms are mainly from the WSW (Table 1) and occur principally in winter.

As the present study is the first attempting to explore the 3-D shelf circulation south of Mallorca, the scenarios we put forth will need to be evaluated by future field efforts. In particular we examine the wind-induced currents under selected atmospheric (sea-breeze and storm) conditions and we study the sensitivity of the shelf circulation to simple "upstream" or far-

field boundary conditions. An understanding of the through-flow associated with far-field conditions (*e.g.*, induced by the pressure gradients of the larger scale currents in the Balearic Sea or Algerian Basin), allows us to interpret local signals within the context of the circulation on the Balearic Islands' shelf region and the neighboring deeper flows. We do not include tidal forcing as tides in this region of the Mediterranean are weak (*e.g.*, Dressler 1980; and Hopkins, 1985); and we also neglect the effect of freshwater/river discharges as they are also very small.

The numerical model of choice uses the finite element method and has been implemented, among others, in the Gulf of Maine (Lynch et al., 1992) and on the continental shelf of the southeastern U.S. (Werner et al., 1992).

2.2 The study area and the mesh

The northeastern limit of the domain is Porto Colom ($3^{\circ}16'E, 39^{\circ}25'N$), the northwestern limit is Torrenova ($2^{\circ}26'E, 39^{\circ}38'N$, located north of the Island of Dragonera), and the offshore extent of the model is the 200 m isobath (Figures 2 and 3a). The cross-shelf boundaries are perpendicular to the shelf from Torrenova (northwestern open boundary) and from Porto Colom (northeastern open boundary). Within this domain we have included the islands Dragonera, Cabrera, Conejera and Redonda. The islands Plana, Pobre and Horadada are represented as a single island.

Discrete bathymetric and coastal boundary data were obtained from nautical charts of the Instituto Hidrográfico de la Marina (chart numbers: 900, 422, 421, 970 and 999); we included all available bathymetric information. The digitization of the land boundary was more arbitrary in that smaller scale features of the coastline were omitted from the digitizing process. Approximately 2500 coastal and bathymetric points were input from the charts.

The model mesh was generated with the TRIGRID algorithm (Henry and Walters, 1992) and is shown in Figure 3. The mesh of linear triangular elements was generated in part based on criteria that keep the local Courant number uniform over the whole grid. In regions where additional refinement was deemed necessary, such as areas of sharp bathymetric gradients or near certain coastline features of interest, additional points were added manually. The final mesh has 3798 nodes, and 6825 elements in the horizontal. In the vertical, 1-D linear elements are deployed under each horizontal node; the nodes in the vertical are uniformly spaced under each horizontal node.

2.3 Governing equations

We solve the linearized 3-D shallow water equations with conventional hydrostatic and Boussinesq approximations and eddy viscosity closure in the vertical. Forcing by winds and sea level data at prescribed frequencies and of arbitrary spatial structure is allowed. Similarly, the density field, if known, may be prescribed as a fixed baroclinic pressure gradient. Details of the model equations, their numerical solution by the finite element method, and its evaluation in field case studies may be found in Lynch and Werner (1987), Lynch et al. (1992) and Werner et al. (1992) and references therein.

We employ the linearized continuity and momentum equations, assuming space-time separation of the form $q(\mathbf{x}, t) = \text{Re}(Q(\mathbf{x})e^{j\omega t})$, with Q the complex amplitude of q and ω the frequency. The horizontal momentum equation is

$$j\omega\mathbf{V} + \mathbf{f} \times \mathbf{V} - \frac{\partial}{\partial z} \left(N \frac{\partial \mathbf{V}}{\partial z} \right) = \mathbf{G} + \mathbf{R} \quad (2.1)$$

At the surface ($z = 0$) and bottom ($z = -h$), boundary conditions are enforced on stress:

$$N \frac{\partial \mathbf{V}}{\partial z} = h\mathbf{\Psi} \quad (z = 0) \quad (2.2)$$

$$N \frac{\partial \mathbf{V}}{\partial z} = k\mathbf{V} \quad (z = -h) \quad (2.3)$$

in which $h\mathbf{\Psi}(x, y)$ is the complex amplitude of the atmospheric forcing and k is a linear slip coefficient. Note that the bottom stress is given in terms of the local velocity, not its vertical average $\bar{\mathbf{V}}$. Vertical averaging of (2.1) yields

$$j\omega\bar{\mathbf{V}} + \mathbf{f} \times \bar{\mathbf{V}} + \frac{k}{h}\mathbf{V}(-h) = -g\nabla\zeta + \mathbf{\Psi} + \bar{\mathbf{R}} \quad (2.4)$$

in which the boundary conditions (2.2) and (2.3) have been incorporated.

In addition we have the continuity equation

$$\frac{\partial W}{\partial z} + \nabla \cdot \mathbf{V} = 0 \quad (2.5)$$

and its vertical average

$$j\omega\zeta + \nabla \cdot (h\bar{\mathbf{V}}) = 0 \quad (2.6)$$

in which:

$\mathbf{R}(\mathbf{x}, y, z) \equiv -\frac{g}{\rho_0} \int_z^0 \nabla \rho dz$ is the baroclinic pressure gradient, assumed known

$\mathbf{G}(\mathbf{x}, y) \equiv -g\nabla\zeta$ is the barotropic pressure gradient, assumed unknown

$\rho(x, y, z, t)$ is the fluid density

$\zeta(x, y)$ is the complex amplitude of the free surface elevation

$W(x, y, z)$ is the vertical velocity

$V(x, y, z)$ is the horizontal velocity

$\bar{V}(x, y)$ is the vertical average of V

ω is the radian frequency

j is the imaginary unit, $\sqrt{-1}$

$h(x, y)$ is the bathymetric depth

f is the Coriolis vector, directed vertically

$N(x, y, z)$ is the vertical eddy viscosity

g is gravity

(x, y) are the horizontal co-ordinates

z is the vertical co-ordinate, positive upward and

∇ is the horizontal operator $(\partial/\partial x, \partial/\partial y)$.

Solving for \bar{V} from (2.4) and using (2.6) results in a "wave" or Helmholtz equation for ζ

$$j\omega\zeta - \nabla \cdot \left[\frac{(j\omega + \tau')(gh\nabla\zeta - h\Psi' - h\bar{R}') - f' \times (gh\nabla\zeta - h\Psi' - h\bar{R}')}{(j\omega + \tau')^2 + f'^2} \right] = 0 \quad (2.7)$$

where the primed quantities contain contributions from the stress term evaluated at the bottom and are computed before assembling (2.7) (see Lynch and Werner, 1987 and Lynch et al. 1992). Boundary conditions on the barotropic flow include specifying the free-surface elevation, requiring no-normal flow through solid boundaries, or allowing outflow by an imposed radiation condition on determined cross-shelf boundaries. The radiation condition assumes negligible acceleration of the vertically averaged cross-shelf flow on the cross-shelf boundary and relates the remaining terms in the tangential (or cross-shelf) momentum equation to the normal transport through that section (for details see Lynch et al. 1992 and Werner et al. 1992).

Once ζ is obtained from (2.7), the reconstruction of the vertical structure of the horizontal velocity components is computed. Lastly, vertical velocities are subject to the kinematic boundary condition at the bottom, $z = -h(x, y)$, and are obtained by integrating (2.5) vertically upward. An alternative formulation for the computation of the vertical velocity is given in Lynch and Naimie (1992).

In all cases considered here the value of the linear bottom stress coefficient k (equation 3) is set to 0.0025 m/s; $k = C_d|V|$ where V is evaluated near the bottom. A commonly chosen value of C_d in 3-D shelf models is ~ 0.005 (e.g., Davies and Furnes, 1980). The value of 0.0025 m/s chosen herein for k implies a background velocity of 0.5 m/s which could be considered as an upper limit. The imposed value of the vertical eddy viscosity will vary

depending on the case considered and is given below. The magnitude of the vertical eddy viscosity reflects the levels of turbulent kinetic energy in a given region and, in general, is difficult to determine. Turbulence closure schemes (*e.g.*, Rodi, 1984) and surface mixed layer models (*e.g.*, Price et al. 1986) provide more realistic treatments of this problem. However, for the purpose of our diagnostic study, we will keep the eddy viscosities temporally and spatially constant.

2.4 Results

All cases were run on the horizontal mesh shown in Figure 3a. We have used 11 nodes in the vertical in our solutions, *i.e.*, a total of 41778 (x, y, z) nodes. Experiments with 21 nodes showed only minor differences. The run time on the VAXstation 3100/M76 is of 3.5 minutes of CPU per case. We considered: (i) the steady state circulation induced by a prescribed upstream condition, (ii) the circulation generated by idealized sea-breeze conditions, and (iii) the circulation generated by a storm condition.

2.4.1 The Steady State Circulation

The sensitivity of the through-flow in a given model-domain as related to the upstream (or far-field) condition is well known (*e.g.*, see Wright et al. 1986). It represents the transport into or out of the model domain due to remote conditions and may be considered as a background flow component upon which local forces, such as sea-breezes, act.

We examined the flow generated by prescribing a free-surface tilt across the open boundary off Porto Colom. In view of the study of Mateu (1989) which suggested a cyclonic circulation in the Bahía de Palma, we imposed a sea surface slope that sloped down from the coast to zero at the shelf edge (Figure 4a). The total transport *into* the model domain was of 0.13 Sverdrups. We examined the sensitivity to the structure of the upstream sea-surface slope generating the inflow and found essentially identical results within the model domain. The elevation of the free surface over the 200 m isobath was held fixed (clamped) at zero and the elevation off Torrenova was allowed to adjust to the radiation condition applied therein. The value of the vertical eddy viscosity N was set to $0.0025 \text{ m}^2/\text{s}$ and was constant in space and time. We chose a rather weak value for N since tides are very small in this region of the Mediterranean and we had no particular strong wind conditions in mind. We clamped the offshore open boundary at zero to effectively isolate the shelf circulation from that of the deep ocean. This still allows weak "interaction" with the offshore region in that cross-isobath flow at the shelf edge may occur in response to the flows generated within

the computational domain.

Figure 4b shows that the flow adjustment is mainly geostrophic in all the domain (as can be expected for the chosen value of N), with isopleths of surface elevation being mostly parallel to depth contours. An exception is found between the Island of Cabrera and Cabo Salinas where the modeled flow crosses isobaths, veering to their right. The distribution of the transport through Cabo Salinas, Cabrera and south of Cabrera (that originated upstream) is given in figure 4c.

Figure 4d shows the detailed distribution of the free-surface in the vicinity of Cabrera and its splitting around the islands. Figure 4b shows the 1 cm isopleth intersecting the coast in the Ensenada de La Rápita. This is likely due to the broadening of the flow (and thus a relaxation of the required pressure gradient) west of Cabo Salinas and is in contrast to the flow's constriction between Cabo Salinas and Cabrera and its increased speed (and hence increased slope of the free-surface).

The depth-averaged flow is shown in Figure 4e for the entire domain and for the vicinity of Cabrera in Figure 4f. Near Cabrera the flow circulates around the island-complex. See Figure 4c for details of transport between the neighboring islands of Conejera and Horadada. While – in this case – the surface flow (not shown) is very similar to the depth-averaged flow, the bottom flow shows the expected veering of the flow to the left of the flow above it (see Figure 4g for the detail near Cabrera). A quiet or “shadow” zone is apparent just west of Cabrera over a relatively flat region of the continental shelf. This quiet zone coincides with regions of accumulation of larvae (F. Vives, private communication) and fine silts and clays (J.J. Fornos, private communication) suggesting that in fact that this is a region of weak currents relative to neighboring areas. The steady results shown herein are likely to be an oversimplification and additional structure to the flow past these islands (*e.g.*, wake eddies) may be expected as discussed by Wolanski et al. (1987) and Deleersnijder et al. (1992).

West of the Cabrera Island-complex, the flow meanders following topographic features: part of it flows around the outer boundary of the Bahía de Palma, reaching the Island of Dragonera, and part enters the Bahía de Palma itself (roughly 5% of the total input transport). The currents are strongest around Dragonera, both within the strait (between Mallorca and Dragonera) and on Dragonera's offshore —western— coast, reaching 15 cm/s.

2.4.2 Sea Breeze Conditions

Sea breeze conditions are prevalent during summer months in Mallorca (Ramis et al. 1990) with near-surface wind-speeds in the Bahía de Palma of up to 10 m/s. We describe next simultaneous wind and current meter data for the summer of 1989.

Wind data. To compare model results with observations we used simultaneous wind and current meter data obtained in the Bahía de Palma during summer 1989. The wind data were collected at Palma airport from July 9 to August 13, 1989, every 30 minutes. We identified the period of 31 days from July 13 to August 13 as that containing the cleanest sea breeze signal. The data were low pass filtered with a 3-hour cut-off to remove high frequency fluctuations. Figure 5 shows that the sea breeze is mainly from the southwest, reaches maximum amplitudes of 7 m/s at noon and decays at nighttime to very small - practically zero - values.

For use in the harmonic model, we extracted the prevailing frequencies from the above wind-record. Harmonic analysis showed that we can reproduce the power of the experimental wind data using the signal generated by addition of a (single) periodic component plus a steady component. Since the observed data are not exactly sinusoidal, the amplitude of the simulated signal is slightly lower than the amplitude of the observations, the total power being identical however. We have therefore used a periodic signal of frequency $\omega = 2\pi/24 \text{ h}^{-1}$, of 2 m/s amplitude, and of phase $3\pi/2$, for both the north-south and east-west components. The steady wind component has $(u, v) = (0.64, 1.6) \text{ m/s}$. A seven day time series of this signal is shown in figure 6. The similarity between the observed and simulated signals despite using only one periodic plus one steady component is quite satisfactory.

Current meter data. Data were obtained from two Endeco 174SSM current meters moored at 30 m depth, about 2.4 km off Cape Enderrocat, in the eastern part of the Bahía de Palma only a few km from the Palma airport. Data were recorded at 10 m (current meter A10) and 25 m (current meter A25) from 7 July to 9 August 1989, with a sampling interval of 2 minutes. Wind data coincident with the available current meter data were used in our analyses.

The signal corresponding to a 24-hour period was extracted using classical methods of harmonic analysis. For a rigorous purpose of model testing, it would be necessary to compare the observed and simulated current response at a period of 24 hours. However, since the amplitude of the measured current signal at diurnal frequency was smaller than 1 cm/s the uncertainties in amplitude and phase cannot be overlooked, and therefore only order of magnitude statements are possible.

Model results. We computed the model response to the steady and the periodic (24-hour period) wind forcings with wind stress computed from $\tau_w = \rho_a C_{dw} U_{wind} |U_{wind}|$ and $C_{dw} = 1.1 \times 10^{-3}$. We used a vertical eddy viscosity of $100 \text{ cm}^2/\text{s}$ (Davies, 1987). We clamped the boundary at Porto

Colom to zero as well as the offshore boundary condition and kept the radiation condition off Torrenova.

The response of the surface currents within the Bahía de Palma to forcing by the steady wind component is shown in Figure 7a and three nodes below the surface in Figure 7b. [Recall that the nodes are stretched in the vertical and that there are 11 uniformly distributed nodes in the vertical under each horizontal node. Thus three nodes below the surface at a location where the bottom depth is 30 m is at 9 m from the surface, 3 m below the surface in where the bottom is at 10 m, and so on.] While the surface currents are into the Bay (Fig. 7a), the subsurface currents show more structure, with recirculation features and compensatory flows out of the Bay (Fig. 7b). The current ellipses at the surface and three nodes below the surface are shown in Figures 7c and 7d. The amplitude of the ellipses decays from roughly 2 cm/s at the surface to 1 cm/s three nodes below. The rotation in the surface is mainly clockwise, while three nodes below the currents tends to rotate counterclockwise in the western of the Bay.

Although the available observations at one location indicate that model results are in order-of-magnitude [$O(1 \text{ cm/s})$] agreement with available data, the weakness of the observed and modeled signals does not allow for the model's validation. Further data are needed for an in-depth calibration of these results and the field experiment would need to be redesigned. We will discuss these briefly in Section 5. A test of the model's sensitivity to different parameters such as vertical eddy coefficient indicated that lower values of the vertical eddy viscosity ($50 \text{ cm}^2/\text{s}$ instead of $100 \text{ cm}^2/\text{s}$) induces higher intensities in the upper layer; however, no significant changes were noted overall.

For the region of the Bahía de Palma, the surface and bottom flows plotted every 3 hours are shown in Figures 8(a-d) and 9(a-b). The breeze increases from a northeastward wind stress of $0.8 \times 10^{-2} \text{ Pa}$ (Figure 8a) to a maximum $1.14 \times 10^{-2} \text{ Pa}$ (Figure 8b). The breeze then relaxes to $0.8 \times 10^{-2} \text{ Pa}$ (Figure 8c) reaching zero in Figure 8d. Perhaps the most notable feature of Figures 8 and 9 is the spatial structure associated with these simplified conditions. Vertically, the top and bottom flows almost always oppose each other. Horizontally, flows around capes, headlands and, in nearshore regions in general, show features that can lead to small-scale flow features commonly associated with the gradients in bottom topography and bottom stress. The cross-bay surface flow when the wind-stress has reached zero (Figure 8d) also shows a recirculation in the northern reaches of the Bahía de Palma which appears consistently in smaller neighboring embayments. A split in the flow south of Cabo Blanco is also suggested where north of Cabo Blanco the flow returns into the Bahía de Palma while south of the Cabo, the flow is eastward.

2.4.3 Storm Conditions

Wind measurements collected every 3 hours at Palma de Mallorca airport over 18 years (1967-1984) indicate that in the southern coast of Mallorca storms are mostly from the WSW and between 11 and 16 knots (Table 1). Since these data were collected on land, these values have been increased (by a factor of 1.5) and accordingly, in our storm simulations, we have used a wind forcing of 25 knots from the WSW with a period of 4 days. The vertical eddy coefficient was set to $0.1500 \text{ m}^2/\text{s}$ (Davies, 1987) and was held spatially and temporally constant.

Model results when the wind forcing is at its maximum from the WSW, are shown in Figures (10-12). A southeastward coastal current is established (Fig. 10) with the most intense currents found off Dragonera and around Cabrera where magnitudes of 50 cm/s are reached. Inside the Bahía de Palma (Fig. 11) the currents reach speeds of the order of 10 cm/s. The currents at depth are weaker and have an on-shore component (not shown). The sea surface elevation at this time (Figure 12) is generally depressed along the coast, except within embayments where maximum elevations are found on the embayments' northeastern coast where the wind effectively piles water up against the coast. In the Bahía de Palma, the elevation along the western wall drops 2.6 cm relative to the northeastern corner. The same feature is observed east of Cabo Blanco. Upon the winds' relaxation some evidence for east-west "sloshing" is observed within the embayments.

2.5 Concluding remarks and suggestions

We have explored certain aspects of the circulation off the southern coast of the Island of Mallorca diagnostically. Solutions on a 3-D mesh with sufficient resolution to study detailed flows (wind-driven and remotely forced) can be efficiently computed for a given forcing-frequency on a microcomputer allowing thus for additional sensitivity studies of the region to be within reach. We considered the effects of upstream/remote forcing, sea breeze effects and a stormy condition. Although no data is available for significant comparison or calibration purposes what we have learned in this first step allows us to draw the following preliminary conclusions and to make specific recommendations:

- continue sensitivity studies to non-local forcing, *e.g.*, sensitivity to upstream boundary conditions. Field estimates of the transport off Porto Colom under the present mesh would be of great use in fixing the transport entering or leaving the model domain,
- additional checkpoints for the model results may be obtained by estimating the fraction of transport occurring between Mallorca and the Cabrera island-complex and that between Cabrera and the shelf edge,

- the region west of the Island of Cabrera appears to be a region of weakened currents, making it perhaps a region for accumulation of particles or larvae swept in from other regions. Lagrangian drifter studies of the region should be of interest for studies of the dispersal of larvae and dissolved substances, and
- future studies of sea breeze effects need to consider the upper water column in more detail, as the upper 20 meters may be where the wind forced response is trapped. CTD/hydrographic data will be essential to make these studies successful.

We close with comments on the sea breeze modeling and the field measurements. Descriptions of the issues faced in studying currents in the diurnal band are found in Rosenfeld (1987 and 1988) in a study off the US California coast. For one, wind/sea-breeze forced currents at 24-hour periods are very close to the K_1 tidal currents requiring some care in distinguishing between the tidal and the sea-breeze currents. Rosenfeld's studies clearly showed the surface enhancement of the currents due to the diurnal wind field and was additionally able to identify the contribution of tidal K_1 currents at depth. Since harmonic analysis of A10 and A25 indicate weak amplitudes in the diurnal band (less than 1 cm/s) it may be that the contribution of the sea breeze was in fact surface-trapped in the layers above 10 m and thus the upper current meter A10 may have missed the contribution of the sea breeze. At the same time though, since there are no data on the structure of the K_1 tide in this region we cannot presently discern between the two contributions. Perhaps measurements of the tidal contribution can be made during the fall or spring when the sea breezes have subsided; these measurements should prove valuable for future studies of the sea breeze induced circulation. Further, the effect of diurnal heating cycle and its impact on the time-dependence of the mixed layer was also shown by Rosenfeld (1987) to be key in the explanation of the observed diurnal current fields. To describe the heating cycle additional hydrographic data is needed. These observations together with our model findings offer clear indications to what may be the issues to consider in future field attempts to study the effect of the summer sea breeze on the currents off Mallorca.

Acknowledgments. F.W. thanks the Departament de Física of the UIB for their generosity and support during his stay as a Visiting Professor of the Fall of 1991. Partial support from the FICITIB is gratefully acknowledged. The many conversations with Profs. Sergio Alonso, Damiá Gomis, Clemente Ramis and José Luis López Jurado clarified aspects related to the atmospheric and oceanic regime of the study site. We are particularly thankful to

José Luis López Jurado (I.E.O.) and Francisco Arredondo (INCIMA) for providing the wind and currentmeter data. Our colleagues at the Departament de Geografia of the UIB generously provided their expertise and equipment in helping us digitize the model domain. Roy Walters and Peggy Sullivan of the USGS (Tacoma, WA) kindly provided us with the TRIGRID package.

REFERENCES

- Davies, A. M., 1987: Spectral models in continental shelf sea oceanography. In: *Three Dimensional Coastal Ocean Models* Coastal and Estuarine Sciences 4, N.S. Heaps, Editor. American Geophysical Union, Washington, D.C., 71-106.
- Davies, A. M. and G. K. Furnes, 1980: Observed and computed M_2 tidal currents in the North Sea. *J. Phys. Oceanogr.*, **10**, 237-257.
- Deleersnijder, E., A. Norro and E. Wolanski, 1992: A three-dimensional model of the water circulation around an island in shallow water. *Cont. Shelf Res.*, **12**, 891-906
- Dressler, R., 1980: Hydrodynamic investigation of the M_2 tide and of some tsunamis of the European Mediterranean Sea. *Mitt. Inst. Meereskd., Univ. of Hamburg*, **23**, 1-30.
- Font, J., Salat, J. and Tintoré, J., 1988: Permanent features of the circulation in the Catalán Sea. *Oceanol. Acta (special issue, 'Pelagic Mediterranean Oceanography')*, **9**, 51-57.
- Guillén, J., 1987: La sedimentación carbonatada en la plataforma continental de Campos (sur de Mallorca). *Tesina de licenciatura*. Facultat de Geologia. Universitat de Barcelona. Spain.
- Henry, R. F. and R. A. Walters, 1992: A geometrically-based, automatic generator for irregular triangular networks. *Comm. Appl. Num. Meths.*, (in press).
- Hopkins, T. S., 1985: Physics of the Sea. In: *Key Environments. Western Mediterranean*. R. Margalef, Ed., Pergamon Press, 100-125.
- La Violette, P. E., J. Tintoré and J. Font, 1990: The surface circulation of the Balearic Sea. *J. Geophys. Res.*, **95**, 1559-1568.
- López García, M. J., C. Millot, J. Font, and E. García-Ladona, 1992: Surface circulation variability in the Balearic basin. *J. Geophys. Res.*, **99**, 3285-3296.

- Lynch, D. R. and C. E. Naimie, 1992: The M_2 tide and its residual on the New England Banks. *J. Phys. Oceanogr.*, (accepted).
- Lynch, D. R. and F. E. Werner, 1987: Three-dimensional hydrodynamics on finite elements. Part I: Linearized Harmonic Model. *Int. J. for Numerical Methods in Fluids*, **7**, 871-909.
- Lynch, D. R., F. E. Werner, D. A. Greenberg and J. W. Loder, 1992: Diagnostic model for baroclinic, wind-driven and tidal circulation in shallow seas. *Continental Shelf Research*, **12**, 37-64.
- Mateu, G., 1989: La Bahía de Palma de Mallorca (Baleares-España) y los recientes estudios geosísmicos, Bionómico-Sedimentarios y Micropaleontológicos en un litoral de difícil regeneración antrópica. *Rev. Cien. (IEB)*, **4**, 65-81.
- Millot, C., 1991: Mesoscale and seasonal variabilities of the circulation in the western Mediterranean. *Dyn. Atmos. Oceans*, **15**, 179-214.
- Perkins, H., and P. Pistek, 1990: Circulation in the Algerian Basin during June 1986. *J. Geophys. Res.*, **95**, 1577-1585.
- Price, J. F., R. A. Weller and R. Pinkel, 1986: Diurnal cycling: observations and models of the upper ocean response to diurnal heating, cooling, and wind mixing. *J. Geophys. Res.*, **91**, 8411-8427.
- Ramis, C., A. Jansa and S. Alonso, 1990: Sea Breeze in Mallorca. A Numerical Study. *Meteorol. Atmos. Phys.*, **42**, 249-258.
- Rodi, W., 1984: Turbulence Models and Their Application in Hydraulics: A State of the Art Review. 2nd rev. ed., The Netherlands, International Association for Hydraulic Research.
- Rosenfeld, L. K., 1987: Tidal band current variability over the northern California continental shelf, WHOI-MIT Joint Program Doctoral Dissertation. *Woods Hole Oceanographic Institution Technical Report WHOI-87-11*, 237 pp.
- Rosenfeld, L. K., 1988: Diurnal period wind stress and current fluctuations over the continental shelf off northern California. *J. Geophys. Res.*, **93**,

2257-2276.

Werner, F. E., J. O. Blanton, D. R. Lynch and D. K. Savidge, 1992: A numerical study of the continental shelf circulation of the U.S. South Atlantic Bight during the autumn of 1987. *Continental Shelf Research*, (in press).

Wolanski, E., J. Imberger and M. L. Heron, 1984: Island wakes in shallow coastal waters. *J. Geophys. Res.*, **89**, 10553-10569.

Wright, D. G., D. A. Greenberg, J. W. Loder and P. C. Smith, 1986: The steady state barotropic response of the Gulf of Maine and adjacent regions to surface wind stress. *J. Phys. Oceanogr.*, **16**, 947-966.

LIST OF FIGURES

LIST OF TABLES

Table 1. Wind-direction, wind-speed and frequency of occurrence (in %) at Palma airport from 1967 to 1984. Calm wind conditions (< 1 knot) occurred in 40.5% of the record; storms with WSW winds between 11 and 16 knots occurred in 5.1 % of the record.

LIST OF FIGURES

Figure 1. Map of the Balearic Islands. The domain of interest is within the boxed region along the southern coast of the Island of Mallorca.

Figure 2. Bathymetric contours in meters of the model domain.

Figure 3a. Finite element mesh with placenames.

Figure 3b. Detail of the mesh in the vicinity of Cabrera.

Figure 4a. Sea surface elevation in a cross section from Pto. Colom to 200 m isobath: elevation producing 20 cm/s geostrophic currents into the model domain with an input transport of 0.13 Sv (*) and exponential elevation producing the same transport (X).

Figure 4b. Sea surface elevation due to prescribed tilt off Porto Colom (in cm).

Figure 4c. The transport budget due to prescribed tilt off Porto Colom (in %).

Figure 4d. Sea surface elevation in the vicinity of the Cabrera Island-complex due to prescribed tilt off Porto Colom (in cm).

Figure 4e. Depth-averaged flow due to prescribed tilt off Porto Colom.

Figure 4f. Detail of 4b in the vicinity of Cabrera.

Figure 4g. Detail of bottom flow in the vicinity of Cabrera due to prescribed tilt off Porto Colom.

Figure 5. Thirty-two day record of wind data at Palma airport (in m/s). Each plot represents a week.

Figure 6. A week of simulated wind data at Bahía de Palma for modelling purpose under sea breeze conditions (in m/s).

Figure 7a. Response of the surface currents to forcing by the steady wind component for the Bahía de Palma.

Figure 7b. Response of the currents 3 nodes below the surface to forcing by the steady wind component for the Bahía de Palma.

Figure 7c. Response of the surface currents to forcing by the 24-hour wind component for the Bahía de Palma. An asterisk in the center of an ellipse indicates counterclockwise rotation.

Figure 7d. Response of the currents 3 nodes below the surface to forcing by the 24-hour wind component for the Bahía de Palma. An asterisk in the center of an ellipse indicates counterclockwise rotation.

Figures 8a-d. Surface currents in the Bahía de Palma due to 24-hour period sea breeze: (a) increasing breeze of magnitude $|\tau| = 0.80 \times 10^{-2}$ Pa at 0900 hours, (b) maximum breeze $|\tau| = 1.14 \times 10^{-2}$ Pa at 1200 hours, (c) decreasing breeze of magnitude $|\tau| = 0.80 \times 10^{-2}$ Pa at 1500 hours, (d) time at which breeze is zero.

Figures 9a-b. Bottom currents in the Bahía de Palma due to 24-hour period sea breeze: (a) maximum breeze $|\tau| = 1.14 \times 10^{-2}$ Pa, (b) time at which breeze is zero.

Figure 10. Surface currents due to a 4-day period WSW storm of $|\tau| = 0.5$ Pa during maximum wind stress.

Figure 11. A zoom of Figure 10 within the Bahía de Palma.

Figure 12. Sea surface elevation (mm) due to a 4-day period WSW storm of $|\tau| = 0.5$ Pa during maximum wind stress.

Mar

Parece mar que luchas
—¡oh desorden sin fin, hierro incesante!—
por encontrarte o por que yo te encuentre.
¡Qué inmenso demostrarte,
en tu desnudez sola
—sin compañera... o sin compañero
según te diga el mar o la mar—, creando
el espectáculo completo
de nuestro mundo de hoy!
Estás, como en un parto,
dándote a luz —¡con qué fatiga!—
a ti mismo, ¡mar único!,
a ti mismo, a ti sólo y en tu misma
y sola plenitud de plenitudes,
... ¡por encontrarte o porque yo te encuentre!

Juan Ramón Jiménez
(*Diario de un poeta recién casado*).

Capítulo 3

Time and Space Variability in the Eastern Alboran Sea From March to May 1990

Álvaro Viúdez¹
Joaquín Tintoré¹

J. Geophys. Res. (accepted).

¹Dept. de Física, Universitat de les Illes Balears, Spain

Abstract

An intensive field experiment was carried out from March 6 to April 30 1990 in the eastern Alboran Sea to understand the relationship between the large scale circulation and the location of the transition zone between new and longer resident Modified Atlantic Water (MAW). The detection of a strong jet (80 cm s^{-1}) of new MAW with negative vorticity near Morocco coast suggests that the Eastern Alboran Gyre (EAG) was not fully developed. A new state of the circulation in the eastern Alboran basin —intermediate between the EAG (*Víúdez et al.*, [1994]) and the *Lanoix* [1974] state— is presented. Also important is that the Almería-Oran Front was not present in the upper layer, that small scale instabilities were detected in the northern region and that significant non-geostrophic flows were observed. All these features are clearly indicative of the high spatial and temporal variability of a region where complex adjustments between density, velocity and topography occur.

3.1 Introduction

The Alboran Sea is the first Mediterranean basin encountered by the Modified Atlantic Water (MAW, $36.5 < S < 37.5$). Recent international experiments such as *Donde Va?* in 1982 [*Donde Va? Group*, 1984] and the Western Mediterranean Circulation Experiment in 1986 [*La Violette*, 1990] have shown that the circulation of MAW in the Alboran Sea is characterized by high spatial and temporal variability. The large scale circulation is fairly well known and shows that at any one time there is one or two large anticyclonic gyres, one lying in the western Alboran basin (the Western Alboran Gyre) and the other in the eastern Alboran basin (the Eastern Alboran Gyre, EAG). Typical dimensions for the diameter of these gyres are around 100 km while the internal Rossby radius in the Alboran Sea is ~ 20 km [*Gascard and Richez*, 1985].

Several studies in the Alboran Sea have addressed the problem of the variability of the MAW in the western Alboran basin. In situ studies have shown significant mesoscale spatial variability [*Tintoré et al.*, 1991; *Viúdez et al.*, 1994] and remote sensing/numerical studies confirmed such spatial variability and showed the existence of a non negligible temporal variability [*Perkins et al.*, 1990; *Heburn and La Violette*, 1990]. Most of the numerical studies examined the question of the anticyclonic gyre formation and indicated that the existence of the western gyre might be related to the non-linear density advection off the Strait of Gibraltar [*Wang*, 1987]. Meanwhile most of these studies were carried out to understand the dynamics of the western Alboran basin and its relation to the Strait of Gibraltar outflow, much less information exists on the dynamics of the eastern Alboran basin, east of Cape Tres Forcas. The few data available indicate that several circulation patterns are possible. *Lanoix* [1974] found an eastward current with positive vorticity in the south of the eastern basin near the Morocco coast. *Heburn and La Violette* [1990] in an intensive study of the temporal variability using satellite imagery showed that large variations in the surface signature of the two gyres occurs and that one or the other gyre can actually disappear. *Viúdez et al.*, [1994] found in the entire Alboran a wavelike front coupled with two anticyclonic gyre-cyclonic eddy systems.

The eastern boundary of the EAG (when present) forms sometimes a well defined feature called the Almería-Oran Front [*Tintoré et al.*, 1988]. This front results from the convergence, south of Cape Gata, of new MAW and longer resident (and more saline, $S > 37.5$) MAW. *Tintoré et al.*, [1988] described this very intense density front as limited to the upper 300 m and with an associated south-eastward baroclinic current ($50-100 \text{ cm s}^{-1}$). Part of this flow continues eastward and initiates the Algerian Current, confined to the upper 150 m and characterized by a transport of $0.4 - 0.5 \text{ Sv}$ [*Arnone et al.*, 1990]. In summary, these studies in the eastern Alboran basin show

that two very different circulation patterns are generally found: one associated with the existence of the EAG and sometimes the Almería-Oran Front, and the other with no gyre and a pronounced eastward flow at Cape Tres Forcas (see *Heburn and La Violette*, [1990], Figures 1 and 2).

However, even after all these international programs several questions still remain without answer. In particular, the physical mechanism responsible for the collapse of the EAG, the relationship between the gyre and the Almería-Oran density front, and the importance of mesoscale dynamics in the eastern Alboran, are still unknown. The goal of this paper is to address these questions. The work is organized as follows: in Section 2 we briefly present the data collected during an intensive study carried out from March to May 1990. Due to the amount of data available, we identify several important topics that are described in Section 3. In particular, we describe the large scale structures as observed from March 6 to 15, the physical characteristics of the eastward jet found in the southern region and its bio-chemical implications, and also describe the northward jet found in the northeastern Alboran. In the discussion Section, emphasis is made on the characterization of an intermediate state of the circulation and on the importance of mesoscale variability as inferred from comparison between ADCP and geostrophic velocities. Finally, a sketch of the circulation pattern described in this study is presented and discussed.

3.2 Data

The field experiment was carried out from March 6 to April 30, 1990. An extensive dataset from different sources, including AXBT, CTD, ADCP and current meters was obtained. In this section we briefly present the different phases of this field experiment.

On March 9, a 6 hour flight was carried out on a Search and Rescue (SAR) instrumented aircraft at an altitude of 600 feet and a speed of 120 knots. The aircraft was equipped with a RF receiver and data were continuously received onboard. Sippican AN/SSQ-36 expendable bathythermographs (AXBT) were dropped every 10 miles. Temperature accuracy as indicated by the manufacturer is ± 0.2 °C, depth accuracy $\pm 2\%$. Radiofrequency interference caused bad receptions for those AXBT dropped near the coast (shallow waters) and resulted in 46 successful drops (Figure 1). Bad weather conditions did not allow samplings to be made in the southern Alboran Sea.

Satellite imagery for the period March 1 through April 30 have been also analysed. Four NOAA 10 AVHRR (Advanced Very High Resolution Radiometer) were selected from a set of approximately 16 scenes of the Alboran basin. These are AVHRR scenes (channel 4) and represent relative sea surface temperature, where the darker shades represent warmer water. The image

for March 16 1990 (Figure 3) is presented at the full resolution of the satellite sensor and in a Mercator projection. All image processing was performed using the NASA developed Sea Pack image processing system [McClain *et al.*, 1992].

The region south of Cape Gata was sampled onboard the R/V García del Cid from March 6 to 15 using a Neil Brown CTD. Vertical casts (Figure 1) were made at 49 stations to determine the vertical structure. Distance between stations was usually around 10 miles except in a west-east cross section, south of Cape Gata, where more intense sampling was made. In addition, continuous surface temperature and salinity were also recorded. Horizontal components of velocity were continuously monitored using a ship mounted ADCP with vertical resolution of 8 m and a maximum depth of 300 m. Five minute averages were carried out, implying a horizontal resolution of 1.5 km. At every station, the continuous monitoring was interrupted and ADCP data were then collected while the ship remained stationary.

Finally, two moorings with 4 Aanderaa current meters each were anchored south of Cape Gata at site B ($36^{\circ} 31.35' N$; $1^{\circ} 37.79' W$) and site C ($36^{\circ} 32.79' N$; $2^{\circ} 01.96' W$), from March 9 to May 15 (Figure 1). The first mooring (B) was deployed over a submarine ridge at a depth of 760 m with current meters placed at 30, 60, 300 and 600 m. The second (C), located 30 km apart, was deployed at a depth of 1100 m, with current meters placed at 30, 60, 300 and 800 m. Sampling period was set to 30 minutes. Figure 2 shows the data obtained for the two moorings at the different depths.

3.3 Results

In this section we initially present the large scale structures detected using satellite imagery, AXBT and CTD data. Next, we study the smaller scale structures detected in the southern and northern Alboran Sea as obtained from CTD and ADCP data and examine their biological effects. Finally, we present the results obtained from the two current meter moorings.

3.3.1 Large scale structures

Satellite imagery for March 16, Figure 3, indicate that in all the Alboran Sea the horizontal surface temperature gradients were weak. However, northeast of Cape Tres Forcas, a well defined gyre/filament was detected. Surface temperature and salinity obtained from CTD and AXBT data were in the range $15-16^{\circ} C$ and $36.4-36.9$. Figure 4 shows that, below the layer of new MAW, a well defined vertical temperature gradient, approximately 40 m thick, was observed. This interface between new and older MAW was also detected in the southern region characterized by strong temperature and

salinity vertical gradients (15.00 —14.00 ‰ ; 37.2 —38.0). Two regions with large horizontal temperature gradients can be also observed (Figure 4) near the Strait of Gibraltar, where the most abrupt adjustment takes place, and south of Cape Gata where the Almería-Oran Front had been observed in previous studies [Tintoré *et al.*, 1988; Arnone *et al.*, 1990].

3.3.2 The eastward jet in the southern Alboran

Northeast of Cape Tres Forcas, a well-defined front was detected below 30 m. Since temperature and salinity effects are additive we only show the resultant density field (Figure 5a). The vertical σ_t distribution shows that this front was found from 30 to 200 m and was characterised by a width of the order of 37 km (20 miles). The stronger density gradients were found between 100 and 200 m (1 σ_t unit in a horizontal distance of 18 km) and were also found at similar latitudes in vertical sections 3 and 5, but 10 km northward in vertical section 4. This northward shift is also visible in Figure 3 and is confirmed by independent ADCP data. Note the doming of isopycnals observed near 36° N between 50 and 100 m (Figure 5a) indicative of strong horizontal shears. This doming was not observed in the other two north-south vertical sections (vertical section 4 in Figure 6a, and section 5 very similar to section 4, not shown). The ADCP eastward velocity component associated with this density gradient (Figures 5b and 6b) was strong reaching values of 80 cm s⁻¹ at 20-30 m. Transport computations showed the total eastward integrated current was high, of the order of 2.4 Sv for vertical section 3, and 2.8 Sv for vertical section 4. As indicated above for the density gradients, the core of the eastward jet (at 20-30 m, 60-80 cm s⁻¹) was observed at different latitudes in vertical sections 3, 4 and 5. The north-south components of the core of the jet were 20, 0 and (-40) cm s⁻¹ in vertical sections 3, 4 and 5 respectively (Figures 5c and 6c), and as a result, the jet had negative vorticity (see also the horizontal distribution of ADCP data, Figure 7). The surface signature of this jet can now be traced in Figure 3 that shows a circular gyre/filament of warm water developing in the southern region whose northern part coincides with the surface location of this jet.

Given the significance of this well defined eastward jet we have tried to establish its biological and chemical effects. The distributions of SiO₂ (Figure 5d) and NO₃ (not shown) show a dome located north of the jet (36° N) and suggest that upward water advection occurred on the northern side of the jet. Accordingly the chlorophyll distribution for vertical section 3 (Figure 5e) showed maxima in the same location.

3.3.3 Northward jet in the northeastern Alboran

The vertical distributions of temperature, salinity and density for CTD vertical section 1 are shown in Figures 8a,b and c. The vertical distribution of σ_t (Figure 8c) shows significant density gradients present from the surface down to 150 m. A similar feature was observed in vertical section 2 (not shown). The largest gradient was located at 100 m ($0.5 \sigma_t$ in 18 km), while at the surface the horizontal temperature range was smaller than 0.75°C (Figure 8a). The satellite imagery (figure 3) shows a boundary region between warm and cold water, at $1^\circ 1' \text{W}$ and $36^\circ 40' \text{N}$, that coincides with the western limit of this northward jet. The analysis of the ADCP data in vertical sections 1 and 2 also show the existence of this northward jet, whose north-south velocity component is shown in Figure 8c. The entire jet occupied the first 110 m with a horizontal northward transport of $\sim 1.6 \text{ Sv}$. The core (maximum velocities of 50 cm s^{-1}) was located at $0^\circ 40' \text{W}$ between 20 and 30 m.

3.3.4 Current meter results

Current meter data were analysed to investigate the magnitude of high and low frequency motions. Low frequency currents were obtained using a low-pass complex filter with a cutoff period of 33 hours. The residual current at 30 and 60 m had a mean value of 10 cm s^{-1} to the southeast (note that this is approximately the same direction as the expected current associated with the Almería-Oran Front). No significant differences were found in the low frequency currents at 30 and 60 m on both the B and C moorings. However an exception was found in the last part of the recorded period (from April 17 to the end). During this period B30 and B60 indicate a progressive rotation from south-east to the north-east with an associated amplitude increase reaching 35 cm s^{-1} (Figure 9a). This surface current modification was associated with a temperature increase and a salinity decrease suggesting the presence of new MAW. At 300 and 600/800 m, the residual current was only $1\text{-}2 \text{ cm s}^{-1}$ without dominant direction (not shown). At higher frequencies we found strong inertial components (with maximum amplitudes of 30 cm s^{-1}) in the upper layer (30, 60 m, Figure 9b). This high frequency component of the velocity should be carefully analysed and taken into account before detailed analysis of ADCP data in the Alboran Sea is made. The inertial component at 300 and 600 m was smaller, though still significant ($5\text{-}10 \text{ cm s}^{-1}$). Inertial amplitudes decayed in a few days. Also, it is important to note, that a small tidal component (semidiurnal, Figure 9c) was detected with 10 cm s^{-1} amplitude at 30-60 m, and about $5\text{-}10 \text{ cm s}^{-1}$ at 300-600 m.

3.3.5 Geostrophic computations

Geostrophic velocities were computed using 300 m as the reference level, similar to the reference level taken with the ADCP (i.e., the ADCP data at any point are the deviation from the mean ADCP value around 300 m). This choice allowed us to compare the geostrophic and ADCP currents. Figure 10a shows that the eastward jet previously described was approximately in geostrophic balance. The slight differences can be explained by the discrete sampling showed here. Continuous ADCP data (Figure 7) actually describe in detail the core of the jet with maximum values for the east component of $\sim 100 \text{ cm s}^{-1}$ in vertical section 3, and 90 cm s^{-1} in section 4. An important difference was found at mid-depth (50 m) where the ADCP data indicated maximum velocities, while geostrophic computations showed maximum velocities at the surface. North of the jet, the westward geostrophic current reached maximum values of 50 cm s^{-1} , significantly higher than the 20 cm s^{-1} ADCP values. Differences between ADCP and geostrophic computations also exist in vertical section 3, near $36^\circ 20' \text{ N}$. These differences are clearly high (larger than the expected maximum magnitude of inertial waves at this depth) and suggest the existence of transient adjustment processes, likely associated with mesoscale variability. On the other hand, in vertical section 4, the same westward current (Figure 6b, 30 cm s^{-1} core) extends down to 200 m and is comparable to the geostrophic computations shown in Figure 10b. The northward current observed in Figure 8d was also mainly geostrophic.

3.4 Discussion

Our analyses of in situ data collected in March 1990 describe the existence of a strong eastward jet with negative vorticity as the main feature present in the eastern region. In this section we discuss the results presented and suggest that this new circulation pattern (not previously described using “in situ” data) was actually a transition state, intermediate between the fully developed EAG (Viúdez *et al.*, [1994]) and the Lanoix [1974] state).

In all the region sampled, the upper layer was occupied by new MAW (with salinities between 36.4 and 36.9). This is fairly different from previous studies where more saline waters (~ 37.8) were found west of the Almería-Oran Front [Tintoré *et al.*, 1988; Arnone *et al.*, 1990]. In our study the two current meter moorings (B and C) and several CTD and AXBT stations (i.e. between $1^\circ - 2^\circ \text{ W}$ and $36^\circ - 36^\circ 40' \text{ N}$) made in the area where the Almería-Oran Front had been previously reported did not show clear evidence of the front in the upper layer. Neither a fully developed gyre/front structure, or an eastward jet with positive vorticity near the Morocco coast

were present. Instead, we found a well defined eastward jet with negative vorticity in the southern region. This eastward jet is similar to the one described by *Lanoix* [1974] except that the one described here has negative vorticity. This difference and the presence of a circular pattern in the satellite thermal image (whose northern part coincides geographically with the jet, Figure 3) suggest that the state of the circulation in the eastern Alboran basin in March 1990, was an intermediate state where the EAG was not fully developed and that instead, a smaller anticyclonic gyre was observed in the southern part of the eastern Alboran basin. A sketch of the new circulation pattern in the upper layer (~ 50 m) is shown in Figure 11. This state would correspond to the satellite image of July 07 1982 in the history of the gradual redevelopment of the EAG [*Heburn and La Violette* 1990]. The hypothesis that this jet is part of a small anticyclonic gyre is strongly reinforced by transport values. The jet has a transport of about 2.8 Sv, a value higher than previously reported computations for the Algerian Current. For example, *Arnone et al.* [1990] found only 0.4–0.5 Sv at 3° E, in May–June 1986, similar to the geostrophic transport computed by *Perkins and Pistek* [1990]. The total eastward transport in the eastern Alboran basin when the EAG was well developed in October 1992 was 2.2 Sv, with 1.2 Sv associated with the gyre and the other 1 Sv with the wave-like front [*Viúdez et al.*, 1994]. The high value of 2.8 Sv found in March 1990 also suggests the existence of a splitting of the flow that recirculates closing the EAG and that also forms, eastward of the gyre, the origin of the Algerian Current [*Heburn and La Violette*, 1990; *Viúdez et al.*, 1994].

The latitude of the two current meters moorings ($\sim 36^\circ 30'$ N) marks the northern boundary of the Almería–Oran front when observed. At the beginning of the study period both current meters were clearly westward of the northward jet described in Figure 8d. As a result, the shift in current meter data observed only at B, suggests that the northward jet had shifted its initial location to a more westward location. It is frequent to observe from satellite imagery a northeastward current along Cape Gata when the EAG is present [*Heburn and La Violette*, 1990; *Viúdez et al.*, 1994]. Thus the progressive increase of a north-east current measured in the upper current meters might be associated with the formation of the EAG, therefore reinforcing the idea that the March 1990 state was a transient state. Further support for this evolving situation is given by the differences between ADCP and geostrophic velocities. While geostrophic computations mostly generally agree with ADCP data in the eastward (except in the upper 50 m) and northward jet, the presence of important deviations from geostrophy (larger than the expected magnitude of inertial waves) found mainly in the middle of the eastern Alboran basin is indicative of the rapidly changing state of the circulation.

The second important point to be discussed on a global frame is the

importance of mesoscale features. The domes observed from the AXBT data in the northern Alboran basin, near the Spanish coast, reveal the significant mesoscale variability of this region. For example, Figure 4 shows that rising of the new/older MAW interface (between the 14 and 15 °C isotherms) occurs at 36° 20' N, between 3° 30' W and 2° 40' W. This feature is better observed in a northwest-southeast vertical section (section A17 AXBT, Figure 12a), where the entire temperature field between 14 and 15 °C forms a well defined dome. The depth of the 14.5 isotherm (Figure 12b) shows a circular structure that corresponds to a cyclonic eddy. The dynamic effects in the vertical velocity of mesoscale cyclonic eddies found along the boundary of the large scale Western Alboran Gyre have been studied by *Tintoré et al.* [1991] and *Viúdez et al.* [1994]. *Tintoré et al.* [1991] found that the vertical motion associated with these mesoscale eddies was an order of magnitude higher than the large-scale vertical motion. Unstable filamentary features of the Almería-Oran Front have been also recently observed from remote sensing observations [*Davies et al.*, 1993], showing that these filaments have length scales comparable to the front itself, growing and decaying on a timescale of a few days.

In summary, we have described physical and biological observations of the eastern Alboran basin that characterize a transient state of the circulation, intermediate between the fully developed EAG [*Viúdez et al.*, 1994] and the *Lanoix* [1974] pattern. Although the importance of mesoscale structures in the adjustment process has been addressed, their influence on the large scale circulation is still unknown, as it is the case of other Mediterranean sub-basins (e.g. *La Violette*, [1994]). Further studies are needed to clarify the EAG formation (large scale), its relation to the Almería-Oran front and the quantitative importance of mesoscale eddies in the Alboran Sea.

Acknowledgements. This work would not have been possible without the expertise of all the people onboard the R/V García del Cid, specially J. Font, J. Salat, M. Manríquez and A. Castellón (ICM). We gratefully also acknowledge the cooperation of the 801 Squadron of Search and Rescue, based in Palma de Mallorca, from the Ministerio de Defensa, who operated the aircraft. W. Wright (NASA) and P. E. La Violette (MSURC) were essential in the collection of the AXBT data. We thank R. Arnone and P. E. La Violette for processing the satellite images and for useful discussions and editing of manuscript. We are also particularly thankful to A. Folkard and P. Davies (The University of Dundee) for useful discussion on the temporal variability from SST. This study is a UIB contribution to the Euromodel project, funded by E.C. MAST programme (MAS2-CT93-0066) and by CICYT, AMB93-1046-CE. One of the authors (AV) acknowledges a PFPI grant from the CICYT.

REFERENCES

- Arnone, R. A., D. A. Wiesenburg and K. D. Saunders, 1990: The origin and characteristics of the Algerian Current. *J. Geophys. Res.*, **95**(C2), 1587-1598.
- Davies, P. A., A. M. Folkard, and G. C. d'Hières, 1993: Remote sensing observations of filament formation along the Almeria-Oran front. *Ann. Geophysicae*, **11**, 419-430.
- Donde Va? Group, 1984: ¿Donde Va? An oceanographic experiment in the Alboran Sea, The oceanographic report. *Eos Trans. AGU*, **65**(36), 682-683.
- Gascard, J. C., and C. Richez, 1985: Water masses and circulation in the western Alboran Sea and in the strait of Gibraltar. *Progress in Oceanography*, **15**, 157-216.
- Heburn, G. W., and P. E. La Violette, 1990: Variations in the structure of the anticyclonic gyres found in the Alboran Sea. *J. Geophys. Res.*, **95**(C2), 1599-1613.
- Lanoix, F., 1974: Projet Alboran, Etude hydrologique et dynamique de la Mer d'Alboran. *Tech. Rep. 66, NATO, Brussels*. 39 pp. plus 32 figs.
- La Violette, P. E., 1986: Short term measurements of surface currents associated with the Alboran Sea during ¿Donde Va? *J. Phys. Oceanogr.*, **16**, 262-279.
- La Violette, P. E., 1990: The Western Mediterranean Circulation Experiment (WMCE): Introduction. *J. Geophys. Res.*, **95**, (C2), 1511-1514.
- La Violette, P. E. (editor), 1994: Seasonal and interannual variability in the Western Mediterranean. *Springer Verlag/AGU Volume*. In press.
- McClain, C. R., G. Fu, M. Darzi, and J. Firestone, 1992: PC-SeaPack User's Guide Version 4.0. *NASA/Goddard Space Flight Center TM 104557*, 280 pp.
- Parrilla, G., T. H. Kinder, and R. H. Preller, 1986: Deep and Intermediate

Mediterranean Water in the western Alboran Sea. *Deep-Sea Res.*, **33**, 55-88.

Perkins, H., T. Kinder, and P. E. La Violette, 1990: The atlantic inflow in the Western Alboran Sea. *J. Phys. Oceanogr.*, **20**, 242-263.

Perkins, H. and P. Pistek, 1990: Circulation in the Algerian Basin during June 1986. *J. Geophys. Res.*, **95**, (C2), 1577-1585.

Tintoré, J., P.E. La Violette, I. Blade, and A. Cruzado, 1988: A study of an intense density front in the eastern Alborán Sea: The Almería-Oran Front. *J. Phys. Oceanogr.*, **18**, 1384-1397.

Tintoré, J., D. Gomis, S. Alonso, and G. Parrilla, 1991: Mesoscale dynamics and vertical motion in the Alborán Sea. *J. Phys. Oceanogr.*, **21**, 811-823.

Viúdez, A., J. Tintoré, and R. L. Haney, 1994: Three-dimensional structure of the two anticyclonic gyres in the Alboran Sea. *J. Phys. Oceanogr.*, (accepted).

Wang, D. P., 1987: The strait surface outflow. *J. Geophys. Res.*, **92**, 10807-10825.

LIST OF FIGURES

1. The Alboran Sea. CTD, AXBT locations and current meter moorings. The different vertical sections are referenced.
2. Data recorded periods of the current meters.
3. Satellite thermal imagery for March 16. Darker shades represent warmer water.
4. West-east temperature distribution from AXBT data (vertical section A1).
5. South-north vertical distribution in vertical section 3: (a) σ_t , (b) east-west ADCP component (continuous contour line means eastward direction), (c) north-south ADCP component (continuous contour line means northward direction), (d) SiO_2 , and (e) chlorophyll.
6. South-north vertical distribution in vertical section 4 CTD: (a) σ_t , (b) east-west ADCP component (continuous contour line means eastward direction), and (c) north-south ADCP component (continuous contour line means northward direction).
7. Horizontal distribution of ADCP data at 10 m.
8. West-east vertical distribution in vertical section 1 CTD: (a) temperature, (b) salinity, (c) σ_t , and (d) north-south ADCP component (continuous contour line means northward direction).
9. Time series of B60 current meter (60 m). (a) Stick diagram of the low-pass (33 h) filtered, (b) inertial component (U component), and (c) tidal (semidiurnal) component (U component).
10. East-west geostrophic velocity for (a) vertical section 3 CTD, and (b) vertical section 4 (continuous contour line means eastward direction).
11. Upper layer circulation pattern.
12. (a) Temperature distribution in the AXBT vertical section A17, and (b) depth of 14.5 °C isotherm from AXBT data.

Soledad

En ti estás todo, mar, y sin embargo,
¡qué sin ti estás, qué solo,
qué lejos, siempre, de ti mismo!

Abierto en mil heridas, cada instante,
cual mi frente,
tus olas van, como mis pensamientos,
y vienen, van y vienen,
besándose, apartándose,
con un eterno conocerse,
mar, y desconocerse.

Eres tú, y no lo sabes,
tu corazón te late y no lo sientes...
¡Que plenitud de soledad, mar sólo!

Juan Ramón Jiménez
(*Diario de un poeta recién casado*).

Capítulo 4

Three-Dimensional Structure of the Two Anticyclonic Gyres in the Alboran Sea

Álvaro Viúdez¹
Joaquín Tintoré¹
Robert L. Haney²

J. Phys. Oceanogr. (Accepted).

¹Dept. de Física, Universitat de les Illes Balears Palma de Mallorca, Spain.

²Department of Meteorology, Naval Postgraduate School, Monterey, CA, US.

Abstract

The circulation and dynamics of the Modified Atlantic Water have been studied using data from an intensive field experiment carried out between September 22 and October 7, 1992. Data included 134 CTD casts, ADCP and satellite imagery. A well defined wavelike front was observed with two significant anticyclonic gyres in the western and eastern Alboran Sea. Smaller scale cyclonic eddies were also observed. The front separates the more saline, older Modified Atlantic Water ($S > 38$) in the northern region from the fresher, more recent Modified Atlantic Water ($S < 36.8$) in the south. The associated baroclinic jet had a mean transport of 1 Sv and maximum geostrophic velocities of 1.0 m s^{-1} . The three-dimensional structure and spatial scales of both gyres were similar, *i.e.* 90 km long and 220 m deep. In the eastern Alboran, northeast of Oran, the origin of the Algerian Current was also detected with an eastward transport of 1.8 Sv. The general picture can be presented as a structure formed by a wavelike front coupled with two large anticyclonic gyre–small cyclonic eddy systems.

The relative importance of stratification, relative vorticity, and Froude number in the distribution of Ertel's potential vorticity has been examined and potential vorticity conservation is used to infer vertical motion. The vertical velocity forcing has been computed using the quasi-geostrophic Q vector formulation of the Omega equation. It is found that the strong meridional shears due to mesoscale phenomena in the western Alboran play a main role in this forcing. The vertical velocities associated with these mesoscale structures reach maximum absolute values of 15 m/day.

4.1 Introduction

The Mediterranean Sea is a semi-enclosed basin whose large scale circulation is mainly controlled by the excess of evaporation over the fresh water input from precipitation and rivers. A two-layer flow through the Strait of Gibraltar compensates for the water and salt deficit with Atlantic Water (AW, $S < 36.5$) flowing in the upper layer into the Alboran Sea and Mediterranean Water (MW, $S > 38.4$) flowing westward below. Being the westernmost Mediterranean sub-basin, the Alboran Sea is the first to receive the incoming AW. The AW is modified in the Alboran Sea, acquiring characteristics intermediate between the underlying MW and the AW, and is termed Modified Atlantic Water (MAW) or Atlantic-Mediterranean Interface Water (A-MIW; Gascard and Richez, 1985).

The dynamics associated with the incoming AW in the Alboran Sea has been described in several field experiments. The large anticyclonic gyre that is formed west of Cape Tres Forcas (the Western Alboran Gyre, WAG) was discovered in the late sixties (Seco 1959; Donguy 1962). Lanoix (1974) from one month of ship data obtained the dynamic topography field for the entire Alboran sub-basin, showing the WAG and an eastward current along the Moroccan coast in the eastern Alboran. After several field experiments in the western Alboran (Cano and de Castillejo 1972; Gascard and Richez 1985; Heburn and La Violette 1990; Tintoré et al. 1991) including recent international experiments such as *Donde Va?* in 1982 (*Donde Va?* Group 1984; La Violette 1986; Parrilla and Kinder 1987) and the Western Mediterranean Circulation Experiment in 1986 (La Violette 1990) the WAG is considered a quasi permanent feature. More recently, studies concerned with the inflow variability (Perkins et al. 1990) and mesoscale cyclonic eddies (Tintoré et al. 1991) have clarified the dynamical description of the Western Alboran addressing the importance of mesoscale features. An exhaustive recent summary of the field and numerical experiments can be found in Speich (1992).

In the Eastern Alboran Sea less information is available, but several studies (Lanoix 1974; Cheney 1978; Cheney and Doblár 1982; Heburn and La Violette 1990; Viúdez and Tintoré 1994) have shown that a second anticyclonic gyre (the Eastern Alboran Gyre, EAG) or an eastward current along the Moroccan coast can be present. Variations in the structure of the WAG and EAG have been studied by Heburn and La Violette (1990) from satellite imagery, showing that the disappearance of either gyre occurs on a time scale of one to two weeks. In the easternmost Alboran, an intense density front (Almería-Oran Front) is sometimes present, which appears to be controlled by the size and position of the EAG (Tintoré et al. 1988; Arnone et al. 1990).

In summary, the large scale circulation of the MAW in the Alboran Sea shows the presence of an eastward jet, and one or two large anticyclonic gyres lying in the western and eastern Alboran basin. At smaller scales, jet

fluctuations and eddies distort this large scale picture. Both gyres, the jet and the Almería-Oran front were always studied as individual systems (with the exception of the satellite imagery studies), and as a result, a quasi-synoptic 3D dynamical study of the entire Alboran basin was never carried out. The goal of this work is to present the quasi-synoptic physical characteristics, with emphasis on the importance of the mesoscale dynamics (and especially the vertical motions) in the entire Alboran Sea system. With such a purpose we carried out a field experiment over a high resolution regular grid (20' longitude \times 10' latitude) covering the Alboran Sea. We describe how the data were obtained in Section 4.2. From these data we compute the dynamic fields (Section 4.3), the potential vorticity distribution (Section 4.4), and the quasi-geostrophic vertical velocities using the Omega equation (Section 4.5).

4.2 Data

The field experiment was carried out from September 17 to October 7, 1992, on board R/V García del Cid. From September 18 to 19 we sampled the first eight stations (Fig. 1) using a Neil Brown Mark III CTD. For ease of reference we denote the south-north vertical sections using a letter (from A to P) and each station is then identified by the letter of its vertical section plus a number (Fig. 1). Due to a failure in the CTD reception system the casts continued with a Sea Bird SBE - 25 CTD from September 21 (first station, A01) to October 7 resulting in 134 stations in a quasi-regular grid covering the entire Alboran Sea. Distance between stations was usually 20' longitude \times 10' latitude ($\sim 30 \times 18$ km). The vertical profiles were made to 600 m except in coastal regions and in vertical sections D and K where they reached the bottom. The vertical resolution of each CTD profile after filtering and interpolation was 1 m. In addition, continuous surface temperature and salinity data were collected. Horizontal components of velocity were continuously monitored using a ship mounted ADCP with vertical resolution of 8 m and a maximum depth of 300 m. Five minute averages were carried out while under way, implying a resolution of 1.5 km. Satellite imagery for the period September 12 to October 11 have been also analysed. Eight NOAA 11 and NOAA 9 AVHRR (Advanced Very High Resolution Radiometer) images were selected (channel 4) and represent relative sea surface temperature. All selected images were geographically located.

4.3 Observations

At large scale, the density field exhibits a wavelike pattern with two bowls of warm and less saline water. The temperature, salinity and density dis-

tributions at 100 m are shown in Fig. 2. Maximum horizontal gradients of the front at this depth are 1.5°C , 1.2 psu and $2 \sigma_t$ in about 20 km, gradients being stronger in the western Alboran ($\sim 4^{\circ} 00' \text{ W}$). The wavelike front, a result of the incoming Atlantic inflow at the Strait of Gibraltar, separates older MAW (colder and more saline, and therefore denser) located in the northern Alboran Sea, from the more recent MAW (warmer and less saline, and therefore less dense) located in the south. The front extends from Gibraltar to the eastern Alboran basin reaching the African coast the first time west of Cape Tres Forcas ($3^{\circ} 20' \text{ W}$) and the second time near Oran ($0^{\circ} 30' \text{ W}$) where the Algerian Current begins.

The two large bowls of warmer and lighter than ambient water embedded in the southern part of the front are the WAG and EAG. Two mesoscale eddies located southwest of each anticyclonic gyre are also clearly observed between the gyres and the coast. North of the front is a region of homogeneous temperature and salinity (with some exception in the northeastern most sampled region at $1^{\circ} \text{ W } 37^{\circ} \text{ N}$). In summary, the density field presents a wavelike front coupled with two anticyclonic gyre-cyclonic eddy systems.

A clear characteristic of both gyres is the large vertical thickness of the homogeneous salinity layer of recent advected MAW (with $S < 36.6$) which occupies a considerable part of the gyres (Fig. 3). The vertical temperature gradients, however, remain significant here. These characteristics have their origin in the vertical structure of the surface Atlantic inflow (Fig. 4) which presents a homogeneous salinity layer but with vertical temperature gradients. This Atlantic inflow near the Strait of Gibraltar exhibits a well-known (Gascard and Richez 1985) subsurface relative salinity minimum ($S < 36.5$). This relative salinity minimum flows out of the Strait of Gibraltar throughout the Alboran Sea and can be used as a tracer, since, assuming homogeneous mixing, the relative minimum does not lose its relative minimum condition although its absolute salinity value will increase by local mixing (salinity gradients will decrease also). A scheme of this feature is represented in Fig. 5. Although a full exploitation of this feature to map the mean particle trajectories requires a denser sampling, several questions arise from our observations. Subsurface salinity minimum following a 3D path are not easy to visualize, but from Fig. 6 we can infer the different depths and locations of the water with salinity values less than 36.45 psu. Initially, the minimum appears in the Atlantic jet near the Strait of Gibraltar between 0 and 100 m depth. Eastward the minimum fills the core of the WAG from 50 to 150 m. Next, this water is observed between 10 and 40 m near the African coast, west of Cape Tres Forcas, where the flow acquires a northeastward direction, and then follows an anticyclonic path in the EAG at ~ 50 m depth which is observed in an intermittent way due to the discrete sampling. The core of the EAG also has a subsurface salinity minimum, but of a higher value (Fig. 7). Therefore we can infer from these observations that the AW is in some way

advected from the Strait of Gibraltar, across the geostrophic stream function, and into the core of the WAG. We anticipate now that the geostrophic current obtained, if stationary, cannot be responsible for such advection.

A consequence of this homogeneous salinity layer is that whereas, say at 100 m, the salinity gradients reproduce the wavelike front better than the gyres, the temperature gradients reproduce the WAG better than the front (Fig. 2). To measure the relative importance of each contribution to the density field, we have computed the density distribution at 100 m taken into account only temperature or salinity variations. Fig. 8 shows that the temperature gradients at 100 m mainly control the density gradients in the WAG, whereas salinity gradients control the density gradient in the front. The vertical distributions of temperature and salinity in the core of both anticyclonic gyres are quite similar (Fig. 9). Both gyres present a subsurface salinity minimum between 20 and 140 m approximately, but the EAG has higher salinities and lower temperatures, and therefore denser water. Both profiles contrast with the typical vertical distribution north of the front, where a clear thermocline can be observed at about 20–30 m depth.

The vertical extension of the gyres is of the order of 200–220 m, the WAG being deeper (compare $27.0 \sigma_t$ surface) and with stronger density gradients (Fig. 3). However, the surface signature is weak. The horizontal temperature distribution at 10 m (Fig. 10) is quite different from the two gyre system described before, and quite similar to the satellite image (Fig. 11) obtained on September 28, 1992. The most relevant feature in this satellite image is the temperature gradient beginning at Cape Tres Forcas and progressing northeastward, being very similar to the in situ surface temperature distribution. This is a track of the front, but the thermal pattern is not closed and therefore the EAG is not observed. The similarity of both pictures in the western Alboran increases if we ignore the cold filament in Fig. 11 extending from the Spanish to the Moroccan coast following a curved path, which is too narrow to be captured by our sampling. Also, the horizontal extension of the gyres (from the African coast to $\sim 36^\circ 20' N$) is smaller than usually derived from satellite imagery when the gyres reach their maximum width (e.g. Heburn and La Violette 1990).

Between Almería and Oran the front does not acquire the large differences in salinity and temperature which characterize the Almería-Oran density front reported in previous studies (Tintoré et al. 1988; Arnone et al. 1990) but conserves its structure without changes in the gradients. The origin of the Algerian Current can be observed where the front reaches the African coast at about $0^\circ 30' W$. Some indication of a new more relaxed density gradient can be found in the northeastern boundary of the sampled region, but the incomplete sampling prevents further conclusions.

In order to obtain the 3D dynamic topography field, and hence all the dynamic variables, we interpolate the dynamic height data computed at each

CTD station onto a regular grid of $\sim 9.3 \times 6.7$ km, the vertical resolution being 1 m. The objective analysis used was a method of successive corrections using weighting functions normalized in such a way that the result after infinite iterations can be demonstrated to be equivalent to the result of an optimal interpolation (OI) method (Brathset 1986; Franke 1988). The characteristic scale of the weight functions, which plays the role of a correlation function in OI methods, has been estimated by cross validation and has been set equal to 20 km (D. Gomis and M. Pedder, personal communication).

The dynamic topography was computed twice using a reference level of 200 and 300 m respectively, resulting mean differences in the geostrophic transport between stations of about 10 %. The 200-250 m level is the approximate zero level separating eastward-flowing AW from westward flowing MW and has been used frequently in geostrophic computations (e.g. Lanoix 1974; Perkins et al. 1990). In order to include the crucial dynamic information in the coastal zones where water depth is only 200 m, especially at the african coast, and to compare our results with previous works we decided to take the reference level at 200 m. The results are summarized in Figs. 12 and 13. The wavelike jet dominates the circulation, coupled with two anticyclonic gyre-cyclonic eddy systems. We will use the geostrophic transport function (Fig.13) to distinguish unambiguously between the wavelike jet or wavelike front (wavelike isolines) and the gyres (closed isolines). Maximum values of geostrophic velocity are about 1 m s^{-1} in the Atlantic jet north of the WAG. Note that from this geostrophic circulation the core of the gyres are isolated from the jet, and therefore the geostrophic circulation cannot produce the interchange of water between jet and gyres as we previously described for the AW. The ADCP data reproduces a circulation very similar to the geostrophic one, both anticyclonic gyres being well observed (Fig. 14). The ADCP data requires a posterior careful processing, calibration and filtering of tidal and inertial waves, and therefore a limited use is made of this data here. Nevertheless, from Fig. 14 we can observe the clear deviation from geostrophy of the flow at $5^\circ \text{ W } 35^\circ 50' \text{ N}$. This ageostrophic circulation, pointing south-eastward, might be responsible for advecting AW into the core of the WAG.

The geostrophic transport (from 10 to 200 m, Fig. 13) of the wavelike jet is very close to 1 Sv, whereas the mean geostrophic transport of the WAG and EAG is 1.6 and 1.2 Sv respectively. It must be noted that the jet transport (~ 1 Sv) differs from the input and output transport in the Alboran Sea. The input transport between stations A01-A03 and the output between stations P10-P08 (origin of the Algerian Current) is 1.8 Sv. Such variations are due to the recirculation and splitting of the flow that takes place mostly south of the main jet.

The geostrophic relative vorticity field (Fig. 15) shows the importance of several mesoscale phenomena. Negative relative vorticity is associated with the large anticyclonic gyres, values being higher in the WAG where

$\zeta = -0.6f \sim -5 \times 10^{-5} \text{ s}^{-1}$ ($f = 8.57 \times 10^{-5} \text{ s}^{-1}$ is the planetary vorticity at 36° N), whereas large positive values are due to three mesoscale phenomena (A, B and C in Fig. 16): (A) the cyclonic eddies, $\zeta = 0.4f \sim +3.5 \times 10^{-5} \text{ s}^{-1}$; (B) the curvature change of the jet west of Cape Tres Forcas, $\zeta = 0.4f \sim +3.5 \times 10^{-5} \text{ s}^{-1}$; and (C) the strong meridional shear $-\partial u/\partial y$ (located at $4^\circ 30' \text{ W } 36^\circ 10' \text{ N}$) due to the large differences between the speed of the jet (up to 1 m s^{-1}) and the slow waters in the north, $\zeta = 0.6f \sim +5 \times 10^{-5} \text{ s}^{-1}$.

Having described the geostrophic velocity and vorticity field we close this section with some results concerning static and baroclinic stability. Brunt-Väisälä frequency profiles were computed from the 1 m spaced density data using the adiabatic leveling method (Bray and Fofonoff 1981; Millard et al. 1990). The vertical stratification during the cruise (September-October) presents a clear horizontal anisotropy (Fig. 17). The largest values of squared Brunt-Väisälä frequency N^2 (200-300 cycles²/hour²) are located at $\sim 30 \text{ m}$ depth. Such large values due to vertical temperature differences, characterize the thermocline, which is present north of the wavelike front, where the currents are very weak. Relative maximum values of N^2 (50-100 cph², in the western Alboran) extends down (Fig. 18) following the tilt of the density field to the bottom of both gyres ($\sim 150 \text{ m}$) where the stratification becomes greater ($100 < N^2 < 140 \text{ cph}^2$ in the WAG, and $60 < N^2 < 100 \text{ cph}^2$ in the EAG).

The distribution of the vertical shear $U_z^2 + V_z^2$ at 100 m is shown in Fig. 19. Isolines of vertical shear follow the wavelike jet reaching absolute maximum values north of the WAG and relative maxima at the changes of flow curvature (crests and troughs). Flows with strong velocity shears may be unstable with respect to small perturbations. Baroclinic instability depends primarily on vertical shear in the jet stream, and therefore, the north of the WAG might be a place for baroclinic instability processes.

4.4 Potential Vorticity

For adiabatic, frictionless motion, Ertel's potential vorticity (PV)

$$q = \rho^{-1}(2\Omega + \nabla \times \mathbf{u}) \cdot \nabla \rho \quad (4.1)$$

is conserved following a particle. Here Ω is the earth's angular velocity, \mathbf{u} is the water velocity relative to the earth, and ρ is the water density. Therefore, if dissipative effects and diabatic processes are insignificant, q is a conservative property and under these conditions it can be used as a tracer of the circulation.

We follow Pollard and Regier (1992) in using the hydrostatic approximation and f -plane geometry, reducing (4.1) to

$$q = -fg^{-1}N^2(1 + \zeta f^{-1} - F), \quad (4.2)$$

where N^2 is the Brunt-Väisälä frequency, ζ is the geostrophic relative vorticity, $F = (U_z^2 + V_z^2)/N^2$ is the Froude number, and (U, V) is the geostrophic velocity. The terms on the right hand side of (4.2) represent contributions to q from the planetary vorticity, the (vertical component of) geostrophic relative vorticity, and the horizontal components of geostrophic relative vorticity, respectively.

In this section we investigate the importance of stratification, relative vorticity and Froude number in the PV distributions and show how this give us an order of magnitude of the associated vertical motion. We will concentrate on the baroclinic jet and WAG between stations D04, D07, E04 and E07 because the flow is approximately zonal reaching the maximum velocities and strongest shears, and because the temporal scale of the motion (the time required to the flow to travel from vertical section D to E at 100 m is less than one day) justifies the assumption of adiabatic motion in the PV conservation. Therefore, from the regular 3D matrix horizontally interpolated (vertical spacing of 1 m) we extract the vertical cross sections closest to the vertical section D and E. Since the maximum distance between the interpolated and the original meridional vertical sections is less than 5 km (half of the x -spacing) we will denote these interpolated vertical sections also as D and E. The different terms in (4.2) are shown in Fig. 20. The zone we are interested in (bounded by a box in those panels) extends from 60 m (below the thermocline) to 140 m including the eastward jet as well as the northern circulation of the WAG. Note that this box is below the effects of surface-layer mixing.

In order to understand the several terms in (4.2) we show first the density distributions (Fig. 20a). Thickness increases with depth between isopycnals greater than $\sim 28.4 \sigma_t$ in vertical section D and greater than $\sim 28.2 \sigma_t$ in vertical section E (observe left side of the box); thickness is more or less constant over that isopycnals, and decreases for smaller density values (right side of the box), and as a result, as we commented in Section 4.3, high stratification values extend down from the thermocline to the bottom of the WAG. Moreover the thickness in vertical section E is smaller in relation to vertical section D. ?

The vertical distributions of N^2 (Fig. 20b) shows the significant increase of stratification in the area bounded by the box between vertical sections D and E. Typical values in the box are 25-30 cph^2 in vertical section D and 50-100 cph^2 in vertical section E. Observe also the smoothed field in section E in relation with Fig. 18 due to the differences between horizontal OI and vertical local bivariate interpolation method.

The zonal geostrophic velocity distribution (Fig. 20c) for vertical section

D shows the strong eastward flow reaching maximum velocities of 100 cm s^{-1} at 10 m depth. The zonal geostrophic velocity is close to zero in the core of the WAG, while the westward flow (corresponding to the southern WAG) reaches maximum values of $\sim 60 \text{ cm s}^{-1}$. The eastward flow slows in vertical section E (maximum velocities of 60 cm s^{-1}) at the same time that it becomes wider (from station E3 to E8). The speed of the flow in the box decreases by about 20 cm s^{-1} whereas the westward flow remains very similar in both vertical sections.

The relative vorticity distribution ζ/f (Fig. 20d) in vertical section D presents a clear separation between positive and negative values. The eastward flow is divided in two symmetric parts: a cyclonic (corresponding mainly to the wavelike jet) and an anticyclonic part (corresponding mainly to the WAG). That is because the positive relative vorticity of the wavelike jet between stations D5 and D6 is produced by meridional shear (the curvature of the jet being here small). This separation occurs approximately in the middle of stations D5 and D6. The WAG has two vertical regions of high relative vorticity separated by a region of smaller relative vorticity in the center of the gyre where the horizontal velocity is uniform near zero (Fig. 20c). Maximum relative vorticity values are about $\pm 0.6f$ in the first 30 m and typical values of $\pm 0.3f$ in the box in vertical section D. Vertical section E shows quite a different picture. Although the relative vorticity in the southern part of the WAG is similar, the relative vorticity corresponding to the eastward flow has decreased to $0.1f$ (a decrease of 50% in relation with section D) due to the smaller meridional shear. Observe also the vertical tilting of ζ isolines produced by the vertical tilting in the zonal geostrophic velocities.

The geostrophic vertical shear $U_z^2 + V_z^2$ (Fig. 20e) reaches maximum values in the eastward flow of $50 \times 10^{-6} \text{ s}^{-2}$ at $\sim 120 \text{ m}$ in section D, and $40 \times 10^{-6} \text{ s}^{-2}$ in section E. Note how the strong vertical shear is confined to a narrow area between stations D4 and D7 (due to the vertically oriented frontal surface), while the vertical shear in section E occupies a wider area. This is a result of the different slope of maximum density gradient with respect to depth in vertical sections D and E. Vertical section D presents a vertically oriented frontal area between stations D4 and D7, while vertical section E presents a sloping of the frontal zone (this is also clearly observed from the zonal geostrophic velocity distributions in Fig. 20c). It is well-known (e.g. Holton 1979, p. 242) that a stationary frontal zone must slope with depth: a vertically oriented frontal surface is not a baroclinically stable configuration. It follows that the configuration of the eastward jet is baroclinically more stable in vertical section E than in vertical section D.

A change in the Froude number $(U_z^2 + V_z^2)/N^2$ in (4.2), along with conservation of q , suggest a possible conversion of horizontal relative vorticity to vertical vorticity. The vertical distributions of F (Fig. 20f) can be explained

in terms of the vertical shear and stratification. Large values of the Froude number (0.4 in section D and 0.2 in section E) are located in the eastward flow at about 100 m, and are of the same order as ζ/f in the box. Both distributions exhibit a similar vertical structure (the vertical tilt of vertical shear in section E is compensated by the tilt of stratification), but F values in section E have decreased about 50% in relation to section D.

The resulting PV distribution is shown in Fig. 20g. In vertical sections D and E large negative values of relative vorticity dominate the PV distribution altering the PV field produced by the rather uniform horizontal distributions of stratification from the surface to ~ 80 m (places A, B and C in Fig. 20g). In the left side of the box in section D negative relative vorticity and large Froude number combine to reduce the absolute PV, whereas in the right side positive relative vorticity and large Froude number compensate each other increasing absolute PV. In section E however the combined effects of relative vorticity and Froude number are small compared to 1, and therefore the PV distribution is very similar to the N^2 distribution. Comparing both PV fields in the upper part of the two boxes we can observe how PV has been advected from box D into box E smoothing the PV gradients between surface (eastward jet) and deep (bottom of the WAG) PV distributions. A series of plots (for vertical section D, for the vertical section in the middle of D and E, and for section E) of PV and density distributions in the box is shown in Fig. 21. The three small areas represent three particles of fluid limited by the same density and PV values, labeled A, B and C. From vertical section D to E we can observe how particles move southward (to the left side of the box), particles A and B have a downward motion, meanwhile particle C is more static. Therefore we can infer that, between vertical sections D and E, besides of the southward advection due to the small horizontal curvature of the flow, downward motion must take place in the middle of the box, with a zone of zero vertical motion to its right. An order of magnitude of this vertical motion can be given if local changes in the PV are neglected. In this case the vertical motion of a zonal flow implies

$$(u, w) \cdot \left(\frac{\partial q}{\partial x}, \frac{\partial q}{\partial z} \right) = 0. \quad (4.3)$$

Since the trajectory of the fluid particle must be on a q -surface

$$dq = \frac{\partial q}{\partial x} dx + \frac{\partial q}{\partial z} dz = 0$$

over the trajectory, and from (4.3), on a q -surface, and in finite-difference form

$$w = -u \left(\frac{\partial q / \partial x}{\partial q / \partial z} \right) = u \frac{\Delta Z}{\Delta X}, \quad (4.4)$$

where ΔZ and ΔX are the spatial increments in the particle trajectory. Since the trajectory of the four fluid particles has been previously obtained we can compute the order of magnitude of their vertical motion. Using $u = 0.6 \text{ m s}^{-1}$, the mean eastward (along-front) horizontal geostrophic velocity at 80 m, $\Delta X = 30 \text{ km}$, the distance between interpolated vertical sections, and $\Delta Z = 10 \text{ m}$ the vertical displacement, then $w = \Delta Z \times u / \Delta X \sim 20 \times 10^{-5} \text{ m s}^{-1}$.

4.5 Vertical velocity from QG theory

Vertical velocities on wavelike circulations have been obtained in several previous works, most notably with Gulf Stream meanders (Chew et al. 1985; Bower 1989). Usually the results agree well with the theory of baroclinic waves which predicts that upward vertical motion takes place upstream (downstream) of the crest (trough) and downward vertical motion takes place downstream (upstream) of the crest (trough) (e.g. Palmén and Newton 1969, p. 144; Holton 1979, p. 136). In this situation the differential vorticity advection term in the Omega equation (see e.g. Holton 1979, p. 136) plays the main role in forcing the vertical velocities. In the Alboran Sea the vorticity field is modified by the presence of the inflow at the Strait of Gibraltar (which produces strong horizontal shears) and by the presence of coastal boundaries. Furthermore, mesoscale processes (eddies and meanders along the jet) distort the typical vorticity field of an unbounded wavelike circulation. The vertical motion associated with large scale and mesoscale circulation in the Alboran Sea was studied by Tintoré et al. (1991) who found that vertical velocities due to mesoscale phenomena are an order of magnitude larger than the vertical motion associated with the large-scale gyres.

A derivation of the generalized Omega equation without cancellation of terms on the f -plane, without heating and friction, is given in the Appendix. See also the Appendix for the definition of the symbols used. Equation (4.9) establishes that in quasi-geostrophic theory, on the f -plane, the vertical velocity is forced solely by the divergence of \mathbf{Q} . Furthermore if ageostrophic motion is neglected in the thermodynamic equation then

$$\left(\frac{\partial}{\partial t} + \mathbf{V} \cdot \nabla\right) \nabla \rho = \frac{-\rho_0}{2g} \mathbf{Q}, \quad (4.5)$$

and \mathbf{Q} is proportional to the time rate of change of the density gradient moving with the horizontal geostrophic velocity (Hoskins et al. 1978). The \mathbf{Q} field at 100 m is shown in Fig. 22. In the northwestern part of the WAG ($4^\circ 30' \text{ W}$, $36^\circ 00' \text{ N}$) $-\mathbf{Q}$ vectors point northward (\mathbf{Q} southward) in a similar direction to the horizontal density gradient. Therefore, the fluid particles following geostrophic motion in this region have tend to increase their horizontal density gradient (as a result, the geostrophic transport function indicates a zone

of confluence, Fig. 13). On the other hand, in the northeastern part of the WAG (4° 00' W, 36° 00' N) $-\mathbf{Q}$ vectors point southward (\mathbf{Q} northward) in a direction opposite to the horizontal density gradient, and therefore the fluid particles must have a tendency to decrease their horizontal density gradient (as a result, the geostrophic transport function indicates a zone of diffuence). Similar features can be observed in the south of the WAG and north of the EAG and a confluent zone at the beginning of the Algerian Current. The north of the gyres, therefore, can be associated with zones of frontogenesis, and the pattern of vertical velocities could be similar to the four-quadrant model (e.g. Carlson, p. 366) for a confluent jet streak (a core of locally maximum wind speeds, usually in the upper troposphere), i.e., confluent in the entrance and diffluent at the exit. Ageostrophic motion in this model is related to the flow acceleration at the jet entrance and deceleration at the jet exit and therefore it is directed toward low pressure at the jet entrance and toward high pressure at the jet exit. This results in convergence in the left entrance and right exit regions, and divergence in the right entrance and left exit regions.

The $\nabla \cdot \mathbf{Q}$ term was computed at each grid point using central differences directly from the dynamic topography field (in such a way that a maximum of five grid points in each horizontal axis was required) using the expanded expression

$$\begin{aligned} \nabla \cdot \mathbf{Q} = 2f(& -U_{xx}V_z - U_xV_{xz} + V_{xx}U_z + V_xU_{xz} \\ & -U_{yy}V_z - U_yV_{yz} + V_{yy}U_z + V_yU_{yz}) \end{aligned}$$

and the contribution of each term was analysed. The result showed that $U_{yy}V_z$ (meridional change of meridional shear U_y times vertical shear V_z) is dominant. The empirical error in the term $U_{yy}V_z$ at 100 m can be roughly estimated assuming a random error in the density data from 200 to 100 m to be $\varepsilon_\rho = 10^{-2} \text{ kg m}^{-3}$. Using a trapezoidal rule of integration to obtain the dynamic height from specific volume anomalies the error in the geostrophic velocity U obtained from a second order derivative (e.g. Atkinson 1988, p. 319) is $\varepsilon_U(100 \text{ m}) \sim (1/3) \times 10^{-2} \text{ m s}^{-1}$, which implies $\varepsilon_{U_{yy}} = 4\varepsilon_{U_y}/\Delta y^2 \sim (1/4) \times 10^{-9} \text{ m}^{-1} \text{ s}^{-1}$. The error in V_z can be obtained from the "thermal wind" relation (4.7) $\varepsilon_{V_z} = g\varepsilon_\rho/(f\rho\Delta x) \sim (1/8) \times 10^{-3} \text{ s}^{-1}$. And finally $\varepsilon_{U_{yy}V_z} \sim ((\varepsilon_{U_{yy}}V_z)^2 + (U_{yy}\varepsilon_{V_z})^2)^{1/2} \sim 12 \times 10^{-13} \text{ m}^{-1} \text{ s}^{-2}$ for high values of V_z ($5 \times 10^{-3} \text{ s}^{-1}$) and U_{yy} ($10^{-9} \text{ m}^{-1} \text{ s}^{-1}$), resulting $2f\varepsilon_{U_{yy}V_z} \sim 20 \times 10^{-17} \text{ m}^{-1} \text{ s}^{-3}$, which implies an error of 30% in the large divergence of \mathbf{Q} values.

Divergence of \mathbf{Q} at 100 m can be identified from the \mathbf{Q} field (Fig. 22). Divergence of the tendency of the density gradient of the fluid following geostrophic motion takes place mainly in the ~~the~~ northern and southern part of the WAG. In the classical quasi-geostrophic formulation of the Omega

equation the forcing is discussed in terms of geostrophic differential relative vorticity advection and the Laplacian of density advection. A drawback of this interpretation is that the two expressions are not fully independent: there exist a high degree of cancellation and addition between both terms. The result is that, in practice, it is very difficult isolate the two effects. The term $2f^{-1}\Psi_{yyy}\Psi_{xz}$ (Ψ being the dynamic height), which is the most important one in our computations, is a contribution from the term $-f\frac{\partial U_y}{\partial y}\frac{\partial V}{\partial z}$ in the differential vorticity advection, and from the term $g\rho_0^{-1}\frac{\partial^2 U}{\partial y^2}\frac{\partial \rho}{\partial x}$ in the Laplacian of density advection. Although in the northern WAG the term $-2f^{-1}\Psi_{yyx}\Psi_{yz}$ becomes also significant (which comes from $-f\frac{\partial U_y}{\partial x}\frac{\partial U}{\partial z}$ in the differential vorticity advection, and from $g\rho_0^{-1}\frac{\partial^2 V}{\partial y^2}\frac{\partial \rho}{\partial y}$ in the Laplacian of the density advection) the importance of $2f^{-1}\Psi_{yyy}\Psi_{xz}$ means that in the north of the WAG, a basic assumption of the four-quadrant model, which is for the pure confluent case where $\partial\rho/\partial x = 0$, does not hold. Since the magnitude of relative vorticity advection usually increases with z (z positive upward) rising motion occurs in areas of positive vorticity advection, and downward motion in areas of negative vorticity advection. The effect of the Laplacian of the density advection produces a variant of the four-quadrant model rotating counterclockwise the pattern in the case of dense advection (see e.g. Carlson 1991, Fig. 15.3). The contributions to $\nabla \cdot \mathbf{Q}$ from all the terms produce the result shown in Fig. 24. The north of the WAG is similar to the dense advection variation of the quadrant model. West of Cape Tres Forcas, at $3^\circ 20' \text{ W } 35^\circ 30' \text{ N}$, where the direction of the flow changes quickly, there is a negative advection of relative vorticity ($-\mathbf{V} \cdot \nabla\zeta < 0$) in the western part and positive advection of relative vorticity ($-\mathbf{V} \cdot \nabla\zeta > 0$) in the eastern part, which implies downward and upward motion respectively. The presence of the coast, however, can make these results questionable because of the limitation of QG theory in the presence of steep topography.

The Omega equations (4.9) and (4.10) were solved with a vertical spacing of 4 m by a direct matrix inversion method based on the algorithm SYMMLQ (Paige and Saunders 1975) which solves the equations by an algorithm based upon the Lanczos process. Sensitivity tests showed that no significant differences in the absolute values of vertical velocities were caused by the use of $N^2(x, y, z)$ or $\bar{N}^2(z)$ distributions, and the horizontal pattern of w (zones of upward and downward motion) remained unchanged. As boundary conditions we imposed zero vertical velocity in the top, bottom and lateral boundaries. Using $\partial w/\partial z = 0$ at the bottom, did not change the results significantly. The distribution of the w field at 100 m is shown in Fig. 25. This distribution is closely related to the $\nabla \cdot \mathbf{Q}$ distribution, which has been noted already. We have indicated in Fig. 25 the quadrants in the WAG corresponding to the four-quadrant model modified by density advection, and the downward/upward motion upstream/downstream of the trough west of

Cape Tres Forcas. Maximum significant values of $|w|$ are $15-20 \times 10^{-5} \text{ m s}^{-1}$.

The vertical distribution of w in a south-north vertical section between vertical sections D and E (corresponding to the section in Fig. 21b) is shown in Fig. 26. Downward motion occurs in the wavelike front (at 36° N) and upward motion in the north (at $36^\circ 15' \text{ N}$). Such motion agrees with that inferred from the PV and σ_t conservation.

4.6 Discussion

The quasi-geostrophic vertical velocity field associated with a wavelike front coupled with two large anticyclonic gyre-small cyclonic eddy systems has been obtained. Maximum significant values of quasi-geostrophic vertical velocity of $15-20 \times 10^{-5} \text{ m s}^{-1}$ correspond mainly to mesoscale features in the western Alboran Sea (especially the convergence of water in the northern WAG, the western mesoscale cyclonic eddy and the change of curvature of the jet west of Cape Tres Forcas). This order of magnitude agrees with PV conservation along isopycnals. Relative vorticity and Froude number variations were important in the deduction of vertical motion from PV conservation. This agrees with the importance of changes in both horizontal and vertical components of vorticity in the forcing of quasi-geostrophic vertical velocities in the Omega equation. It should be noted that relative vorticity has been neglected in the divergence term, $(\zeta_T + f)w_{zz}$ in (4.8), but relative vorticity advection terms are included in the forcing $\nabla \cdot \mathbf{Q}$ term]. In relation with the vertical velocities obtained in the box in vertical sections D and E it should be noted that, though w is $\sim 10 \times 10^{-5} \text{ m s}^{-1} \sim 10 \text{ m d}^{-1}$, the horizontal advection is also large and therefore the vertical displacements are only about 10 m. The vertical displacements are larger in other areas, e.g. west of Cape Tres Forcas, in the cyclonic eddies, or also in the northeast of the WAG (36° N , $3^\circ 30' \text{ W}$) where $w \sim 5 \times 10^{-5} \text{ m s}^{-1}$ but the horizontal advection is small. Such upwelling in the north of the WAG would be an explanation of the cold narrow filaments observed in satellite imagery. Upwelled cold waters are then advected into the wavelike circulation and are useful tracers of the motion.

A potentially important criticism of our results concerns the synopticity of the analysed fields. Heburn and La Violette (1990) showed from satellite imagery that the disappearances of either gyre occurs on a time scale of one to two weeks. Nevertheless in our satellite imagery -from Sept 19 to Oct 4, 1992- the large-scale pattern was similar, indicating that at least the WAG was always present.

The Alboran Sea remains one with complex dynamics. Perhaps one of the more important problems concerns the development and maintenance of the gyres. The fact that the gyres disappearances do not have a regular pe-

riod makes it very difficult to infer the causes, although some correlation has been found between atmospheric forcing and the disappearances of the gyres (Heburn and La Violette 1990; Perkins et al. 1992). Since horizontal temperature gradients of recent MAW in the gyres are significant in the horizontal density gradients, and these temperature gradients in the gyres result from the incoming temperature of AW at the Strait of Gibraltar, which is related with the upwelled waters in the Atlantic Ocean (Gascard and Richez 1985), it may be reasonable infer that modifications in the surface temperature field incoming from the Strait of Gibraltar should have influence in the geostrophic balance of the flow in the western Alboran. We formulate the gyre maintenance problem as follows: the geostrophic circulation is closed in both gyres; this closed circulation is produced by the presence of light water in the core of both gyres; this light water is *geostrophically isolated* and, due to turbulent mixing, the density gradients in the gyres will decrease until disappear. In other words, geostrophy alone cannot be responsible of the gyres maintenance for a long period of time. On the other hand we have found, from salinity conservation, that surface water interchange between the core of the gyres and the outside must occur, such circulation being ageostrophic (as has been also shown by the preliminary ADCP data). Therefore the gyres, that are mainly in geostrophic balance, require that ageostrophic circulation or temporal variability take place for their maintenance. While this ageostrophic motion would be present at the western part of the WAG, vertical shear (on which baroclinic instability primarily depends) is relatively large at the north of the WAG. Here the strong zonal eastward flow (vertically oriented frontal surface with a large northward component of relative vorticity, U_z) must evolve to a more stable configuration (sloping of the frontal zone with a large negative vertical component of relative vorticity) acquiring anticyclonic motion. This kind of influence on the WAG could be related to the observed fluctuations in the strength of the eastward flow (Perkins et al. 1990). It would be noted that an increase of the anticyclonic motion will decrease the large meridional shear ($\sim +0.6f$) in the north of the jet but will decrease also the anticyclonic vorticity of the WAG ($\sim -0.6f$) in such a way that inertial instability could be important.

The above comments seem to indicate that the dynamics of the western Alboran is mainly a frontal dynamics (more than in the eastern Alboran) where ageostrophic terms must be significant [the importance of the non linear terms in the western Alboran has been also the conclusion of several recent works (Perkins et al. 1990 and Speich 1992)]. In the eastern Alboran new features also emerge from the data. The wavelike front does not acquire the large differences in salinity and temperature which characterize the Almería-Oran density front. This means that such a front is not the eastern boundary of the EAG, i.e. the two phenomena are not necessarily related. Another interesting point concerns the two mesoscale cyclonic eddies. The

existence of these two eddies in a similar position relative to the anticyclonic gyres seems to indicate that they are part of the same stable structure.

Acknowledgements. This work would not have been possible without the expertise of all the people inboard the R/V García del Cid, specially J. Font, J. Salat, M. Manríquez, E. G. Górriz, J. Sánchez, M. Lloret (ICM), J.-M. Pinot and A. Álvarez (UIB). J. L. López-Jurado (IEO) shared generously the CTD profiler. We thank also the courtesy of Moroccan and Algerian authorities and the Service Hydrographique of Alger. We thank J. Casanovas (UV) for processing the satellite images. D. Gomis (UIB) clarified aspects related to OI. Comments of two anonymous reviewers are also grateful. This study is a UIB contribution to the Euromodel project, funded by E.C. MAST programme (MAS2-CT93-0066) and by CICYT, AMB93-1046-CE. Partial support for this study was also obtained from the Office of Naval Research (RLH). One of the authors (AV) acknowledges a PFPI grant from the CICYT.

4.7 Appendix: Derivation of the Omega equation for $N^2(x, y, z)$

The thermodynamic, hydrostatic and vorticity equations are combined to cancel the height-tendency terms in such a way that a generalized Omega equation on an f -plane, without friction and heating, is written as

$$\underbrace{\nabla^2(N^2 w)}_{L_1} + f(\zeta_T + f)w_{zz} + \underbrace{f[\nabla \mathbf{w} \cdot (-V_T, U_T)_z]}_{L_2} \underbrace{- fw(\zeta_T)_{zz}}_{L_3} = \underbrace{f\nabla^2[\mathbf{V}_T \cdot (-V, U)_z]}_{R_1} + \underbrace{f(\mathbf{V}_T \cdot \nabla \zeta_T)_z}_{R_2} + f(\zeta_{ag})_{zt} \quad (4.6)$$

(e.g. Pauley and Nieman 1992). Our objective is to express (4.6) in such a way that analytical cancellation of terms does not occur. The horizontal velocity field $\mathbf{V}_T = \mathbf{V} + \mathbf{v}$ and the relative vorticity $\zeta_T = \zeta + \zeta_{ag}$ are decomposed into geostrophic plus ageostrophic components, the geostrophic velocity satisfying the “thermal wind” relation

$$f(-V, U)_z = g\rho_0^{-1}\nabla\rho, \quad (4.7)$$

where g is the acceleration of gravity, ρ is density and ρ_0 is a mean constant density value. The ageostrophic velocity satisfies the continuity equation

$$u_x + v_y + w_z = 0$$

since the geostrophic velocity is non-divergent ($U_x + V_y = 0$). The term by term decomposition is as follows:

$$\begin{aligned} L_1 &= N^2\nabla^2 w + w\nabla^2 N^2 + 2\nabla \mathbf{w} \cdot \nabla N^2 \\ L_2 &= f \underbrace{\nabla \mathbf{w}_z \cdot (-V, U)_z}_{L_{21}} + f \underbrace{\nabla \mathbf{w} \cdot (-V, U)_{zz}}_{L_{22}} + f[\nabla \mathbf{w} \cdot (-v, u)_z]_z \\ L_{21} &= u_{xx}V_z + v_{xy}V_z - u_{xy}U_z - v_{yy}U_z \\ L_{22} &= g\rho_0^{-1}\nabla \mathbf{w} \cdot \nabla \rho_z = -\nabla \mathbf{w} \cdot \nabla N^2 \\ L_3 &= \underbrace{-fw(\zeta_g)_{zz}}_{L_{31}} - fw(\zeta_{ag})_{zz} \\ L_{31} &= g\rho_0^{-1}w(\rho_{xx} + \rho_{yy})_z = -w\nabla^2 N^2 \\ R_1 &= \underbrace{f\nabla^2[\mathbf{V} \cdot (-V, U)_z]}_{R_{11}} + f \underbrace{\nabla^2[\mathbf{v} \cdot (-V, U)_z]}_{R_{12}} \end{aligned}$$

$$R_{12} = -(u_x V_z)_x + (v_x U_z)_x - u_x V_{zx} + v_x U_{zx} - (u_y V_z)_y + (v_y U_z)_y - u_y V_{zy} + v_y U_{zy} - \mathbf{v} \cdot (\nabla \zeta_g)_z$$

$$R_2 = \underbrace{f(\mathbf{V} \cdot \nabla \zeta_g)_z}_{R_{21}} + \underbrace{f(\mathbf{V} \cdot \nabla \zeta_{ag})_z}_{R_{22}} + \underbrace{f(\mathbf{v} \cdot \nabla \zeta_g)_z}_{R_{23}} + \underbrace{f(\mathbf{v} \cdot \nabla \zeta_{ag})_z}_{R_{24}}$$

$$R_{22} = \mathbf{V} \cdot (\nabla \zeta_{ag})_z + U_z v_{xx} - U_z u_{yx} + V_z v_{xy} - V_z u_{yy}$$

$$R_{23} = \mathbf{v} \cdot (\nabla \zeta_g)_z + \mathbf{v}_z \cdot \nabla \zeta_g$$

$$R_{24} = \mathbf{v} \cdot (\nabla \zeta_{ag})_z + \mathbf{v}_z \cdot \nabla \zeta_{ag}$$

Terms R_{11} and R_{21} can be written in a more simplified way as the divergence of \mathbf{Q} (Hoskins et al. 1978)

$$\mathbf{Q} \equiv 2f(\mathbf{V}_x \cdot \nabla \alpha, \mathbf{V}_y \cdot \nabla \alpha),$$

where $\alpha \equiv g\rho_0^{-1}\rho$.

After simplification the LHS and RHS of the generalized Omega equation are written as

$$\begin{aligned} \text{LHS} &= \nabla \cdot (N^2 \nabla \mathbf{w}) + f(\zeta_T + f)w_{zz} + \underbrace{f(u_{xx}V_z - v_{yy}U_z)}_{D_1} + \underbrace{f[\nabla \mathbf{w} \cdot (-v, u)]_z}_{T_1} - fw(\zeta_{ag})_{zz}, \\ \text{RHS} &= \nabla \cdot \mathbf{Q} + f\mathbf{V}_T \cdot (\nabla \zeta_{ag})_z + \underbrace{f(U_z v_{xx} - V_z u_{yy})}_{D_2} + f\mathbf{v}_z \cdot \nabla \zeta_g + \underbrace{f\mathbf{v}_z \cdot \nabla \zeta_{ag}}_{T_2} + f(\zeta_{ag})_{zt} \\ &\quad + \underbrace{f[-(u_x V_z)_x + (v_x U_z)_x - u_x V_{zx} + v_x U_{zx} - (u_y V_z)_y + (v_y U_z)_y - u_y V_{zy} + v_y U_{zy}]}_{D_3}. \end{aligned}$$

Terms D_1 , D_2 and D_3 can be written as the divergence of a vector \mathbf{Q}_{ag}

$$\mathbf{Q}_{ag} \equiv 2f(\mathbf{v}_x \cdot \nabla \alpha, \mathbf{v}_y \cdot \nabla \alpha),$$

and $\mathbf{Q}_T \equiv \mathbf{Q} + \mathbf{Q}_{ag} = 2f[(\mathbf{V}_T)_x \cdot \nabla \alpha, (\mathbf{V}_T)_y \cdot \nabla \alpha]$. There is still some cancellation between terms T_1 and T_2 that can be avoided if $T_1 - T_2$ is expressed as

$$T_1 - T_2 = \nabla \mathbf{w} \cdot (-v, u)_{zz} - (\nabla^2 u, \nabla^2 v) \cdot (-v, u)_z$$

to obtain

$$\begin{aligned} \nabla \cdot (N^2 \nabla \mathbf{w}) + f(\zeta_T + f)w_{zz} + f\nabla \mathbf{w} \cdot (-v, u)_{zz} - fw(\zeta_{ag})_{zz} &= \\ \nabla \cdot \mathbf{Q}_T + f\mathbf{V}_T \cdot (\nabla \zeta_{ag})_z + f(\nabla^2 U_T, \nabla^2 V_T) \cdot (-v, u)_z + f(\zeta_{ag})_{zt}. \end{aligned} \quad (4.8)$$

At first order of approximation but keeping the N^2 terms [see e.g. Pauley and Nieman (1992) for a scaling discussion] the ageostrophic forcing is neglected in the RHS of (4.8), the relative vorticity ζ_T is considered small

in relation to planetary vorticity f , and terms including products of two ageostrophic factors are also neglected in the LHS of (4.8) to obtain

$$\nabla \cdot (N^2 \nabla \mathbf{w}) + f^2 w_{zz} = \nabla \cdot \mathbf{Q}. \quad (4.9)$$

This equation can be derived in a more direct way from a generalized Omega equation [in terms of the horizontal divergence of the ageostrophic horizontal pseudovorticity (Hoskins 1975)] by the substitution of geostrophic for total velocity gradients (Davies-Jones 1991). It should be noted that (4.9) reduces to the quasi-geostrophic Omega equation if $N^2(x, y, z)$ is replaced by a mean profile $\bar{N}^2(z)$:

$$\bar{N}^2 \nabla^2 w + f^2 w_{zz} = \nabla \cdot \mathbf{Q}. \quad (4.10)$$

REFERENCES

- Akima, H., 1978: A method of bivariate interpolation and smooth surface fitting for values given at irregularly distributed points. *ACM-TOMS*, 4, n.2.
- Akima, H., 1984: On estimating partial derivatives for bivariate interpolation of scattered data. *Rocky Mountain Journal of Mathematics*, 14, n.1.
- Arnone, R. A., D. A. Wiesenburg and K. D. Saunders, 1990: The origin and characteristics of the Algerian Current. *J. Geophys. Res.*, 95, 1587-1598.
- Atkinson, K. E., 1988: *An introduction to numerical analysis*, 2nd. ed., John Wiley & Sons, 693 pp.
- Bower, A. S., 1989: Potential vorticity balances and horizontal divergence along particle trajectories in Gulf Stream Meanders East of Cape Hatteras. *J. Phys. Oceanogr.*, 19, 1669-1681.
- Brathset, A. M., 1986: Statistical interpolation by means of successive correction. *Tellus*, 38A, 439-447.
- Bray, N. A., and N. P. Fofonoff, 1981: Available potential energy for MODE eddies. *J. Phys. Oceanogr.*, 11, 30-47.
- Cano, N. and F. F. de Castillejo, 1972: Contribución al conocimiento del Mar de Alborán III. Variaciones del remolino anticiclónico. *Bol. Inst. Esp. Oceanogr.*, 157, 3-7 plus 18 Figs.
- Carlson, T. N., 1991: *Mid-Latitude Weather Systems*. HarperCollins Academic, London, UK, 507 pp.
- Cheney R. E., 1978: Recent observations of the Alboran Sea frontal system. *J. Geophys. Res.*, 83, 4593-4597.
- , and R. A. Doblar, 1982: Structure and variability of the Alboran Sea frontal system. *J. Geophys. Res.*, 87, 585-594.
- Chew, F., J. M. Bane, and D.A. Brooks, 1985: On vertical motion, diver-

- gence, and the thermal wind balance in cold-dome meanders: a diagnostic study. *J. Geophys. Res.*, **90**, 3173-3183.
- Davies-Jones, R., 1991: The frontogenetical forcing of secondary circulations. Part I: the duality and generalization of the Q-vector. *J. Atmos. Sci.*, **48**, 497-509.
- Donde Va? Group, 1984: Donde Va? An oceanographic experiment in the Alboran Sea. The oceanographic report. *Eos Trans. AGU*, **65**, 682-683.
- Donguy, J. R., 1962: Hydrologie en mar d'Alboran. *Cah. Oceanogr.*, **14**, 573-578.
- Franke, R., 1988: Statistical interpolation by iteration. *Mon. Wea. Rev.*, **116**, 961-963.
- Gascard, J. C., and C. Richez, 1985: Water masses and circulation in the western Alboran Sea and in the Straits of Gibraltar. *Progress in Oceanography*, **15**, 157-216.
- Heburn, G. W., and P. E. La Violette, 1990: Variations in the structure of the anticyclonic gyres found in the Alboran Sea. *J. Geophys. Res.*, **95**, 1599-1613.
- Holton, J. R., 1979: *An Introduction to Dynamic Meteorology*, 2nd ed., Academic Press, 391 pp.
- Hoskins, B. J., 1975: The geostrophic momentum approximation and the semigeostrophic equations. *J. Atmos. Sci.*, **32**, 233-242.
- , I. Draghici, and H.C. Davies, 1978: A new look at the w -equation. *Quart. J. R. Met. Soc.*, **104**, 31-38.
- Lanoix, F., 1974: Projet Alboran, Etude hydrologique et dynamique de la Mer d'Alboran. Tech. Rep. 66, NATO, Brussels. 39 pp. plus 32 figs.
- La Violette, P. E., 1986: Short term measurements of surface currents associated with the Alboran Sea during 'Donde Va?'. *J. Phys. Oceanogr.*, **16**, 262-279.

- , 1990: The Western Mediterranean Circulation Experiment (WMCE): Introduction. *J. Geophys. Res.*, **95**, 1511-1514.
- Millard, R. C., W. B. Owens, and N. P. Fofonoff, 1990: On the calculation of the Brunt-Väisälä frequency. *Deep-Sea Res.*, **37**, 167-181.
- Paige, C. C., and M. A. Saunders, 1975: Solution of sparse indefinite systems of linear equations. *SIAM J. Numer. Anal.*, **12**, 617-629.
- Palmen, E., and C. W. Newton, 1969: *Atmospheric Circulation Systems*. Academic Press, 603 pp.
- Pauley, P. M., and S. J. Nieman, 1992: A comparison of quasigeostrophic and nonquasigeostrophic vertical motions for a model-simulated rapidly intensifying marine extratropical cyclone. *Mon. Wea. Rev.*, **120**, 1108-1134.
- Parrilla, G. and T. H. Kinder, 1987: The physical oceanography of the Alboran Sea. *NORDA Rep.*, **184**, 26 pp.
- Perkins, H., T. Kinder, and P. E. La Violette, 1990: The atlantic inflow in the Western Alboran Sea. *J. Phys. Oceanogr.*, **20**, 242-263.
- Pollard, R. T., and L. Regier, 1992: Vorticity and vertical circulation at an ocean front. *J. Phys. Oceanogr.*, **22**, 609-625.
- Press, W. H., B. P. Flannery, S. A. Teukolsky, and W. T. Vetterling, 1986: *Numerical recipes: the art of scientific computing*, Cambridge University Press, 818 pp.
- Seco, E., 1959: La capa de velocidad cero en el mar de Alborán. *Rev. Ceincas.*, **XXV**, 765-779.
- Speich, S., 1992: Étude du forçage de la circulation océanique par les détroits: cas de la mer d'Alboran. *Doctoral dissertation, Université Paris VI*. 245 pp.
- Tintoré, J., P. E. La Violette, I. Blade, and A. Cruzado, 1988: A study of an intense density front in the eastern Alboran Sea: The Almería-Oran Front. *J. Phys. Oceanogr.*, **18**, 1384-1397.

- , D. Gomis, S. Alonso, and G. Parrilla, 1991: Mesoscale dynamics and vertical motion in the Alboran Sea. *J. Phys. Oceanogr.*, **21**, 811-823.
- Viúdez A., and J. Tintoré, 1994: Time and space variability in the eastern Alboran Sea from March to May 1990. *J. Geophys. Res.*, (accepted).

LIST OF FIGURES

1. The Alboran Sea (bottom topography in m). The different vertical CTD sections are referenced.
2. (a) Temperature ($\Delta = 0.25^\circ\text{C}$), (b) salinity ($\Delta = 0.2$ psu) and (c) σ_t ($\Delta = 0.2 \sigma_t$) horizontal distributions at 100 m. Interpolation method: successive corrections (referenced in the text).
3. (a) Temperature ($\Delta = 0.5^\circ\text{C}$), (b) salinity ($\Delta = 0.2$ psu), and (c) σ_t ($\Delta = 0.2 \sigma_t$) distributions on vertical section 20. Interpolation method: local bivariate (Akima 1978; Akima 1984).
4. (a) Temperature ($\Delta = 0.5^\circ\text{C}$), (b) salinity ($\Delta = 0.2$ psu) and (c) σ_t ($\Delta = 0.2 \sigma_t$) distributions on vertical section A. Interpolation method: local bivariate.
5. Sketch to represent how the relative subsurface salinity minimum S_m flowing throughout the Alboran Sea is used as a tracer. Assuming homogeneous mixing the relative salinity minimum does not lose its minimum condition over the trajectory between points (A) and (B).
6. Isosurface of 36.45 psu. (a) Top view, (b) lateral view. The box is that represented in Fig. 1. The z -spacing between data points is 1 m. The lateral boundary represents the surface limited by the external CTD stations, and not the coastal boundary.
7. Isosurface of 36.7 psu. Western and Eastern Alboran gyres are referenced. The box is that represented in Fig. 1. The z -spacing between data points is 1 m.
8. The density field ($\Delta = 0.2 \sigma_t$) at 100 m due to (a) the observed salinity field and the mean temperature on this layer (14.2°C); (b) due to the observed temperature field and the mean salinity on this layer (37.6 psu). Interpolation method: successive corrections.
9. Temperature, salinity and σ_t profiles at: (a) station D03 (Western Gyre), (b) station L06 (Eastern Gyre), and (c) station G07 (Northern Alboran).
10. Temperature distribution at 10 m ($\Delta = 0.5^\circ\text{C}$). Interpolation method: successive corrections.
11. Satellite thermal imagery (September 28, 1992). Bright blue means colder water.

12. Geostrophic velocity field at 10 m. Reference vector is 1.5 m s^{-1} .
13. Geostrophic transport function at 10 m ($\Delta = 0.2 \text{ Sv}$).
14. ADCP data at 40 m deep. Reference vector is 1 m s^{-1} .
15. Geostrophic vorticity field, ζ/f , at 10 m ($\Delta = 0.2$).
16. Isosurface of positive geostrophic vorticity ($3 \times 10^{-5} \text{ s}^{-1}$). The isosurface of dynamic height of 0 dyn cm is plotted just to locate the wavelike flow. The z -spacing between data points is 1 m.
17. Distribution of the squared Brunt-Väisälä frequency at 30 m ($\Delta = 50 \text{ cph}^2$). Interpolation method: successive corrections.
18. Squared Brunt-Väisälä frequency on vertical section E ($\Delta = 50 \text{ cph}^2$). Interpolation method: local bivariate.
19. Distribution of vertical shear $U_z^2 + V_z^2$ at 100 m ($\Delta = 10 \times 10^{-6} \text{ s}^{-2}$).
20. Vertical distributions in vertical section D and E of: (a) σ_t ($\Delta = 0.2 \sigma_t$), (b) Squared Brunt-Väisälä frequency ($\Delta = 25 \text{ cph}^2$), (c) zonal component of the geostrophic velocity field ($\Delta = 10 \text{ cm s}^{-1}$, solid contour lines indicates eastward direction), (d) relative geostrophic vorticity ζ/f ($\Delta = 0.1$), (e) geostrophic vertical shear $U_z^2 + V_z^2$ ($\Delta = 10 \times 10^{-6} \text{ s}^{-2}$), (f) Froude number $(U_z^2 + V_z^2)/N^2$ ($\Delta = 0.1$), and (g) potential vorticity ($\Delta = 0.5 \times 10^{-9} \text{ m}^{-1} \text{ s}^{-1}$).
21. Vertical distributions of PV ($\Delta = 0.5 \times 10^{-9} \text{ m}^{-1} \text{ s}^{-1}$) and σ_t ($\Delta = 0.2 \sigma_t$) in the box for: (a) vertical section D, (b) vertical section between D and E, and (c) vertical section E. The three small marked areas represent particles of fluid limited by the same values of PV and σ_t .
22. \mathbf{Q} vector at 100 m. Reference vector is $200 \times 10^{-13} \text{ s}^{-3}$.
23. Mean squared Brunt-Väisälä frequency profile (cph^2). Horizontal bars represent the value $\bar{N}^2(z) \pm$ one standard deviation.
24. $\nabla \cdot \mathbf{Q}$ distribution at 100 m ($\Delta = 20 \times 10^{-17} \text{ m}^{-1} \text{ s}^{-3}$).
25. Vertical velocity distribution at 100 m ($\Delta = 5 \times 10^{-5} \text{ m s}^{-1}$).
26. Vertical velocity distribution between vertical sections D and E ($\Delta = 5 \times 10^{-5} \text{ m s}^{-1}$).

Aun cuando el mar es grande,
como es lo mismo todo,
me parece que estoy ya a tu lado...

Ya sólo el agua nos separa,
el agua que se mueve sin descanso,
¡el agua, sólo el agua!

Juan Ramón Jiménez
(*Diario de un poeta recién casado*).

Capítulo 5

Diagnosis of Mesoscale Ageostrophic Motion through Density Dynamical Assimilation: Application to the Alboran Sea

Álvaro Viúdez¹
Robert L. Haney²
Joaquín Tintoré¹

J. Phys. Oceanogr. (Submitted).

¹Departament de Física, Universitat de les Illes Balears, Palma de Mallorca, Spain.

²Department of Meteorology, Naval Postgraduate School, Monterey, CA.

Abstract

The three-dimensional (3D) velocity field is diagnosed through density dynamical assimilation in a primitive equation (PE) model with mesoscale resolution. The ageostrophic motion is computed from fields produced by short-term backward and forward integrations of the PE model initialized with quasi-synoptic CTD data from the Alboran Sea (Western Mediterranean). A weight function is applied to the resulting time-series of model variables to obtain the final, dynamically balanced, density and 3D velocity fields. The weight function is based on the Digital Filter Initialization (DFI) method of Lynch and Huang (1992), modified here to account for the non-stationary spin-up effects in the time series. The diagnosed ageostrophic motion is checked by comparison of the vertical velocity field with that obtained from the classical quasigeostrophic (QG) ω -equation. The two-methods produce generally similar results, with typical vertical motions in the range of 10-20 m d^{-1} associated with jet meanders. Local differences are attributed to known limitations of the QG theory, but could also be partly due to computational errors associated with the high order derivatives required by the QG method. The general success of this approach could provide an alternative to QG diagnosis in mesoscale dynamics.

5.1 Introduction

The importance of ageostrophic motion in mesoscale oceanic features (eddies, fronts, meanders and filaments) has been addressed in recent years in a number of papers. Vertical motions in mesoscale oceanic eddies and fronts, and their biological influences (transport of phytoplankton across the thermocline and phytoplankton growth in the euphotic zone) have been the subject of several recent studies [Woods et al. 1977, Woods et al. 1986, Leach 1987, Woods 1988, Pollard and Regier (1990,1992)]. Regions of upwelling and downwelling with maximum values of $10\text{-}40\text{ m d}^{-1}$ characterize the vertical motion in Coastal Transition Zone (CTZ) filaments (Haidvogel et al. 1991; Walstad et al. 1991; Dewey et al. 1991) resulting in the subduction of nutrient rich coastal water along the filaments (Washburn et al. 1991). In Gulf Stream meanders significant deviations from geostrophy ($\sim 20\text{ cm s}^{-1}$) can be produced by curvature effects (Johns et al. 1989; Kontoyiannis and Watts 1990), while cross-stream circulation and vertical motions (of about 10 m d^{-1}) have been also recently reported and studied with numerical models (Chew et al. 1985, Bower and Rossby 1989, Bower 1991, Samuelson 1991, Onken 1992).

The interest in the above mentioned mesoscale phenomena, and the practical fact that today's computer capabilities limit the use of General Circulation Models (GCMs) in the study of these features, implies that three-dimensional high-resolution mesoscale models are required to study such phenomena (as has been pointed out recently by Onken 1992). At the same time, other authors have focused on the importance that dynamically adjusted fields have in the initialization of prognostic models. In order to use such models in a predictive mode, they must be initialized using data assimilation techniques (Moore 1991, Walstad et al. 1991, Milliff and Robinson 1992).

Two alternative approaches for recovering directly the 3D quasigeostrophic (QG)/semi-geostrophic (SG) circulation from knowledge of the geostrophic flow, along with diabatic and frictional effects, for periodic or unbounded domains have been given by Keyser et al. (1992). These are (a) from the ω -equation (Hoskins et al. 1978) and divergence equation; and (b) from equations for the psi vector and for the vertical shear of the nondivergent ageostrophic current. These methods are, however limited to the QG or SG assumptions, and QG vertical motions can differ substantially from PE vertical motions (Moore and VanKowe 1992).

Therefore, two important problems facing the physical oceanographic community are to diagnose the mesoscale ageostrophic motion and to obtain the adjusted 3D velocity and mesoscale density fields from hydrographic data. Both problems have been relatively well solved in separate ways. This paper deals with the solution as a whole by diagnosing the total 3D velocity field and the corresponding equilibrated density field through experimental

density data assimilation in a PE model. Although this problem has been already addressed in prognostic computations with a QG model (e.g. Milliff and Robinson 1992), and recently by De Young et al. (1993) with a diagnostic coastal circulation model, a PE model will be employed here with a purpose focused on the mesoscale ageostrophic motion.

As is well known, ageostrophic motion in PE computations is not always free of computational noise and transient effects of the assimilation process (e.g. gravity-inertia waves). In particular, since the vertical velocity is computed by the vertical integration of the horizontal velocity divergence, it is quite susceptible to noise in the horizontal, and therefore the accuracy of the numerical resolution in PE simulations may often be judged a posteriori by the adequacy of the vertical velocity field (e.g. Haidvogel et al. 1991). The vertical velocity field will provide a check on the model diagnosed ageostrophic motion: our confidence in the ageostrophic velocity field diagnosed from the PE model will be based on a comparison between the vertical velocity fields obtained from the PE model and from QG theory. Therefore, the aim of this work is (a) to describe the approach followed to obtain an initial balanced state of mesoscale 3D velocity and density fields (density data assimilation in a PE model), and (b) to interpret the diagnosed ageostrophic motion by comparison of PE and QG vertical velocity fields. The remainder of this paper is as follows: Section 5.2 deals with the hydrographic data set; Section 5.3 gives a brief description of the PE model; the data assimilation process is described in Section 5.4; finally Section 5.5 presents the results and discussion.

5.2 The data

The hydrographic data was obtained from a field experiment carried out in September 1992 in the Alboran Sea (Western Mediterranean). The domain and CTD stations are represented in Fig. 1. Since the data set is described in detail in Viúdez, Tintoré and Haney 1994 (hereinafter VTH94), only a brief summary of the general Mediterranean-Alboran dynamics and the new data will be given here for completeness.

The Mediterranean Sea is a semi-enclosed basin whose large scale circulation is mainly controlled by the excess of evaporation over fresh water input from precipitation and rivers. A two-layer flow through the Strait of Gibraltar compensates for the water and salt deficit with Atlantic Water (AW, $S < 36.5$) flowing in the upper layer into the Alboran Sea, and Mediterranean Water (MW, $S > 38.4$) flowing westward below (e.g. Parrilla and Kinder 1987). Being the westernmost Mediterranean subbasin, the Alboran Sea is the first to receive the incoming Atlantic Water. The AW is modified in the Alboran Sea, acquiring characteristics intermediate between

the underlying MW and the AW, and is termed Modified Atlantic Water (MAW) or Atlantic-Mediterranean Interface Water (A-MIW, Gascard and Richez 1985). The large scale circulation of the MAW in the Alboran Sea shows the presence of an eastward jet, and one or two large anticyclonic gyres (Western and Eastern Alboran Gyres, WAG and EAG) lying in the western and eastern Alboran basin (*e.g.* Heburn and La Violette 1990; VTH94). At smaller scales, jet fluctuations and eddies (Perkins et al. 1990; Tintoré et al. 1991; VTH94) as well as the observed collapse of the gyres (Heburn and La Violette 1990) distort this large scale picture, characterizing the Alboran Sea as a zone of high mesoscale variability.

The hydrographic state of the Alboran Sea during the recent cruise of September 1992 corresponds to the above two-gyres general description (see VTH94 for details). At large scale, the density field exhibits a wavelike pattern with two bowls of warm and less saline water. The temperature, salinity and density distributions at 100 m (Fig. 2 in VTH94) reached maximum horizontal gradients of 1.5°C , 1.2 psu and $2 \sigma_t$, respectively, in about 20 km, with the stronger gradients occurring in the western Alboran ($\sim 4^{\circ} 00' \text{ W}$). The wavelike front, a result of the incoming Atlantic inflow at the Strait of Gibraltar, separates older MAW (colder and more saline, and therefore denser) located in the northern Alboran Sea, from the more recent MAW (warmer and less saline, and therefore less dense) located in the south. The two large bowls of warmer and lighter water in the southern part of the basin are the WAG and the EAG, their vertical extension being of the order of 200-220 m. The two mesoscale eddies located southwest of each anticyclonic gyre, clearly observed between the gyres and the coast, identify the density field during that time as a wavelike front coupled with two anticyclonic gyre-cyclonic eddy systems.

The surface dynamic topography field, computed in VTH94, is reproduced in Fig. 2. The reference level used was 200 m since this is the common reference level in the Alboran Sea (*e.g.* Lanoix 1974; Perkins et al. 1990), and since 200-250 m is the approximate zero level separating eastward-flowing AW from westward-flowing MW. The wavelike jet dominates the circulation, coupled with two anticyclonic gyre-cyclonic eddy systems. Maximum values of geostrophic velocity are 1 m s^{-1} in the Atlantic jet north of the WAG.

5.3 The models of vertical motion

The QG vertical velocity field was computed in VTH94 using the \mathbf{Q} vector formulation of the ω -equation (Hoskins et al. 1978) modified in order to take into account horizontal variations of the squared Brunt-Väisälä frequency N^2 (see *e.g.* Davies-Jones 1991)

$$\nabla \cdot (N^2 \nabla w_{\text{QG}}) + f^2 \frac{\partial^2 w_{\text{QG}}}{\partial z^2} = \nabla \cdot \mathbf{Q}, \quad (5.1)$$

where $N^2 \equiv -g\rho_0^{-1}\partial\rho/\partial z$ is the squared Brunt-Väisälä frequency, g is the acceleration of gravity, ρ is the density, ρ_0 is a mean constant density value, $\nabla \equiv (\partial/\partial x, \partial/\partial y)$, w_{QG} is the QG vertical velocity, f is the Coriolis parameter at 36° N, $\mathbf{Q} \equiv \frac{2g}{\rho_0}(\frac{\partial \mathbf{V}}{\partial x} \cdot \nabla \rho, \frac{\partial \mathbf{V}}{\partial y} \cdot \nabla \rho)$, and $\mathbf{V} \equiv (U, V)$ is the geostrophic velocity. The resulting QG vertical velocity at 100 m from VTH94 is reproduced in Fig. 3. Maximum significant vertical velocities are $15\text{-}20 \times 10^{-5} \text{ m s}^{-1}$ and correspond to mesoscale phenomena (eddies, lateral shear, curvature).

The vertical velocity was also computed using a multi-level primitive equation model (Haney 1985). This is done, following Lynch and Huang (1992), by applying a weight function based on a digital filter to the time-series of model variables generated by short-term forward and backward integrations of the model starting from the objectively analysed fields. The model governing equations are those of an adiabatic, frictionless, Boussinesq, hydrostatic and incompressible sea and are given by

$$\frac{\partial u'}{\partial t} = -\frac{1}{\rho_0} \frac{\partial p'}{\partial x} + f v' + F' \quad (5.2)$$

$$\frac{\partial v'}{\partial t} = -\frac{1}{\rho_0} \frac{\partial p'}{\partial y} - f u' + G' \quad (5.3)$$

$$\frac{\partial \rho}{\partial t} = -\left[\frac{\partial(\rho u)}{\partial x} + \frac{\partial(\rho v)}{\partial y} + \frac{\partial(\rho w)}{\partial z} \right] \quad (5.4)$$

$$\frac{\partial u}{\partial x} + \frac{\partial v}{\partial y} + \frac{\partial w}{\partial z} = 0 \quad (5.5)$$

$$p = \rho_0 g H - \int_{-H}^z \rho g \alpha \zeta, \quad (5.6)$$

$$F = -\left[\frac{\partial(uu)}{\partial x} + \frac{\partial(uv)}{\partial y} + \frac{\partial(uw)}{\partial z} \right] \quad (5.7)$$

$$G = -\left[\frac{\partial(vu)}{\partial x} + \frac{\partial(vv)}{\partial y} + \frac{\partial(vw)}{\partial z} \right], \quad (5.8)$$

where for any quantity q ,

$$\bar{q} \equiv \frac{1}{H} \int_{-H}^0 q dz \quad (5.9)$$

$$q' \equiv q - \bar{q}. \quad (5.10)$$

In the above equations, (5.2) and (5.3) predict the evolution of the shear currents (u', v') which are driven by the internal pressure field p' , and the

shear part of the momentum advection terms (F', G'). The vertical mean currents (\bar{u}, \bar{v}) are not predicted during the short backward and forward integrations but are held constant at their initial geostrophic values,

$$(\bar{u}, \bar{v}) = \frac{1}{\rho_0 f} (-\bar{p}_x, \bar{p}_y)_{t=0}. \quad (5.11)$$

To solve the above equations, the boundary condition $w = 0$ at $z = 0$ and $-H$ is used, while at the lateral boundaries, an open boundary radiation condition (Ross and Orlanski 1982) is utilized. An isopycnal condition is imposed at the initial time along (and at all grid points landward of) what corresponds to the northern and southern coastlines of the Alboran Sea. As a result, the only places where the open boundary condition plays a role is at the open boundary close to the Strait of Gibraltar, where there is strong cross boundary flow and at the eastern boundary where the currents are quite weak except for the Algerian Current in the southern part of the domain. As it turns out (see also VTH94), the internal forcing in the Alboran Sea (*e.g.* geostrophic vorticity advection) is so strong that the effect of the open boundaries on the interior solution, away from the immediate vicinity of the boundary, is small. The numerical discretization makes use of an energy conserving centered finite difference scheme on the Arakawa B-grid (Arakawa and Lamb 1977). The time differencing uses the leapfrog scheme, with an Euler-backward scheme (Matsuno 1966) used every eighth time-step in order to prevent solution separation. See Haney (1974) for numerical details.

5.4 Data assimilation

5.4.1 Density field preprocessing

In order to prepare from the CTD profiles a 3D density field adequate to insert into a model regular grid some preprocessing of the hydrographic data was developed. First, the boundary geometry of the data domain was slightly modified to fit to a flat bottom domain of 200 m depth. This allowed us to simplify the model geometry and avoid topographic effects in the vertical velocity field (De Young et al. 1993) in order to better compare the resulting vertical velocity with the QG results in VTH94. A few (12) coastal CTD profiles were vertically extended to 200 m using information of the closest profile. Secondly, to be consistent with the model vertical resolution (4 meters) we filter out all short vertical scales in each CTD profile (vertical resolution of 1 m) by applying a simple vertical running average over 5 m. The condition of no normal geostrophic flow was imposed at the coast by replacing the coastal temperature and salinity data by the southern (northern) boundary mean temperature and salinity profile in each southern (northern) land grid

point, in a similar way to that carried out by Milliff and Robinson (1992) with dynamic height anomalies. This condition on the initial fields produces only minor differences in the flow, as inferred from the visual comparison of the measured and mean density profiles along the coastal boundaries (almost zonal) in Fig. 4 relative to the meridional density changes, and from comparison of the resulting transport function (Fig. 5) with the original one (Fig. 2). Next, in order to obtain the regular 3D salinity and temperature field, the salinity and temperature data computed at each CTD station ($\sim 30 \times 18$ km separation) was horizontally interpolated onto a regular grid of $\sim 9.3 \times 6.7$ km (the same horizontal resolution as in VTH94). The objective analysis used was a method of successive corrections using weight functions normalized in such a way that the result after infinite iterations can be demonstrated to be equivalent to the result of an optimal interpolation (OI) method (Brathset 1986; Franke 1988). The characteristic scale of the weight functions, which plays the role of a correlation function in OI methods, was set equal to 20 km (VTH94). Finally, the in situ density was computed from the analysed temperature and salinity values at each grid point using the standard equation of state for seawater (Millero et al. 1980). The final in situ density field is defined at grid points of a $50 \times 40 \times 48$ regular matrix covering a vertical extension from 10 to 198 m (Fig. 6).

5.4.2 The development of ageostrophic motion

The essence of the dynamic initialization process is the development, or spin-up, of the ageostrophic motion through the model dynamics. To achieve this development, the PE model is first initialized with the analysed density field and the corresponding geostrophic (non-divergent) velocities. The time step Δt was 450 s (7.5 minutes) which is about 20 times less than the CFL limit for vertical displacements ($\Delta z/w \sim 10^4$ s for $\Delta z = 4$ m and $w = 40 \times 10^{-5}$ m s $^{-1}$). Since we are using a dynamical model only with a diagnostic purpose, the time variable is somewhat ambiguous. On the one hand it is an iterative mathematical parameter only necessary for the model to reach an adjusted state (diagnostic purpose). But, on the other hand, it has its proper physical meaning since it takes part in the local change and advection terms in the primitive equations (prognostic purpose). A perhaps more important consideration in the initialization process is the time required for the model to reach the adjusted state (or spin-up time) in relation to the time scale of the adjusted state itself. Since the former is much less than the latter we obtain the adjusted state by using a modified version of the digital filter initialization (DFI) technique applied to time series of forward and backward integrations from the initial time developed by Lynch and Huang (1992). The forward and backward integrations serve to hold the synoptic scale features stationary while the application of the digital filter to the time series serves

to remove the higher frequency oscillations that accomplish the adjustment.

The average absolute vertical velocity at each time t_n

$$\langle W \rangle (t_n) \equiv \frac{\int_V |w(t_n)| dV}{\int_V dV}, \quad (5.12)$$

where V is the box volume corresponding to the horizontal area marked in Fig. 5 (or Northern WAG, NWAG) with vertical limits of $z = -10$ m and $z = -198$ m, is used to monitor the global behavior (spin-up) of the divergent part of the horizontal velocity field (which is entirely ageostrophic). The time evolution of $\langle W \rangle$, both for the forward and backward integration, is shown in Fig. 7. The magnitude of the average absolute vertical velocity increases monotonically from $t_0 = 0$ to $t_M = 6$ hours approximately ($M = 48$). Beyond that time $\langle W \rangle$ seems to have an oscillatory behavior, both for the forward and backward integration. We therefore deduce that the primary spin-up of ageostrophic motion takes place in the first 6 hours of forward/backward integrations, and beyond that time, the ageostrophic spin-up stops, t_M being the time (forward and backward) when the spin-up has been completed. Figs. 8a and b illustrate how much water parcels are advected and distorted in the first 6 and 24 hours, respectively. Basically 6 hours is not long enough for water parcels at this depth to be advected to the next grid point, and forward and backward integrations produce nearly the same locations of advected water parcels.

However, due to the small (second order) accelerations during the ageostrophic development, the short time-scale local variability is dominated by gravity-inertia waves, that, due to being generated by non homogeneous forcing (ageostrophic development) have a great influence on the divergent part of the horizontal velocity, and hence, on the vertical velocity. The 24-hour hodographs at each grid point at 100 m in the NWAG area for the forward and backward integrations are shown in Figs. 9a,b. The relatively small variations in the velocity (second order in relation to the absolute velocity values) are mainly inertial oscillations that have a clockwise (anticlockwise) rotation in the forward (backward) integration when positive (negative) time increases, or in other words, clockwise rotation when time increases from -24 to +24 hours. These oscillations are a physical consequence of the adjustment process. Notice that the largest oscillations occur where the initial (geostrophic) currents, and flow curvature, are largest. This is because the departure of the solution (adjusted state) from local geostrophic balance, as determined by the (F', G') terms (or Rossby number), is greatest in regions where the momentum advection terms are the greatest. The fact that the hodographs are not perfect circles is related to the non-linear interaction of the adjustment (or spin-up) process (which includes accelerations) with the developed inertial motion, as well as with the advection of synoptic scale features. The time-series of vertical velocity, at the same grid points, are rep-

resented in Figs. 10a,b for the forward and backward integrations. Observe that at some grid points the vertical velocity increases in the same direction (either positive or negative) in both the forward and backward integrations (area label S, or Symmetric), while it increases in opposite directions at other grid points (area label A, or Antisymmetric). For further reference we denote these grid points as S and A, respectively. Observe also that the vertical velocity changes sign at most the A grid points during both ± 24 hour integrations. It will be seen later that the vertical velocity in the adjusted state (solution) will tend to be large at the S points and small at the A points.

One way to mitigate the influence of the pure inertial waves in the time-series is to compute the mean of each variable (ρ, V) at the two times $-t_n$ and $+t_n$. Since we are integrating a numerical model without damping terms, the backward integration is as useful as the forward one, with the advantage that in the backward integration the inertial waves rotate in an opposite sense of the inertial waves of the forward integration, and therefore the mean $\hat{a}(t_n) \equiv \frac{1}{2}[a(+t_n) + a(-t_n)]$, where a is any variable, will largely eliminate the effect of pure inertial waves on the velocity time-series, and such an average will also remove any linear trend in the time-series due to the motion of synoptic scale features. The corresponding hodograph of this mean over the ± 24 h of forward/backward integrations at each grid point of the NWAG area at 100 m (Fig. 9c) shows that a major part of the inertial oscillations have been removed, and a deceleration of the flow, rather than a turning of the current, during the first 6 h of spin-up is clearly observed. The mean time-series of vertical velocity (Fig. 10c) show that a major part of the sign changes in w have been also removed, and as a consequence, zones of upward and downward motion are clearly identified along the ± 24 hours integration. The mean vertical velocity field at the end of the spin-up time [*i.e.* $\hat{w}(t_M) \equiv \frac{1}{2}[w(-t_M) + w(+t_M)]$], (Fig. 12), is quite similar to the QG vertical velocity (Fig. 3). Apart from a few differences (to be discussed later) the pattern of upward and downward motion, as well as the the order of magnitude (both fields have maximum significant vertical velocities of $15\text{-}20 \times 10^{-5} \text{ m s}^{-1}$), agree very closely. Note that the magnitude of the vertical velocity would be under estimated, especially at S grid points, if the mean $\hat{w}(t_n)$ is computed at $t_n < t_M$. In the next subsection we introduce a particular way to take into account the uncertainty in the selection of t_M by mean of the application of a weight function centered at $\pm t_M$ to the the time-series.

5.4.3 Weight function

In the previous subsection the importance of two phenomena in the adjustment process, namely the development of ageostrophic motion and the inertial wave generation, has been emphasized. Because of the rapid spin-up of the ageostrophic currents during the early part of the forward and backward

integrations, a small but important modification to the digital filter initialization method of Lynch and Huang (1992) has been made in this study. The Lynch and Huang method, which uses a weight function based on a digital filter, has been successfully used to produce dynamically balanced mass and wind fields which, when used as initial conditions in atmospheric prediction models, eliminate spurious oscillations in the forecast fields. The filter eliminates oscillations with frequencies higher than a specified cutoff frequency ω_c . The filter coefficients, with a Lanczos window, are given by

$$c_n \equiv c(t_n) \equiv \left\{ \frac{\sin[n\pi/(N+1)]}{n\pi/(N+1)} \right\} \left[\frac{\sin(n\omega_c \Delta t)}{n\pi} \right] \quad (5.13)$$

for $n = 1 \dots N$, with $\pm t_N$ being the filter domain (Fig. 11). The value chosen for the cutoff frequency corresponded to a period of 6 h. As shown by Lynch and Huang (1992), application of c to the time-series of model variables generated by the backward/forward integrations removes high frequency oscillations and leaves only the low frequencies ($\omega < \omega_c$), or "slow mode", at $t = 0$. The minor deficiency of the Lynch and Huang method that had to be overcome for the present study is illustrated in Figs. 10a,b which shows the time evolution of $w(t)$ at several individual grid points during the backward and forward integration. We focus on $w(t)$ because of its important role in the adjustment process and because it is the field variable that undergoes the greatest change during the adjustment. It is clear that the straight forward application of a low-pass digital filter, of the type used by Lynch and Huang (1992), will recover some, but by no means all, of the developed synoptic scale value of w . This is because of the prominence of the spin-up signal in the time-series (S grid points) during the first few hours. In order to eliminate some of this spin-up effect from the time series of the ageostrophic velocities, we applied instead a symmetric weight function (Fig. 11) to the time-series of model variables defined by

$$h_n \equiv h(t_n) \equiv \begin{cases} \frac{1}{2} c_{n-M} & , \quad n \in [0, 2M] \\ h_{-n} & , \quad n \in [-1, -2M], \end{cases}$$

with $N = M = 48$ ($t_N = t_M = 6$ h). The dynamically adjusted state of a model variable a at the time $t = 0$, denoted \bar{a} , is computed from

$$\bar{a} \equiv \sum_{n=-2M}^{2M} a_n h_n. \quad (5.14)$$

Note that the weight function h is only the renormalized forward and backward translation of c a time interval equivalent to the spin-up period t_M , and that the application of h instead of c produces similar results in A grid points but very different results in S grid points. In fact, the application of h can be considered as the mean between the application of c at $-t_M$ and at

$+t_M$ since it represents the mean of two weighted averages centered at $+t_M$ and at $-t_M$, respectively

$$\bar{a} = \frac{1}{2} \sum_{n=-M}^M c_n a_{n+M} + \frac{1}{2} \sum_{n=-M}^M c_n a_{n-M}. \quad (5.15)$$

The weight function in (5.14), or (5.15), represents a simple but effective way of estimating the dynamically adjusted fields at $t = 0$ in the presence of a significant spin-up signal in the forward and backward integrations, and it also tends to reduce the effect of any uncertainty in the selection of t_M . While Lynch and Huang (1992) applied c to the forward and backward time-series centered at $t = 0$ we are applying c to the forward and backward time-series centered at $t = +t_M$ and at $t = -t_M$ in order to avoid the spin-up time. Studies of the sensitivity of the solution to the choice of t_M are presently in progress. Since the weight function h has been especially designed to take into account the non-stationary behavior (the spin-up process) which occurs only during a specific time interval (between $-t_M$ and $+t_M$) it is not appropriate to apply h to others places in the time-series. In other words, the convolution of h with a for a lag different from zero is not appropriate, and therefore h should not be considered a filter, but rather a weight function. Nevertheless, the application of h to the time-series a is equivalent to applying the filter c to the mean function

$$b_n \equiv \frac{1}{2}(a_{n+M} + a_{n-M}) \quad (5.16)$$

defined for $n \in [-M, M]$, since from (5.15),

$$\bar{a} = \sum_{n=-M}^M c_n b_n. \quad (5.17)$$

Thus \bar{a} represents the same digital filter initialization method that of Lynch and Huang (1992) but applied to the mean time-series b instead of to the original time-series a . It therefore represents an average of the dynamically balanced "slow modes" at t_M and t_{-M} , which we hereby take as a valid approximation to the "slow mode" at $t = 0$. The weighted vertical velocity field \bar{w} (Fig. 13) is very similar to the mean $\hat{w}(t_M)$ shown in Fig. 12, confirming the smooth behavior of $w(t)$ around $t = t_M$.

5.5 Results and discussion

The application of a weight function to the time-series generated by short-term forward and backward integrations of a PE model starting from the objectively analysed density field has provided a dynamically adjusted state

whose vertical velocity is very similar to that diagnosed by the QG theory (compare Figs. 3 and 12). It can be seen that the general position, orientation and magnitude of most of the centers of significant vertical motion in the WAG are similar in both the PE and QG interior solutions. While a good qualitative and quantitative agreement is observed from the visual comparison between w_{qg} (Fig. 3) and $\hat{w}(t_M)$ (Fig. 12) or \bar{w} (Fig. 13), some differences are also observed. These can be divided into (a) boundary and (b) interior differences. No relevant conclusions can be obtained from the boundary differences, since they are due to more or less arbitrary boundary specifications of w in the PE model and in the ω -equation, as well as approximations in the derivatives at the open boundaries. In fact, the proper boundary conditions for the computing ψ vector equations from hydrographic data have not been determined (Xu and Davies-Jones 1993). On the other hand interior differences (and specifically those in the northern WAG where QG values are significantly larger than the PE results) must be caused by the different degree of the physical approximations (PE and QG), or by computational errors.

The major interior differences are in the predicted values of sinking motion along the main jet and the rising motion to the left (north) of it. The QG solution clearly predicts a much stronger vertical circulation along and to the left of the jet, with the maximum sinking motion in the jet being about twice that of the PE solution and with two centers of strong rising motion to the left of the jet [at $(-4.25^\circ, 36.2^\circ)$ and $(-3.5^\circ, 35.9^\circ)$, respectively] apparently associated with jet meanders. Other differences in magnitude between the PE and QG solutions exist in the trough between the WAG and EAG. These differences between QG and PE vertical velocities, especially associated with curved jet-streaks, have been recently addressed in atmospheric flows by Pauley and Nieman (1992) and Moore and Van-kowe (1992). The results of these studies showed that QG theory tends to over estimate the magnitude of the vertical velocity in regions of cyclonic curvature and to under estimate it in regions of anticyclonic curvature. These differences arise both from neglecting the relative vorticity compared to f in the vertical stretching term [f^2 terms on the left side of (5.1)] and the neglect of ageostrophic advection in the forcing [right side of (5.1)]. Since it is also possible that some of the differences between our QG and PE results are due to computational errors [it should be noted that the term $\nabla \cdot \mathbf{Q}$ in (5.1) requires third derivatives of the dynamic height field], a further examination of these differences are left for future studies with perhaps higher resolution data.

It must be noted that, although the vertical velocity values might appear high, the water particles do not remain in these high vertical velocity regions for a long period of time, since they are advected by the horizontal velocity through a quasi stationary disturbance field. A way to visualize the 3D

motion, although by means of a diagnosed velocity field at $t = 0$, is by plotting the streamlines produced by the 3D velocity field. These streamlines correspond to the path lines, or trajectories, in the situation in which the mesoscale fields are moving much slower than the particle speed ($\partial v / \partial t \cong 0$, *i.e.* when the motion is steady). Streamlines in the vicinity of the wave-like jet have been represented (Fig. 14) to illustrate the relative importance of the ageostrophic motion. The streamlines experience vertical displacements of ~ 20 m in the trough between the WAG and EAG.

Since the vertical velocity, $O(5 \times 10^{-5} \text{ m s}^{-1})$, is computed in the PE model from the divergence of the horizontal velocity, $O(5 \times 10^{-1} \text{ m s}^{-1})$, which is the divergence of the horizontal ageostrophic velocity, $O(5 \times 10^{-2} \text{ m s}^{-1})$, the confidence in the horizontal irrotational ageostrophic motion diagnosed by the PE model is high. Furthermore, since the model does not separate between non-divergent and irrotational parts there is no reason to doubt the horizontal non-divergent ageostrophic motion, since the correction of the irrotational part has been demonstrated.

The density dynamical assimilation using a PE model with mesoscale resolution has provided a reliable way to obtain the ageostrophic circulation and the corresponding dynamically adjusted density field. An important future step is to verify the solutions obtained here with direct, or indirect, in situ measurements of the vertical velocity field, independent of dynamical computations. The dynamically adjusted state so obtained is useful for posterior analysis of the dynamically balanced 3D motion (slow mode) as well as for initializing prognostic computations using PE models. Although a relatively simple PE model (with density conservation equation) was used in a simple model geometry (flat bottom), a more sophisticated PE model (with separate salinity and temperature conservation, and state equation for sea water) could be employed in a more complicated (realistic) geometry. Finally, methods of including important diabatic effects, which are inherently irreversible, will require considerable research with the present methodology.

Acknowledgements. We thank all the people inboard the R/V García del Cid during the Alboran 1992 field experiment, especially J. Font, J. Salat, M. Manríquez, E. García, J. Sánchez, M. Lloret (ICM), J-M. Pinot and A. Álvarez (UIB). Interpolation routines were provided by D. Gomis (UIB). The computations were carried out on the Cray-YMP at NPS. We especially thank B. Hale for helping to implement the PE model calculation and R. Schwanz, D. Burych, M. McCann and M. Koebbe, for assistance with the computers. This study is a UIB contribution to the Euromodel project, funded by E.C. MAST programme (MAS2-CT93-0066) and by CI-CYT, AMB93-1046-CE. Partial support for this study was also obtained from the Office of Naval Research (RLH). One of the authors (AV) acknowledges

a PFPI grant from the CICYT.

REFERENCES

- Arakawa, A., and V. R. Lamb, 1977: Computational design of the basic dynamical process of the UCLA general circulation model. *Methods in Computational Physics*, Vol 17, J. Chang, Ed., Academic Press, 173-265.
- Bower, A. S., and T. Rossby, 1989: Evidence of cross-frontal exchange process in Gulf Stream meanders based on isopycnal RAFOS float data. *J. Phys. Oceanogr.*, **19**, 1177-1190.
- Bower, A. S., 1991: A simple kinematic mechanism for mixing fluid parcels across a meandering jet. *J. Phys. Oceanogr.*, **21**, 173-180.
- Brathset, A. M., 1986: Statistical interpolation by means of successive correction. *Tellus*, **38A**, 439-447.
- Chew, F., J. M. Bane, and D.A. Brooks, 1985: On vertical motion, divergence, and the thermal wind balance in cold-dome meanders: a diagnostic study. *J. Geophys. Res.*, **90**, 3173-3183.
- Davies-Jones, R., 1991: The frontogenetical forcing of secondary circulations. Part I: the duality and generalization of the Q-vector. *J. Atmos. Sci.*, **48**, 497-509.
- De Young, B., R. J. Greatbatch, and K. B. Forward, 1993: A diagnostic coastal circulation model with application to Conception Bay, Newfoundland. *J. Phys. Oceanogr.*, **23**, 2617-2635.
- Dewey, R. K., J. N. Moum, C. A. Paulson, D. R. Caldwell, and S. D. Pierce, 1991: Structure and dynamics of a coastal filament. *J. Geophys. Res.*, **96**, 14885-14907.
- Franke, R., 1988: Statistical interpolation by iteration. *Mon. Wea. Rev.*, **116**, 961-963.
- Gascard, J. C., and C. Richez, 1985: Water masses and circulation in the western Alboran Sea and in the Straits of Gibraltar. *Progress in Oceanography*, **15**, 157-216.
- Haidvogel, D. B., A. Beckmann, and K. S. Hedström, 1991: Dynamical simu-

- lations of filament formation and evolution in the Coastal Transition Zone. *J. Geophys. Res.*, **96**, 15017-15040.
- Haney, R. L., 1974: A numerical study of the response of an idealized ocean to large-scale surface heat and momentum flux. *J. Phys. Oceanogr.*, **4**, 145-167.
- , 1985: Midlatitude sea surface temperature anomalies: a numerical hindcast. *J. Phys. Oceanogr.*, **15**, 787-799.
- Heburn, G. W., and P. E. La Violette, 1990: Variations in the structure of the anticyclonic gyres found in the Alboran Sea. *J. Geophys. Res.*, **95**, 1599-1613.
- Hoskins, B. J., I. Draghici, and H.C. Davies, 1978: A new look at the w -equation. *Quart. J. R. Met. Soc.*, **104**, 31-38.
- Johns, E., D. R. Watts, and H. T. Rossby, 1989: A test of geostrophy in the Gulf Stream. *J. Geophys. Res.*, **94**, 3211-3222.
- Keyser, D., B. D. Schmidt, and D. G. Duffy, 1992: Quasigeostrophic diagnosis of three-dimensional ageostrophic circulations in an idealized baroclinic disturbance. *Mon. Wea. Rev.*, **120**, 698-730.
- Kontoyiannis, H., and D. R. Watts, 1990: Ageostrophy and pressure work in the Gulf Stream at 73° W. *J. Geophys. Res.*, **95**, 22209-22228.
- Lanoix, F., 1974: Projet Alboran, Etude hydrologique et dynamique de la Mer d'Alboran. Tech. Rep. 66, NATO, Brussels. 39 pp. plus 32 figs.
- Leach, H., 1987: The diagnosis of synoptic-scale vertical motion in the seasonal thermocline. *Deep-Sea Res.*, **34**, 2005-2017.
- Lynch, P., and X-Y. Huang, 1992: Initialization of the HIRLAM model using a digital filter. *Mon. Wea. Rev.*, **120**, 1019-1034.
- Matsuno, T. 1966: Numerical integrations of the primitive equations by a simulated backward difference method. *J. Meteor. Soc. Japan*, **44**, 76-84.
- Millero, F., C-T. Chen, A. Bradshaw, and K. Schleicher, 1980: A new high

pressure equation of state for seawater. *Deep-Sea Res.*, **27A**, 255-264.

Milliff, R. F., and A. R. Robinson, 1992: Structure and dynamics of the Rhodes Gyre System and dynamical interpolation for estimates of the mesoscale variability. *J. Phys. Oceanogr.*, **22**, 317-337.

Moore, A., 1991: Data assimilation in a quasi-geostrophic open-ocean model of the Gulf Stream region using the adjoint method. *J. Phys. Oceanogr.*, **21**, 398-427.

Moore, J. T., and G. E. VanKowe, 1992: The effect of jet-streak curvature on kinematic fields. *Mon. Wea. Rev.*, **120**, 2429-2441.

Onken, R., 1992: Mesoscale upwelling and density finestructure in the seasonal thermocline—A dynamical model. *J. Phys. Oceanogr.*, **22**, 1257-1273.

Parrilla, G. and T. H. Kinder, 1987: The physical oceanography of the Alboran Sea. *NORDA Rep.*, **184**, 26 pp.

Pauley, P. M., and S. J. Nieman, 1992: A comparison of quasigeostrophic and nonquasigeostrophic vertical motions for a model-simulated rapidly intensifying marine extratropical cyclone. *Mon. Wea. Rev.*, **120**, 1108-1134.

Perkins, H., T. Kinder, and P. E. La Violette, 1990: The atlantic inflow in the Western Alboran Sea. *J. Phys. Oceanogr.*, **20**, 242-263.

Pollard, R. T., and L. Regier, 1990: Large variations in potential vorticity at small spatial scales in the upper ocean. *Nature*, **348**, 227-229.

_____, and _____, 1992: Vorticity and vertical circulation at an ocean front. *J. Phys. Oceanogr.*, **22**, 609-625.

Samuelson, R. M., 1991: Fluid exchange across a meandering jet. *J. Phys. Oceanogr.*, **22**, 431-440.

Ross, B. B., and I. Orlanski, 1982: The evolution of an observed cold front. Part I: numerical simulation. *J. Atmos. Sci.*, **39**, 296-327.

Schröter, J., U. Seiter, and M. Wenzel, 1993: Variational assimilation of

- Geosat data into an eddy-resolving model of the Gulf Stream extension area. *J. Phys. Oceanogr.*, **23**, 925-953.
- Tintoré, J., D. Gomis, S. Alonso, and G. Parrilla, 1991: Mesoscale dynamics and vertical motion in the Alboran Sea. *J. Phys. Oceanogr.*, **21**, 811-823.
- Viúdez, A., J. Tintoré, and R. L. Haney, 1994: Three-dimensional structure of the two anticyclonic gyres in the Alboran Sea. *J. Phys. Oceanogr.* Accepted.
- Walstad, L. J., J. S. Allen, P. M. Kosro, and A. Huyer, 1991: Dynamics of the Coastal Transition Zone through data assimilation studies. *J. Geophys. Res.*, **96**, 14959-14977.
- Washburn, L., D. C. Kadko, B. H. Jones, T. Hayward, P. M. Kosro, T. P. Stanton, S. Ramp, and T. Cowles, 1991: Water mass subduction and the transport of phytoplankton in a coastal upwelling system. *J. Geophys. Res.*, **96**, 14927-14945.
- Woods, J. D., 1988: Mesoscale upwelling and primary production. *Toward a theory of biological physical interactions in the World Ocean*, B. J. Rothschild, Ed., D. Reidal, 650 pp.
- , R. L. Wiley, and M. G. Briscoe, 1977: Vertical circulations at fronts in the upper ocean. *Deep-Sea Res. (Suppl:A Voyage to Discovery)*, **24**, 253-275.
- , R. Onken, and J. Fischer, 1986: Thermohaline intrusions created isopycnally at oceanic fronts are inclined to isopycnals. *Nature*, **322**, 446-449.
- Xu, Q., and R. Davies-Jones, 1993: Boundary conditions for the Psi equations. *Mon. Wea. Rev.*, **121**, 1566-1571.

LIST OF FIGURES

1. The Alboran Sea (bottom topography in m). The different vertical CTD sections are referenced. The box represents the model domain.
2. Geostrophic transport function at 10 m without the boundary condition of no normal geostrophic flow ($\Delta = 0.2$ Sv).
3. Quasigeostrophic (ω -equation) vertical velocity distribution w_{qg} at 100 m ($\Delta = 5 \times 10^{-5}$ m s⁻¹).
4. (a) Measured vertical density distribution along the northern coastal boundary and mean vertical profile which imposed the no normal geostrophic flow condition, (b) the same as (a), but for the southern coastal boundary ($\Delta = 0.2 \sigma_t$, Y-axis represents relative distance in km).
5. Geostrophic transport function at 10 m computed with the boundary condition of no normal geostrophic flow ($\Delta = 0.2$ Sv). The small rectangle represent the Northern Western Alboran Gyre (NWAG) area.
6. Isosurface of 28.0 σ corresponding to the initial density field assimilated by the PE model.
7. Absolute vertical velocity averaged over the NWAG volume, $\langle W \rangle$, as function of the integration time t_n .
8. Advection of water parcels at 100 m in the NWAG area (located at $t = 0$ on a squared black and white grid) after (a) 6 and (b) 24 hours of forward integration. The water advection is less than one distance between consecutive grid points in the first 6 h, and as a result forward and backward (not shown) integrations produce very similar locations of black and white water parcels. The large advection after 24 h produce significant different patterns for the forward and backward (not shown) integrations.
9. Initial horizontal velocity vectors $\mathbf{v}(t = 0)$, and 24-hour hodographs of the horizontal velocity deviation from the initial state, $\mathbf{v}(t_n) - \mathbf{v}(t = 0)$, at each grid point at 100 m in the NWAG area for (a) the forward, (b) the backward and (c) the mean between the forward and backward integrations. The hodographs at each time-step were plotted as points, but the density of points due to the small time interval (7.5 minutes) makes the hodographs appear as continuous lines. Note that the two scales (one for the initial vector and another for the hodographs) differ by one order of magnitude, and that each hodograph begins from a zero value (*i.e.* from each grid point location).

10. Time series (from 0 to 24 hours) of vertical velocity at each grid point at 100 m in the NWAG area for (a) the forward, (b) the backward and (c) the mean between the forward and backward integrations. The distance between consecutive grid points in the Y-axis is equivalent to 100×10^{-5} m s⁻¹. Labels S and A represent areas of symmetric and antisymmetric (in relation to the vertical velocity) grid points. The vertical velocity at each time-step was plotted as points, but the density of points due to the small time interval (7.5 minutes) makes the points appear as continuous lines.
11. The Lynch and Huang (1992) filter (*c*) and the weight function used here (*h*) to compute the final state from the model output.
12. The vertical velocity distribution at 100 m computed as the mean $\hat{w}(t_M) \equiv \frac{1}{2}[w(-t_M) + w(+t_M)]$ between the vertical velocity field at $\pm t_M = \pm 6$ h of forward/backward integrations $\Delta = 5 \times 10^{-5}$ m s⁻¹.
13. Weighted vertical velocity distribution $\bar{w} \equiv \sum_{n=-2M}^{2M} w_n h_n$ at 100 m ($\Delta = 5 \times 10^{-5}$ m s⁻¹).
14. Streamlines of the 3D current in the wave-like jet: (a) top view, (b) western view, and (c) southern view. The “initial” vertical separation [(on the right side of the box] is one grid point (4 m). Vertical displacements of ~ 20 m occur along the jet in the trough between the WAG and EAG.

Te tenía olvidado,
cielo, y no eras
más que un vago existir de luz,
visto —sin nombre—
por mis cansados ojos indolentes.
Y aparecías, entre las palabras
perezosas y desesperanzadas del viajero,
como en breves lagunas repetidas
de un paisaje de agua visto en sueños. . .

Hoy te he mirado lentamente
y te has ido elevando hasta tu nombre.

Juan Ramón Jiménez
(*Diario de un poeta recién casado*).

Capítulo 6

About the Nature of the Generalized Omega Equation

Álvaro Viúdez¹
Joaquín Tintoré¹

J. Phys. Oceanogr. (Submitted).

¹Departament de Física, Universitat de les Illes Balears, Palma de Mallorca, Spain

Abstract

A compact formulation of the generalized Omega equation for hydrostatic, inviscid, isentropic, Boussinesq flow on the f -plane is introduced. The resulting equation establishes that the variation of differential ageostrophic relative vertical vorticity in a water parcel is given by the divergence of only one vector field. Equivalent expressions for the differential ageostrophic vertical stretching and shearing deformation are also introduced.

6.1 Introduction

The quasigeostrophic (QG) Omega equation (ω -equation), widely used in meteorology, has been recently applied in dynamic oceanography in the study and diagnosis of QG vertical velocities from quasi-synoptic density data (Leach 1987, Tintoré et al. 1991, Pollard and Regier 1992, Viúdez et al. 1994). This QG ω -equation admits two formulations: (a) using the Laplacian of the density advection and the differential vorticity advection (e.g. Holton 1992, p. 167), and (b) using the divergence of the \mathbf{Q} vector (Hoskins et al. 1978) which avoids the cancellation and duplication of terms of the former formulation. Recent studies in dynamic meteorology have extended the ω -equation beyond the QG limits and, as a result, generalized ω -equations and generalized \mathbf{Q} vectors have been formulated (e.g. Pauley 1988, Davies-Jones 1991, Pauley and Nieman 1992, Xu 1992). The generalized ω -equation (hereinafter just ω -equation) is usually obtained combining the thermodynamic, hydrostatic and vorticity equations to eliminate the height-tendency terms (e.g. Pauley and Nieman 1992). Since the use of the thermodynamic equation can only eliminate the geostrophic part of the Lagrangian change of differential relative vorticity, the natural way for understanding the ω -equation should be as an expression for the Lagrangian change of the ageostrophic part of this quantity. However, such an interpretation has been hidden in the usual formulations of this equation. The purpose of this note is to introduce such interpretation re-writing the ω -equation as an equation involving the Lagrangian change of differential ageostrophic relative vorticity. In Section 2 we present previous formulations of the ω -equation, and in Section 3 introduce the expression for the rate of change of differential ageostrophic relative vorticity. The derivations of this expression from the previous formulations of the ω -equation are given in Appendices A and B, while equivalent equations for the differential ageostrophic vertical shearing and stretching deformation are introduced in Appendix C.

6.2 Previous formulations of the generalized ω -equation

The w -equation for hydrostatic, inviscid, isentropic, Boussinesq flow on the f -plane can be written as

$$\underbrace{\nabla_{\mathbf{H}}^2(N^2w)}_{L_1} + \underbrace{f(\zeta + f)w_{zz}}_{L_4} + \underbrace{f[\nabla_{\mathbf{H}}w \cdot (-v, u)]_z}_{L_2} - \underbrace{f\omega\zeta_{zz}}_{L_3} = \underbrace{f\nabla_{\mathbf{H}}^2[\mathbf{v}_{\mathbf{H}} \cdot (-V, U)]_z}_{R_1} + \underbrace{f(\mathbf{v}_{\mathbf{H}} \cdot \nabla\zeta)_z}_{R_2} + \underbrace{f\zeta'_{zt}}_{R_3}, \quad (6.1)$$

(Pauley 1988, Pauley and Nieman 1992). See Table 1 for the list of symbols used. Terms L_1 and L_4 are analogous to that in the QG ω -equation (e.g. Holton 1992, p. 166) except that horizontal variations are permitted in the Brunt-Väisälä frequency N^2 , and that the coefficient of the second term is $f(f + \zeta)$ rather than f^2 . Term L_2 results from inclusion of the tilting term in the vorticity equation, and L_3 is the result of retaining the vertical advection of vorticity. On the right-hand side R_1 and R_2 (the Laplacian of the density advection and the differential vorticity advection, respectively) are also analogous to that in the QG ω -equation except that now they utilize the total velocity rather than the geostrophic velocity. Finally R_3 is the local change of differential ageostrophic vorticity. Therefore, this formulation is particularly suitable for use in comparative studies with the classical QG ω -equation written in terms of the Laplacian of the density advection and the differential vorticity advection (e.g. Holton 1992, p. 167). It should be noted that, although the local change of differential ageostrophic relative vorticity is present in (6.1), its advective derivative is hidden in the L_3 and R_2 terms. The derivation of the Lagrangian rate of change of differential ageostrophic relative vorticity ($d\zeta'_z/dt$) from this ω -equation is quite laborious and is therefore given in Appendix A.

More recently Davies-Jones (1991) derived the w -equation

$$\underbrace{f \nabla_H \cdot \frac{d\zeta'_{PH}}{dt}}_{A_1} = 2f \nabla_H \cdot \mathbf{Q}^* - \nabla_H \cdot (N^2 \nabla_H w) - f^2 w_{zz}, \quad (6.2)$$

in terms of the horizontal ageostrophic relative pseudovorticity ζ'_{PH} (Hoskins 1975) and the generalized \mathbf{Q}^* vector

$$\mathbf{Q}^* \equiv \frac{1}{2}(\zeta'_{PH} + \nabla_H b) \cdot \mathbf{G}_H. \quad (6.3)$$

The \mathbf{Q}^* vector is based on the \mathbf{Q} vector first introduced by Hoskins et al. (1978) in order to avoid cancellation and duplication of terms in the QG ω -equation between the Laplacian of the geostrophic density advection and the differential geostrophic vorticity advection. Note also that, although the rate of change of ζ'_z , ($d\zeta'_z/dt$), does not appear explicitly in this version of ω -equation, it is entirely included in the term A_1 since the relative pseudovorticity is non divergent, and

$$\nabla_H \cdot \zeta'_{PH} = -\zeta'_z.$$

The derivation of the equation for the rate of change of ζ'_z from (6.2) is straightforward and is given in Appendix B.

6.3 The rate of change of differential ageostrophic vertical vorticity

In this Section we derive a compact expression for the rate of change of ζ'_z from the vorticity and thermodynamic equations for hydrostatic, inviscid, isentropic and Boussinesq flow on the f -plane. The equation for the vertical component of the relative vorticity can be written

$$\frac{d\zeta}{dt} = \zeta_{\mathbf{3}} \cdot \mathbf{v}_z + f w_z, \quad (6.4)$$

and the thermodynamic equation

$$\frac{d\rho}{dt} = 0. \quad (6.5)$$

The rate of change of differential geostrophic vorticity from (6.4) and (6.5) is respectively

$$\frac{d(\zeta_g)_z}{dt} = -\frac{d\zeta'_z}{dt} - \mathbf{v}_z \cdot \nabla \zeta + (\zeta_{\mathbf{3}} \cdot \mathbf{v}_z)_z + f w_{zz}, \quad (6.6)$$

$$\frac{d(\zeta_g)_z}{dt} = (\mathbf{v}_x \cdot \nabla b)_x + (\mathbf{v}_y \cdot \nabla b)_y + \mathbf{v}_x \cdot \nabla b_x + \mathbf{v}_y \cdot \nabla b_y. \quad (6.7)$$

The horizontal velocity field $\mathbf{v}_H = \mathbf{V} + \mathbf{v}'_H$ and the vertical component of the relative vertical vorticity $\zeta = \zeta_g + \zeta'$ have been decomposed into geostrophic plus ageostrophic components, the geostrophic velocity satisfying the “thermal wind” relation

$$(-V, U)_z = \nabla_H b. \quad (6.8)$$

The ageostrophic velocity satisfies the continuity equation

$$u'_x + v'_y + w_z = 0$$

since the geostrophic velocity is non divergent ($U_x + V_y = 0$). Eliminating the Lagrangian change of differential relative geostrophic vorticity from (6.6) and (6.7), the expression for its ageostrophic part is

$$\begin{aligned} \frac{d\zeta'_z}{dt} = & \underbrace{-(\mathbf{v}_x \cdot \nabla b)_x - (\mathbf{v}_y \cdot \nabla b)_y}_A \\ & \underbrace{-\mathbf{v}_x \cdot \nabla b_x - \mathbf{v}_y \cdot \nabla b_y}_B \\ & \underbrace{-\mathbf{v}_z \cdot \nabla \zeta}_C + \underbrace{(\zeta_{\mathbf{3}} \cdot \mathbf{v}_z)_z + f w_{zz}}_D. \end{aligned} \quad (6.9)$$

The term by term decomposition of (6.9) is as follows:

$$\begin{aligned}
 A &= -\nabla_H \cdot (\mathbf{v}_x \cdot \nabla b, \mathbf{v}_y \cdot \nabla b) \equiv \nabla_H \cdot \mathbf{Q}_{F3} \\
 B &= \underbrace{-\mathbf{v}_{Hx} \cdot \nabla_H b_x - \mathbf{v}_{Hy} \cdot \nabla_H b_y}_{B_1} - \underbrace{\nabla_H w \cdot \nabla_H b_z}_{B_2} \\
 C &= \underbrace{-(U_{xx}b_x + v_{xx}b_y + u_{yy}b_x + V_{yy}b_y)}_{C_1} - \underbrace{\nabla_H \zeta \cdot (\mathbf{u}', \mathbf{v}')_z}_{C_2} + \underbrace{(b_x v'_{xy} + b_y u'_{xy})}_{C_3} - \underbrace{w_z \zeta_z}_{C_4} \\
 D &= \underbrace{\zeta_z w_z}_{D_1} - \underbrace{(\zeta + f) \nabla_H \cdot \mathbf{v}'_{Hz}}_{D_2} + \underbrace{(\zeta'_H \cdot \mathbf{v}'_{Hz})_z}_{D_3} + \underbrace{\nabla_H w \cdot (-V_z, U_z)_z}_{D_4} + \underbrace{\nabla_H w_z \cdot (-V_z, U_z)}_{D_5} \\
 D_5 &= \underbrace{-(u'_{xx}b_x + v'_{yy}b_y)}_{D_{51}} - \underbrace{(v'_{yx}b_x + u'_{xy}b_y)}_{D_{52}}.
 \end{aligned}$$

Terms B_1 , C_1 and D_{51} are the horizontal divergence of the vector \mathbf{Q}_{F2}

$$\mathbf{Q}_{F2} \equiv -(\mathbf{v}_{Hx} \cdot \nabla_H b, \mathbf{v}_{Hy} \cdot \nabla_H b).$$

Terms C_2 and D_2 are the horizontal divergence of the vertical component of the absolute vorticity times the vertical shear of the horizontal ageostrophic velocity

$$C_2 + D_2 = -\nabla_H \cdot [(\zeta + f)\mathbf{v}'_{Hz}].$$

Term C_3 cancels with D_{52} , C_4 with D_1 , and B_2 with D_4 , in such a way that (6.9) is written

$$\frac{d\zeta'_z}{dt} = \nabla_H \cdot \mathbf{Q}_{F3} + \nabla_H \cdot \mathbf{Q}_{F2} - \nabla_H \cdot [(\zeta + f)\mathbf{v}'_{Hz}] + (\zeta'_H \cdot \mathbf{v}'_{Hz})_z. \quad (6.10)$$

Defining the horizontal and vertical components of a vector ξ

$$\begin{aligned}
 \xi_H &\equiv \mathbf{Q}_{F3} + \mathbf{Q}_{F2} - (\zeta + f)\mathbf{v}'_{Hz}, \\
 \xi_{(3)} &\equiv \zeta'_H \cdot \mathbf{v}'_{Hz},
 \end{aligned} \quad (6.11)$$

where $\mathbf{Q}_{F3} + \mathbf{Q}_{F2}$ can also be expressed as $2\mathbf{Q}_{F2} + b_z \nabla_H w$, eq. (6.9) is finally written

$$\frac{d\zeta'_z}{dt} = \nabla \cdot \xi. \quad (6.12)$$

This ω -equation establishes that for hydrostatic, inviscid, isentropic, Boussinesq flow on the f -plane, the variation of differential ageostrophic relative vertical vorticity on a water parcel is given by the 3D divergence of the ξ vector.

At first order of approximation it can be assumed that no change in the differential ageostrophic vorticity following the motion takes place, and that also vertical changes of ξ can be neglected ($\nabla_H \cdot \xi_H = 0$). Therefore, using the standard QG scaling the eq. (6.12) reduces to the QG ω -equation for $N^2(x, y, z)$

$$\nabla_H \cdot (N^2 \nabla_H w_{\text{qg}}) + f^2 (w_{\text{qg}})_{zz} = 2f \nabla_H \cdot \mathbf{Q} \quad (6.13)$$

(Davies-Jones 1991), and to the QG ω -equation for $N^2(x, y, z) \sim \bar{N}^2(z)$

$$\bar{N}^2 \nabla_H^2 w_{\text{qg}} + f^2 (w_{\text{qg}})_{zz} = 2 \nabla_H \cdot \mathbf{Q}. \quad (6.14)$$

In the above, $\bar{N}^2(z) = -f \bar{b}_z(z)$ is a mean profile of static stability, w_{qg} is the QG vertical velocity, and \mathbf{Q} is the geostrophic version of \mathbf{Q}_{F2} . From (6.12) and (6.13) the nonquasigeostrophic ω -equation is

$$\frac{d\zeta'_z}{dt} = \nabla \cdot \xi'. \quad (6.15)$$

where

$$\begin{aligned} \xi'_H &\equiv 2\mathbf{Q}'_{F2} + b_z \nabla_H w_{\text{nqg}} - \zeta' \mathbf{v}'_{Hz}, \\ \xi'_{(3)} &\equiv \zeta'_H \cdot \mathbf{v}'_{Hz} - f(w_{\text{nqg}})_z, \end{aligned} \quad (6.16)$$

where \mathbf{Q}'_{F2} is the ageostrophic part of \mathbf{Q}_{F2} and $w_{\text{nqg}} \equiv w - w_{\text{qg}}$ the nonquasigeostrophic vertical velocity.

Equivalent equations to (6.12) but for the ageostrophic vertical stretching ($\tau' \equiv u'_x - v'_y$) and shearing ($\varsigma' \equiv v'_x + u'_y$) deformation on the f -plane are obtained in Appendix C following a parallel way to the methodology that Davies-Jones (1991) carried out to obtain (6.2).

A direct consequence of applying the divergence theorem to (6.12) [or in a equivalent way to eqs. (6.29) and (6.30)] is that

$$\int_V \frac{d\zeta'_z}{dt} dV = \oint_S \xi \cdot \mathbf{n} dS, \quad (6.17)$$

and therefore the integrated rate of change of differential ageostrophic vorticity (or stretching or shearing deformation) in a volume V depends only on the flux of ξ (or ξ_τ or ξ_ς) across the volume boundary S . If this flux across S is constant, then the integrated rate of change of differential ageostrophic vertical vorticity is conserved. In particular, if $\xi \cdot \mathbf{n} = 0$ at each point of S then

$$\int_V \frac{d\zeta'_z}{dt} dV = 0.$$

This is the case of a fluid, confined in a volume with horizontal and vertical walls, where $\mathbf{v} = \mathbf{0}$ on the vertical walls, and $w = 0$ at the bottom and surface planes, since $\xi \cdot \mathbf{n} = \xi_{(3)} = \nabla_H w \cdot (-v', u')_z = 0$ on both horizontal planes.

6.4 Conclusions

This note has shown that the ω -equation admits a compact interpretation if it is formulated in terms of the rate of change of the differential ageostrophic vertical vorticity. The reason for the simplicity of this new formulation comes from the way in which it is derived, i.e., eliminating the rate of change of differential geostrophic relative vorticity from the vorticity equation. This means that the *generalized ω -equation* should be conceptually interpreted as the equation for the rate of change of differential ageostrophic relative vorticity rather than an equation for the vertical velocity w (which is the case of the QG ω -equation).

The differential ageostrophic vertical vorticity of the fluid parcel is modified by the divergence of the ξ vector field, which has three contributions:

1. \mathbf{Q}_{F3} is the horizontal frontogenesis vector of the 3D motion, since applying the horizontal gradient operator to (6.5)

$$\frac{d\nabla_H \rho}{dt} = \frac{f\rho_0}{g} \mathbf{Q}_{F3}.$$

2. \mathbf{Q}_{F2} is the horizontal frontogenesis vector of the 2D motion, since

$$\left(\frac{d\nabla_H \rho}{dt}\right)_H = \frac{f\rho_0}{g} \mathbf{Q}_{F2}.$$

3. $-(\zeta + f)\mathbf{v}'_{Hz}$ and $\zeta'_H \cdot \mathbf{v}'_{Hz}$ are the combined effects of the vertical shear of the ageostrophic horizontal velocity with the absolute vertical vorticity and ageostrophic horizontal vorticity respectively.

Therefore, when the ω -equation is considered as the equation for the rate of change of the differential ageostrophic vertical vorticity (which is, in our understanding, the natural way), the divergence of vectors \mathbf{Q}_{F3} and/or \mathbf{Q}_{F2} (two generalizations of the geostrophic \mathbf{Q} vector) appears also in the ω -equation in a natural way. While (6.1) is the primitive equation (PE) counterpart to the QG ω -equation written in terms of the Laplacian of the density advection and differential vorticity advection (and therefore is a suitable equation for PE-QG comparative studies), eq. (6.12) is the PE counterpart of the \mathbf{Q} vector formulation of the QG ω -equation (and therefore is a suitable equation for PE-QG comparative studies using the \mathbf{Q} vector formulation).

Acknowledgements. This work was developed during a short stay of one of the authors (AV) at the Naval Postgraduate School (NPS). We are grateful

to Prof. R. L. Haney (NPS) for his helpful suggestions and encouragement. We are also thankful to Dr. C. Ramis for his comments. This work is a UIB contribution of the Euromodel project funded by the E.C. MAST program (MAS2-CT93-0066) and has been also partially funded by CICYT (AMB93-1046-CE). One of the authors (AV) acknowledges a PFPI grant from the CICYT.

6.5 Appendix A: Derivation of (6.12) from (6.1)

Equation (6.1) is for clarity rewritten here

$$\underbrace{\nabla_{\text{H}}^2(N^2w)}_{L_1} + f(\zeta + f)w_{zz} + \underbrace{f[\nabla_{\text{H}}w \cdot (-v, u)_z]}_{L_2} - \underbrace{fw\zeta_{zz}}_{L_3} = \underbrace{f\nabla_{\text{H}}^2[\mathbf{v}_{\text{H}} \cdot (-V, U)_z]}_{R_1} + \underbrace{f(\mathbf{v}_{\text{H}} \cdot \nabla_{\text{H}}\zeta)_z}_{R_2} + f\zeta'_{zt}. \quad (6.18)$$

Our objective is to express (6.18) in such a way that the Lagrangian change of differential ageostrophic vorticity appears explicitly. Using the previous decomposition of the horizontal velocity field $\mathbf{v}_{\text{H}} = \mathbf{V} + \mathbf{v}'_{\text{H}}$ and of the vertical component of the relative vorticity $\zeta = \zeta_{\text{g}} + \zeta'$ into geostrophic plus ageostrophic components, the term by term decomposition of (6.18) is as follows:

$$\begin{aligned} L_1 &= N^2\nabla_{\text{H}}^2w + w\nabla_{\text{H}}^2N^2 + 2\nabla_{\text{H}}w \cdot \nabla_{\text{H}}N^2 \\ L_2 &= f\underbrace{\nabla_{\text{H}}w_z \cdot (-V, U)_z}_{L_{21}} + \underbrace{f\nabla_{\text{H}}w \cdot (-V, U)_{zz}}_{L_{22}} + f[\nabla_{\text{H}}w \cdot (-v', u')_z] \\ L_{21} &= u'_{xx}V_z + v'_{xy}V_z - u'_{xy}U_z - v'_{yy}U_z \\ L_{22} &= g\rho_0^{-1}\nabla_{\text{H}}w \cdot \nabla_{\text{H}}\rho_z = -\nabla_{\text{H}}w \cdot \nabla_{\text{H}}N^2 \\ L_3 &= \underbrace{-fw(\zeta_{\text{g}})_{zz}}_{L_{31}} - fw\zeta'_{zz} \\ L_{31} &= g\rho_0^{-1}w(\rho_{xx} + \rho_{yy})_z = -w\nabla_{\text{H}}^2N^2 \\ R_1 &= f\underbrace{\nabla_{\text{H}}^2[\mathbf{V} \cdot (-V, U)_z]}_{R_{11}} + f\underbrace{\nabla_{\text{H}}^2[\mathbf{v}' \cdot (-V, U)_z]}_{R_{12}} \\ R_{12} &= -(u'_xV_z)_x + (v'_xU_z)_x - u'_xV_{zx} + v'_xU_{zx} - (u'_yV_z)_y + (v'_yU_z)_y - u'_yV_{zy} + v'_yU_{zy} - \mathbf{v}'_{\text{H}} \cdot (\nabla_{\text{H}}\zeta_{\text{g}})_z \\ R_2 &= f\underbrace{(\mathbf{V} \cdot \nabla_{\text{H}}\zeta_{\text{g}})_z}_{R_{21}} + f\underbrace{(\mathbf{V} \cdot \nabla_{\text{H}}\zeta')_z}_{R_{22}} + f\underbrace{(\mathbf{v}' \cdot \nabla_{\text{H}}\zeta_{\text{g}})_z}_{R_{23}} + f\underbrace{(\mathbf{v}' \cdot \nabla_{\text{H}}\zeta')_z}_{R_{24}} \\ R_{22} &= \mathbf{V} \cdot \nabla_{\text{H}}\zeta'_z + U_zv'_{xx} - U_zu'_{yx} + V_zv'_{xy} - V_zu'_{yy} \\ R_{23} &= \mathbf{v}'_{\text{H}} \cdot (\nabla_{\text{H}}\zeta_{\text{g}})_z + \mathbf{v}'_{\text{H}z} \cdot \nabla_{\text{H}}\zeta_{\text{g}} \\ R_{24} &= \mathbf{v}'_{\text{H}} \cdot \nabla_{\text{H}}\zeta'_z + \mathbf{v}'_{\text{H}z} \cdot \nabla_{\text{H}}\zeta' \end{aligned}$$

Terms R_{11} and R_{21} including only geostrophic velocities can be written in a more simplified way as two times the divergence of \mathbf{Q} vector (Hoskins et al. 1978)

$$\mathbf{Q} \equiv -(\mathbf{V}_x \cdot \nabla_H b, \mathbf{V}_y \cdot \nabla_H b). \quad (6.19)$$

After simplification, including cancellation between terms in R_{22} and L_{21} , the LHS and RHS of the ω -equation are written as

$$\begin{aligned} \text{LHS} &= \underbrace{f^{-1} \nabla_H \cdot (N^2 \nabla_H w)}_{D_1} + \underbrace{(\zeta + f) w_{zz}}_{C_1} + \underbrace{(u'_{xx} V_z - v'_{yy} U_z)}_{D_2} + \underbrace{[\nabla_H w \cdot (-v', u')_z]_z}_E - \underbrace{w \zeta'_{zz}}_{B_1}, \\ \text{RHS} &= 2f^{-1} \nabla_H \cdot \mathbf{Q} + \underbrace{\mathbf{v}_H \cdot \nabla \zeta'_z}_{B_2} + \underbrace{(U_z v'_{xx} - V_z u'_{yy})}_{D_3} + \underbrace{\mathbf{v}'_{Hz} \cdot \nabla_H \zeta_g}_{C_2} + \underbrace{\mathbf{v}'_{Hz} \cdot \nabla_H \zeta'}_{C_3} + \underbrace{\zeta'_{zt}}_{B_3} \\ &\quad + \underbrace{[-(u'_x V_z)_x + (v'_x U_z)_x - u'_x V_{zx} + v'_x U_{zx} - (u'_y V_z)_y + (v'_y U_z)_y - u'_y V_{zy} + v'_y U_{zy}]}_{D_4}. \end{aligned}$$

Terms D_1 , D_2 , D_3 and D_4 can be written as the horizontal divergence of two vectors involving ageostrophic velocities

$$\mathbf{Q}'_{F3} \equiv -(\mathbf{v}'_x \cdot \nabla b, \mathbf{v}'_y \cdot \nabla b),$$

$$\mathbf{Q}'_{F2} \equiv -(\mathbf{v}'_{Hx} \cdot \nabla_H b, \mathbf{v}'_{Hy} \cdot \nabla_H b).$$

The horizontal divergence of vectors \mathbf{Q}'_{F3} and \mathbf{Q}'_{F2} can be combined with the horizontal divergence of $2\mathbf{Q}$ to form the horizontal divergence of the two vectors \mathbf{Q}_{F3} and \mathbf{Q}_{F2} involving total velocities: $\mathbf{Q}_{F3} \equiv -(\mathbf{v}_x \cdot \nabla b, \mathbf{v}_y \cdot \nabla b)$ and $\mathbf{Q}_{F2} \equiv -(\mathbf{v}_{Hx} \cdot \nabla_H b, \mathbf{v}_{Hy} \cdot \nabla_H b)$.

Terms $-C_1$, C_2 and C_3 are the horizontal divergence of the absolute vorticity times the vertical shear of the horizontal ageostrophic velocity:

$$-(\zeta + f) w_{zz} + \mathbf{v}'_{Hz} \cdot \nabla_H \zeta_g + \mathbf{v}'_{Hz} \cdot \nabla_H \zeta' = \nabla_H \cdot [(\zeta + f) \mathbf{v}'_{Hz}],$$

and E is the vertical derivative of the horizontal component of the ageostrophic vorticity times the vertical shear of the horizontal ageostrophic velocity:

$$[\nabla_H w \cdot (-v', u')_z]_z = (\zeta'_H \cdot \mathbf{v}'_{Hz})_z.$$

Terms B_1 , B_2 and B_3 are the desired Lagrangian change of differential relative ageostrophic vorticity $d\zeta'_z/dt$, and all the divergent terms can be included in the 3D divergence of only one 3D vector ξ

$$\begin{aligned} \xi_H &\equiv \mathbf{Q}_{F3} + \mathbf{Q}_{F2} - (\zeta + f) \mathbf{v}'_{Hz} \\ \xi_{(3)} &\equiv \zeta'_H \cdot \mathbf{v}'_{Hz}, \end{aligned} \quad (6.20)$$

in such a way that (6.18) is written as (6.12) completing the derivation.

6.6 Appendix B: Derivation of (6.12) from (6.2)

Derivation of (6.12) from (6.2) in terms of Q^* and pseudovorticity vectors is straightforward by using the divergence equation. Term A_1 in (6.2) is decomposed

$$\underbrace{\nabla_H \cdot \frac{d\zeta'_{PH}}{dt}}_{A_1} = \underbrace{\frac{d(\nabla_H \cdot \zeta'_{PH})}{dt}}_{A_2} + \underbrace{\nabla_H u \cdot (\zeta'_{PH})_x + \nabla_H v \cdot (\zeta'_{PH})_y + \nabla_H w \cdot (\zeta'_{PH})_z}_{A_3}. \quad (6.21)$$

Term A_2 is equal to $-d\zeta'_2/dt$ since the relative pseudovorticity is non divergent, and term A_3 is a divergence term since the velocity field is also non divergent

$$A_3 = \nabla \cdot (\nabla_H u \cdot \zeta'_{PH}, \nabla_H v \cdot \zeta'_{PH}, \nabla_H w \cdot \zeta'_{PH}),$$

in such a way that (6.12) is satisfied, and the relations between the ξ components and the Q^* and pseudovorticity components follow

$$\begin{aligned} \xi_{(1)} &= \nabla_H u \cdot \zeta'_{PH} - 2Q^*_{(1)} + f^{-1}N^2w_x - fu'_z \\ \xi_{(2)} &= \nabla_H v \cdot \zeta'_{PH} - 2Q^*_{(2)} + f^{-1}N^2w_y - fv'_z \\ \xi_{(3)} &= \nabla_H w \cdot \zeta'_{PH}. \end{aligned} \quad (6.22)$$

6.7 Appendix C: Equations for the differential ageostrophic vertical stretching and shearing deformation

Equations for the ageostrophic vertical stretching ($\tau' \equiv u'_x - v'_y$) and shearing ($\varsigma' \equiv v'_x + u'_y$) deformation on the f -plane can also be obtained by the appropriate differencing and combination of the horizontal momentum equations. We follow a parallel way to the powerful mathematical methodology that Davies-Jones (1991) carried out to obtain (6.2). First of all we introduce the non divergent vectors $\tau_{\mathbf{3}} \equiv (-u_z, v_z, \tau)$ and $\varsigma_{\mathbf{3}} \equiv (-v_z, -u_z, \varsigma)$, where $\tau \equiv u_x - v_y$ and $\varsigma \equiv v_x + u_y$ are the vertical stretching and shearing deformation. The horizontal momentum equations are used to obtain the equations for $\tau_{\mathbf{3}}$ and $\varsigma_{\mathbf{3}}$

$$\frac{d\tau_{\mathbf{3}}}{dt} = (\tau_{\mathbf{3}} \cdot \nabla)\mathbf{v} + f\varsigma'_{\mathbf{3}}, \quad (6.23)$$

$$\frac{d\varsigma_{\mathbf{3}}}{dt} = (\varsigma_{\mathbf{3}} \cdot \nabla)\mathbf{v} - f\tau'_{\mathbf{3}}, \quad (6.24)$$

and using the following relations for the horizontal part of $\tau_{\mathbf{3}}$ and $\varsigma_{\mathbf{3}}$

$$(\tau_{\mathbf{H}} \cdot \nabla_{\mathbf{H}})\mathbf{v}_{\mathbf{H}} = \tau_{\mathbf{H}} \cdot \mathbf{H}_{\mathbf{H}}, \quad (6.25)$$

$$(\varsigma_{\mathbf{H}} \cdot \nabla_{\mathbf{H}})\mathbf{v}_{\mathbf{H}} = \varsigma_{\mathbf{H}} \cdot \mathbf{J}_{\mathbf{H}}, \quad (6.26)$$

where

$$\mathbf{H}_{\mathbf{H}} \equiv \begin{pmatrix} v_y & v_x \\ u_y & u_x \end{pmatrix},$$

and $\mathbf{J}_{\mathbf{H}} \equiv \text{adj}(\mathbf{H}_{\mathbf{H}})$, the equations for the ageostrophic part of $\tau_{\mathbf{3H}}$ and $\varsigma_{\mathbf{3H}}$ follow

$$\frac{d\tau'_{\mathbf{H}}}{dt} = \underbrace{(\tau_{\mathbf{H}} + \tau_{\mathbf{H}_g}) \cdot \mathbf{H}_{\mathbf{H}}}_{2\mathbf{Q}^*_{\tau}} - fw_z(b, b)_z + \tau v_{\mathbf{H}z} + f\varsigma'_{\mathbf{H}}, \quad (6.27)$$

$$\frac{d\varsigma'_{\mathbf{H}}}{dt} = \underbrace{(\varsigma_{\mathbf{H}} + \varsigma_{\mathbf{H}_g}) \cdot \mathbf{J}_{\mathbf{H}}}_{2\mathbf{Q}^*_{\varsigma}} - fw_z(-b, b)_z + \varsigma v_{\mathbf{H}z} - f\tau'_{\mathbf{H}}, \quad (6.28)$$

where $\tau_{\mathbf{H}_g}$ and $\varsigma_{\mathbf{H}_g}$ are the geostrophic part of $\tau_{\mathbf{H}}$ and $\varsigma_{\mathbf{H}}$ respectively. Defining the following components of the ξ_{τ} and ξ_{ς} vectors

$$\begin{aligned} \xi_{\tau(1)} &\equiv \nabla \mathbf{u} \cdot \tau_{\mathbf{3}} - 2Q^*_{\tau(1)} - \tau u_z - f\varsigma'_{(1)} + fb_z w_z, \\ \xi_{\tau(2)} &\equiv \nabla \mathbf{v} \cdot \tau_{\mathbf{3}} - 2Q^*_{\tau(2)} - \tau v_z - f\varsigma'_{(2)} + fb_z w_z, \\ \xi_{\tau(3)} &\equiv \nabla \mathbf{w} \cdot \tau_{\mathbf{3}}, \end{aligned}$$

$$\begin{aligned}\xi_{\varsigma(1)} &\equiv \nabla \mathbf{u} \cdot \varsigma \mathbf{3} - 2Q_{\varsigma(1)}^* - \varsigma u_z + f\tau'_{(1)} - fb_z w_z, \\ \xi_{\varsigma(2)} &\equiv \nabla \mathbf{v} \cdot \varsigma \mathbf{3} - 2Q_{\varsigma(2)}^* - \varsigma v_z + f\tau'_{(2)} + fb_z w_z, \\ \xi_{\varsigma(3)} &\equiv \nabla \mathbf{w} \cdot \varsigma \mathbf{3},\end{aligned}$$

and using the no-divergence property of $\tau \mathbf{3}$, $\varsigma \mathbf{3}$ and \mathbf{v} , the equations for the differential ageostrophic vertical stretching and shearing deformation follow

$$\frac{d\tau'_z}{dt} = \nabla \cdot \xi_\tau, \quad (6.29)$$

$$\frac{d\varsigma'_z}{dt} = \nabla \cdot \xi_\varsigma. \quad (6.30)$$

REFERENCES

- Davies-Jones, R., 1991: The frontogenetical forcing of secondary circulations. Part I: the duality and generalization of the Q-vector. *J. Atmos. Sci.*, **48**, 497-509.
- Holton, J. R., 1992: An introduction to dynamic meteorology. *Academic Press*, 3rd. ed., 511 pp.
- Hoskins, B. J., 1975: The geostrophic momentum approximation and the semi-geostrophic equations. *J. Atmos. Sci.*, **32**, 233-242.
- Hoskins, B. J., I. Draghici, and H.C. Davies, 1978: A new look at the w -equation. *Quart. J. R. Met. Soc.*, **104**, 31-38.
- Leach, H., 1987: The diagnosis of synoptic-scale vertical motion in the seasonal thermocline. *Deep-Sea Res.*, **34**, 2005-2017.
- Pauley, P. M., and S. J. Nieman, 1992: A comparison of quasigeostrophic and nonquasigeostrophic vertical motions for a model-simulated rapidly intensifying marine extratropical cyclone. *Mon. Wea. Rev.*, **120**, 1108-1134.
- Pauley, P. M., 1988: A diagnosis of nonquasigeostrophic vertical motion. Preprints, *Eighth Conf. Numerical Weather Prediction*, Baltimore, Amer. Meteor. Soc., 424-428.
- Pollard, R. T., and L. A. Regier, 1992: Vorticity and vertical circulation at an ocean front. *J. Phys. Oceanogr.*, **22**, 609-625.
- Tintoré, J., D. Gomis, S. Alonso, and G. Parrilla, 1991: Mesoscale dynamics and vertical motion in the Alboran Sea. *J. Phys. Oceanogr.*, **21**, 811-823.
- Viúdez, A., J. Tintoré, and R. L. Haney, 1994: Three-dimensional structure of the two anticyclonic gyres in the Alboran Sea. *J. Phys. Oceanogr.*, (accepted).
- Xu, Q., 1992: Ageostrophic pseudovorticity and geostrophic C-vector forcing -a new look at the Q vector in three dimensions. *J. Atmos. Sci.*, **49**, 981-990.

TABLE 1. List of symbols.

$\nabla \equiv (\partial_x, \partial_y, \partial_z)$	gradient operator
$\nabla_H \equiv (\partial_x, \partial_y)$	horizontal gradient operator
$\mathbf{v} \equiv (u, v, w)$	velocity vector
$\mathbf{v}_H \equiv (u, v)$	horizontal velocity vector
$\mathbf{V} \equiv (U, V)$	horizontal geostrophic velocity
$\mathbf{v}' \equiv (u', v', w)$	ageostrophic velocity
$\mathbf{v}'_H \equiv (u', v')$	horizontal ageostrophic velocity
$\zeta_3 \equiv \nabla \times \mathbf{v}$	relative vorticity
$\zeta \equiv v_x - u_y$	vertical component of ζ_3
$\zeta_g \equiv V_x - U_y$	geostrophic part of ζ
$\zeta' \equiv v'_x - u'_y$	ageostrophic part of ζ
f	Coriolis parameter (constant)
g	acceleration of gravity
$\rho(x, y, z)$	potential density field
ρ_0	mean constant density value
$b \equiv g(f\rho_0)^{-1}\rho$	buoyancy divided by f
$N^2(x, y, z) \equiv -g\rho_0^{-1}\rho_z$	Brunt-Väisälä frequency
$\zeta_P \equiv (-v_z, u_z, \zeta)$	relative pseudovorticity
$\zeta_{PH} \equiv (-v_z, u_z)$	horizontal relative pseudovorticity
$\zeta'_{PH} \equiv (-v'_z, u'_z)$	ageostrophic part of ζ_{PH}
$\mathbf{G} \equiv \partial v_i / \partial x_j$, for $i, j \in \{1, 2, 3\}$	three-dimensional velocity gradient tensor
$\mathbf{G}_H \equiv \partial v_m / \partial x_n$, for $m, n \in \{1, 2\}$	horizontal velocity gradient tensor

¡Tan finos como son tus brazos,
son más fuertes que el mar!
Es de juguete
el agua, y tú, amor mío me la muestras
como una madre a un niño la sonrisa
que conduce a su pecho
inmenso y dulce...

Juan Ramón Jiménez
(*Diario de un poeta recién casado*).

Capítulo 7

Conclusiones

Aunque las conclusiones de esta tesis han sido ya expuestas en cada uno de los diferentes capítulos y han sido expuestas resumidamente también en la Introducción, parece conveniente volverlas a detallar de una forma más esquemática.

- En el capítulo *An exploratory numerical study of the currents off the southern coast of Mallorca including the Cabrera Island complex* hemos realizado un estudio numérico de la circulación ageostrófica en una zona costera: la plataforma sur de Mallorca-Cabrera. Este trabajo constituye el primer intento de modelización de la circulación en dicha plataforma bajo los efectos de tipo campo remoto, de la brisa y de un temporal. Ha sido de gran importancia la utilización del Método de Elementos Finitos en la resolución de las ecuaciones de aguas poco profundas para tener en cuenta el carácter tridimensional de la circulación y la influencia de la topografía real. Para obtener la distribución cuantitativa del transporte de agua en la plataforma de Mallorca-Cabrera sería de gran utilidad poder medir experimentalmente el transporte a lo largo de la plataforma costera perpendicular a Porto Colom. En futuros estudios de los efectos de la brisa marina sería necesario considerar con más detalle la columna de agua, en particular la profundidad y estructura de la termoclina.
- En el siguiente capítulo, *Time and space variability in the eastern Alboran Sea from March to May 1990*, hemos descrito experimentalmente la circulación en una zona de mar abierto: la cuenca Este del Mar de Alborán. En esta descripción hemos introducido un nuevo estado de la circulación en dicha área —un estado intermedio entre los dos estados más conocidos— y en el cual —debido a la circulación ageostrófica observada— son especialmente importantes las inestabilidades de pequeña escala.
- En el capítulo titulado *Three-dimensional structure of the two anticyclonic gyres in the Alboran Sea* hemos descrito por primera vez la circulación observada en la capa superior en todo el Mar de Alborán como una estructura formada por un frente en forma de onda acoplado con dos sistemas giro anticiclónico mayor—remolino ciclónico menor.

Hemos mostrado que la vorticidad relativa y número de Froude son magnitudes importantes en la conservación de vorticidad potencial en el frente en forma de onda. Hemos calculado, por primera vez a partir de datos hidrográficos, la velocidad vertical quasigeostrófica mediante la resolución numérica de la ecuación Omega quasigeostrófica 3D. La velocidad vertical quasigeostrófica alcanza valores máximos absolutos del orden de 10-20 m/día Este orden de magnitud concuerda con el obtenido mediante el uso de la conservación de vorticidad potencial.

- En el quinto capítulo, *Diagnosis of mesoscale ageostrophic motion through density dynamical assimilation: application to the Alboran Sea*, hemos demostrado la viabilidad del diagnóstico de la velocidad ageostrotrófica por medio de la asimilación dinámica de datos experimentales de densidad en un modelo de ecuaciones primitivas. El resultado final es el estado del sistema en el cual los campos de velocidad y densidad están mutuamente equilibrados. Este estado se obtiene mediante la aplicación de una función de peso sobre las series temporales de las variables generadas por integraciones *hacia adelante y hacia atrás* del modelo numérico.
- En el siguiente capítulo, *About the nature of the generalized Omega equation*, hemos introducido una nueva formulación de la ecuación Omega generalizada para flujos no viscosos, isoentrópicos, bajo las aproximaciones hidrostática, de Boussinesq, y en el plano f . Esta ecuación establece que la variación de vorticidad relativa ageostrófica diferencial en un elemento de fluido es igual a la divergencia de un único campo vectorial. Esta ecuación es la ecuación Omega generalizada escrita en términos del vector \mathbf{Q} , y por lo tanto es útil en estudios comparativos de la velocidad vertical obtenida mediante la resolución de la ecuación Omega quasigeostrófica escrita en términos del vector \mathbf{Q} con la velocidad vertical que satisface las ecuaciones primitivas de Navier-Stokes.

*Oh, sister when I come to knock on your door.
Don't turn away, you'll create sorrow
Time is an ocean but it ends at the shore.
You may not see me
Tomorrow.*

Bob Dylan and Jacques Levy
(Oh, sister).

Forzamiento de flujos ageostróficos. Mar de Alborán y plataforma de Mallorca-Cabrera.

Memoria para la obtención del
título de Doctor en Ciencias Físicas de:
Álvaro Viúdez Lomba

Director:
Dr. Joaquín Tintoré Subirana

VOLUMEN II: FIGURAS

Universitat de les Illes Balears
Junio de 1994

Capítulo 2

An Exploratory Numerical Study of the Currents off the Southern Coast of Mallorca Including the Cabrera Island Complex

Francisco E. Werner¹

Alvaro Viúdez²

Joaquín Tintoré²

J. of Marine Systems, 4, 45-66, 1993.

¹Skidaway Institute of Oceanography, P.O. Box 13687, Savannah, GA 31416, USA

²Grup de Fluids Geofísics, Departament de Física, Universitat de les Illes Balears, Palma 07071, SPAIN

LIST OF FIGURES

LIST OF TABLES

Table 1. Wind-direction, wind-speed and frequency of occurrence (in %) at Palma airport from 1967 to 1984. Calm wind conditions (< 1 knot) occurred in 40.5% of the record; storms with WSW winds between 11 and 16 knots occurred in 5.1 % of the record.

LIST OF FIGURES

Figure 1. Map of the Balearic Islands. The domain of interest is within the boxed region along the southern coast of the Island of Mallorca.

Figure 2. Bathymetric contours in meters of the model domain.

Figure 3a. Finite element mesh with placenames.

Figure 3b. Detail of the mesh in the vicinity of Cabrera.

Figure 4a. Sea surface elevation in a cross section from Pto. Colom to 200 m isobath: elevation producing 20 cm/s geostrophic currents into the model domain with an input transport of 0.13 Sv (*) and exponential elevation producing the same transport (X).

LIST OF FIGURES

Figure 4b. Sea surface elevation due to prescribed tilt off Porto Colom (in cm).

Figure 4c. The transport budget due to prescribed tilt off Porto Colom (in %).

Figure 4d. Sea surface elevation in the vicinity of the Cabrera Island-complex due to prescribed tilt off Porto Colom (in cm).

Figure 4e. Depth-averaged flow due to prescribed tilt off Porto Colom.

Figure 4f. Detail of 4b in the vicinity of Cabrera.

Figure 4g. Detail of bottom flow in the vicinity of Cabrera due to prescribed tilt off Porto Colom.

Figure 5. Thirty-two day record of wind data at Palma airport (in m/s). Each plot represents a week.

Figure 6. A week of simulated wind data at Bahía de Palma for modelling purpose under sea breeze conditions (in m/s).

Figure 7a. Response of the surface currents to forcing by the steady wind component for the Bahía de Palma.

Figure 7b. Response of the currents 3 nodes below the surface to forcing by the steady wind component for the Bahía de Palma.

Figure 7c. Response of the surface currents to forcing by the 24-hour wind component for the Bahía de Palma. An asterisk in the center of an ellipse indicates counterclockwise rotation.

LIST OF FIGURES

Figure 7d. Response of the currents 3 nodes below the surface to forcing by the 24-hour wind component for the Bahía de Palma. An asterisk in the center of an ellipse indicates counterclockwise rotation.

Figures 8a-d. Surface currents in the Bahía de Palma due to 24-hour period sea breeze: (a) increasing breeze of magnitude $|\tau| = 0.80 \times 10^{-2}$ Pa at 0900 hours, (b) maximum breeze $|\tau| = 1.14 \times 10^{-2}$ Pa at 1200 hours, (c) decreasing breeze of magnitude $|\tau| = 0.80 \times 10^{-2}$ Pa at 1500 hours, (d) time at which breeze is zero.

Figures 9a-b. Bottom currents in the Bahía de Palma due to 24-hour period sea breeze: (a) maximum breeze $|\tau| = 1.14 \times 10^{-2}$ Pa, (b) time at which breeze is zero.

Figure 10. Surface currents due to a 4-day period WSW storm of $|\tau| = 0.5$ Pa during maximum wind stress.

Figure 11. A zoom of Figure 10 within the Bahía de Palma.

Figure 12. Sea surface elevation (mm) due to a 4-day period WSW storm of $|\tau| = 0.5$ Pa during maximum wind stress.

Wind Direction	Wind Velocity (Knots)												TOTAL	
	Calm	1-3	4-6	7-10	11-16	17-21	22-27	28-33	34-40	41				
Calm	40.5													40.5
N			0.4	0.2	0.1									0.7
NNE		0.1	0.4	0.3	0.3	0.1								1.2
NE		0.1	0.3	0.4	0.4	0.1								1.3
ENE		0.4	3.6	5.2	3.9	1.2	0.5	0.1						14.9
E		0.2	1.1	1.3	0.6	0.1								4.3
ESE		0.1	0.3	0.3	0.1									2.6
SE		--	0.1	0.1	0.1	--	--							0.3
SSE		--	0.3	0.3	0.1	--								0.7
S		--	0.4	0.3	0.2									0.9
SSW		0.1	1.1	2.0	1.3	0.1	--							4.6
SW		0.1	0.9	2.4	2.4	0.3	--	--						6.0
WSW		0.1	1.9	4.1	5.1	1.1	0.5	0.1	0.1					14.0
W		0.1	0.9	1.0	0.8	0.4	0.2	0.1	--					3.5
WNW		0.1	0.6	1.1	0.8	0.2	0.1	--	--	--				3.1
NW		0.1	0.4	0.8	1.1	0.5	0.2	0.1	0.1	--	--			3.3
NNW		0.1	0.4	0.5	0.4	0.2	0.1	--	--					1.7
Total	40.5	1.5	13.0	20.3	17.8	1.3	1.8	0.5	0.2	--	--			

Table 1

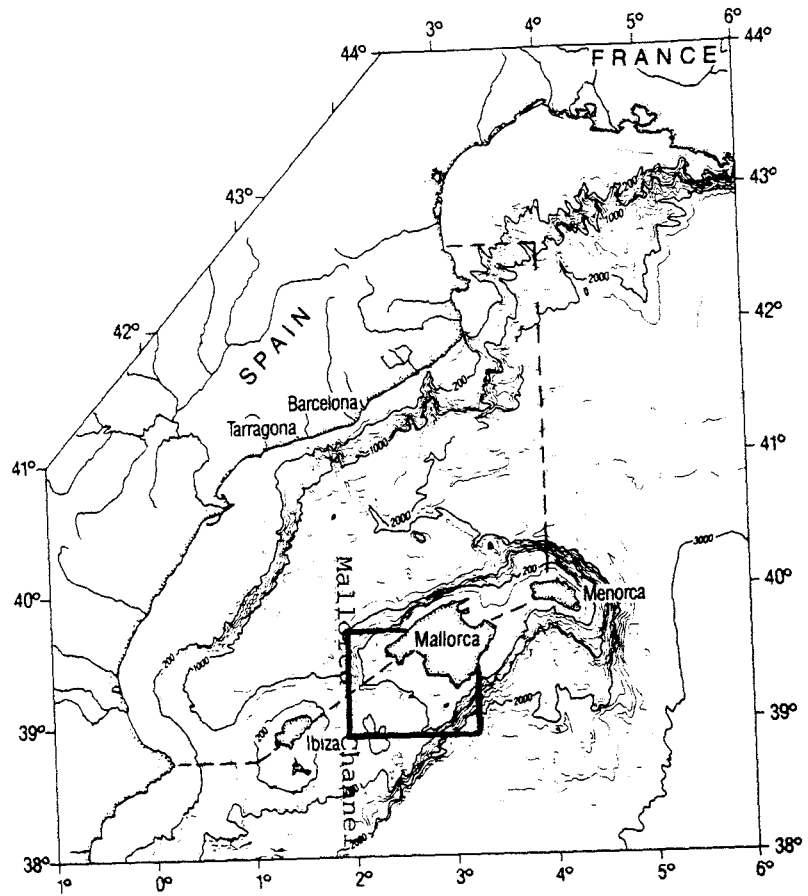


Figure 1

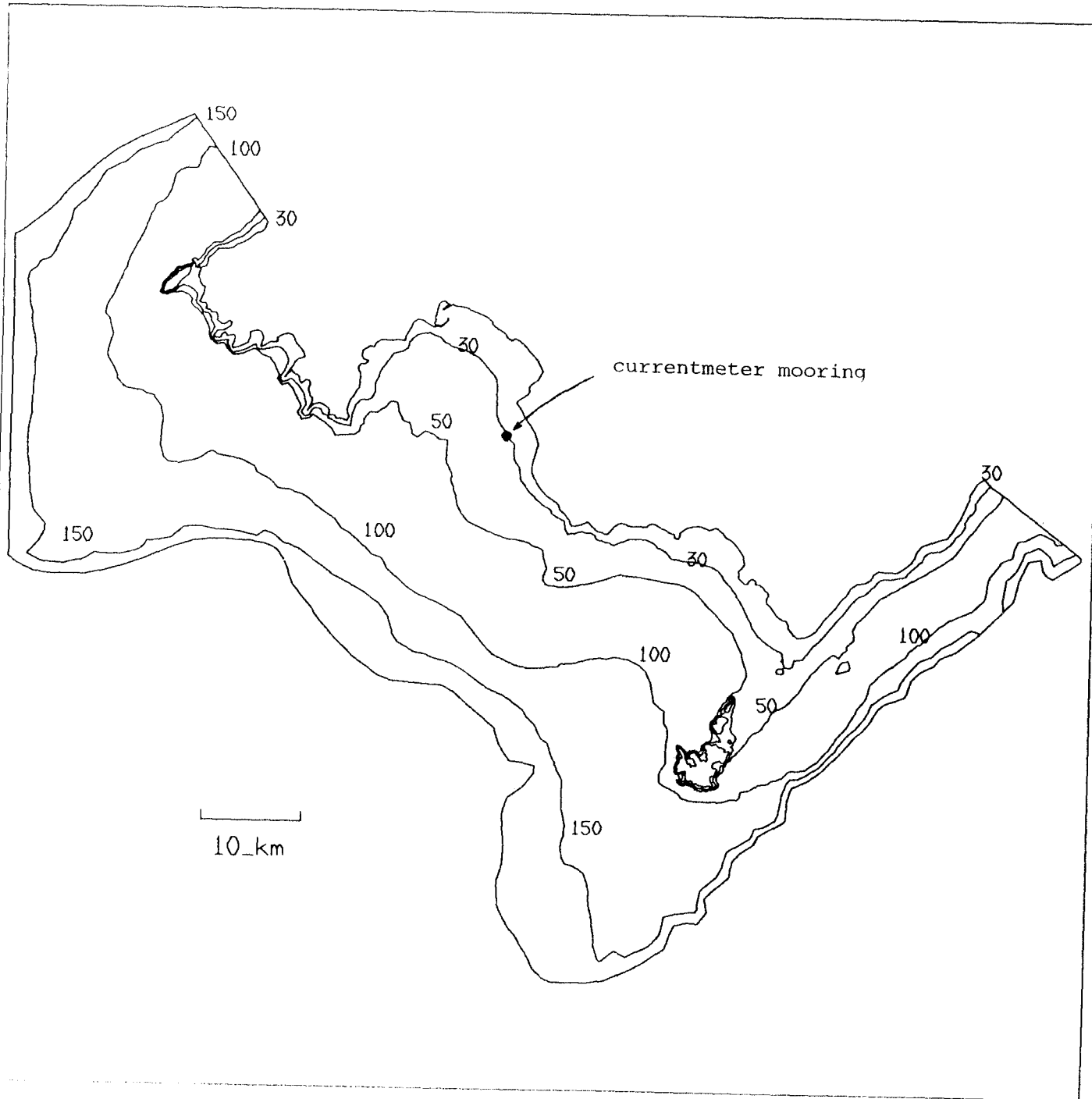


Figure 2

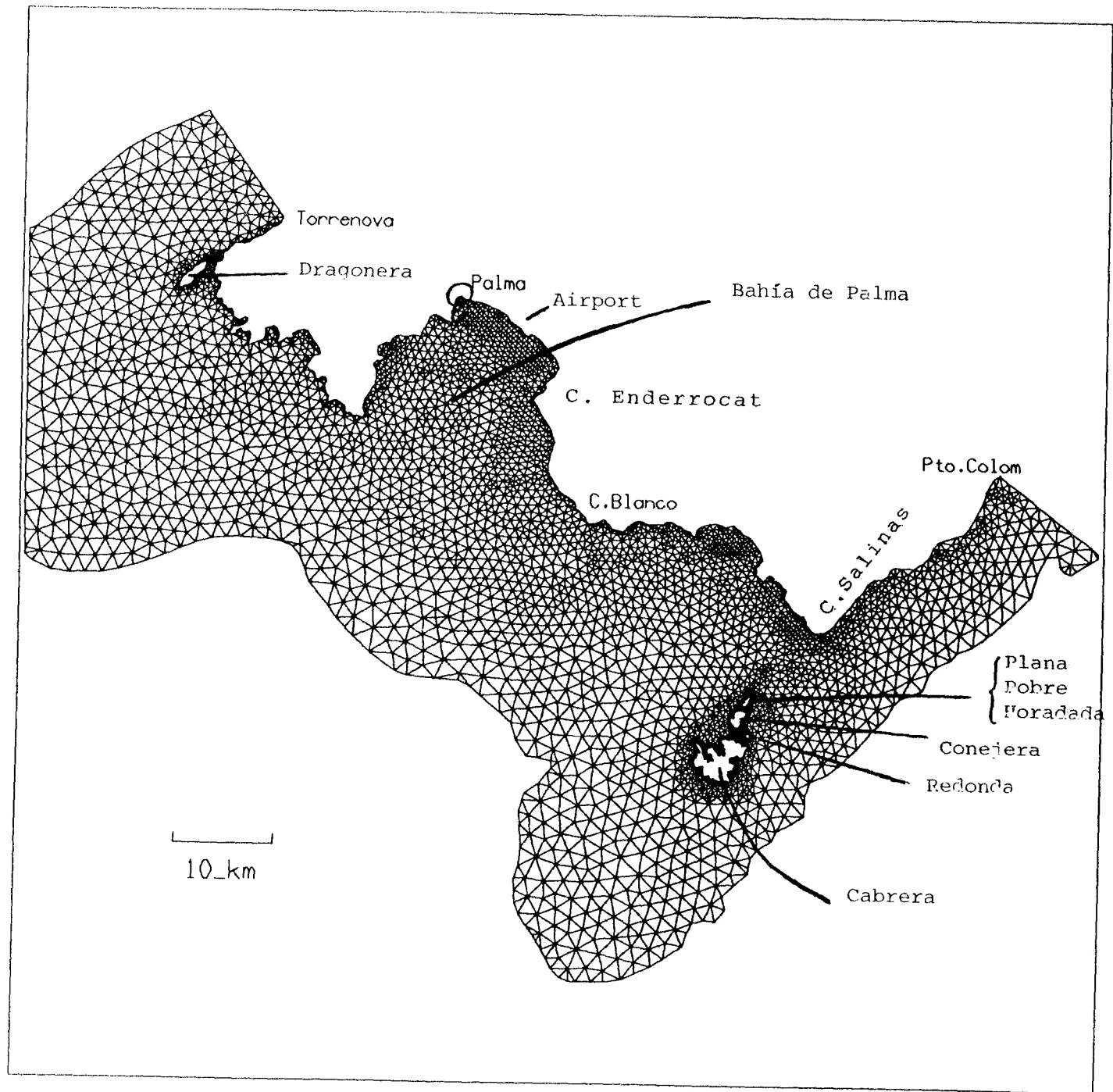


Figure 3a

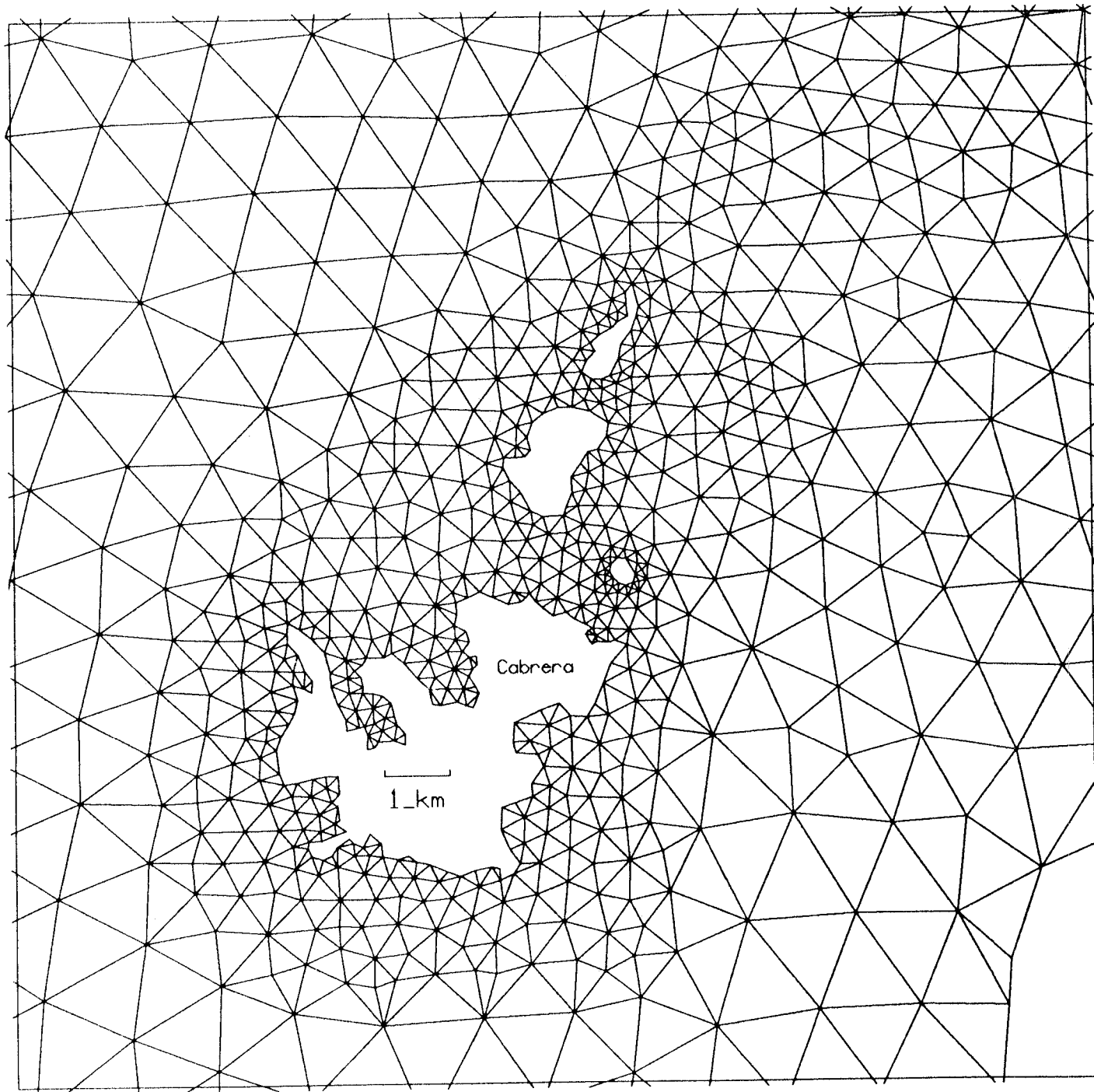


Figure 3b

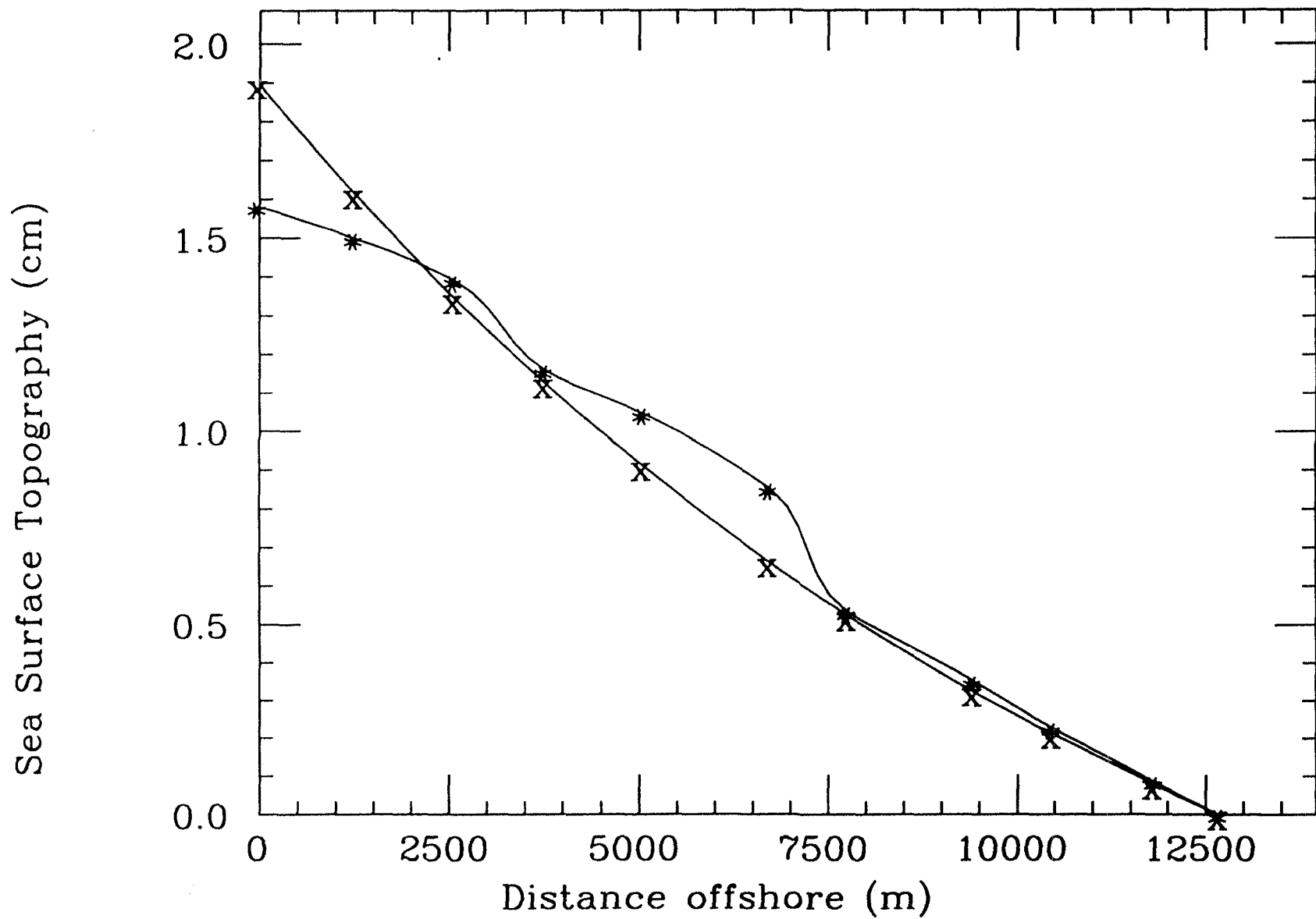


Figure 4a

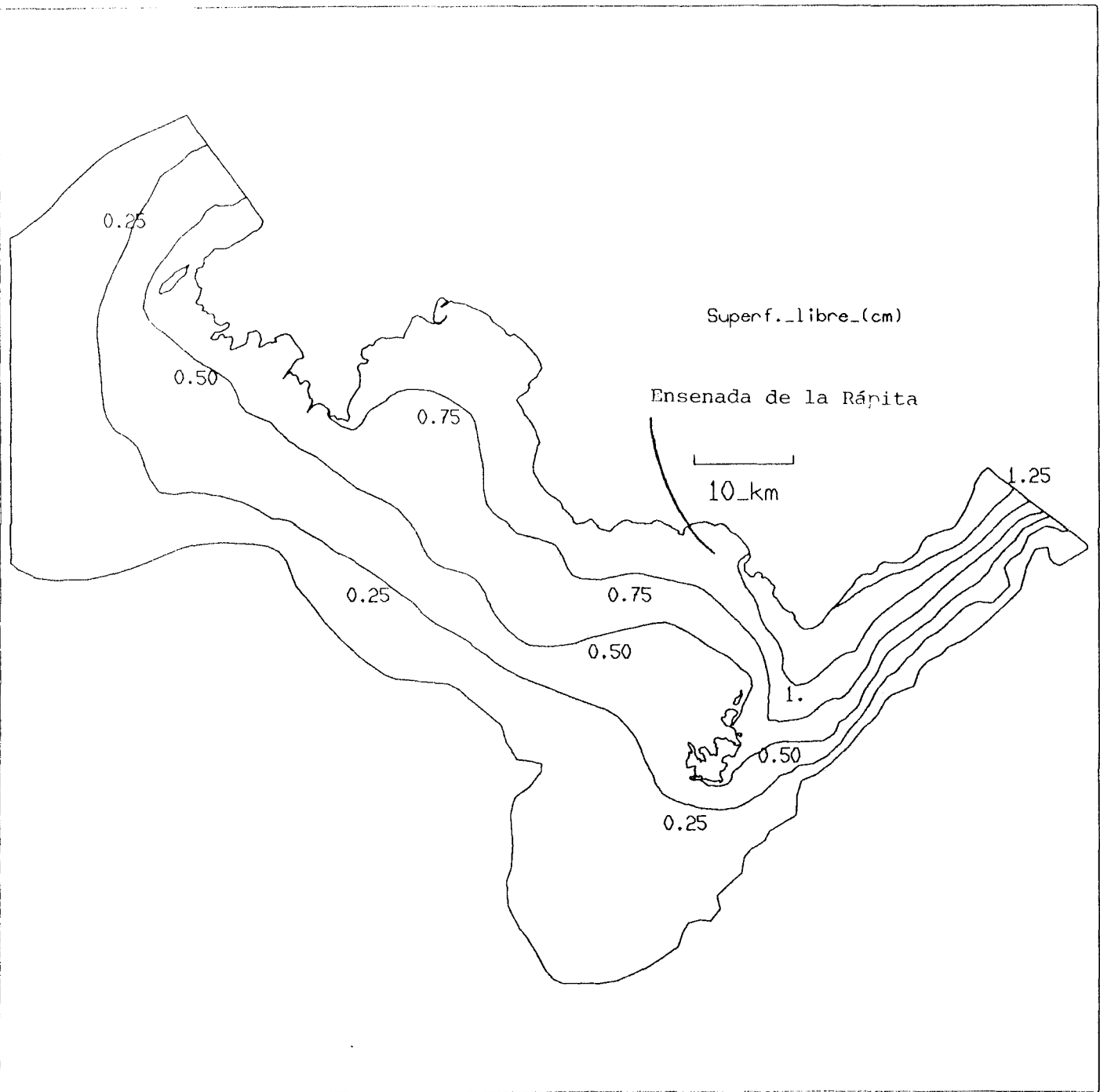


Figure 4b

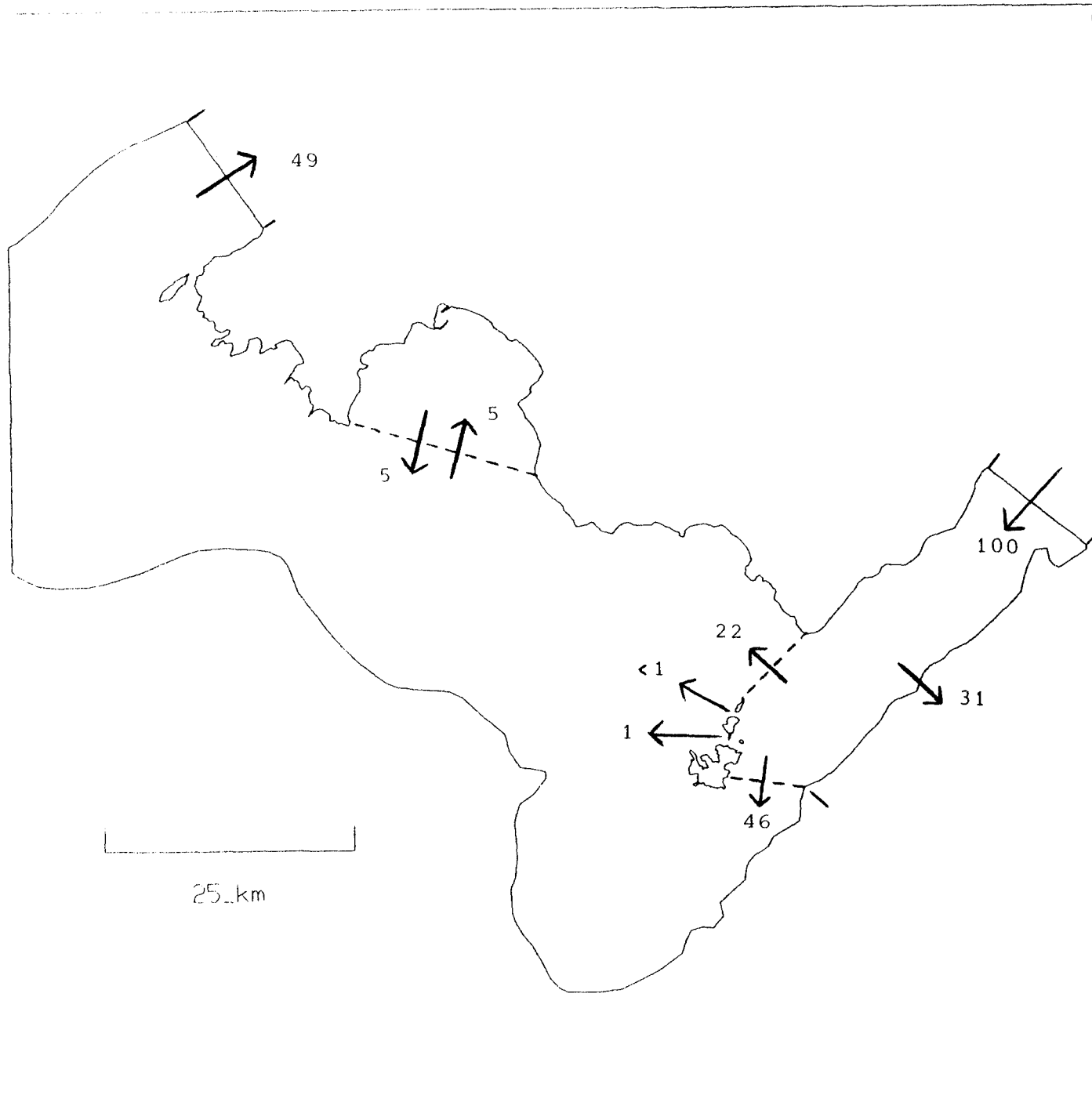


Figure 4c

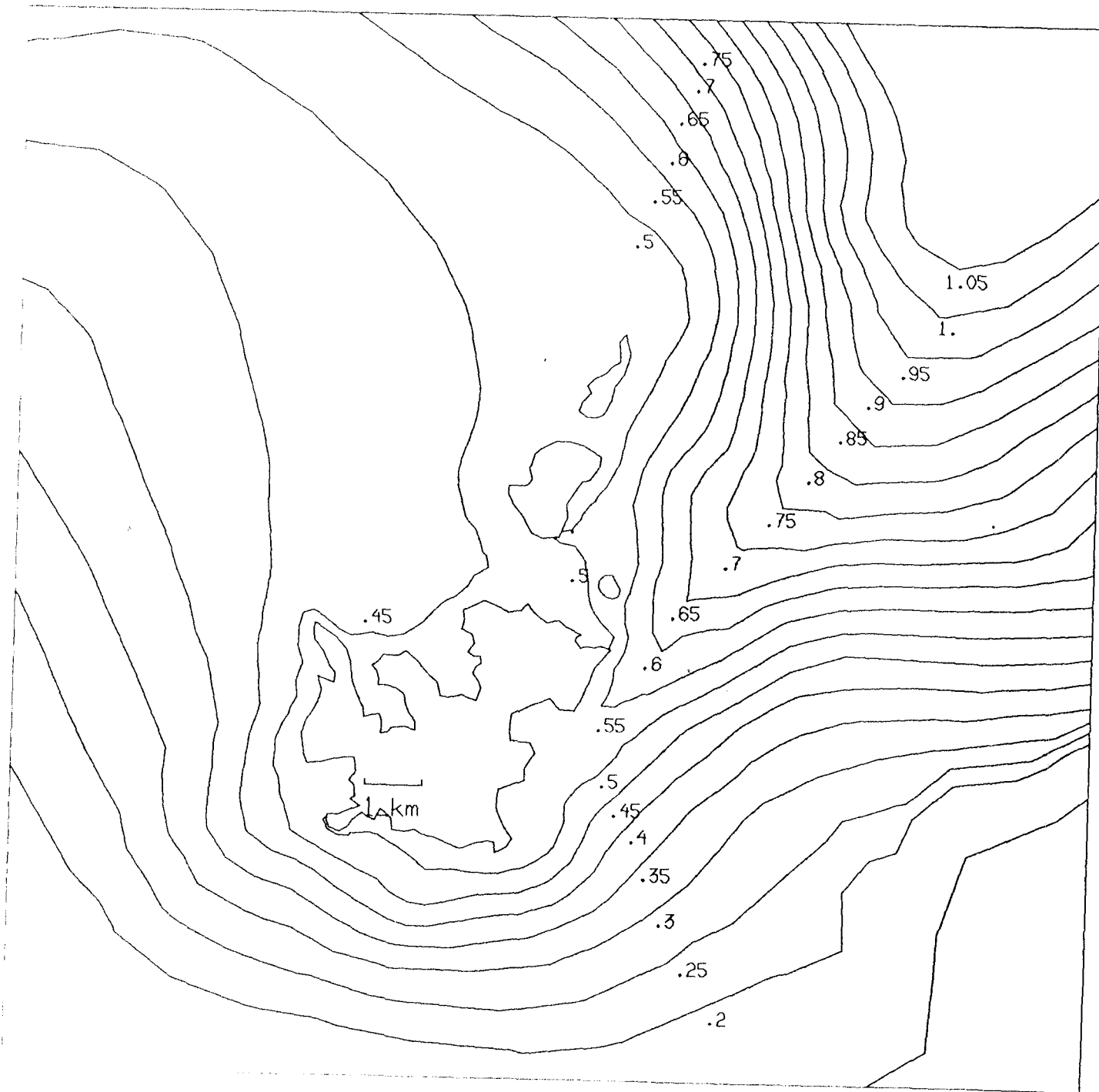


Figure 4d

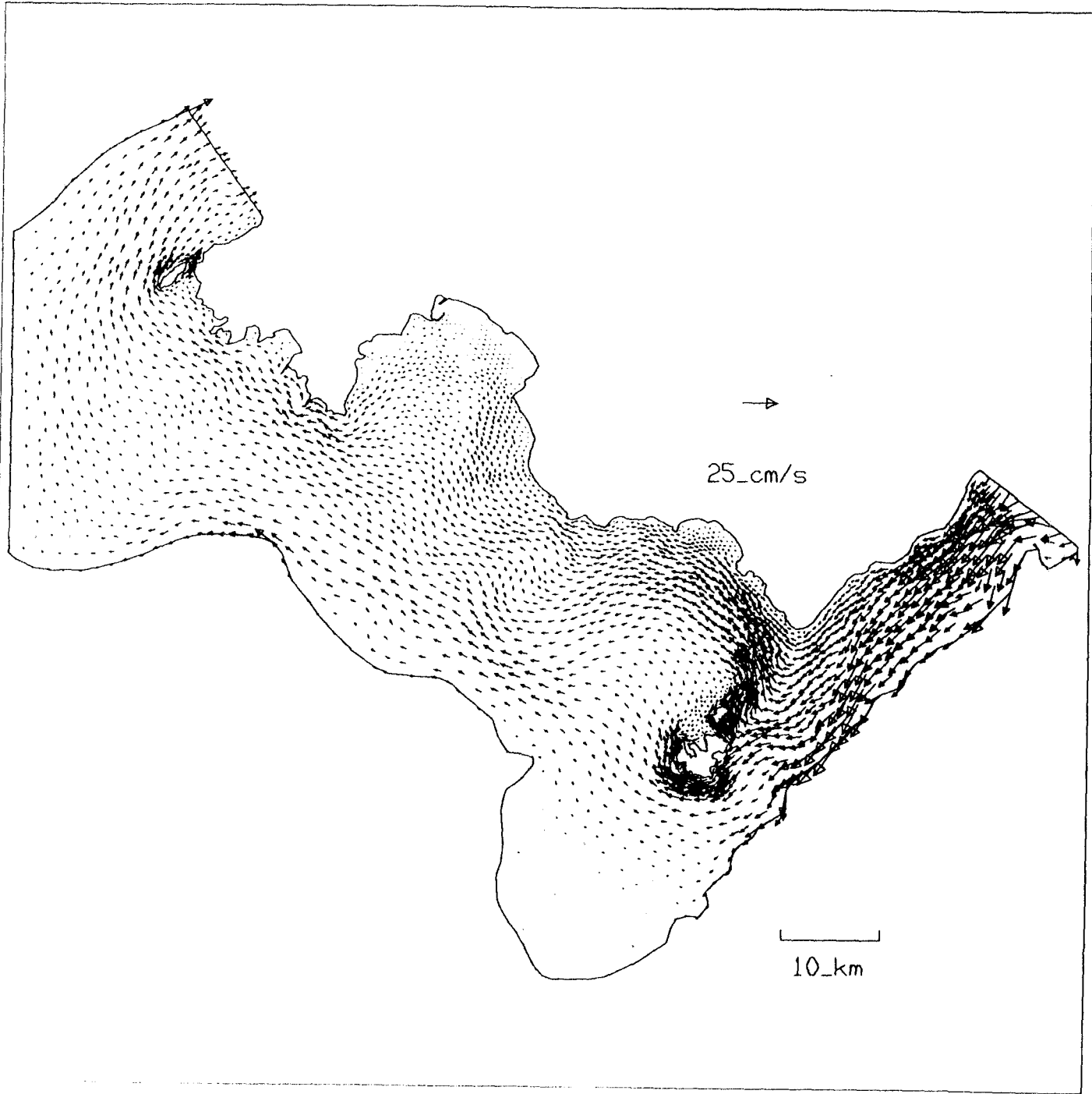


Figure 4e

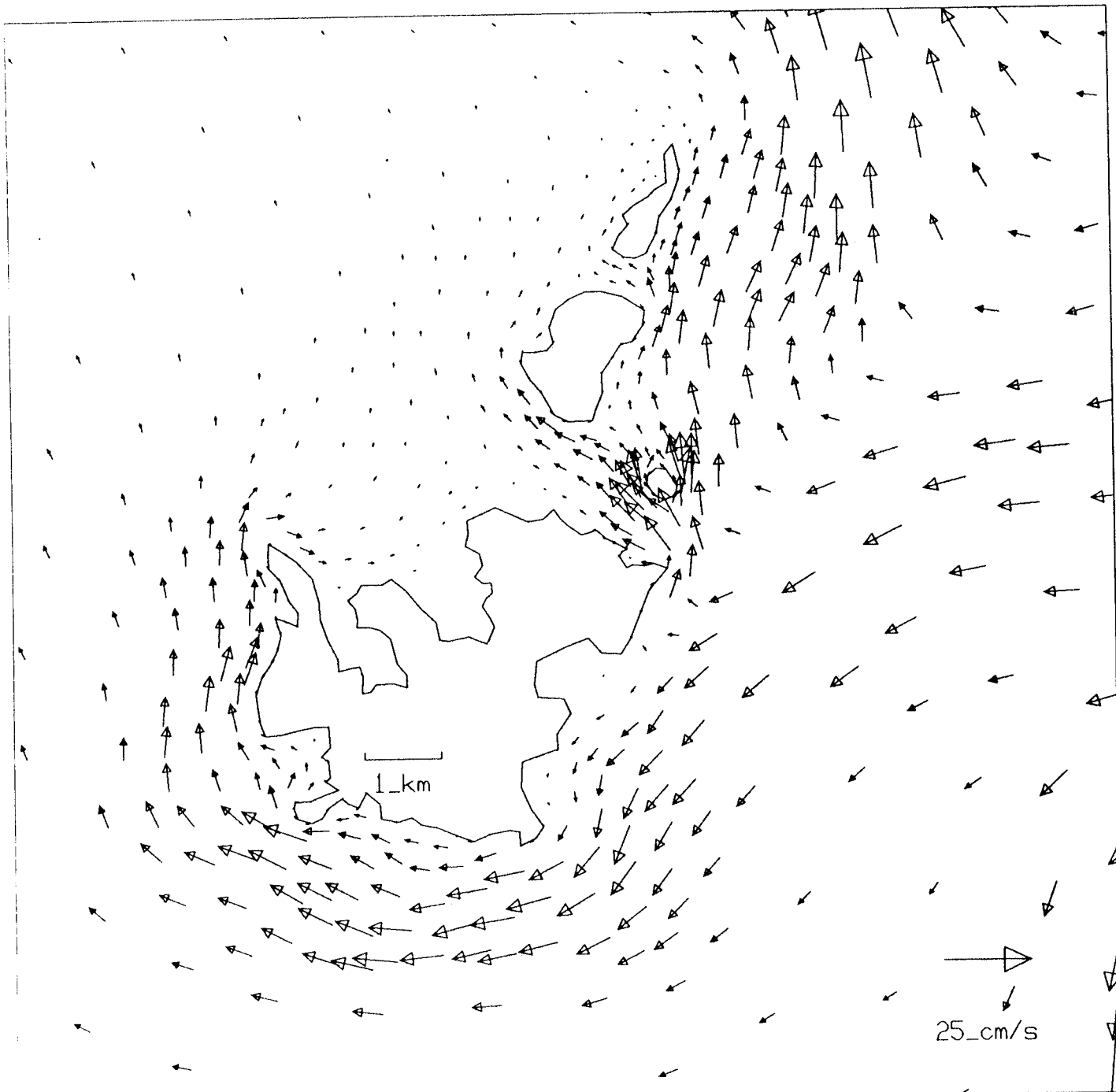


Figure 4f

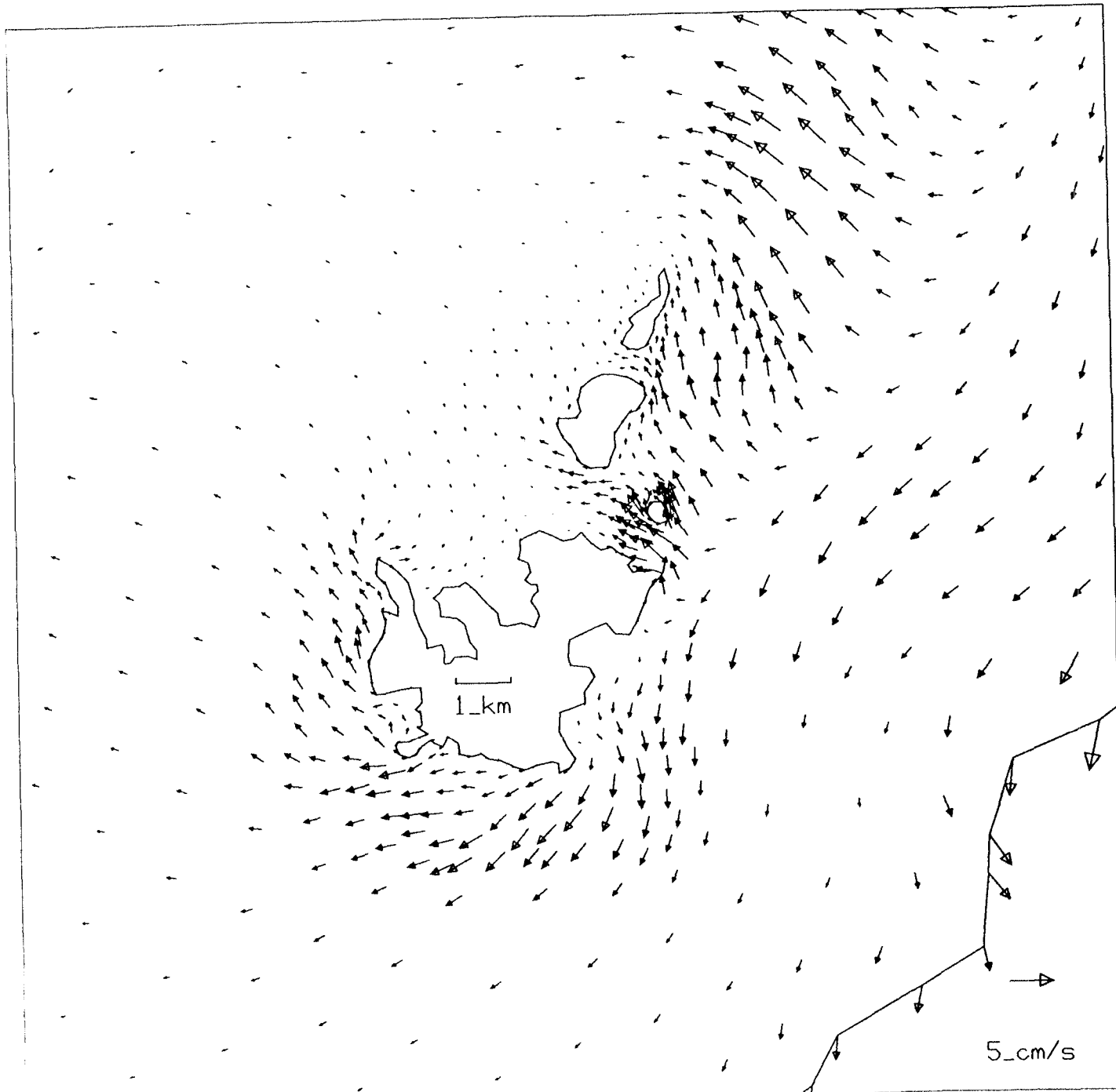


Figure 4g

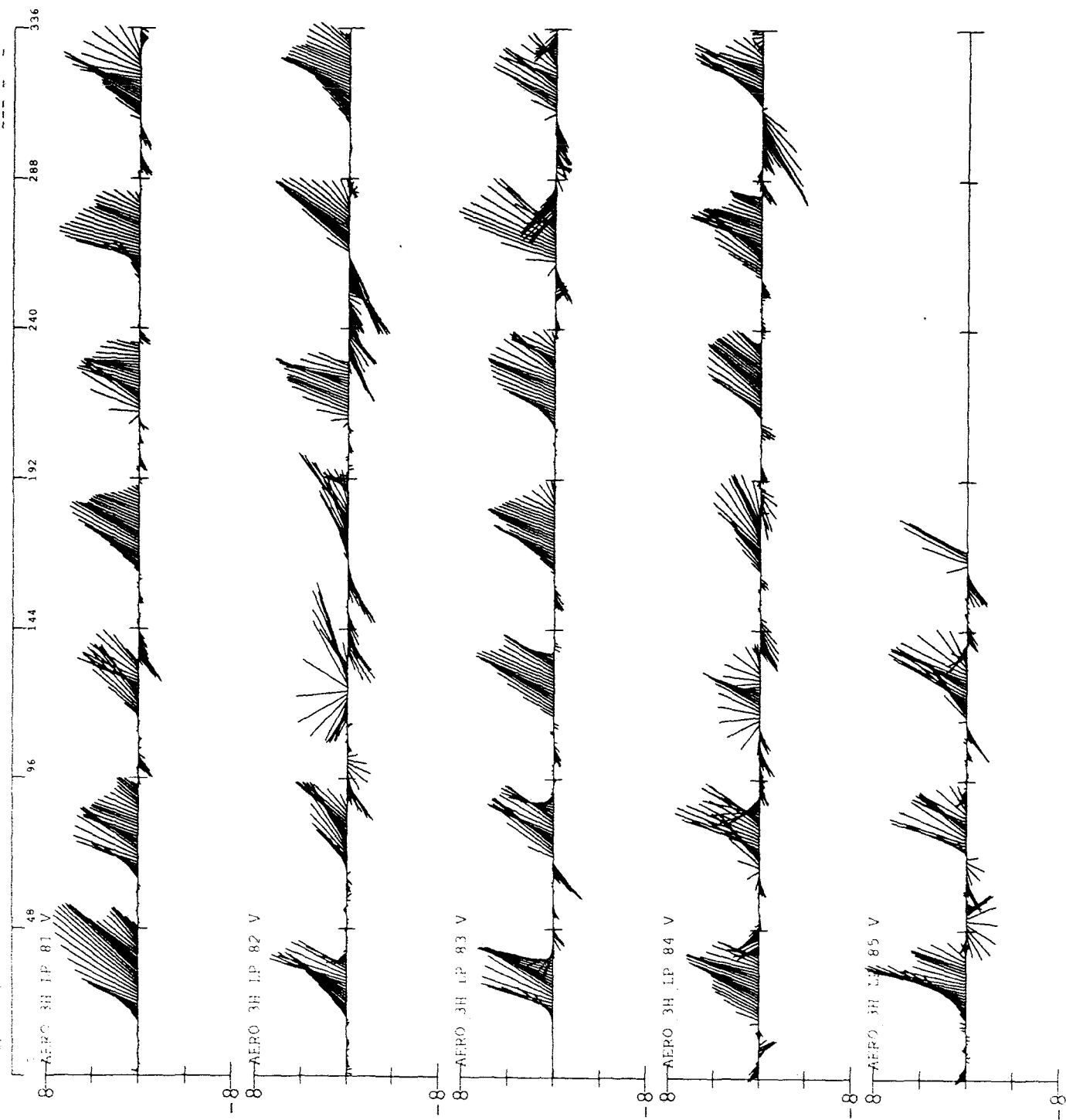


Figure 5

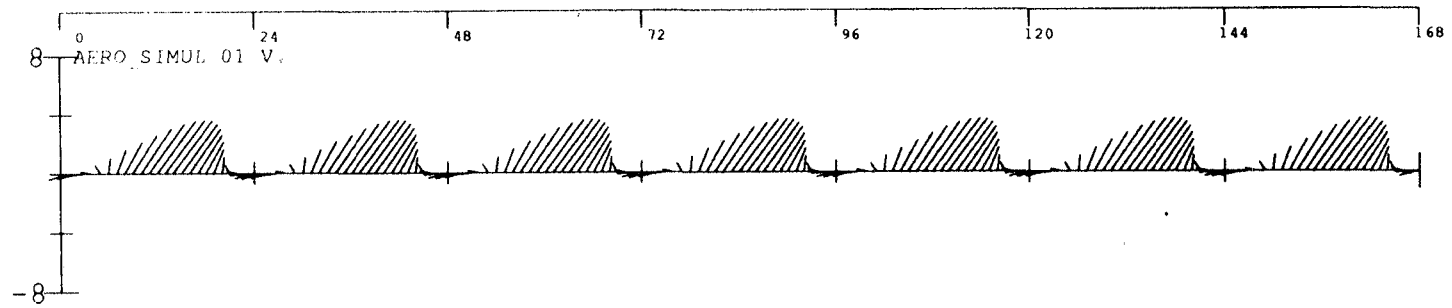


Figure 6

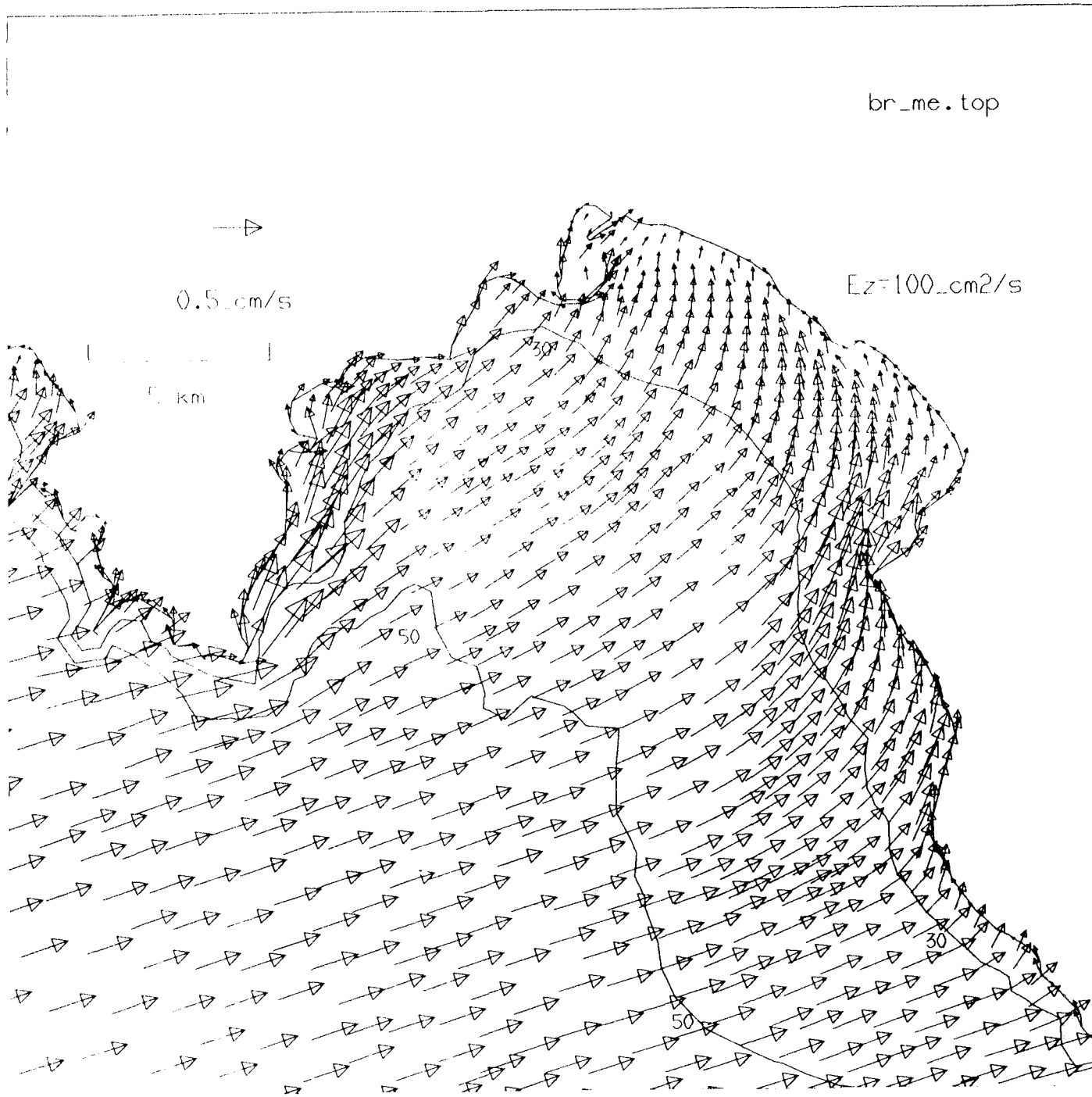


Figure 7a

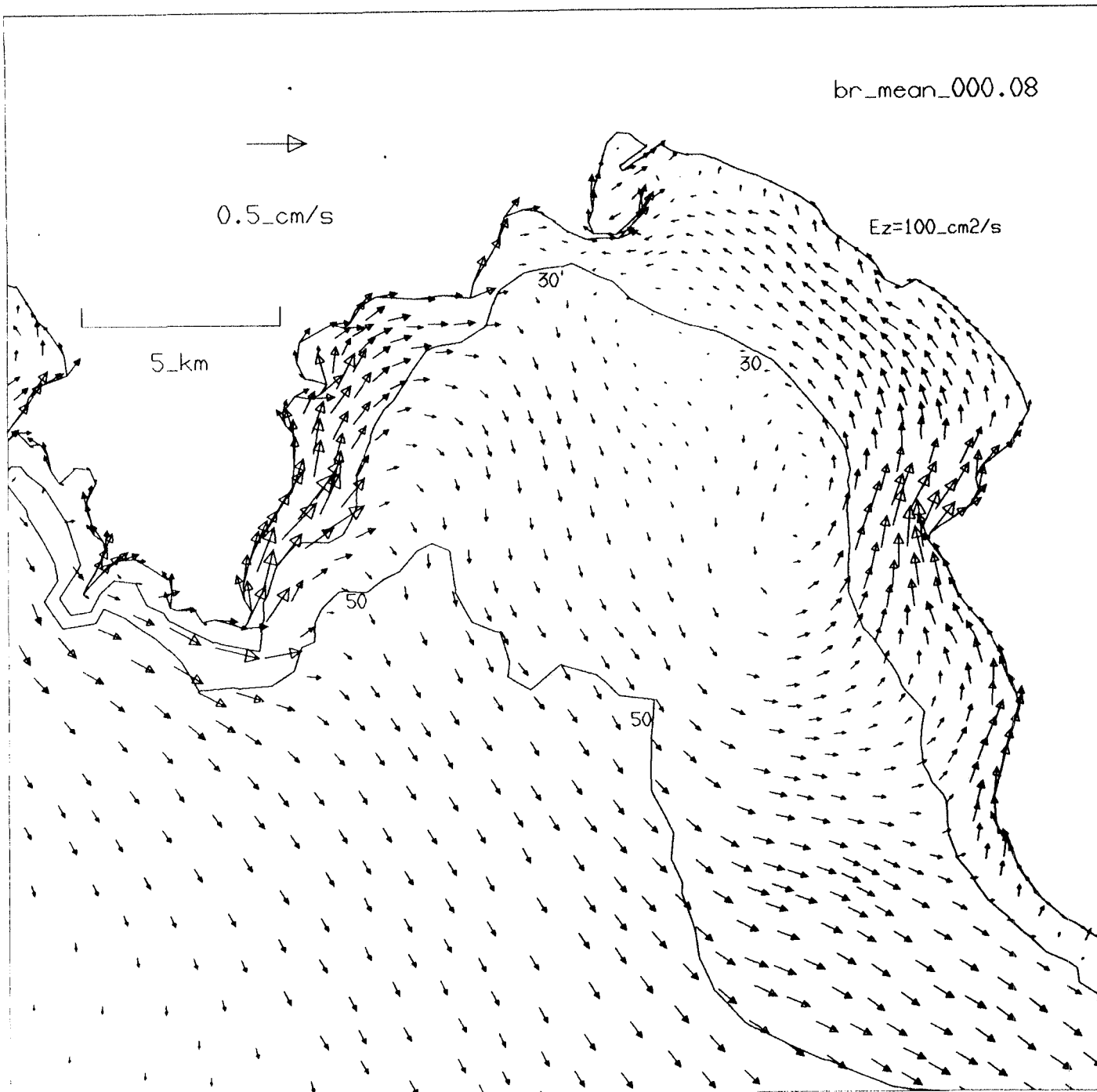


Figure 7b

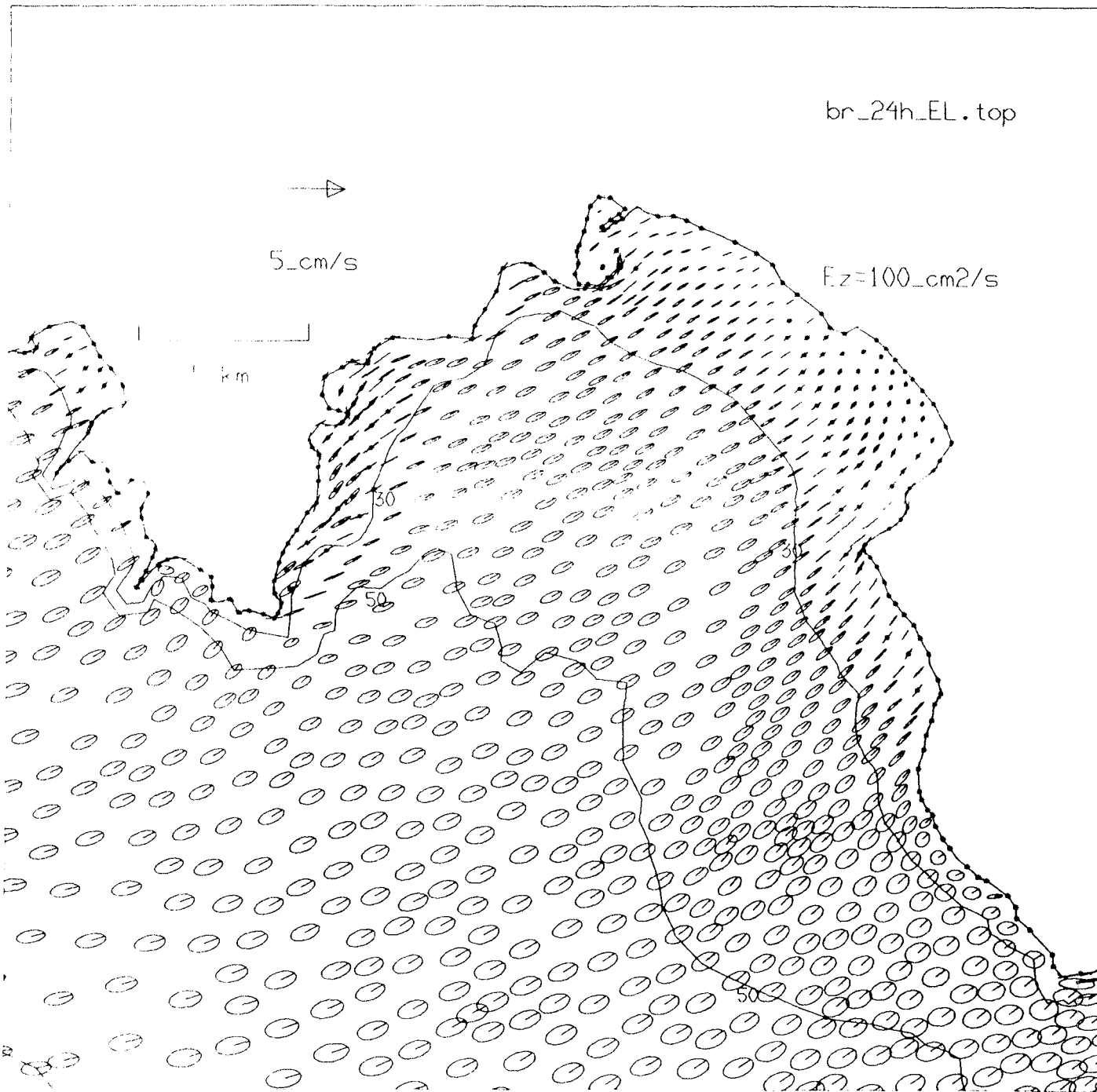


Figure 7c

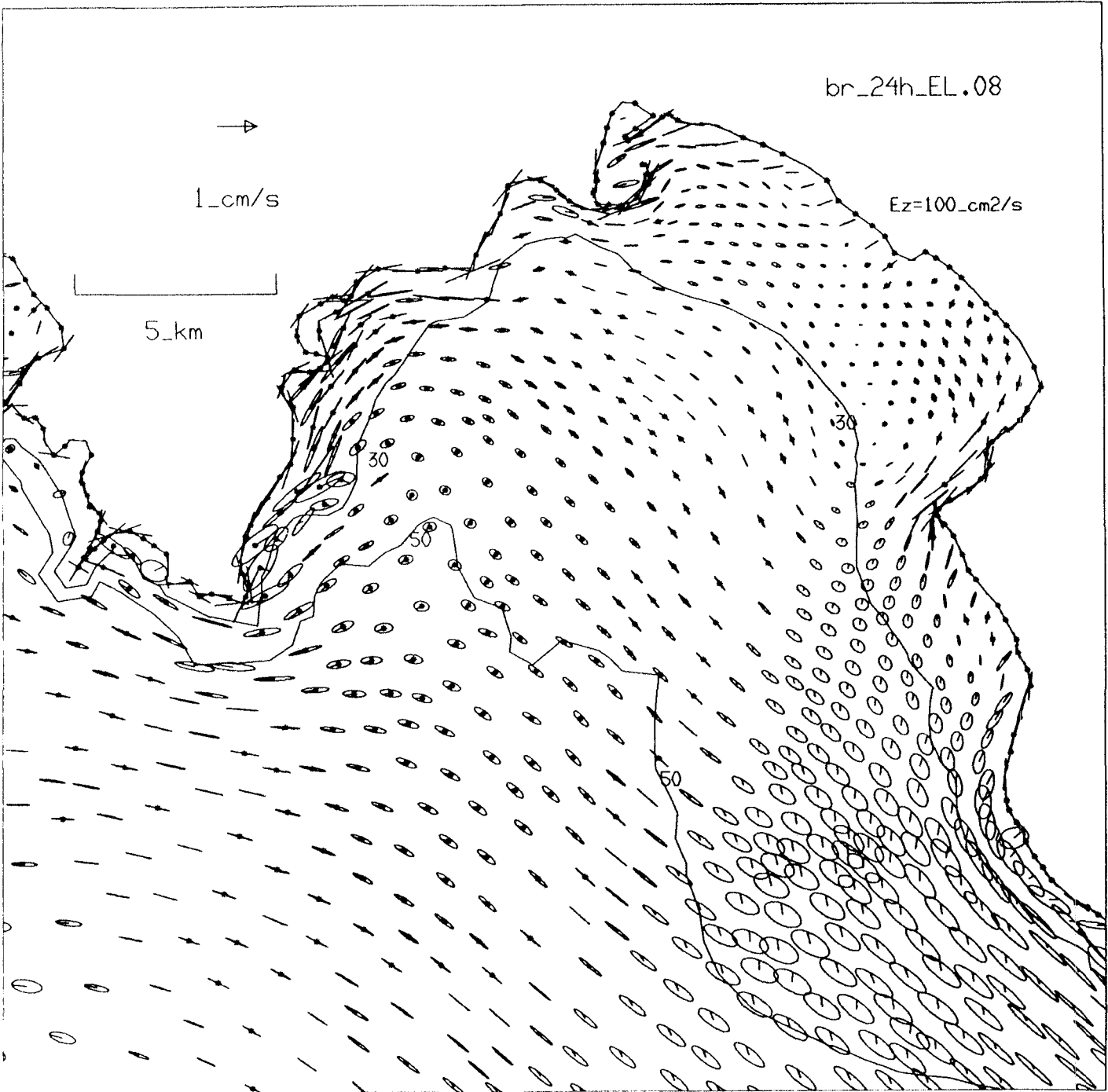


Figure 7d

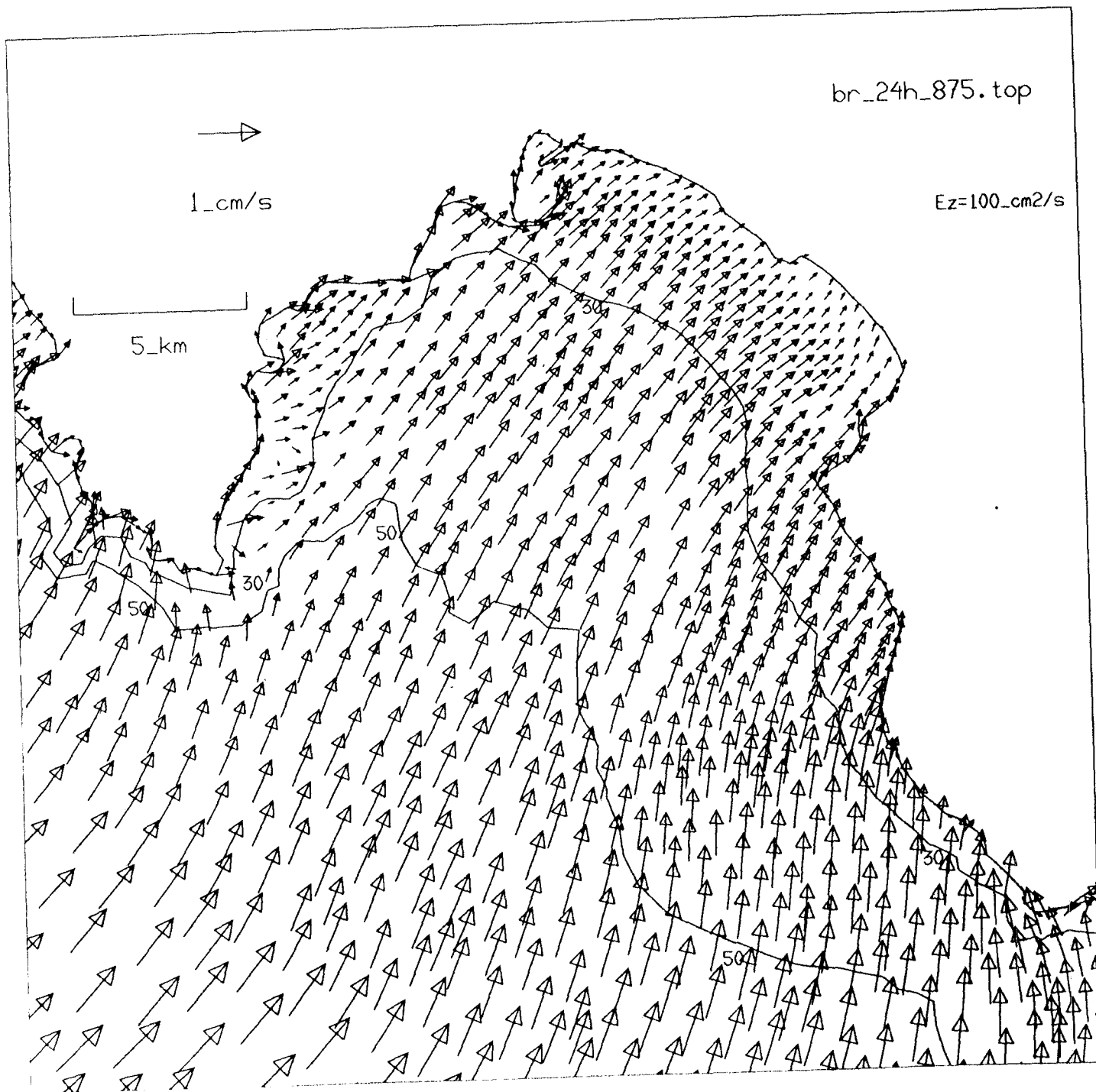


Figure 8a

br_24h_000.top

$Ez=100\text{ cm}^2/\text{s}$



1_cm/s

5_km

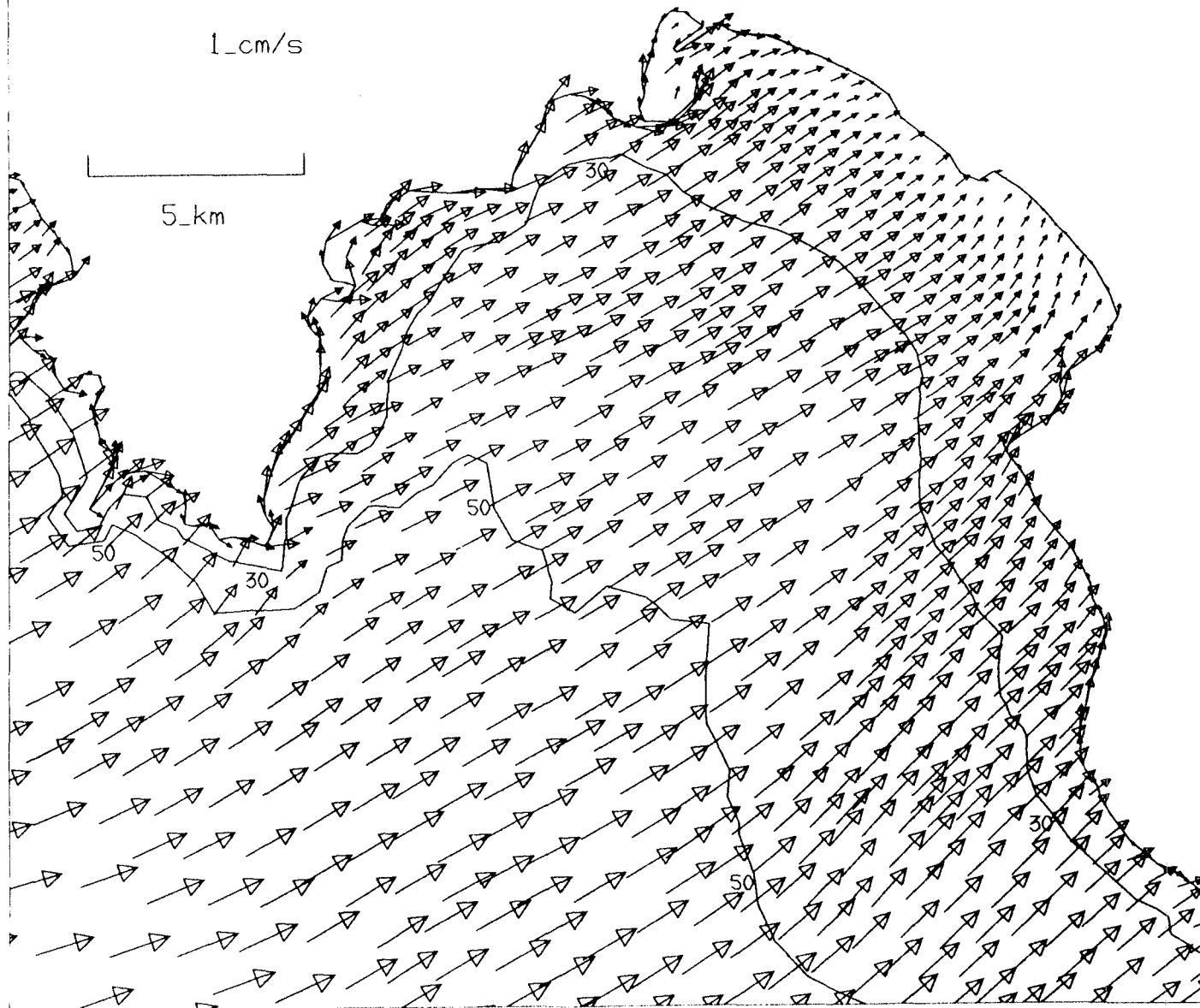


Figure 8b

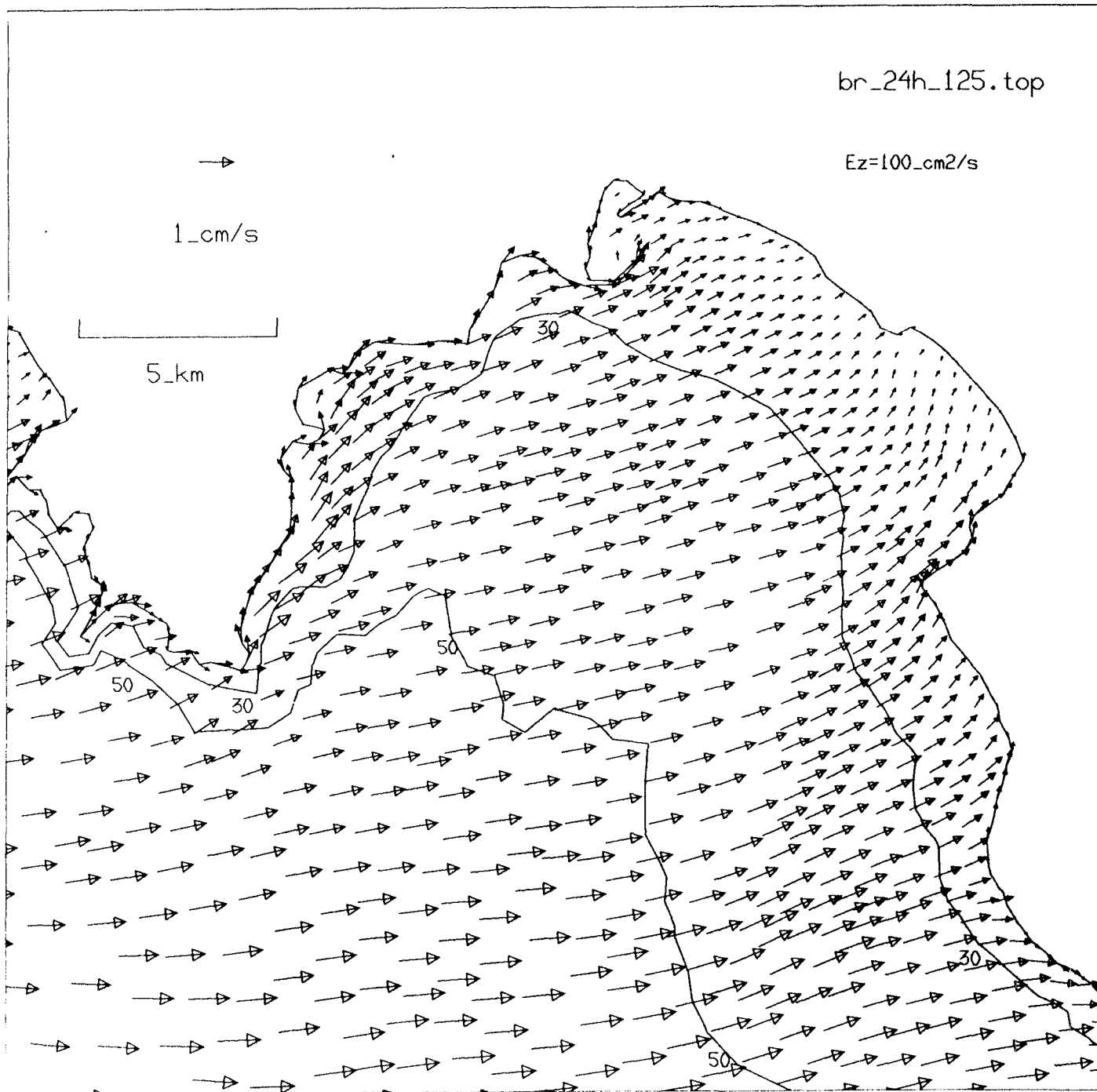


Figure 8c

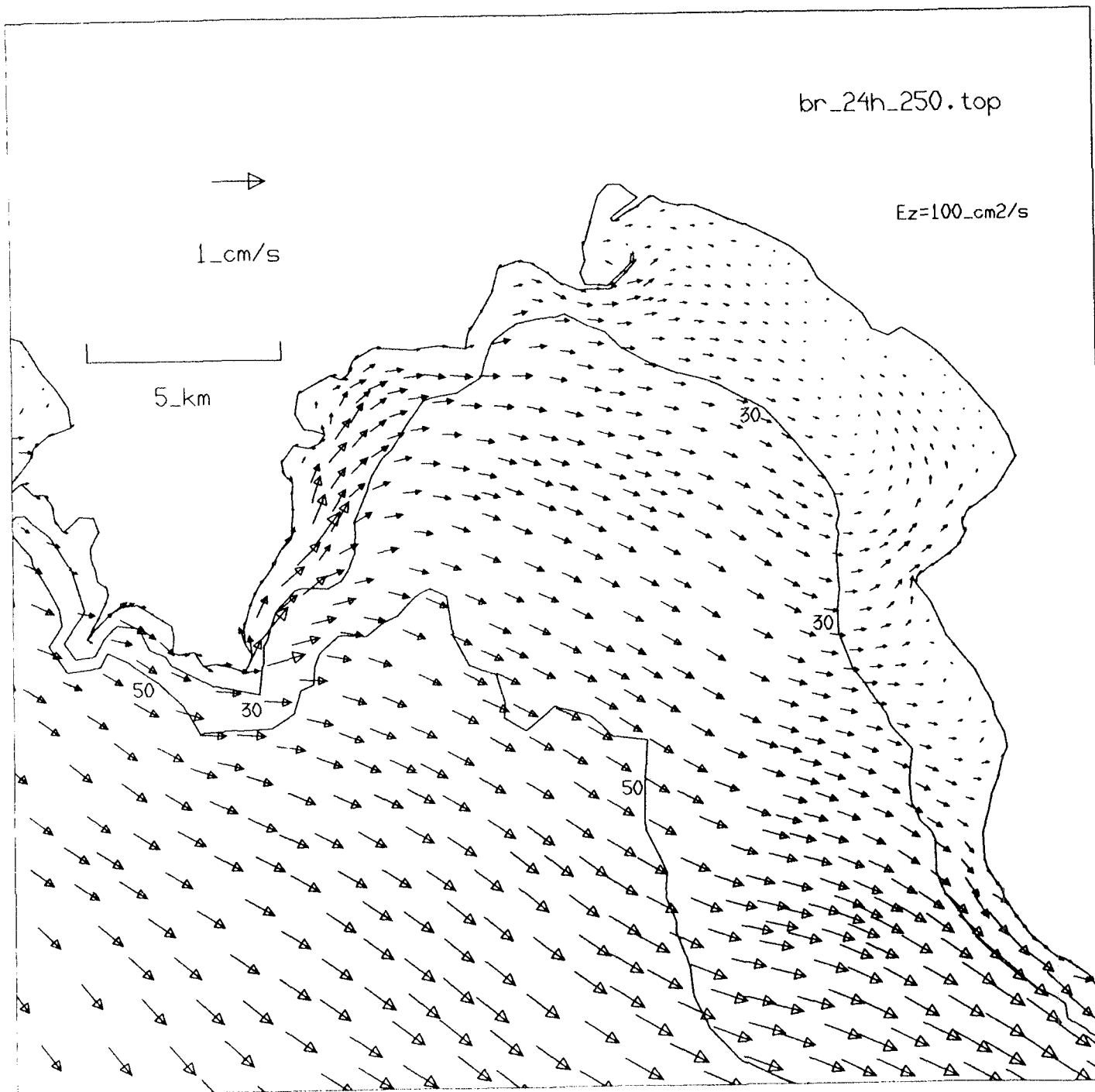


Figure 8d

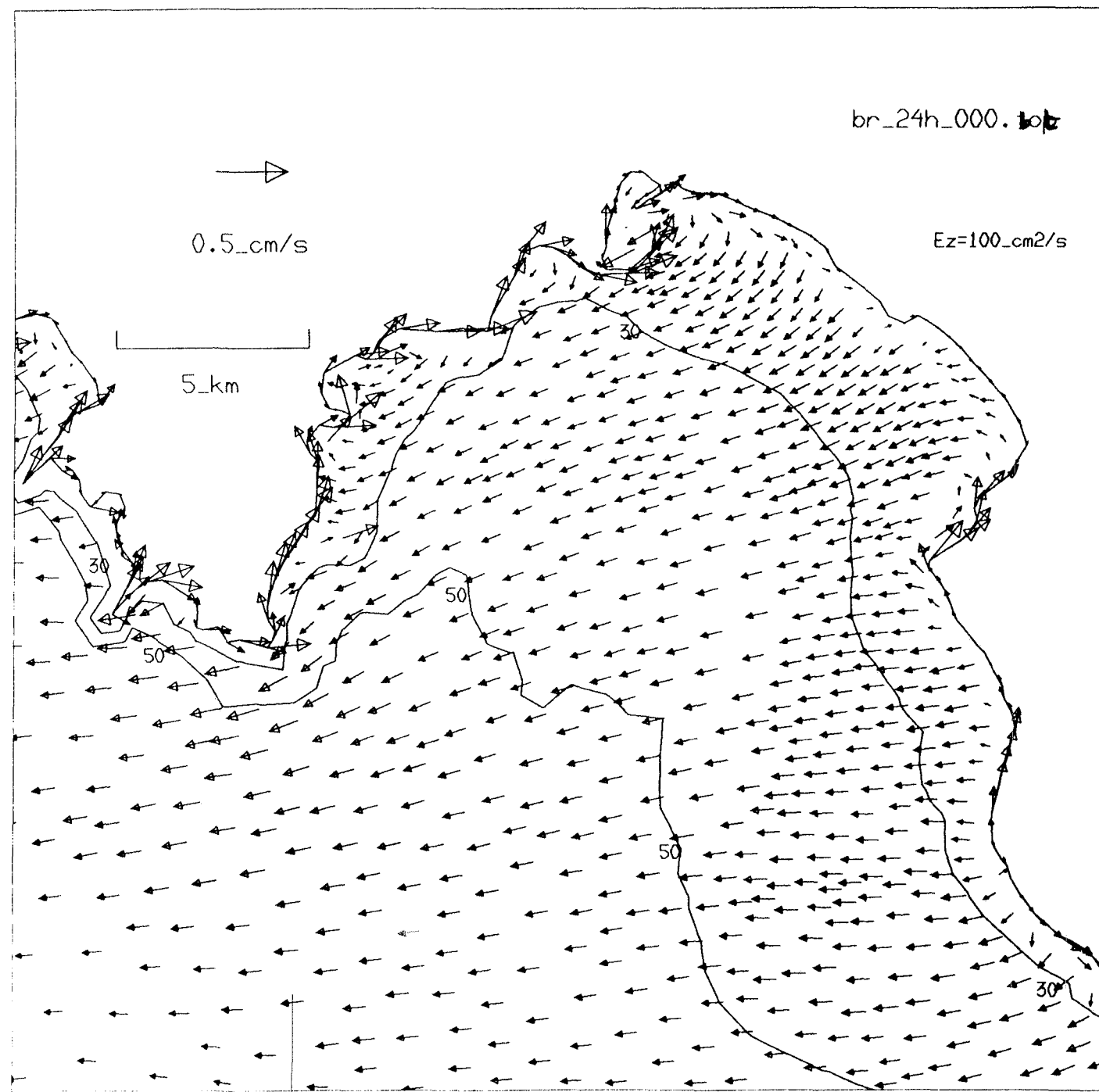


Figure 9a

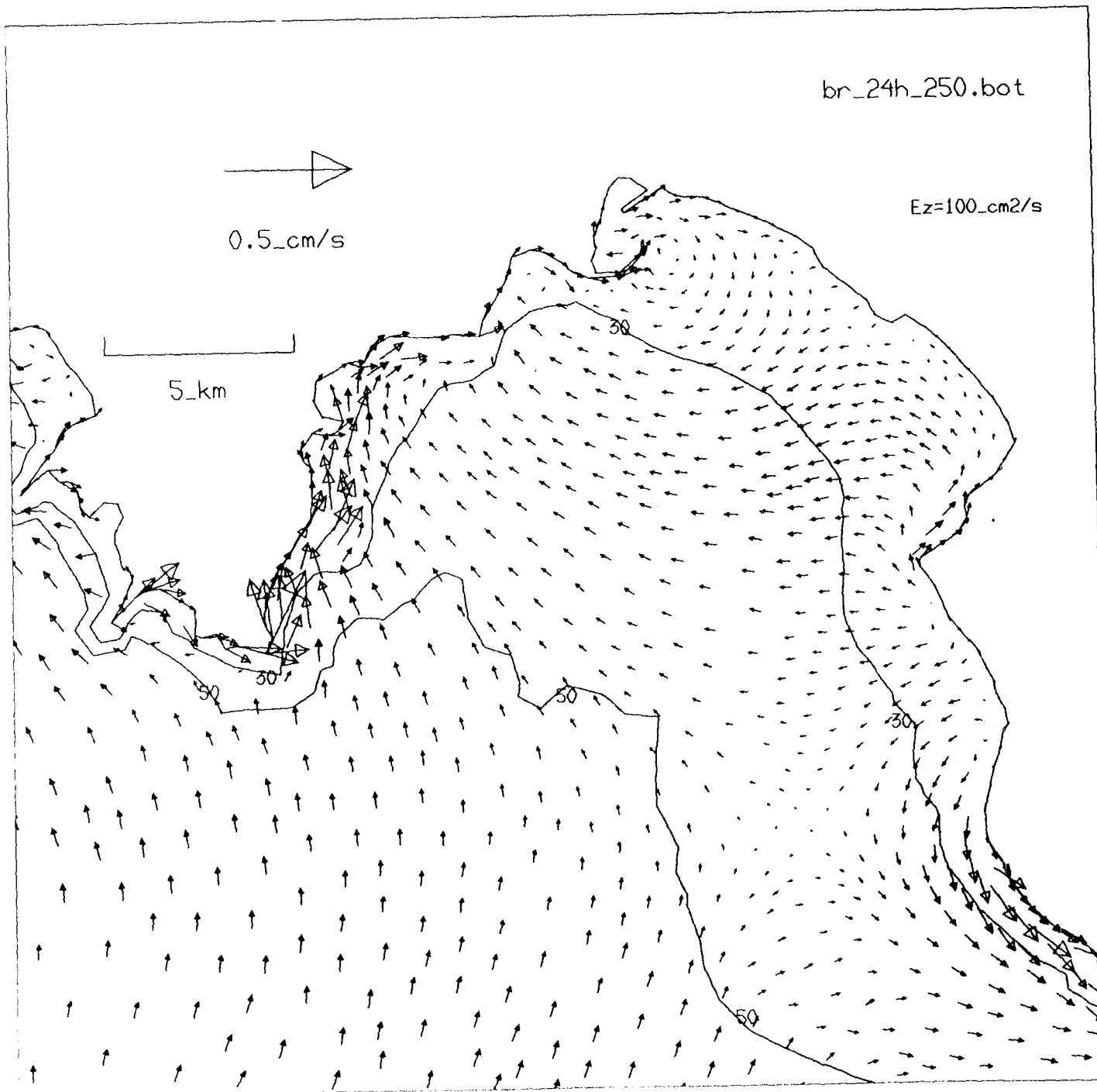


Figure 9b

storm_000.11

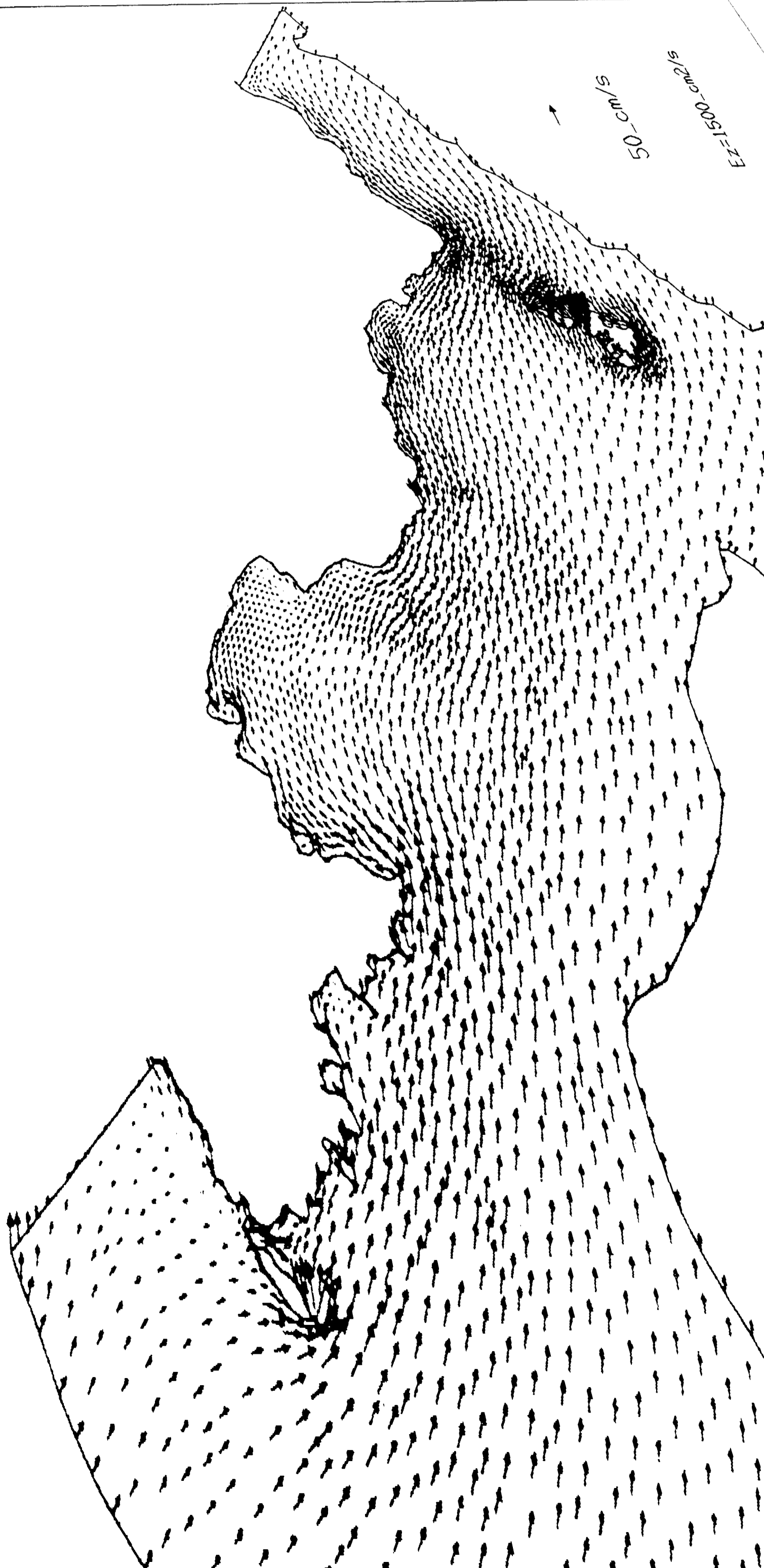


Figure 10

storm_000.11

$Ez=1500\text{-cm}^2/\text{s}$



50_cm/s



5_km

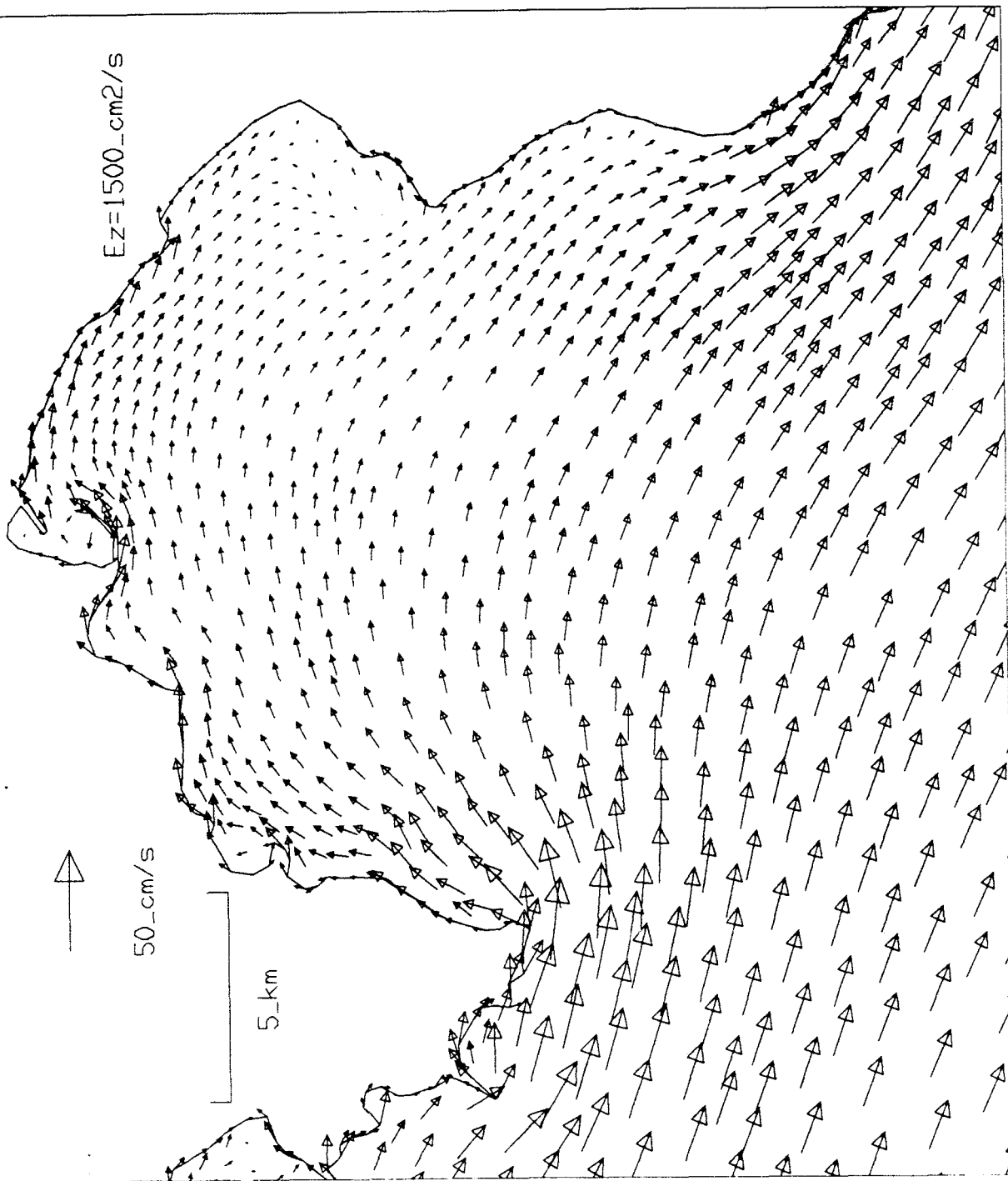


Figure 11

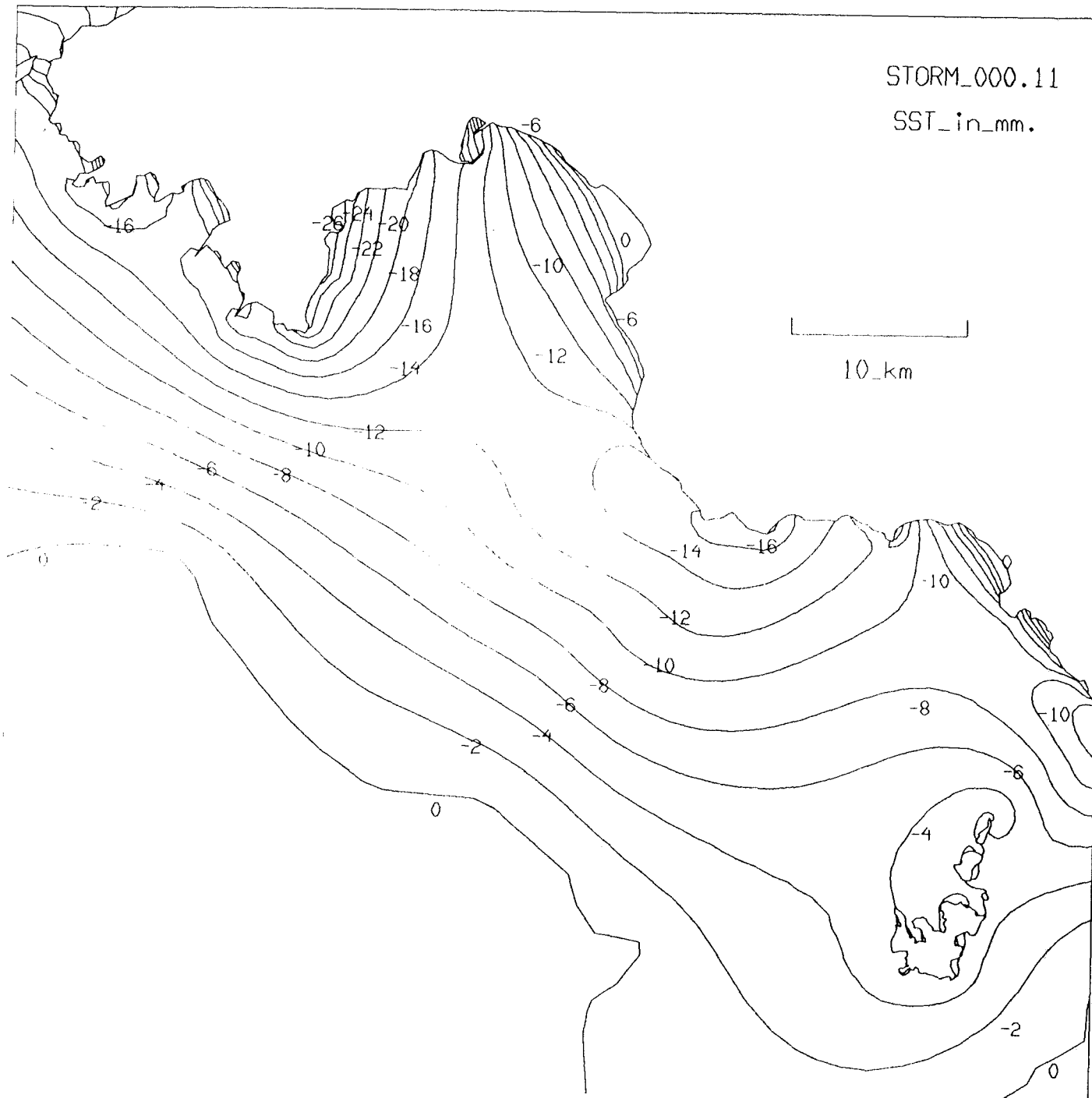
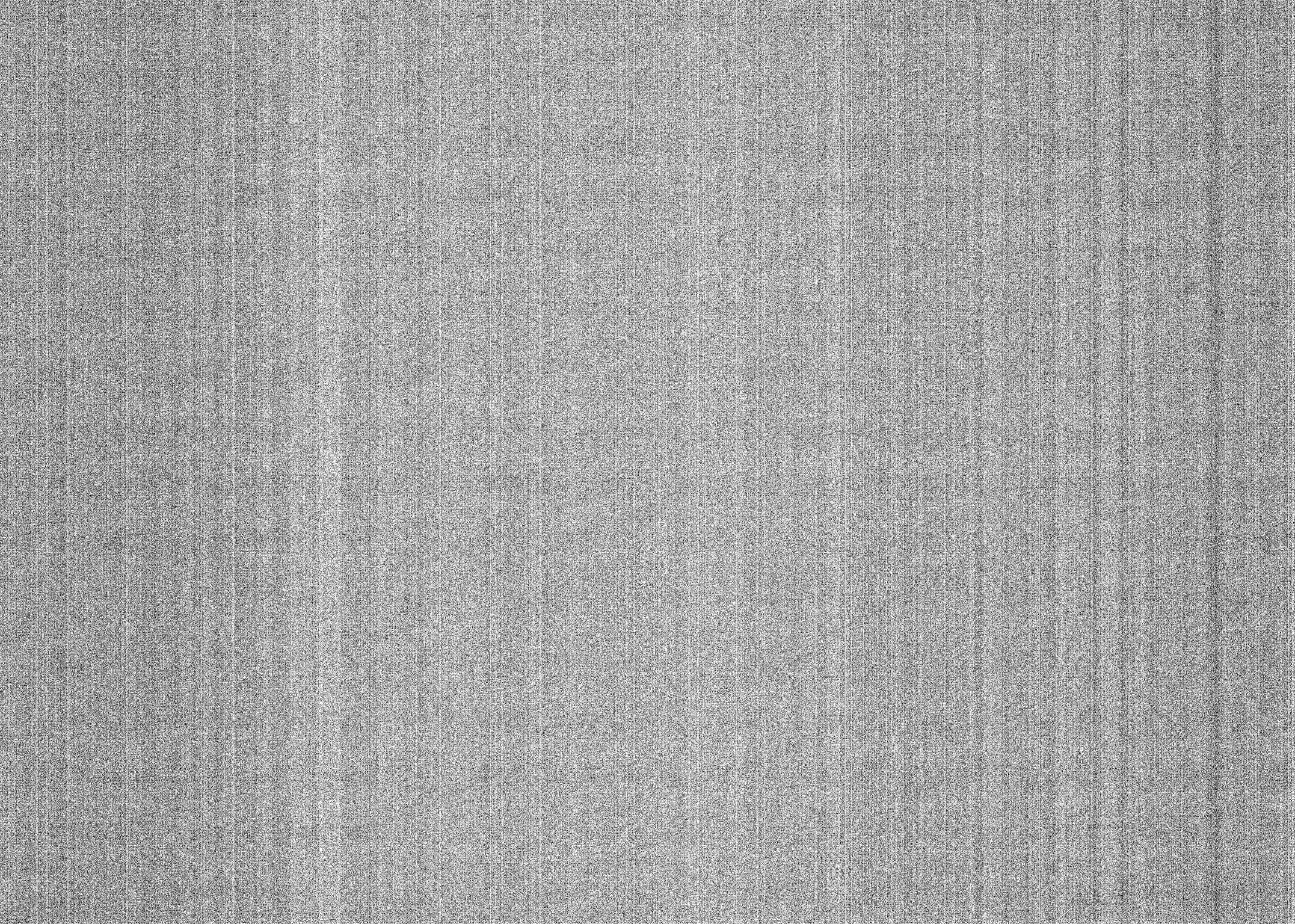


Figure 12



Capítulo 3

Time and Space Variability in the Eastern Alboran Sea From March to May 1990

Álvaro Viúdez¹
Joaquín Tintoré¹

J. Geophys. Res. (accepted).

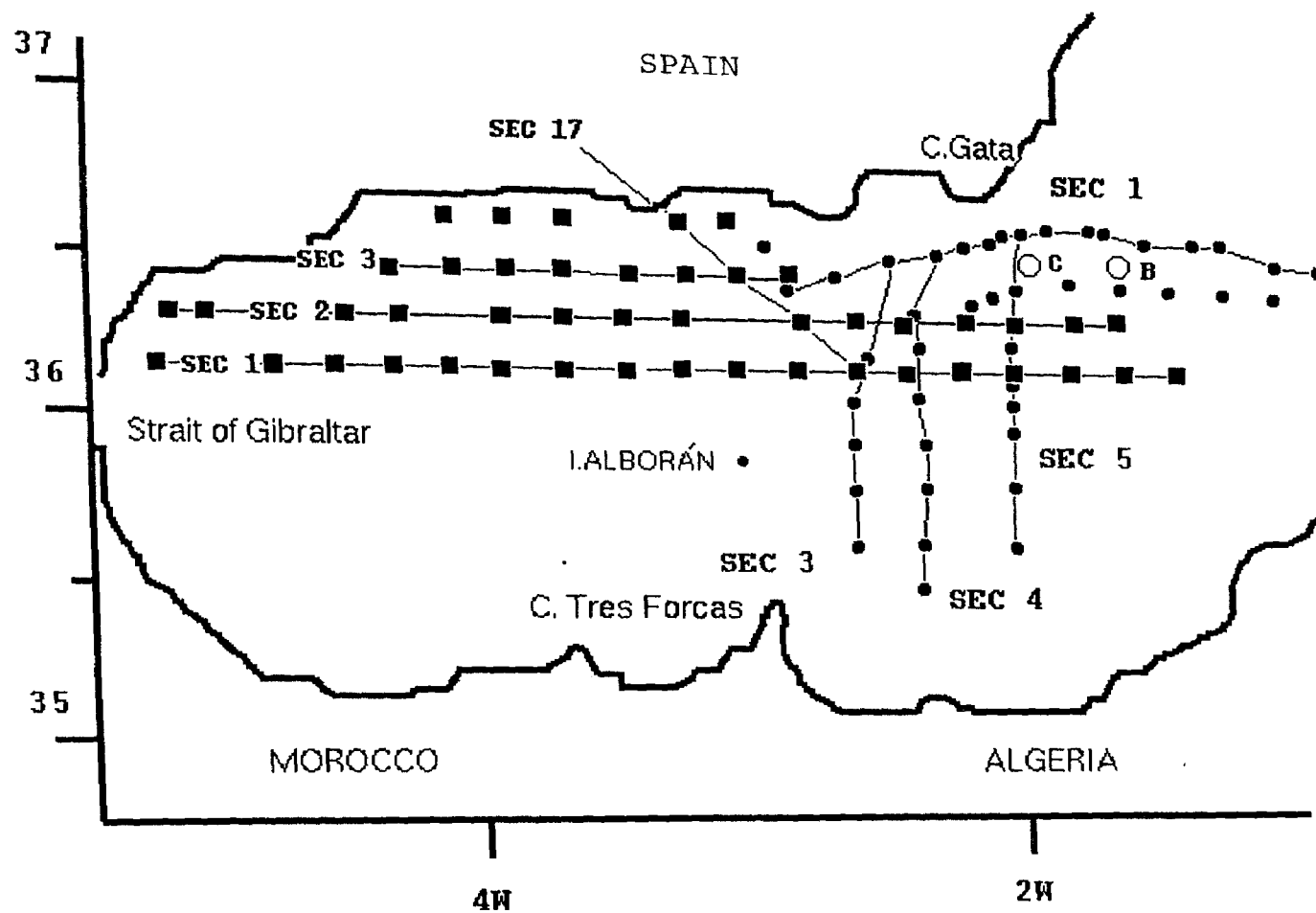
¹Dept. de Física, Universitat de les Illes Balears, Spain

LIST OF FIGURES

1. The Alboran Sea. CTD, AXBT locations and current meter moorings. The different vertical sections are referenced.
2. Data recorded periods of the current meters.
3. Satellite thermal imagery for March 16. Darker shades represent warmer water.
4. West-east temperature distribution from AXBT data (vertical section A1).
5. South-north vertical distribution in vertical section 3: (a) σ_t , (b) east-west ADCP component (continuous contour line means eastward direction), (c) north-south ADCP component (continuous contour line means northward direction), (d) SiO_2 , and (e) chlorophyll.
6. South-north vertical distribution in vertical section 4 CTD: (a) σ_t , (b) east-west ADCP component (continuous contour line means eastward direction), and (c) north-south ADCP component (continuous contour line means northward direction).
7. Horizontal distribution of ADCP data at 10 m.
8. West-east vertical distribution in vertical section 1 CTD: (a) temperature, (b) salinity, (c) σ_t , and (d) north-south ADCP component (continuous contour line means northward direction).
9. Time series of B60 current meter (60 m). (a) Stick diagram of the low-pass (33 h) filtered, (b) inertial component (U component), and (c) tidal (semidiurnal) component (U component).
10. East-west geostrophic velocity for (a) vertical section 3 CTD, and (b) vertical section 4 (continuous contour line means eastward direction).
11. Upper layer circulation pattern.

Time and Space Variability... _____

12. (a) Temperature distribution in the AXBT vertical section A17, and (b) depth of 14.5 °C isotherm from AXBT data.



- CTD STATIONS
- AXBT
- CURRENT METERS

Figure 1

CURRENTMETER DATA FE90

MARCH

APRIL

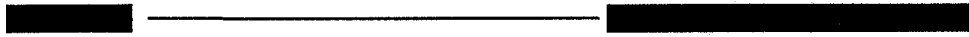
MAY

11 18 25 01 08 15 22 29 06 13

1 10 20 30 40 50 60

MOORING B

30 m.



60 m.



300 m.



600 m.



MOORING C

30 m.



60 m.



300 m.



800 m.



Figure 2

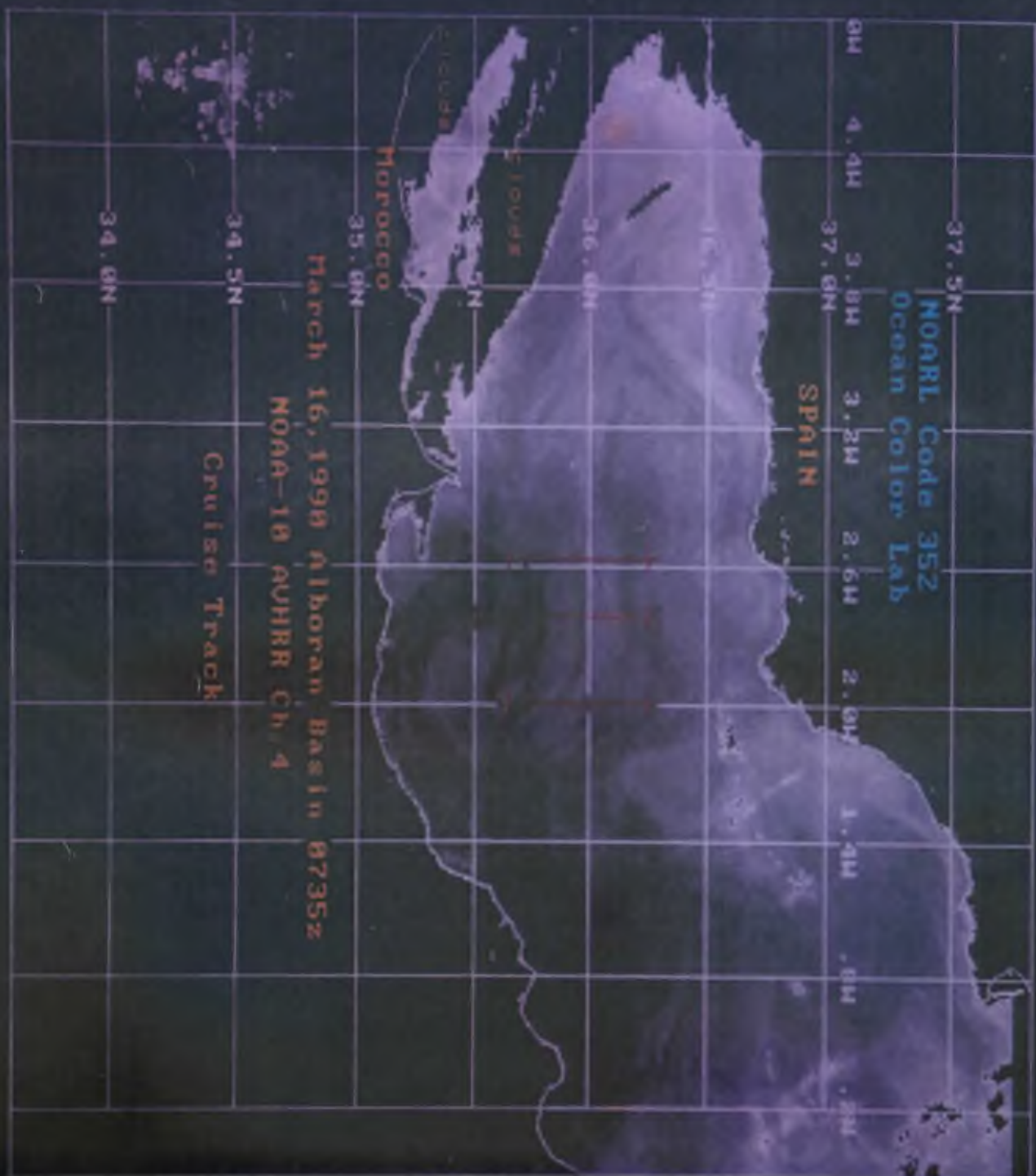
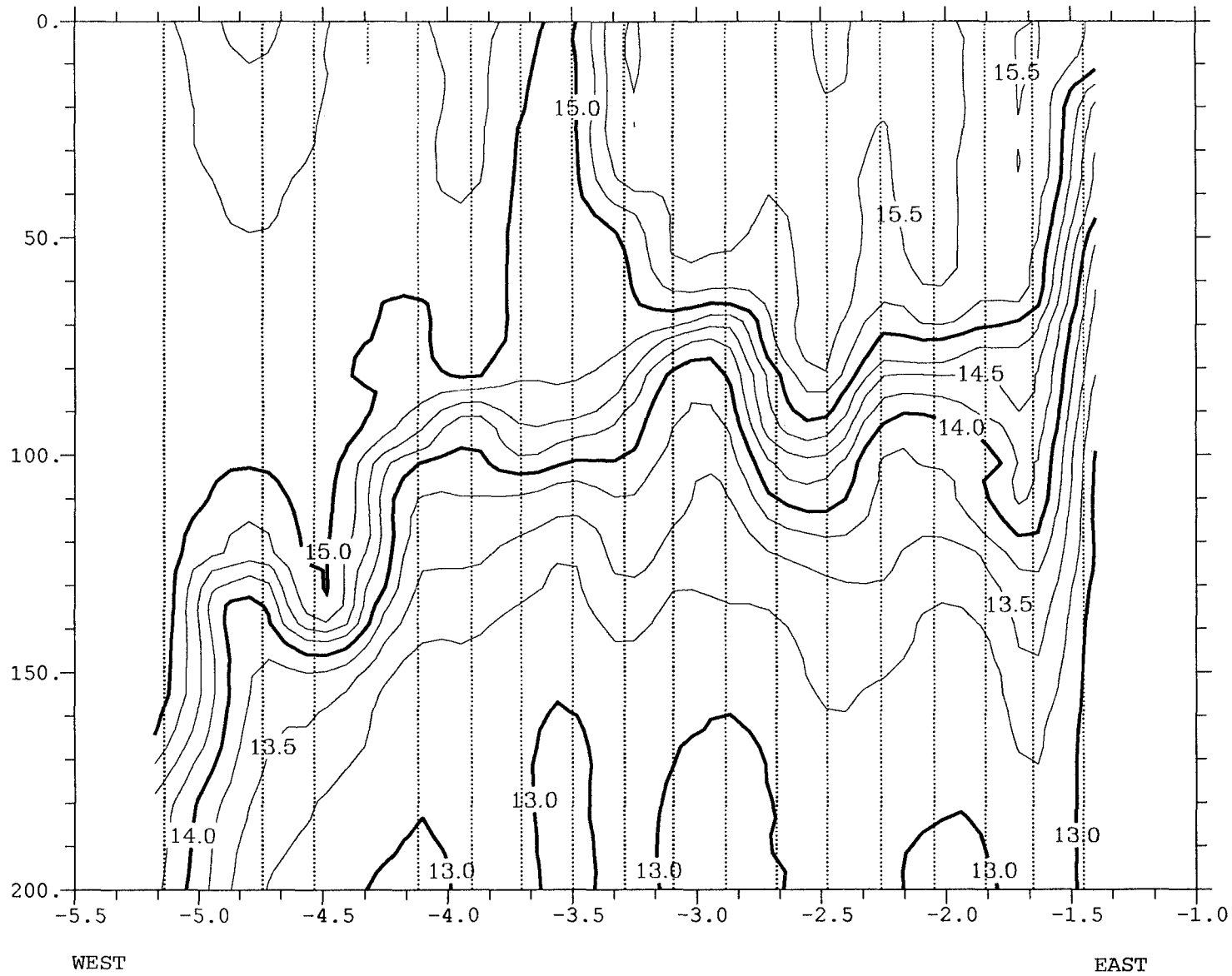
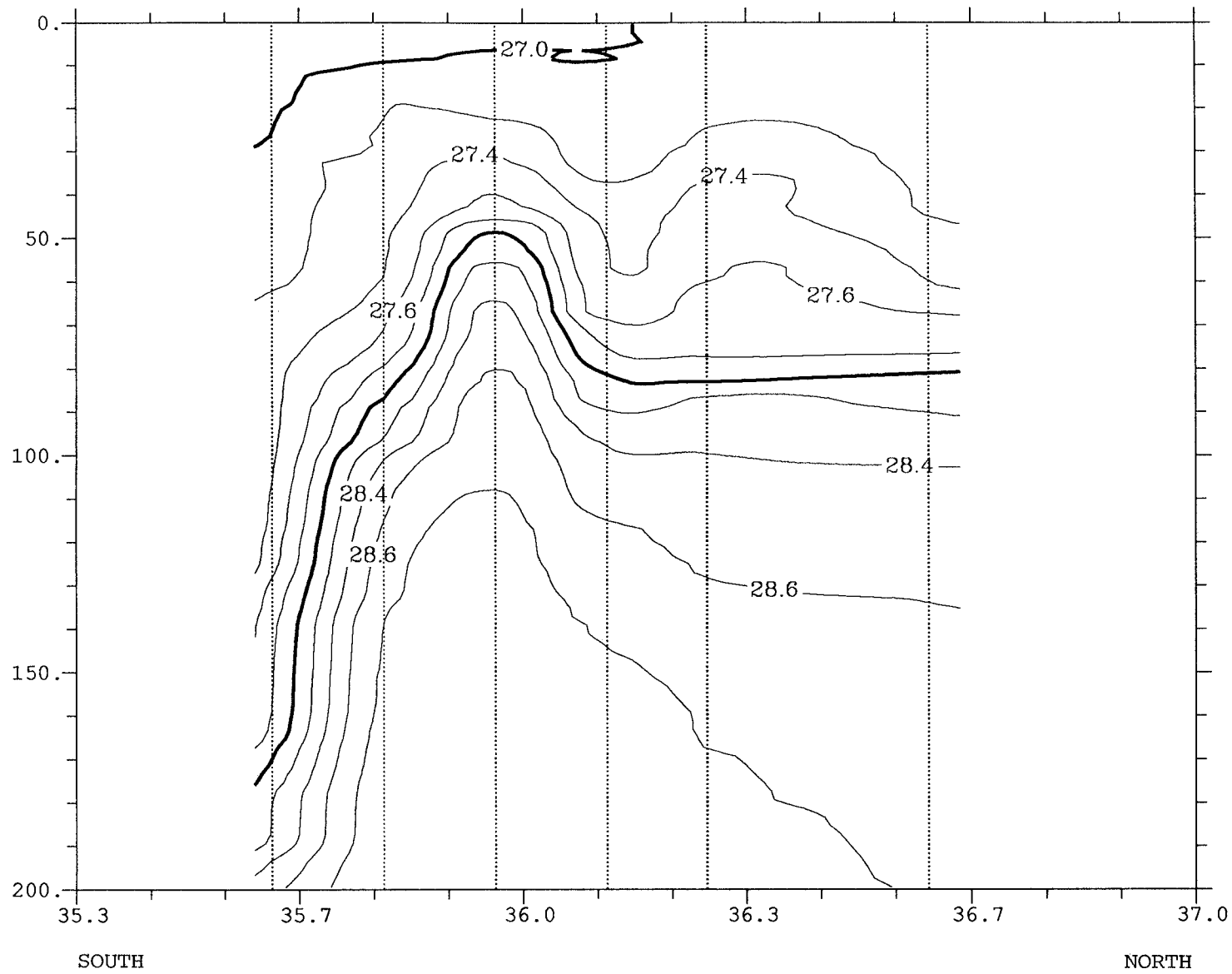


Figure 3



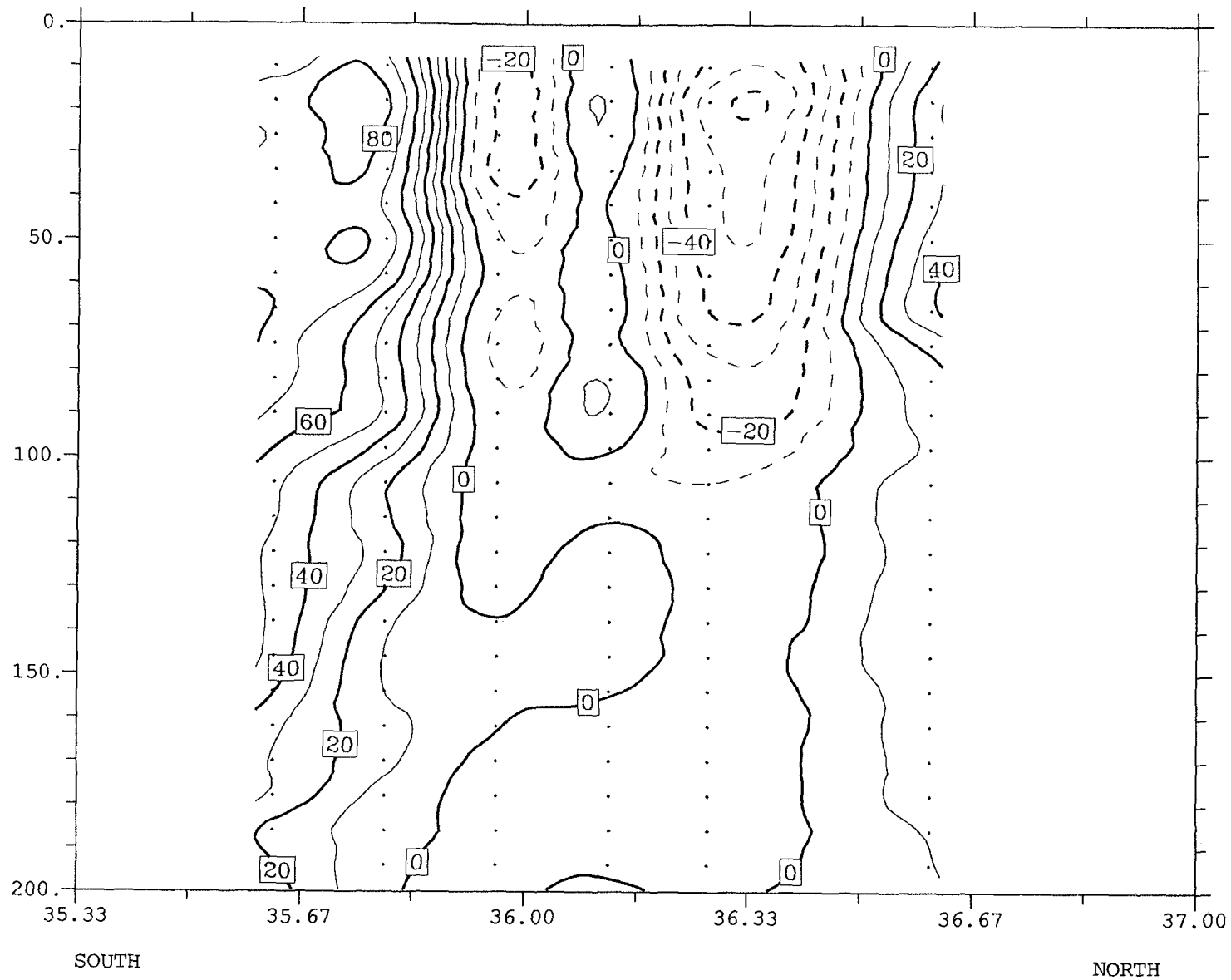
TEMPERATURE SECTION 1. AXBT

Figure 4



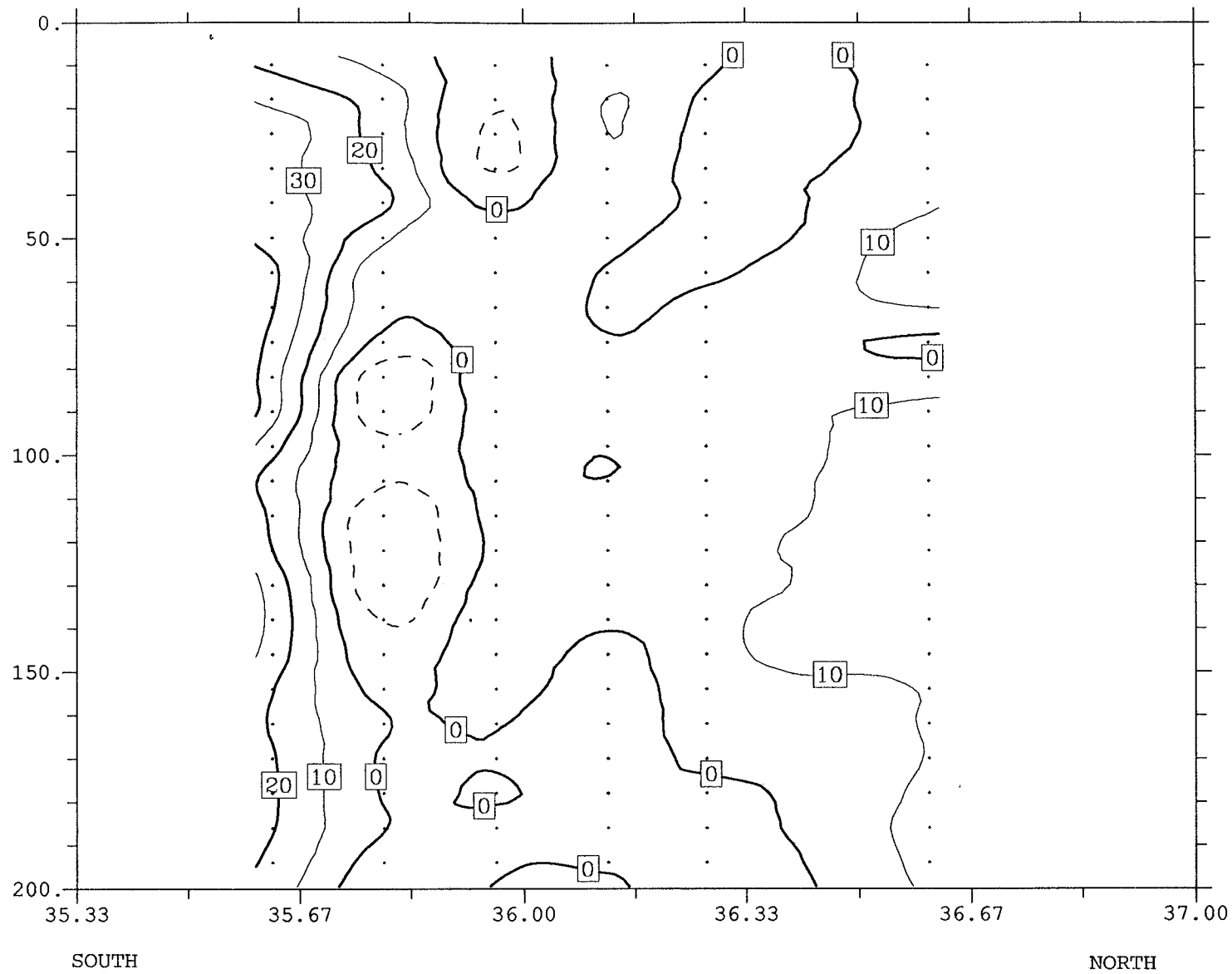
SIGMA-T SECTION 3. CTD

Figure 5a



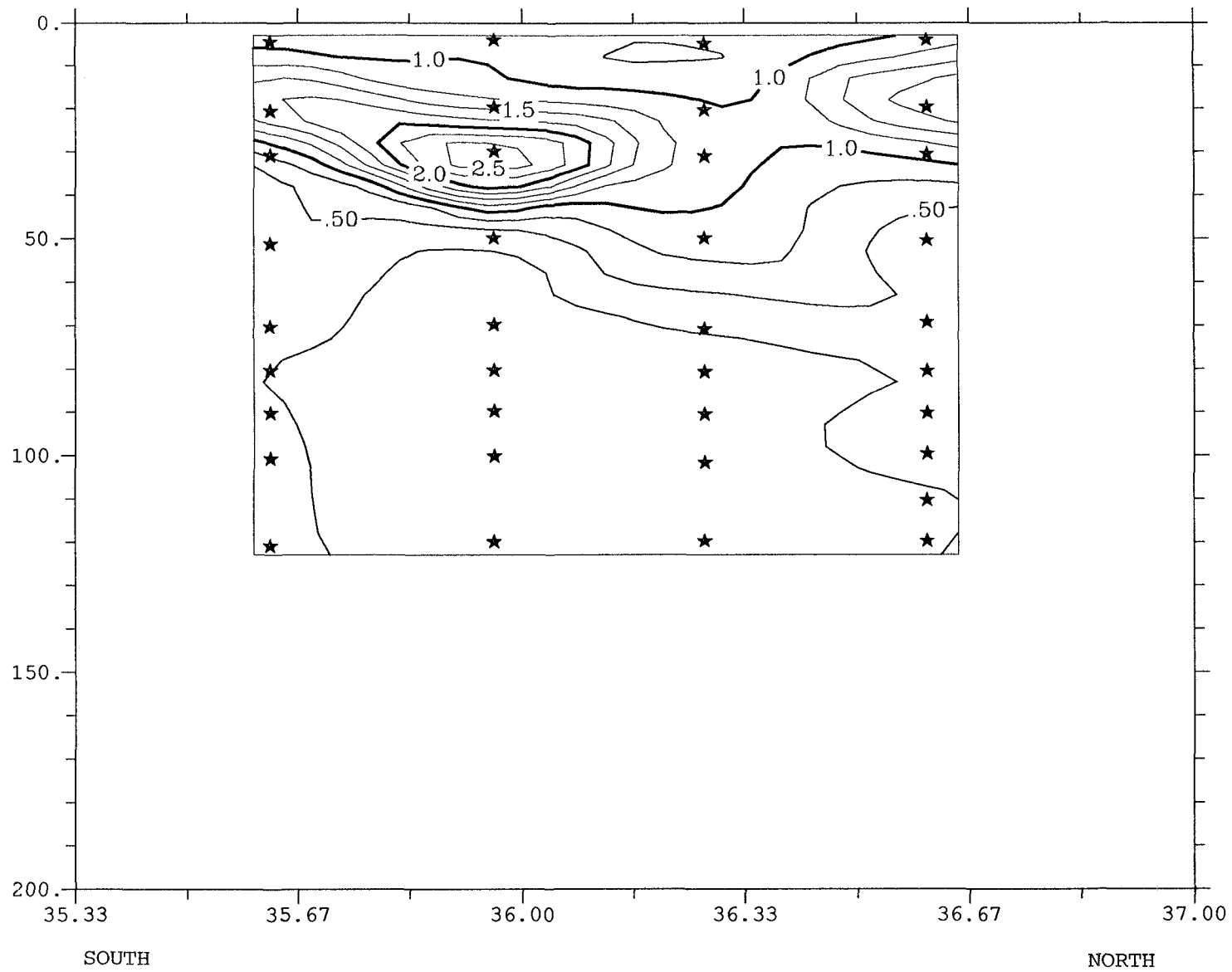
EAST/WEST VELOCITY. SECTION 3. ADCP

Figure 5b



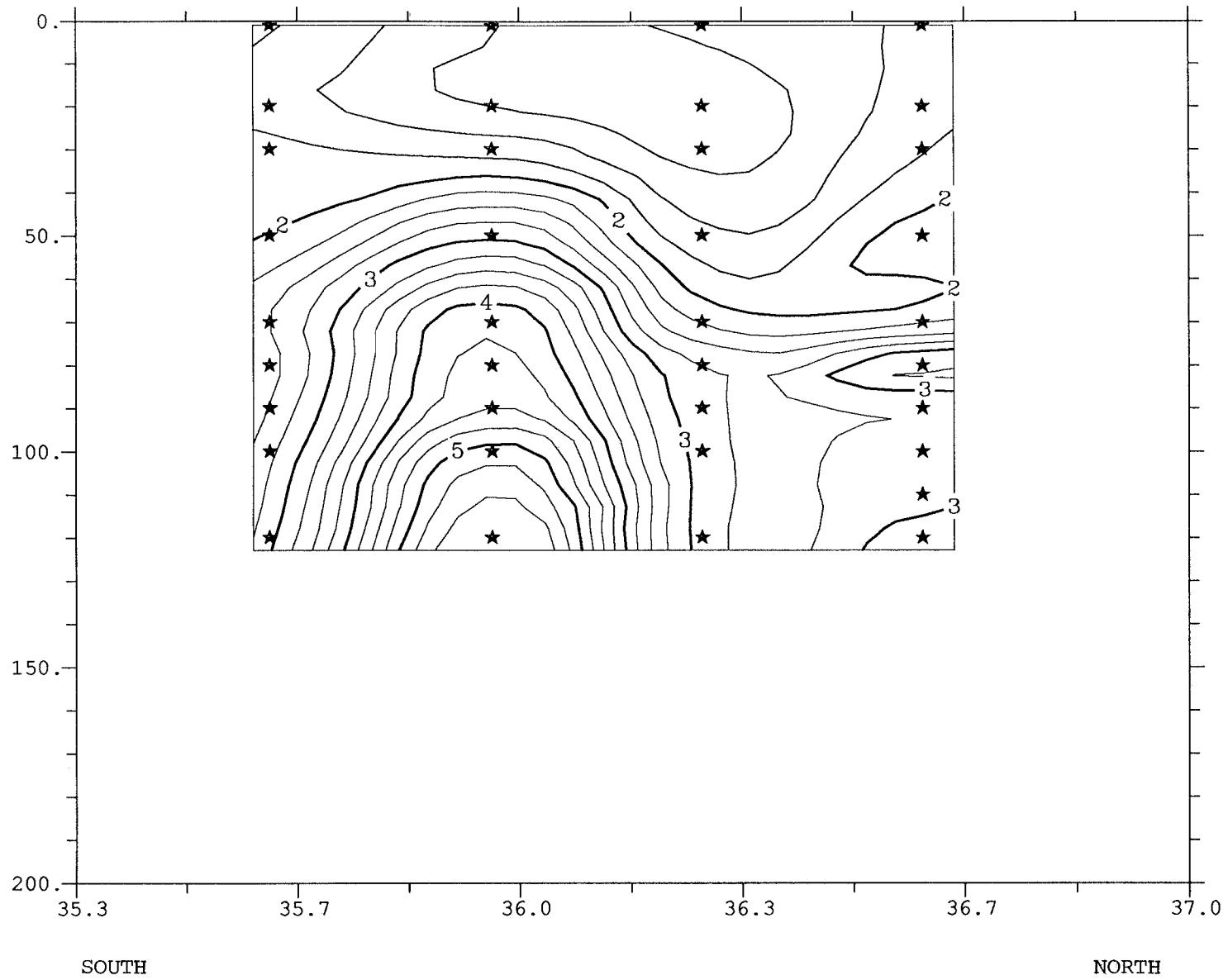
NORTH/SOUTH VELOCITY. SECTION 3. ADCP

Figure 5c



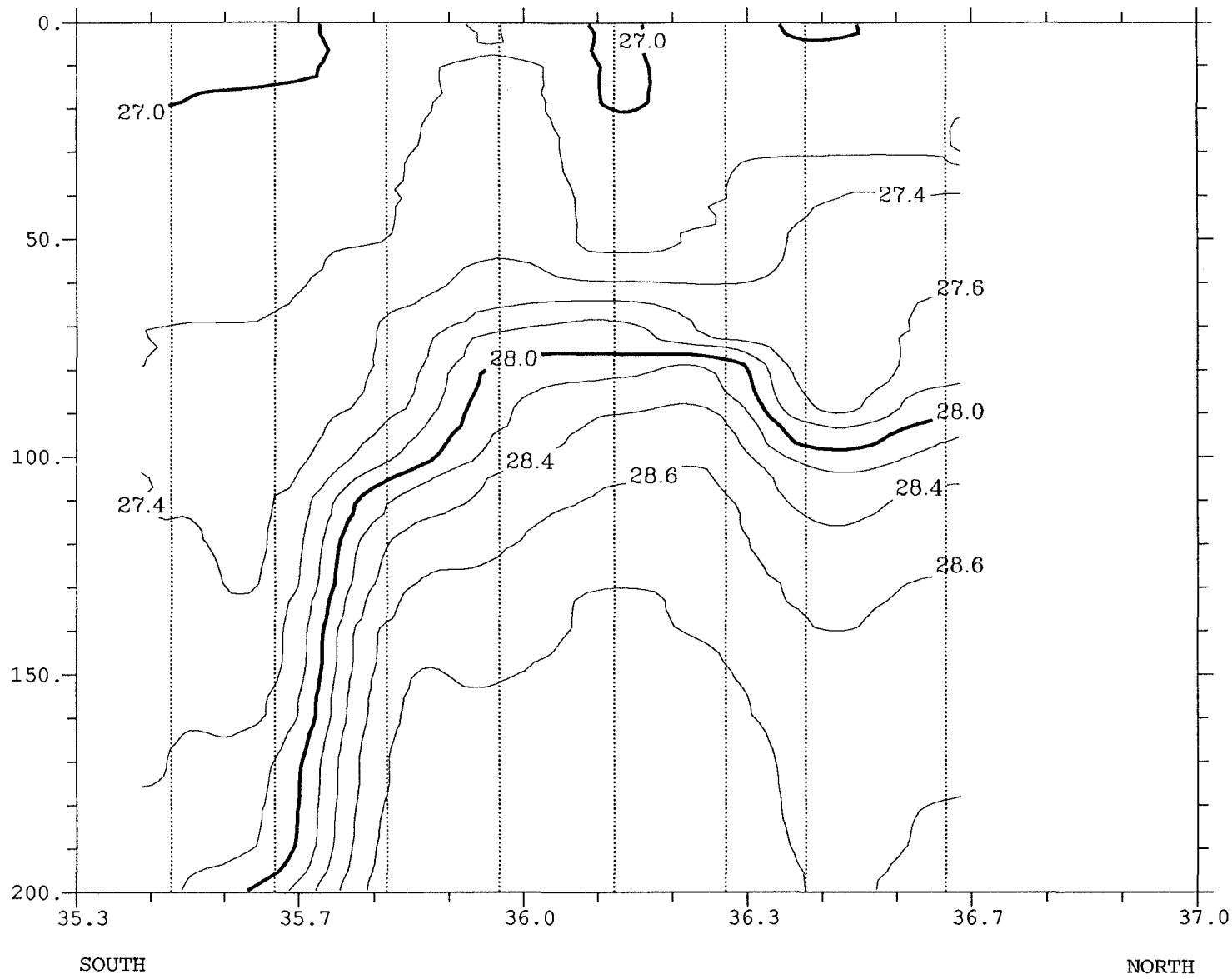
CHLOROPHYLL SECTION 3.

Figure 5d



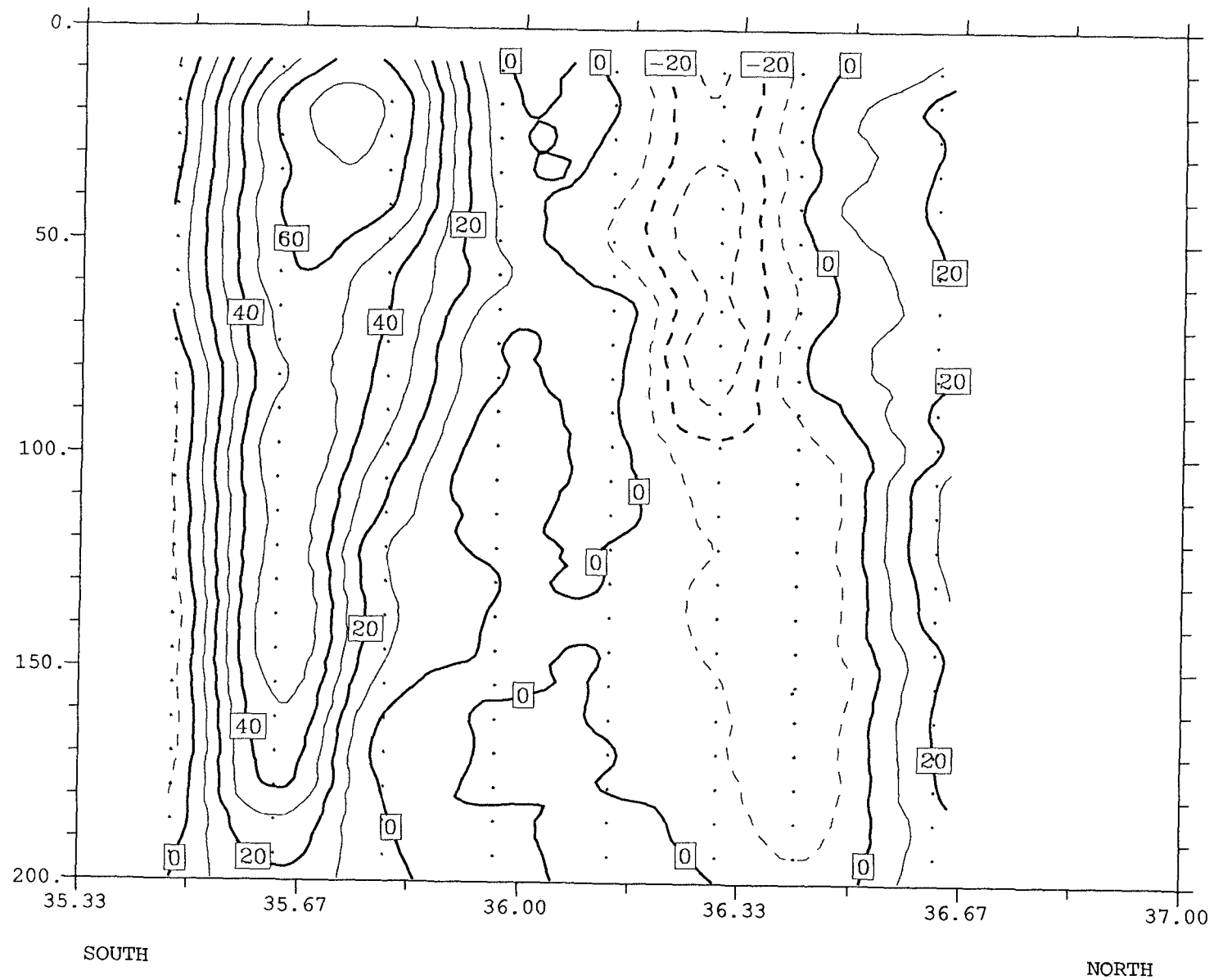
SiO₂ SECTION 3.

Figure 5e



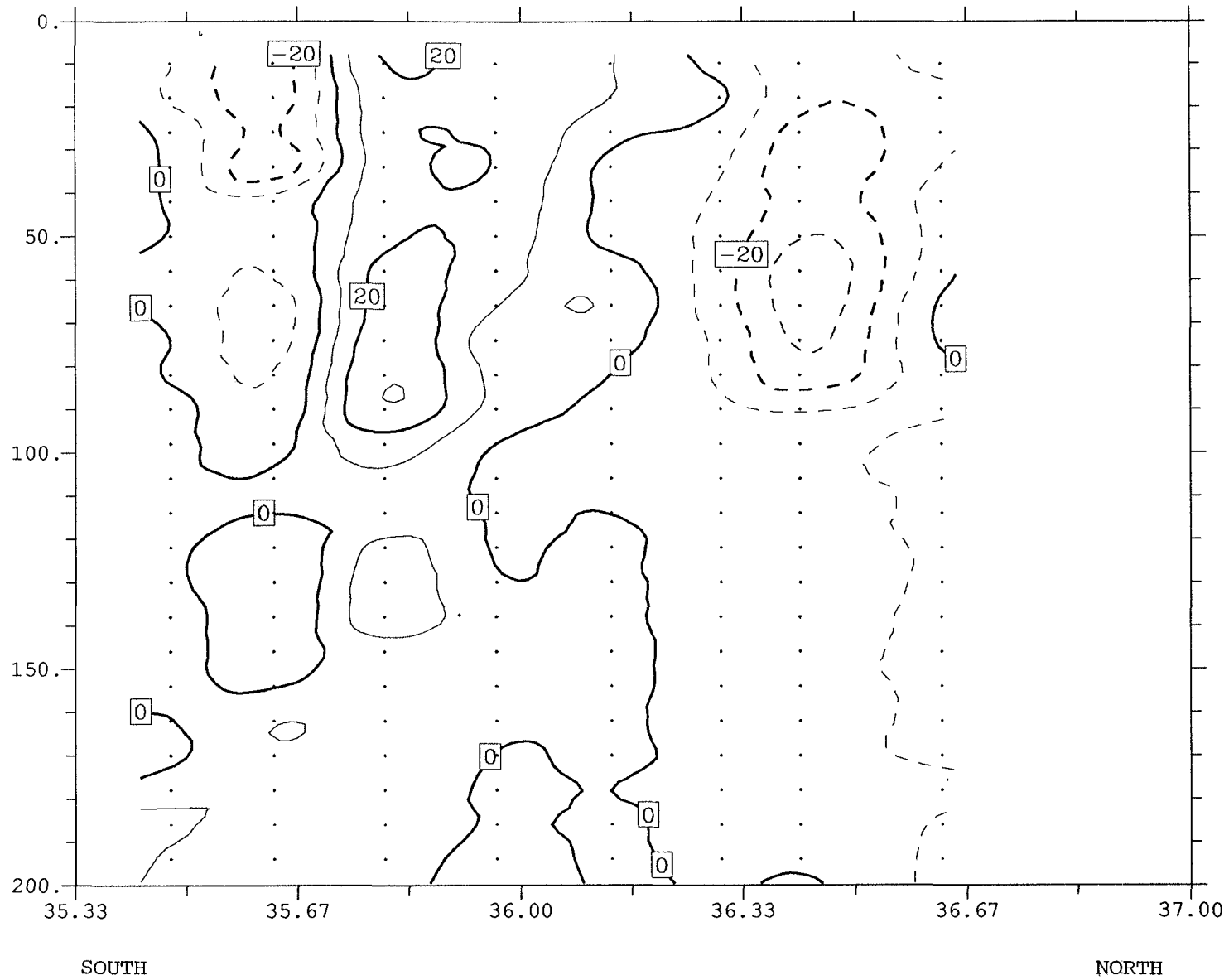
SIGMA-T SECTION 4. CTD

Figure 6a



EAST/WEST VELOCITY. SECTION 4. ADCP

Figure 6b



NORTH/SOUTH VELOCITY. SECTION 4. ADCP

Figure 6c

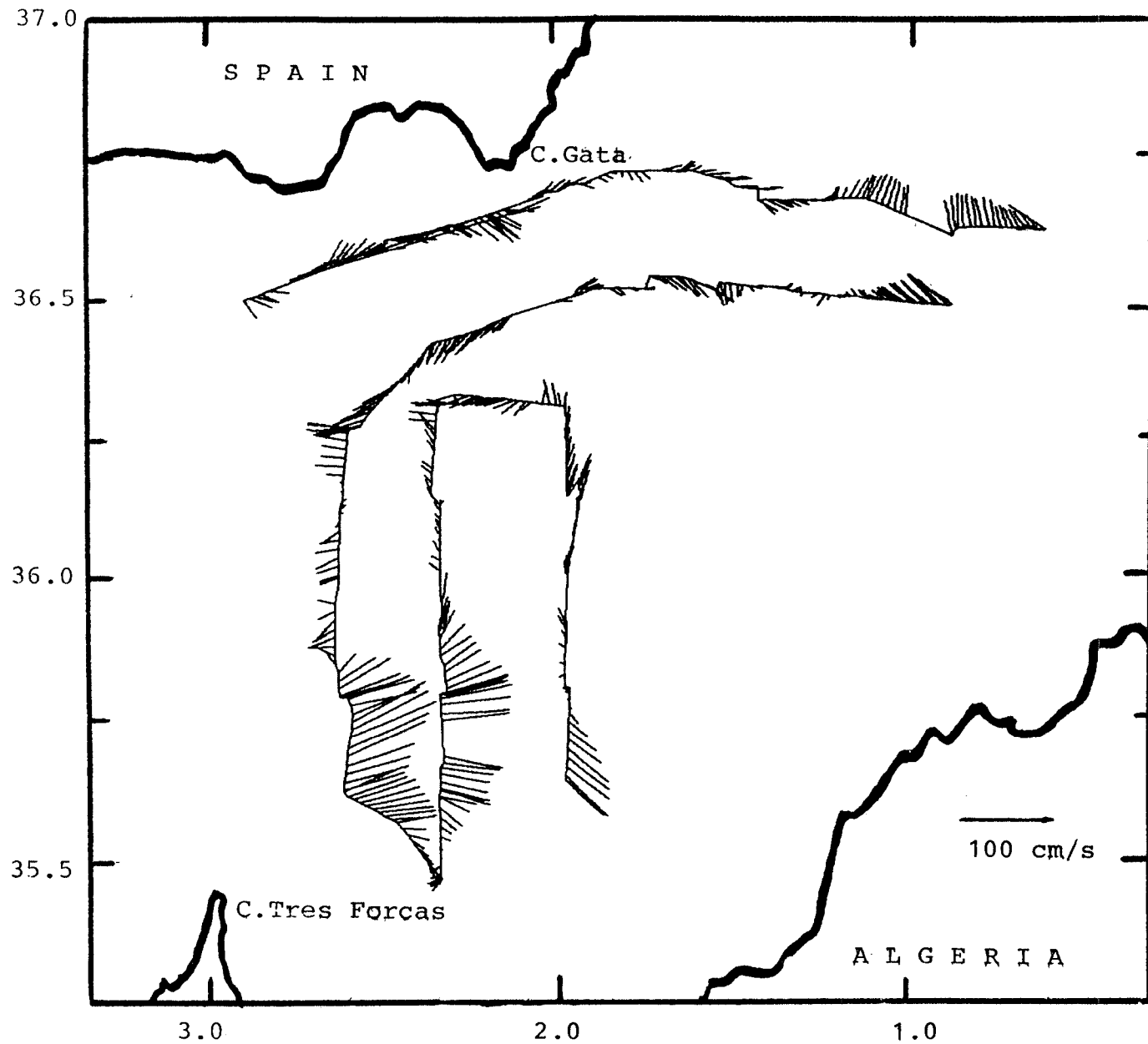
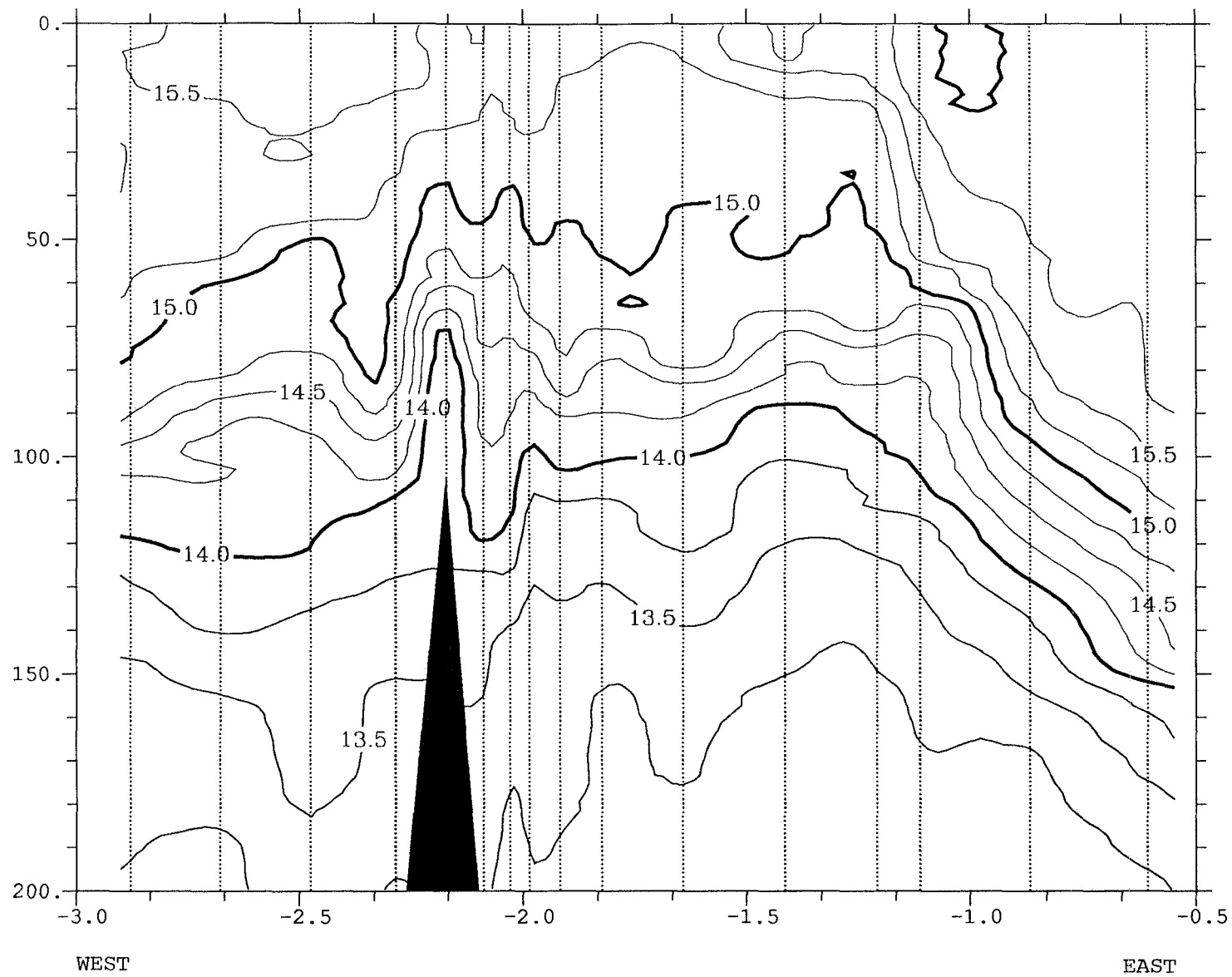
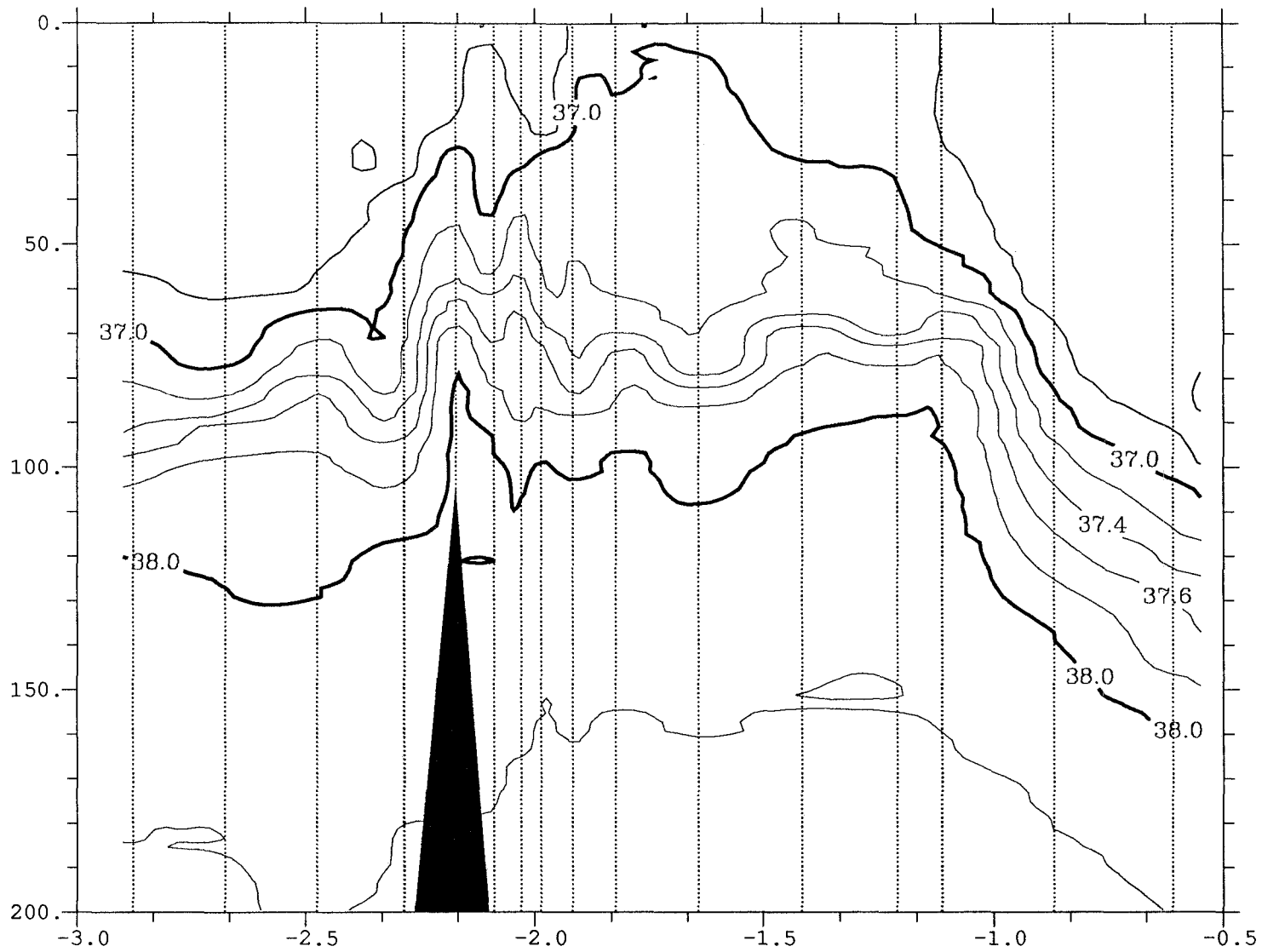


Figure 7



TEMPERATURE SECTION 1. CTD

Figure 8a

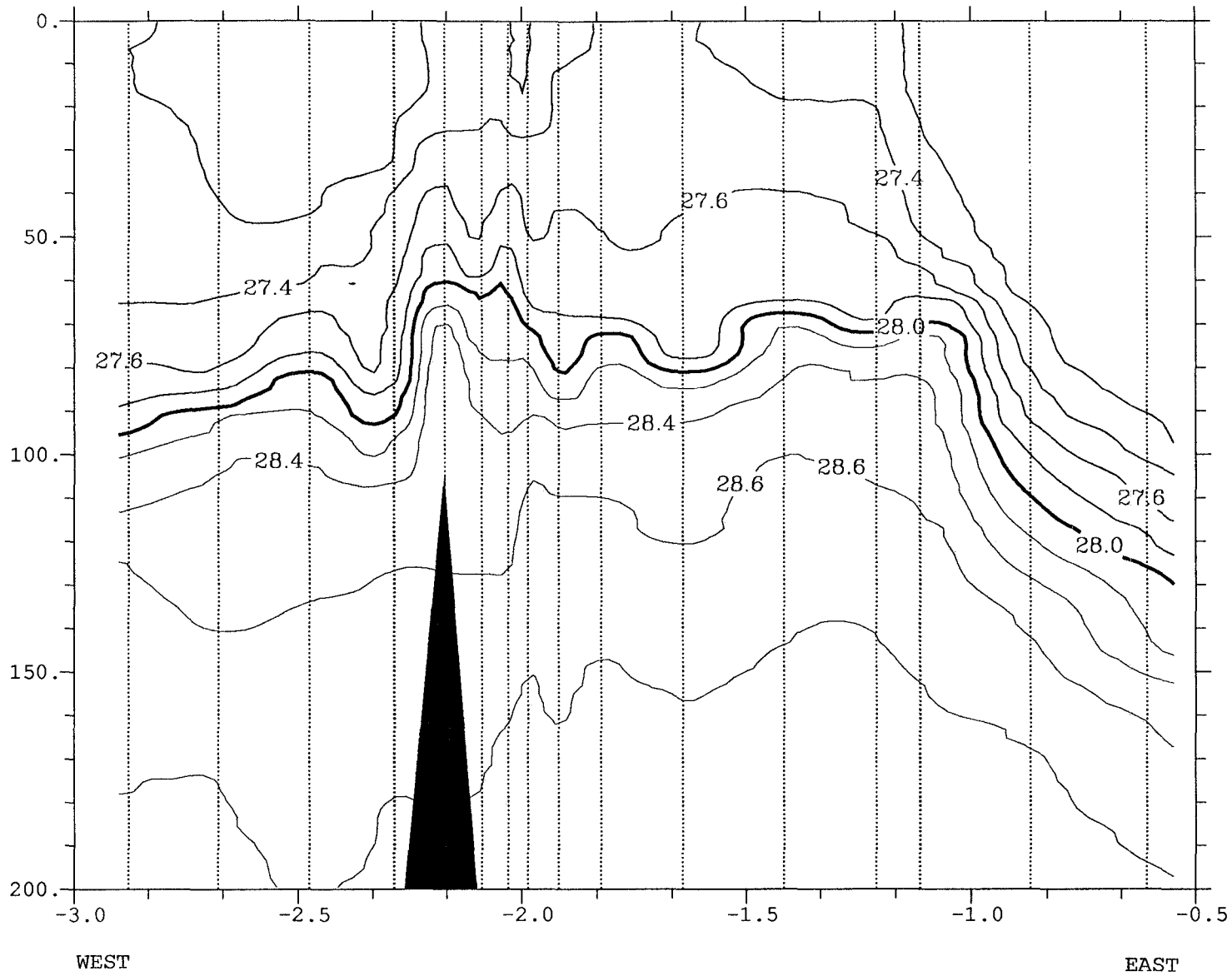


WEST

EAST

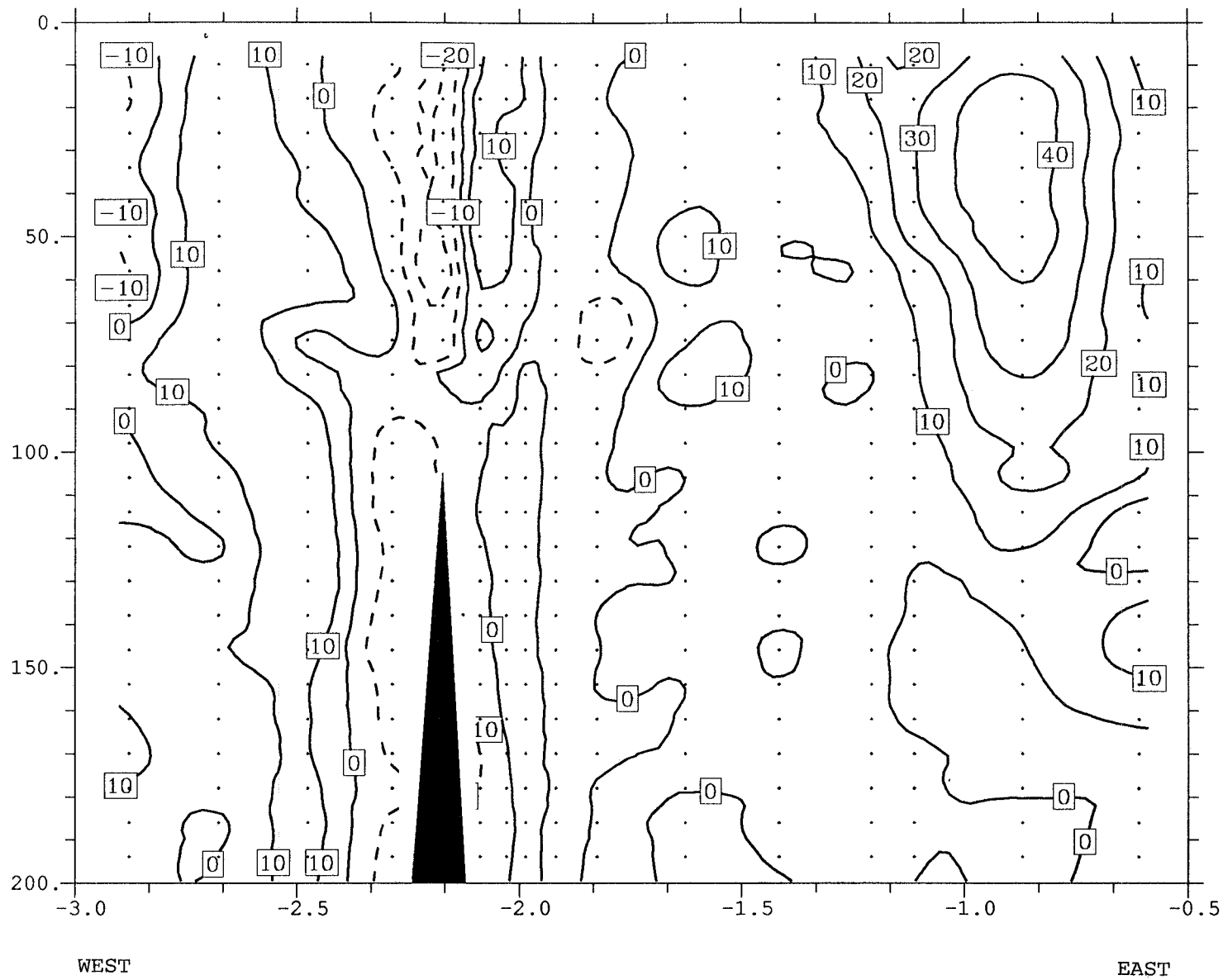
SALINITY SECTION 1. CTD

Figure 8b



SIGMA-T SECTION 1. CTD

Figure 8c



NORTH/SOUTH VELOCITY. SECTION 1. ADCP

Figure 8d

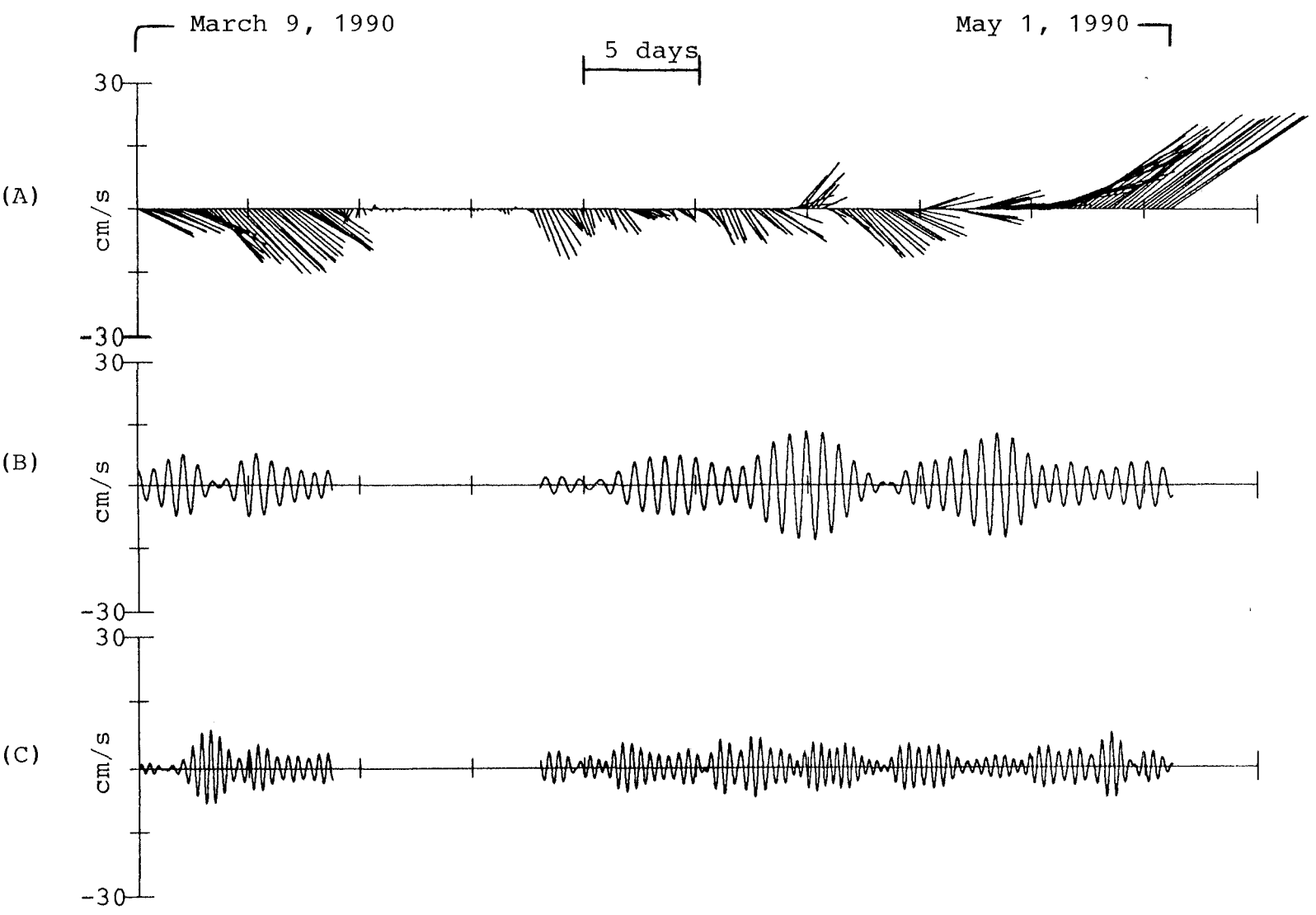
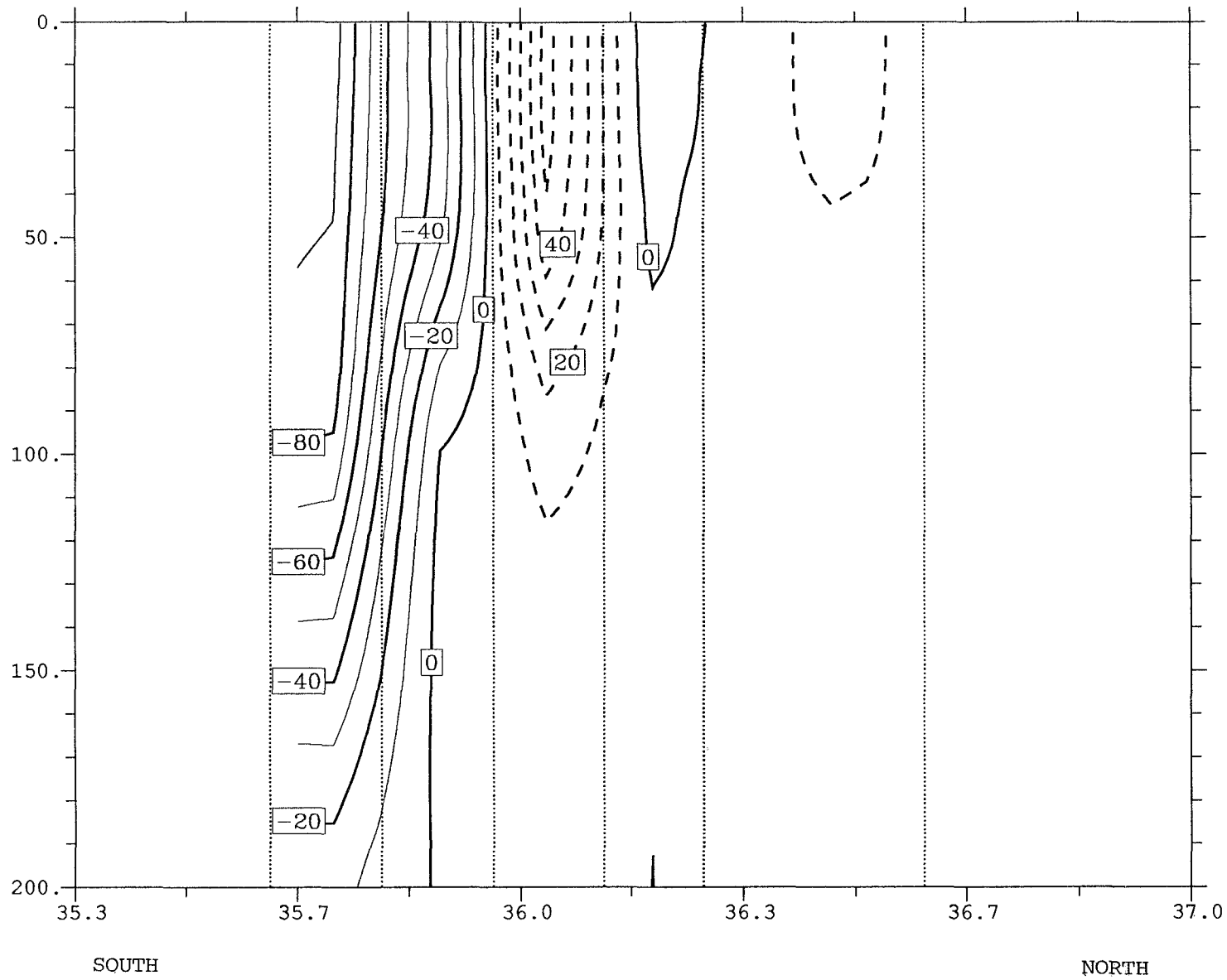
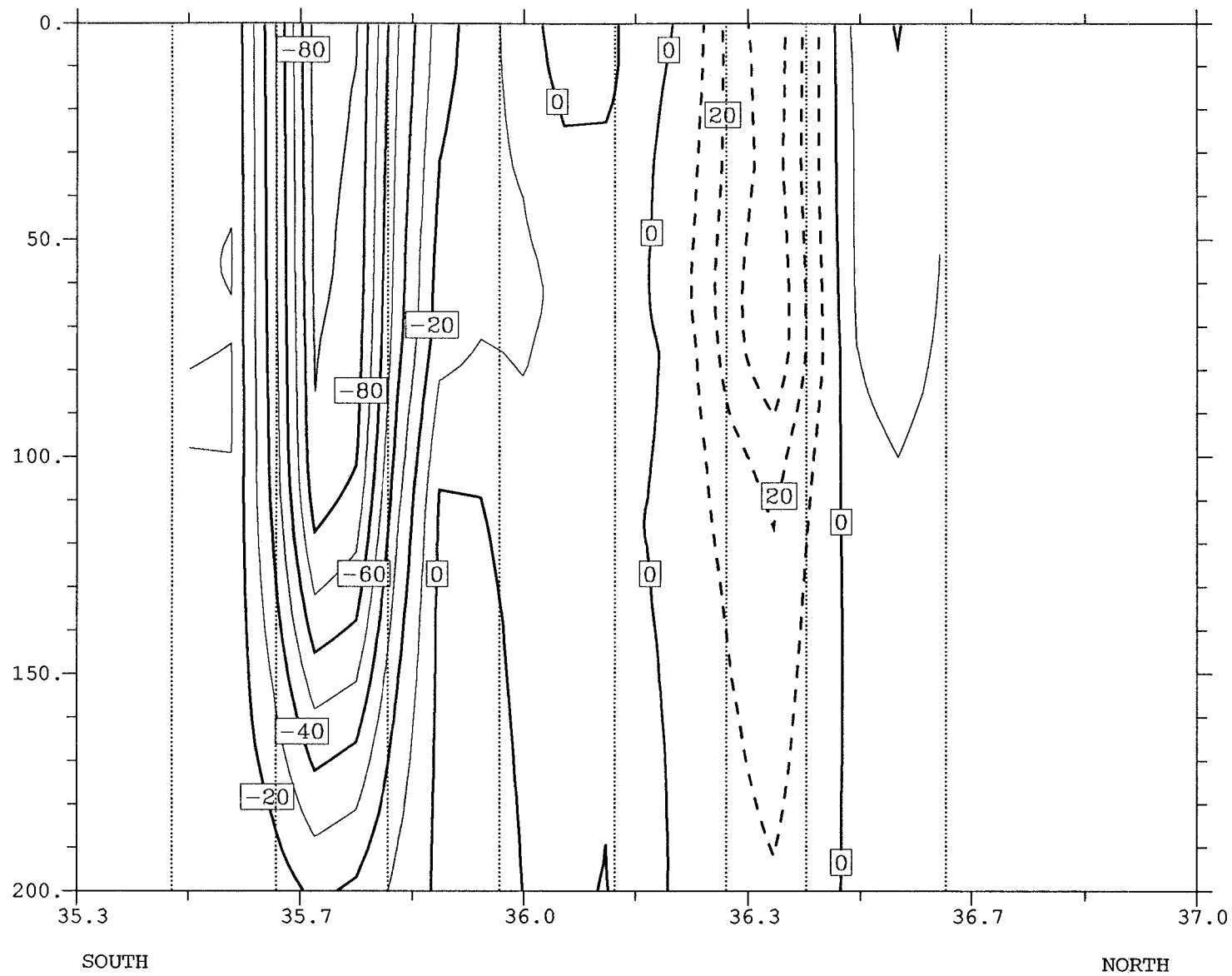


Figure 9



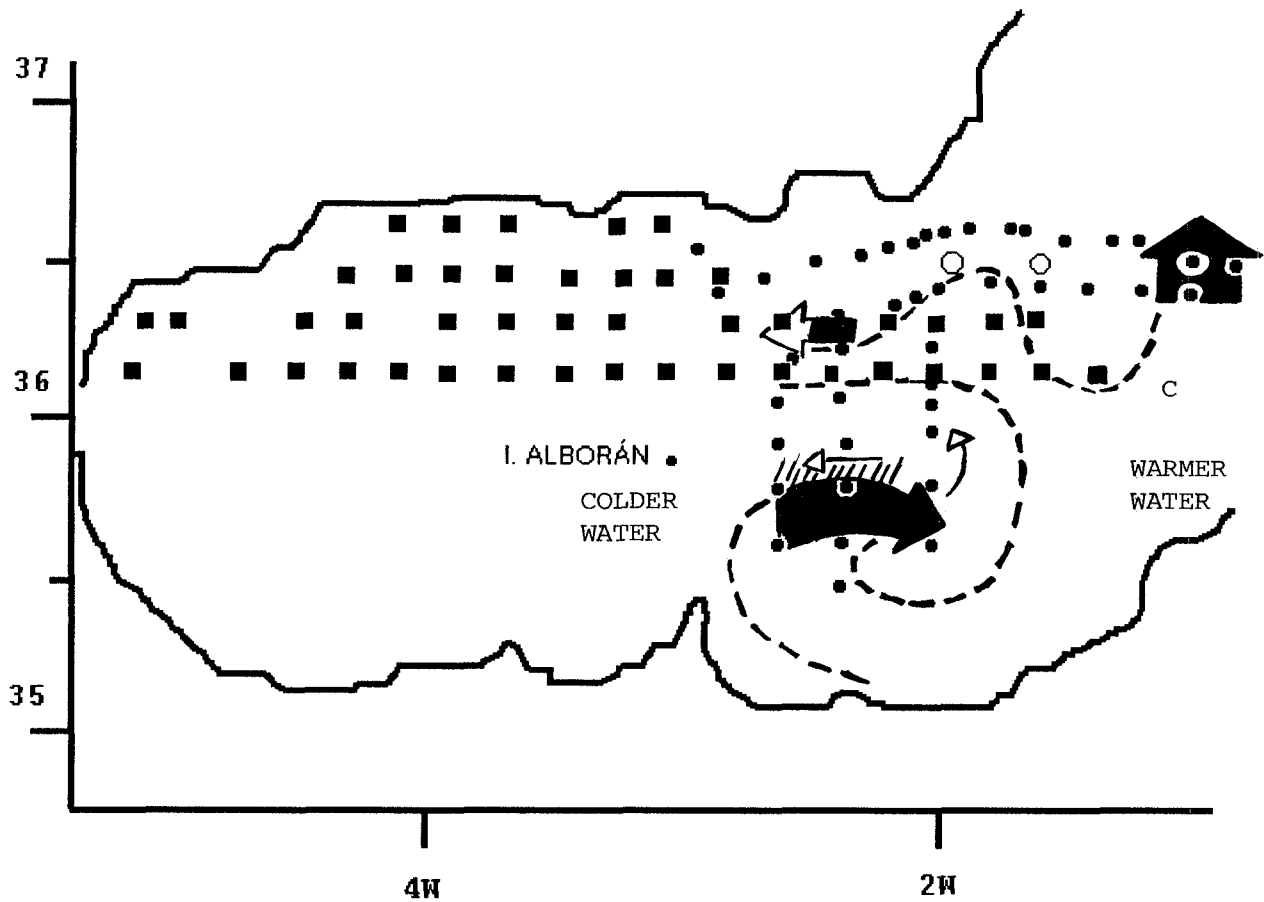
EAST/WEST GEOSTROPHIC VELOCITY SECTION 3. REFERENCE LEVEL 300 m

Figure 10a



EAST/WEST GEOSTROPHIC VELOCITY SECTION 4. REFERENCE LEVEL 300 m

Figure 10b



- CTD STATIONS
- AXBT
- CURRENT METERS



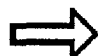

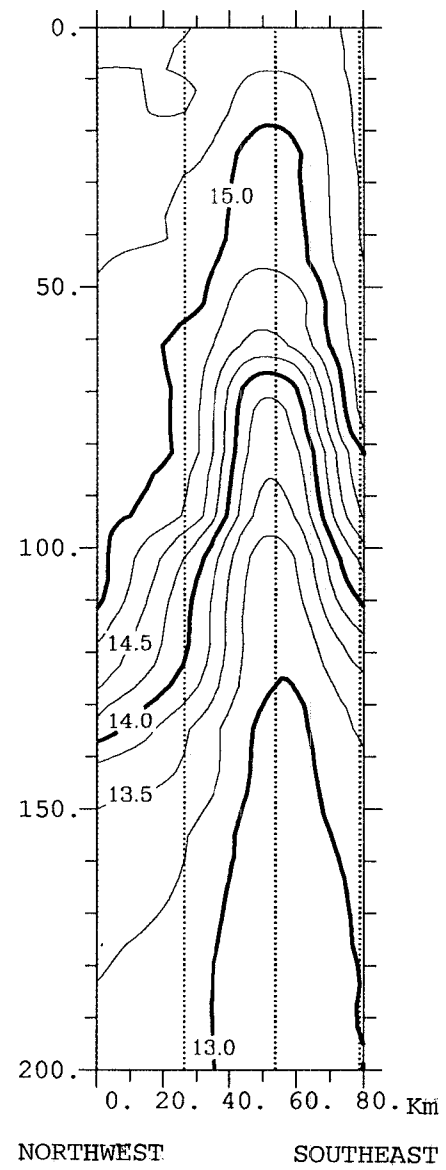
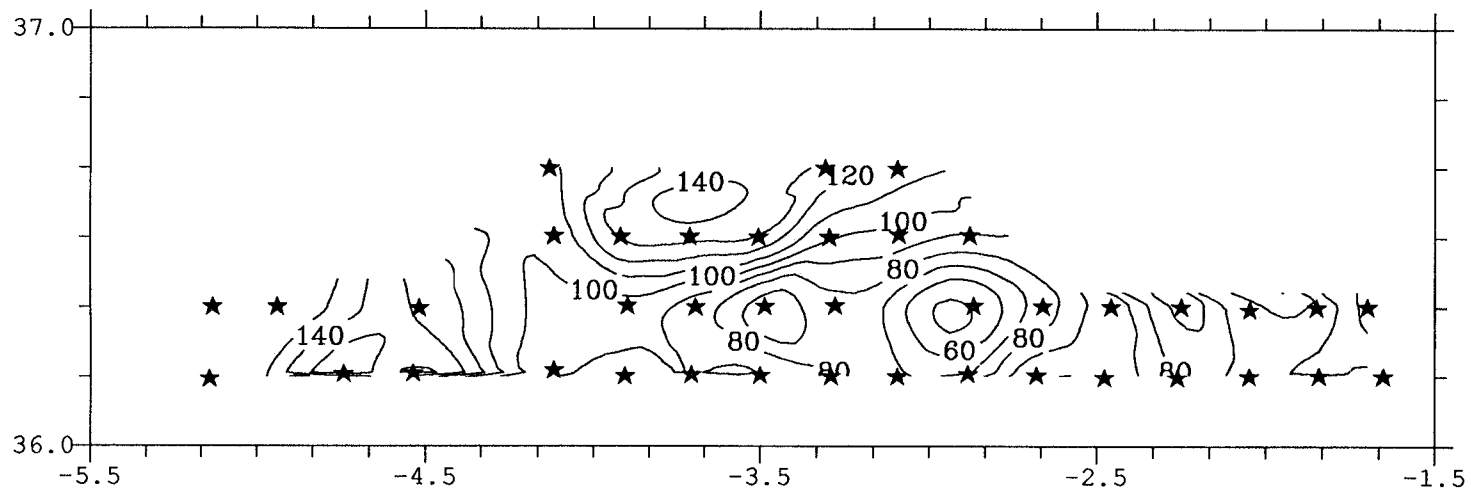
-  DENSITY GRADIENTS
-  AVHRR PATTERNS
-  ADCP CURRENTS
-  CHLOROPHYLL MAXIMUM

Figure 11



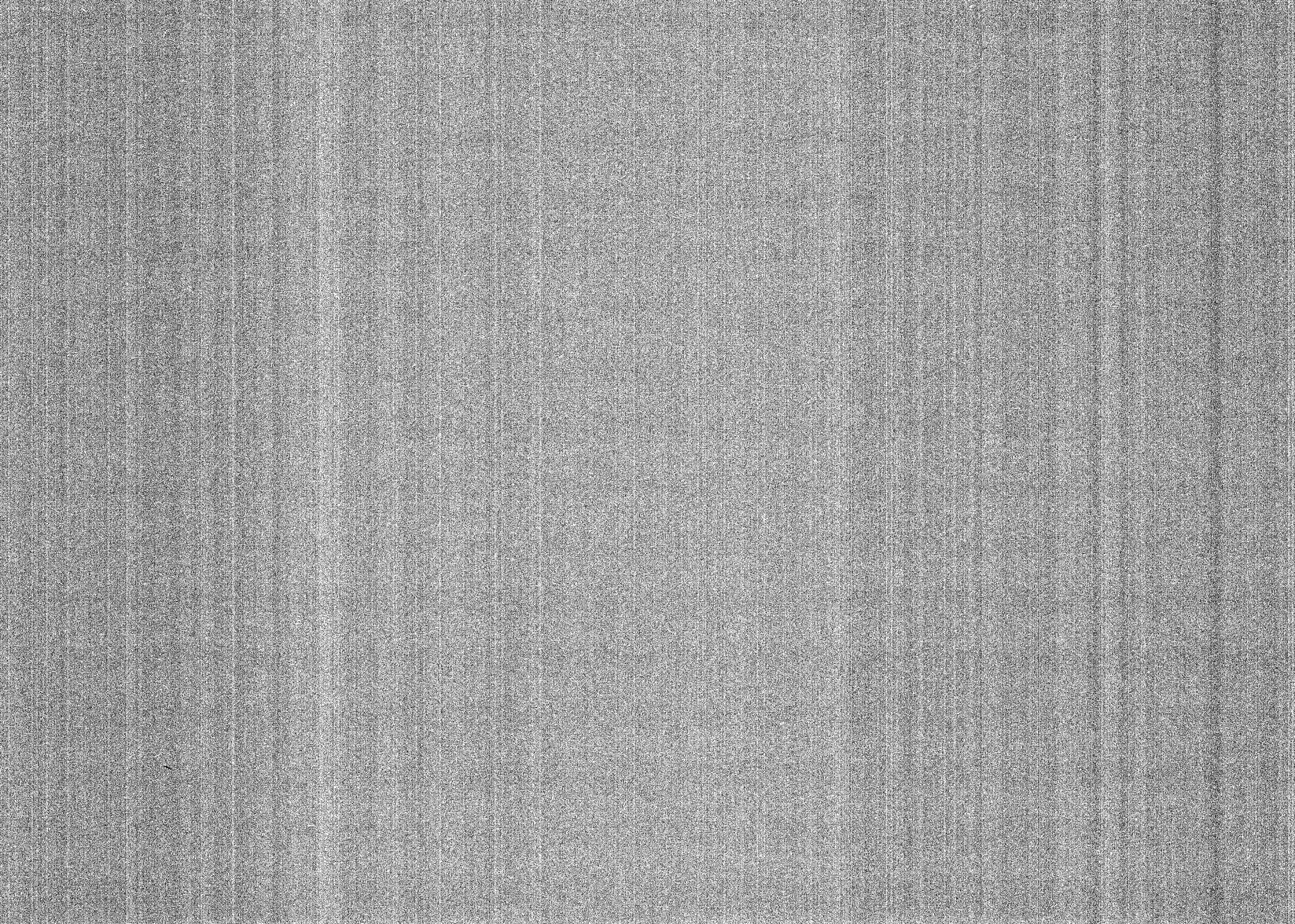
TEMPERATURE SECTION 17. AXBT

Figure 12a



DEPTH OF 14.5 C ISOTHERM.

Figure 12b



Capítulo 4

Three-Dimensional Structure of the Two Anticyclonic Gyres in the Alboran Sea

Álvaro Viúdez¹
Joaquín Tintoré ¹
Robert L. Haney²

J. Phys. Oceanogr. (Accepted).

¹Dept. de Física, Universitat de les Illes Balears Palma de Mallorca, Spain.

²Department of Meteorology, Naval Postgraduate School, Monterey, CA, US.

LIST OF FIGURES

1. The Alboran Sea (bottom topography in m). The different vertical CTD sections are referenced.
2. (a) Temperature ($\Delta = 0.25^\circ\text{C}$), (b) salinity ($\Delta = 0.2$ psu) and (c) σ_t ($\Delta = 0.2 \sigma_t$) horizontal distributions at 100 m. Interpolation method: successive corrections (referenced in the text).
3. (a) Temperature ($\Delta = 0.5^\circ\text{C}$), (b) salinity ($\Delta = 0.2$ psu), and (c) σ_t ($\Delta = 0.2 \sigma_t$) distributions on vertical section 20. Interpolation method: local bivariate (Akima 1978; Akima 1984).
4. (a) Temperature ($\Delta = 0.5^\circ\text{C}$), (b) salinity ($\Delta = 0.2$ psu) and (c) σ_t ($\Delta = 0.2 \sigma_t$) distributions on vertical section A. Interpolation method: local bivariate.
5. Sketch to represent how the relative subsurface salinity minimum S_m flowing throughout the Alboran Sea is used as a tracer. Assuming homogeneous mixing the relative salinity minimum does not lose its minimum condition over the trajectory between points (A) and (B).
6. Isosurface of 36.45 psu. (a) Top view, (b) lateral view. The box is that represented in Fig. 1. The z -spacing between data points is 1 m. The lateral boundary represents the surface limited by the external CTD stations, and not the coastal boundary.
7. Isosurface of 36.7 psu. Western and Eastern Alboran gyres are referenced. The box is that represented in Fig. 1. The z -spacing between data points is 1 m.
8. The density field ($\Delta = 0.2 \sigma_t$) at 100 m due to (a) the observed salinity field and the mean temperature on this layer (14.2°C); (b) due to the observed temperature field and the mean salinity on this layer (37.6 psu). Interpolation method: successive corrections.
9. Temperature, salinity and σ_t profiles at: (a) station D03 (Western Gyre), (b) station L06 (Eastern Gyre), and (c) station G07 (Northern Alboran).

10. Temperature distribution at 10 m ($\Delta = 0.5^\circ\text{C}$). Interpolation method: successive corrections.
11. Satellite thermal imagery (September 28, 1992). Bright blue means colder water.
12. Geostrophic velocity field at 10 m. Reference vector is 1.5 m s^{-1} .
13. Geostrophic transport function at 10 m ($\Delta = 0.2 \text{ Sv}$).
14. ADCP data at 40 m deep. Reference vector is 1 m s^{-1} .
15. Geostrophic vorticity field, ζ/f , at 10 m ($\Delta = 0.2$).
16. Isosurface of positive geostrophic vorticity ($3 \times 10^{-5} \text{ s}^{-1}$). The isosurface of dynamic height of 0 dyn cm is plotted just to locate the wavelike flow. The z -spacing between data points is 1 m.
17. Distribution of the squared Brunt-Väisälä frequency at 30 m ($\Delta = 50 \text{ cph}^2$). Interpolation method: successive corrections.
18. Squared Brunt-Väisälä frequency on vertical section E ($\Delta = 50 \text{ cph}^2$). Interpolation method: local bivariate.
19. Distribution of vertical shear $U_z^2 + V_z^2$ at 100 m ($\Delta = 10 \times 10^{-6} \text{ s}^{-2}$).
20. Vertical distributions in vertical section D and E of: (a) σ_t ($\Delta = 0.2 \sigma_t$), (b) Squared Brunt-Väisälä frequency ($\Delta = 25 \text{ cph}^2$), (c) zonal component of the geostrophic velocity field ($\Delta = 10 \text{ cm s}^{-1}$, solid contour lines indicates eastward direction), (d) relative geostrophic vorticity ζ/f ($\Delta = 0.1$), (e) geostrophic vertical shear $U_z^2 + V_z^2$ ($\Delta = 10 \times 10^{-6} \text{ s}^{-2}$), (f) Froude number $(U_z^2 + V_z^2)/N^2$ ($\Delta = 0.1$), and (g) potential vorticity ($\Delta = 0.5 \times 10^{-9} \text{ m}^{-1} \text{ s}^{-1}$).
21. Vertical distributions of PV ($\Delta = 0.5 \times 10^{-9} \text{ m}^{-1} \text{ s}^{-1}$) and σ_t ($\Delta = 0.2 \sigma_t$) in the box for: (a) vertical section D, (b) vertical section between D and E, and (c) vertical section E. The three small marked areas represent particles of fluid limited by the same values of PV and σ_t .

Three-Dimensional Structure...

22. \mathbf{Q} vector at 100 m. Reference vector is $200 \times 10^{-13} \text{ s}^{-3}$.
23. Mean squared Brunt-Väisälä frequency profile (cph^2). Horizontal bars represent the value $\bar{N}^2(z) \pm$ one standard deviation.
24. $\nabla \cdot \mathbf{Q}$ distribution at 100 m ($\Delta = 20 \times 10^{-17} \text{ m}^{-1} \text{ s}^{-3}$).
25. Vertical velocity distribution at 100 m ($\Delta = 5 \times 10^{-5} \text{ m s}^{-1}$).
26. Vertical velocity distribution between vertical sections D and E ($\Delta = 5 \times 10^{-5} \text{ m s}^{-1}$).

ALBORAN SEA

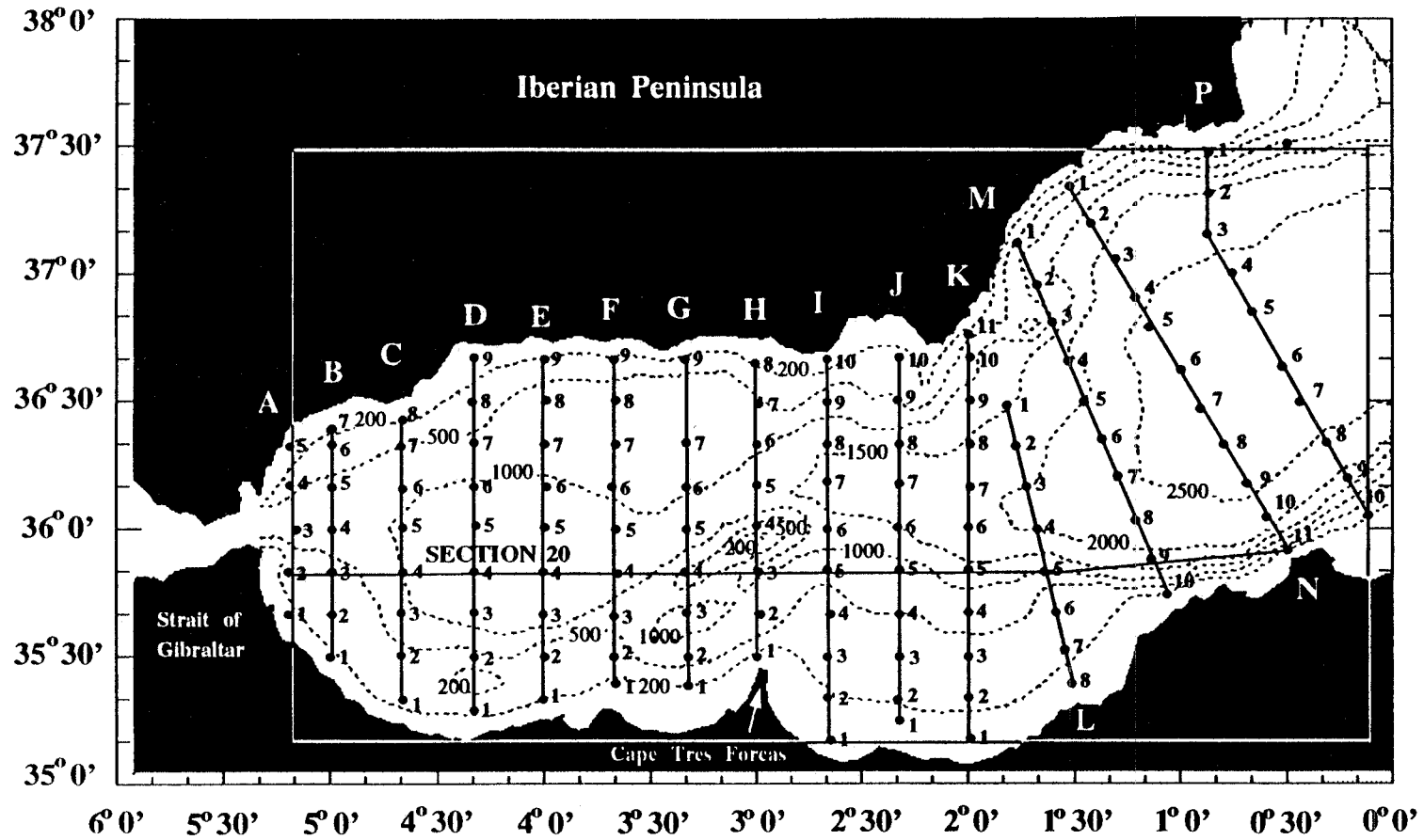
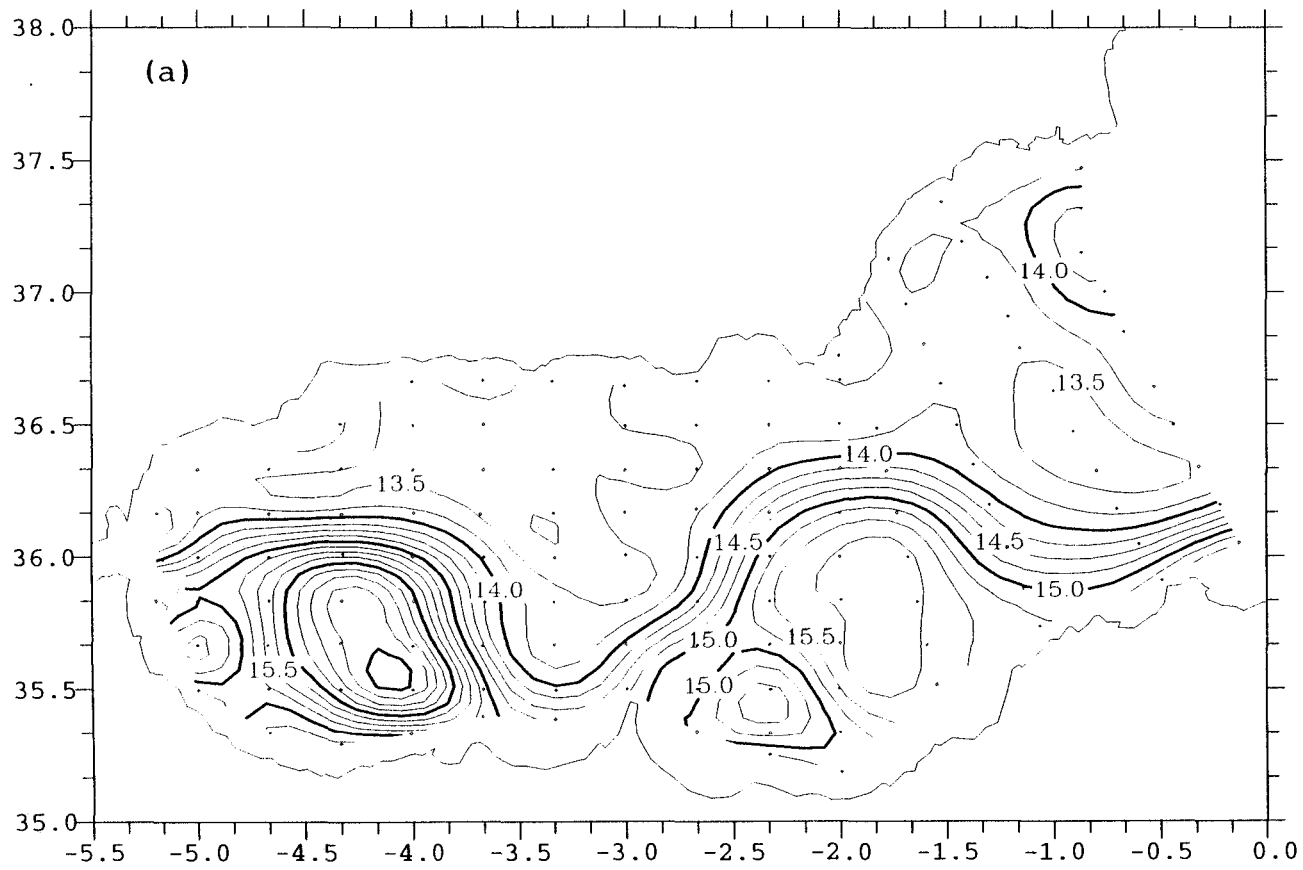
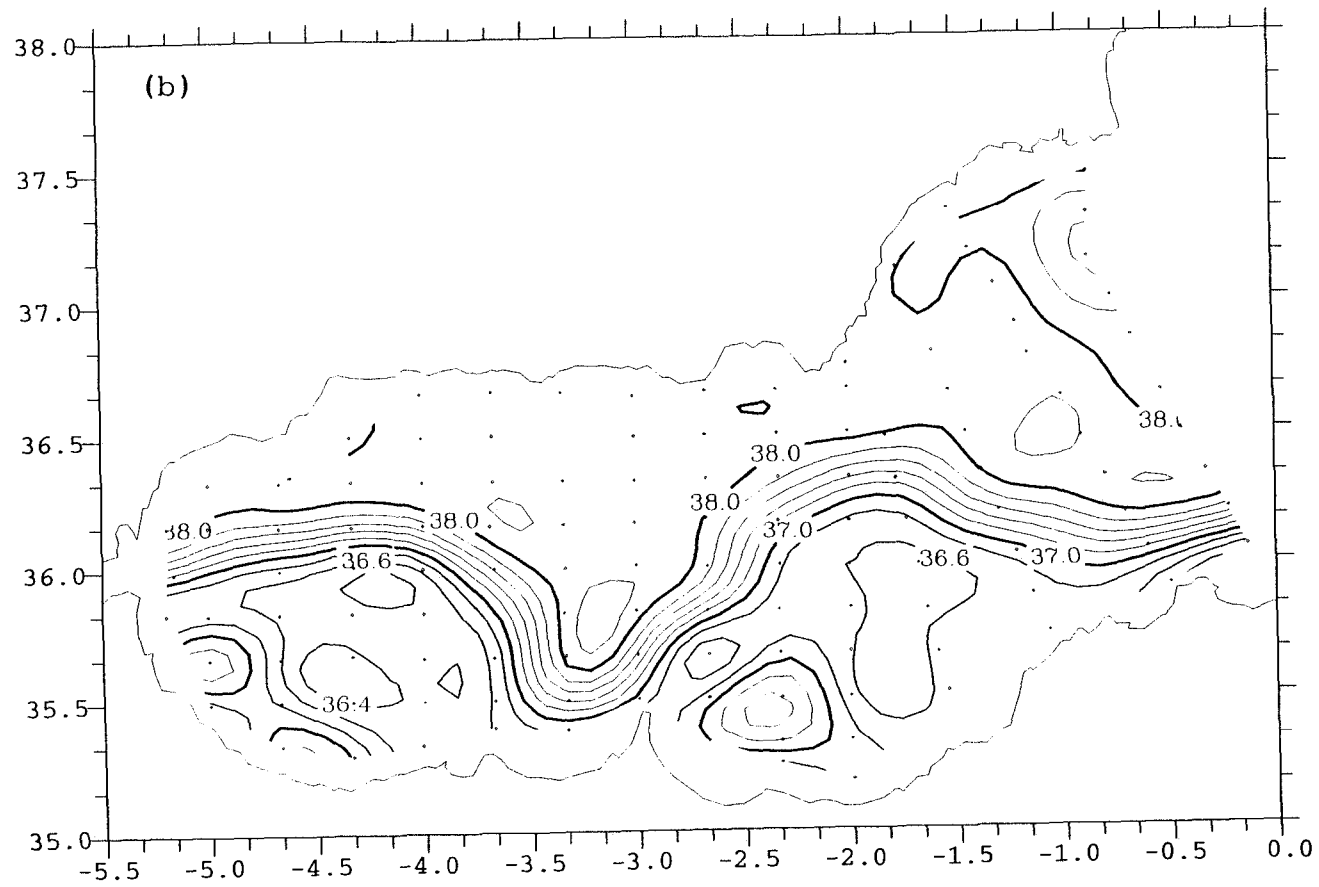


Figure 1



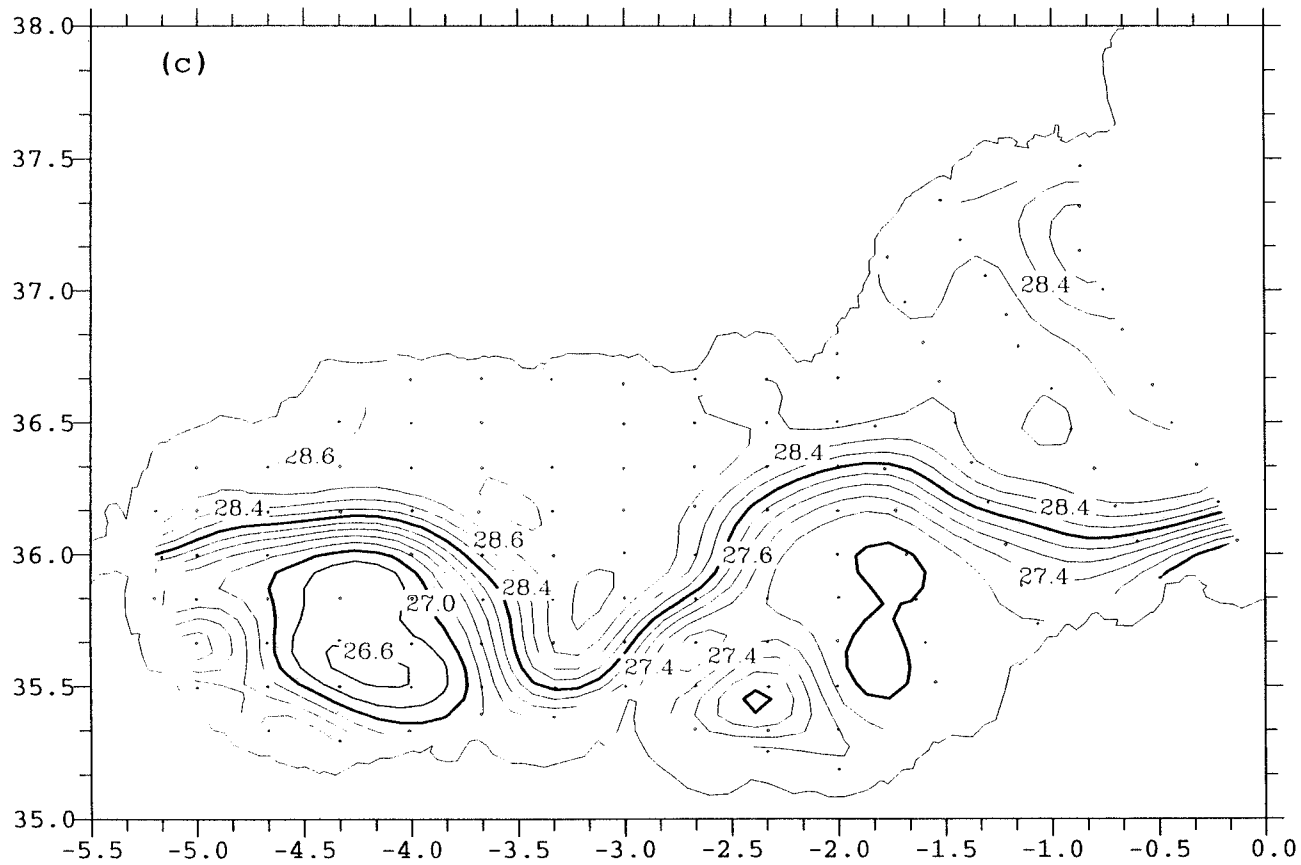
TEMPERATURE AT 100 M.

Figure 2a



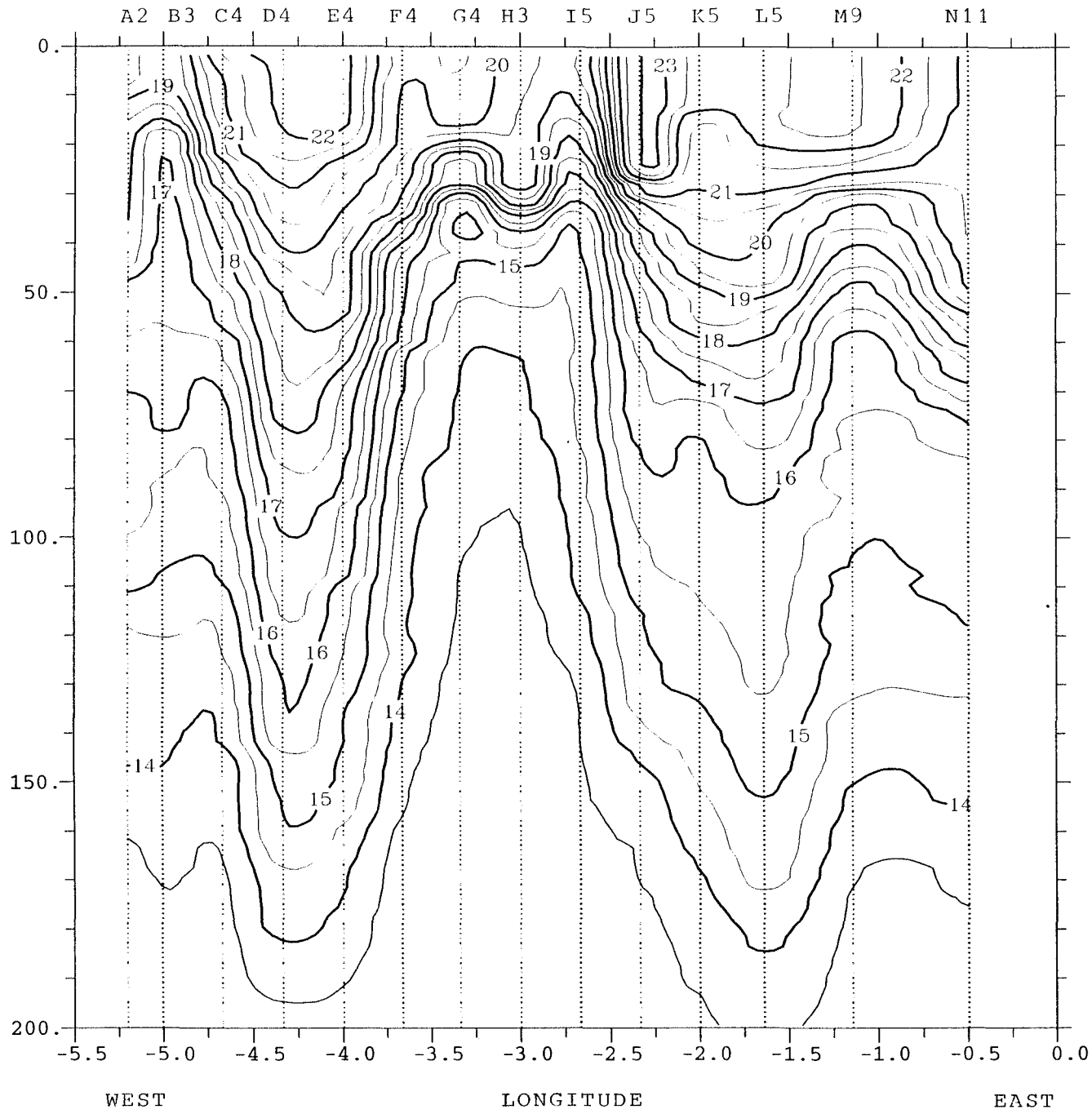
SALINITY AT 100 M.

Figure 2b



SIGMAT AT 100 M.

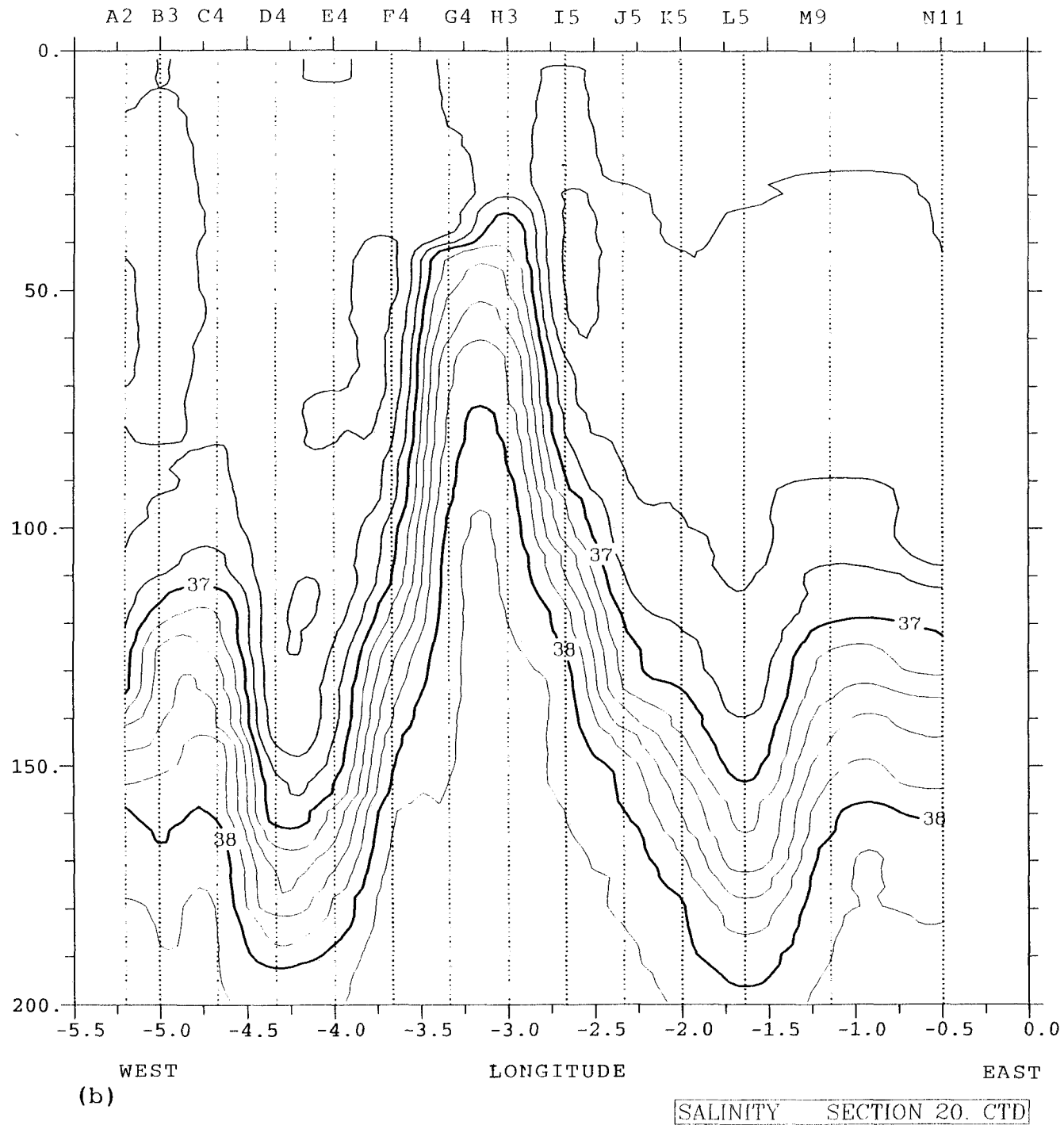
Figure 2c



(a)

TEMPERATURE SECTION 20. CTD

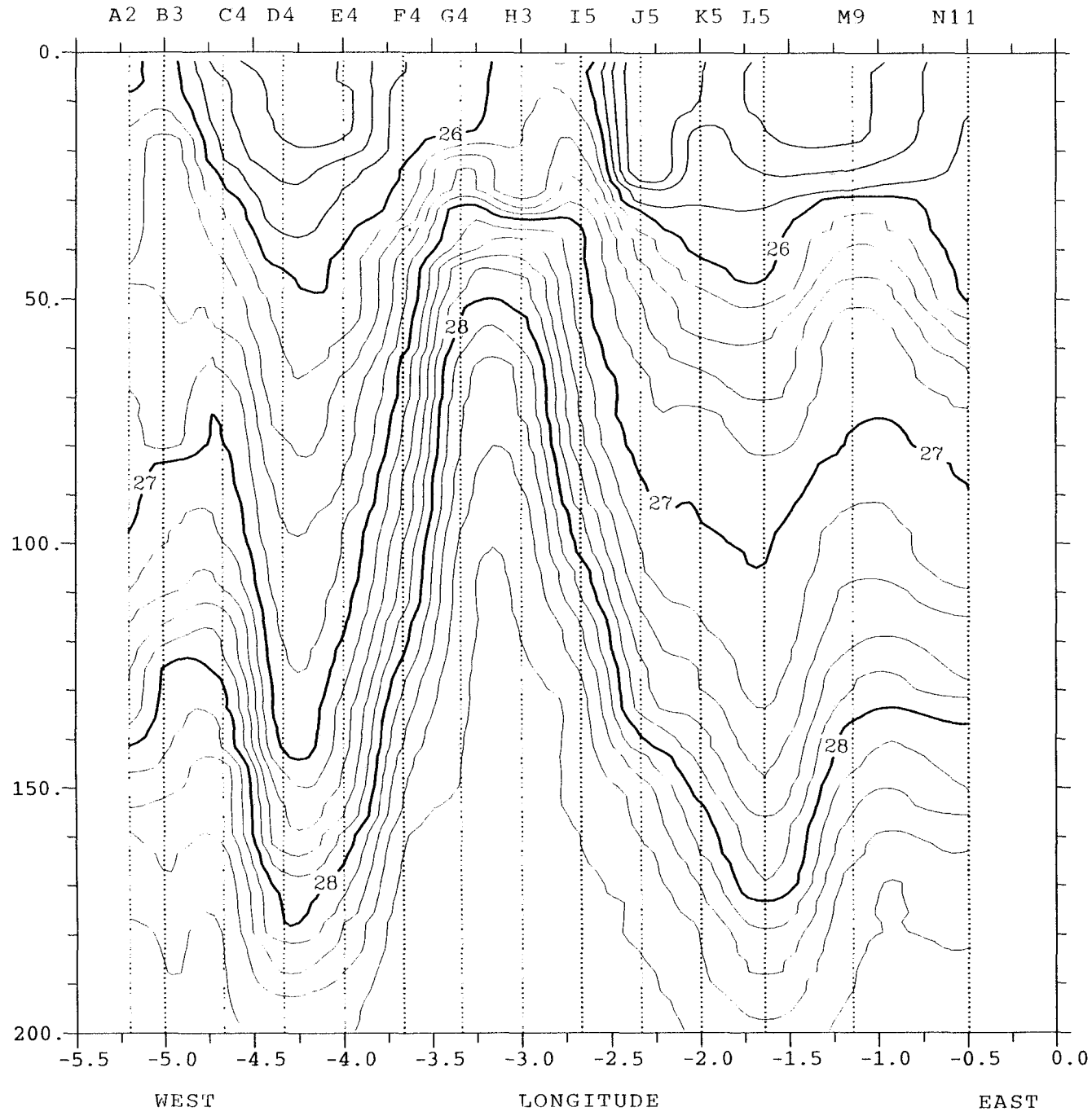
Figure 3a



(b)

SALINITY SECTION 20. CTD

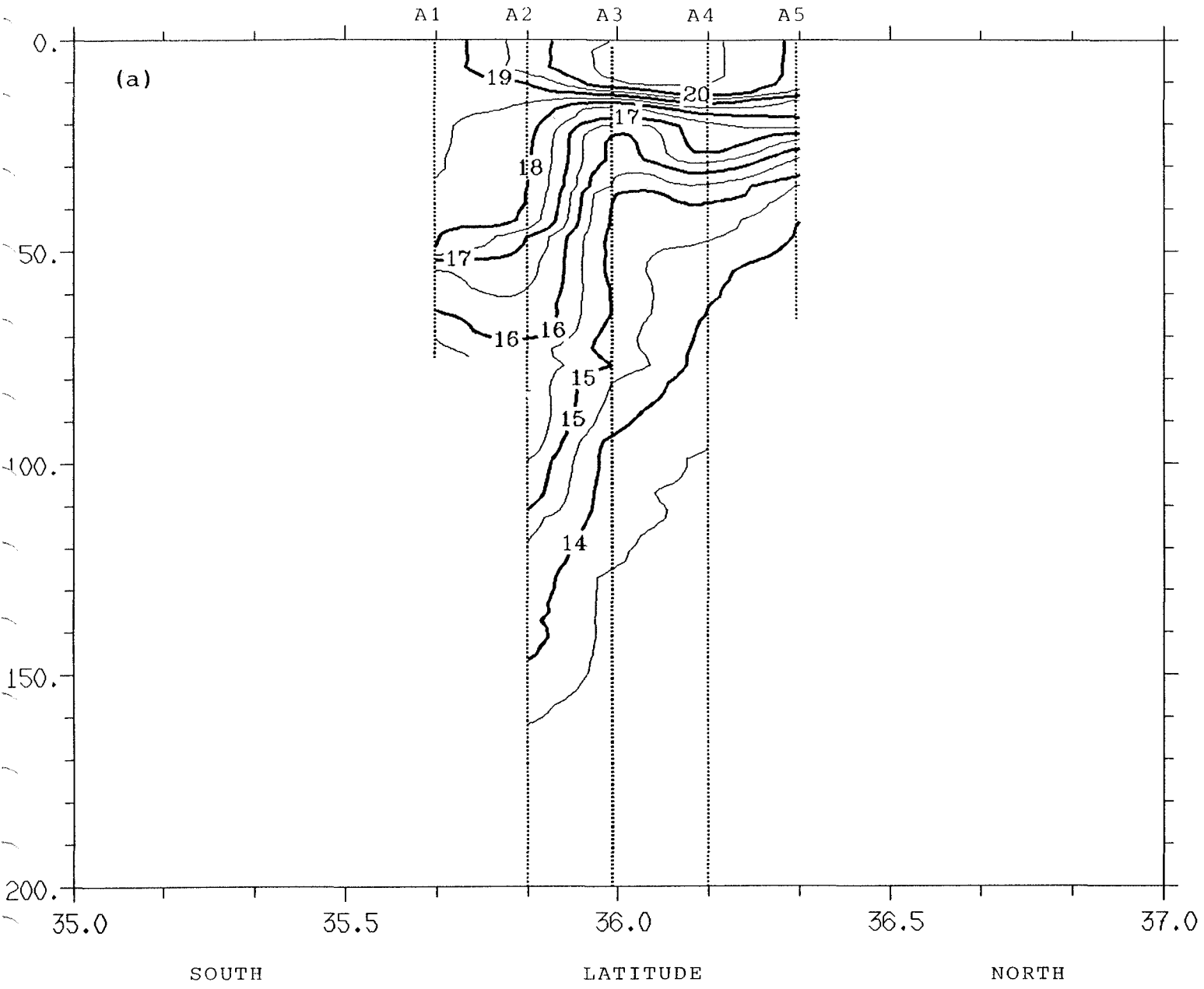
Figure 3b



(c)

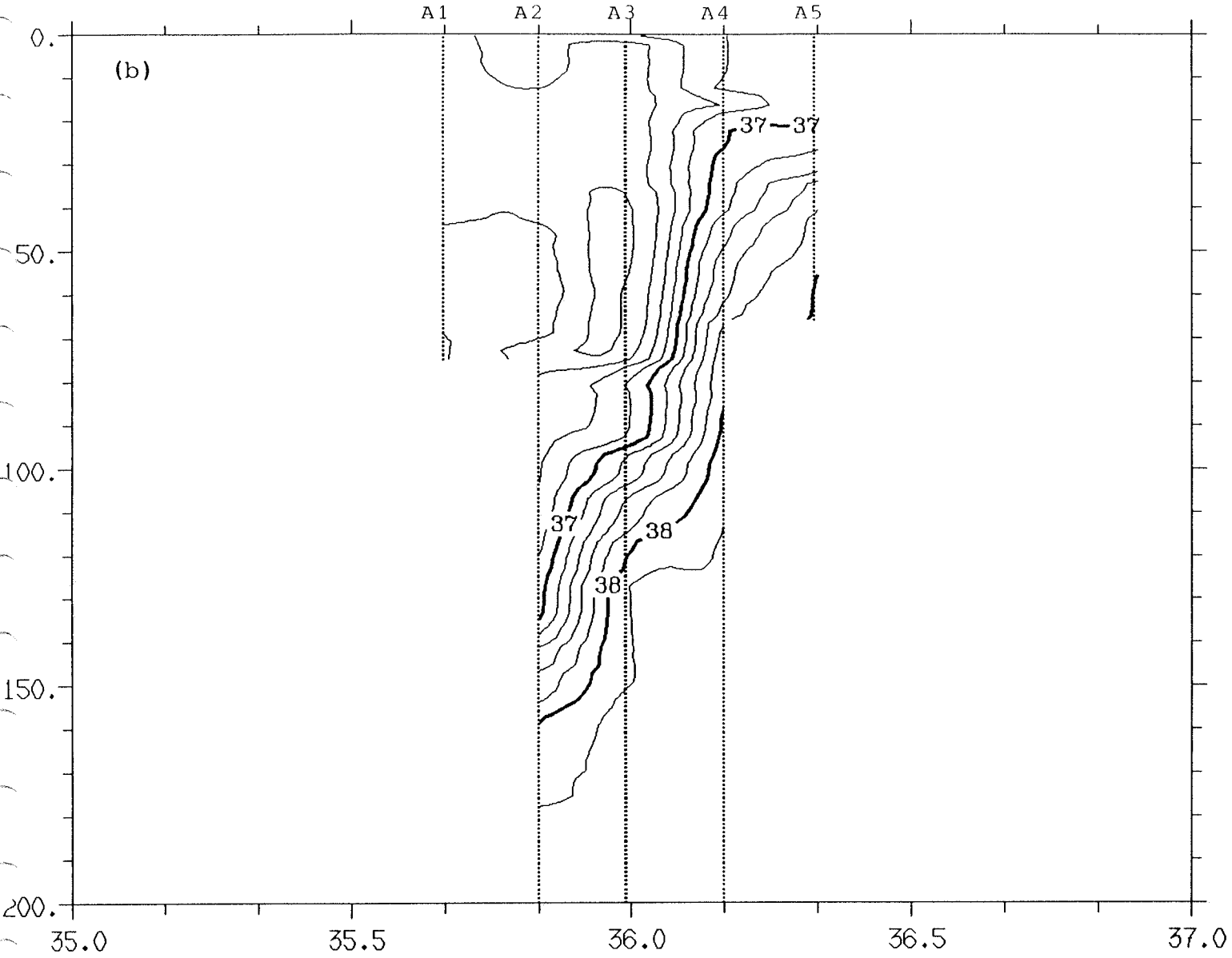
SIGMA-T SECTION 20. CTD

Figure 3c



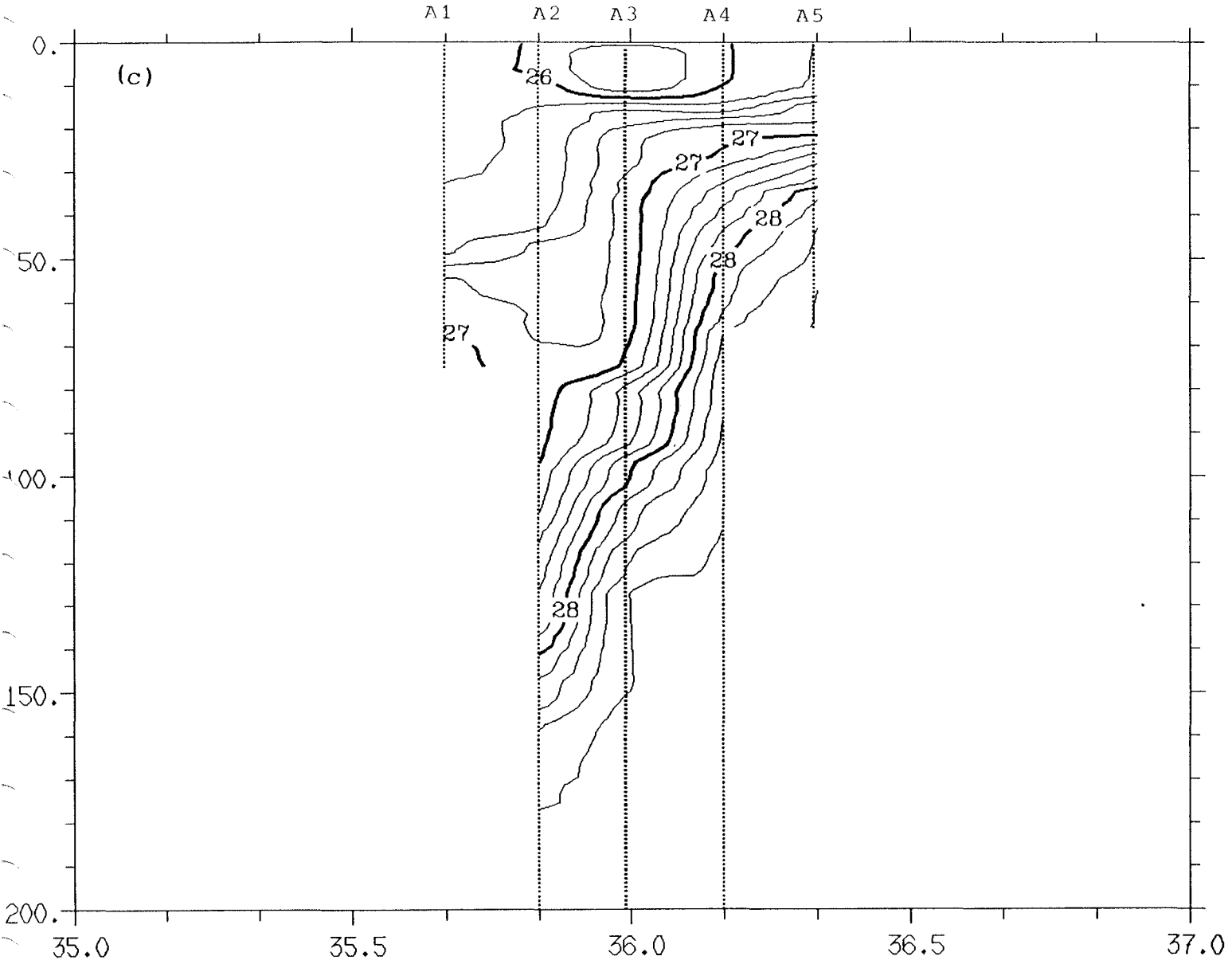
TEMPERATURE SECTION A . CTD

Figure 4a



SALINITY SECTION A . CTD

Figure 4b



SIGMA -T SECTION A . CTD

Figure 4c

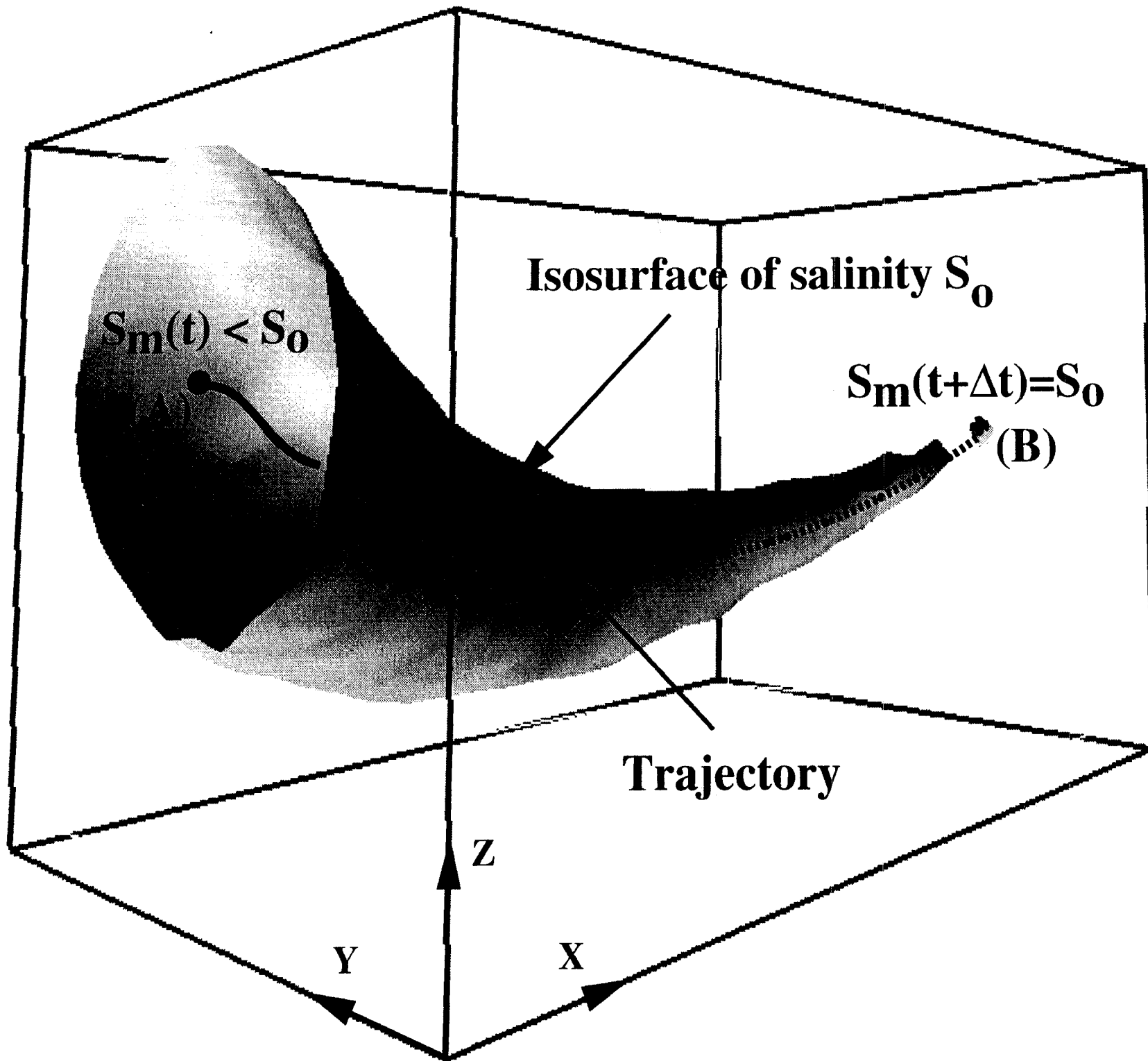
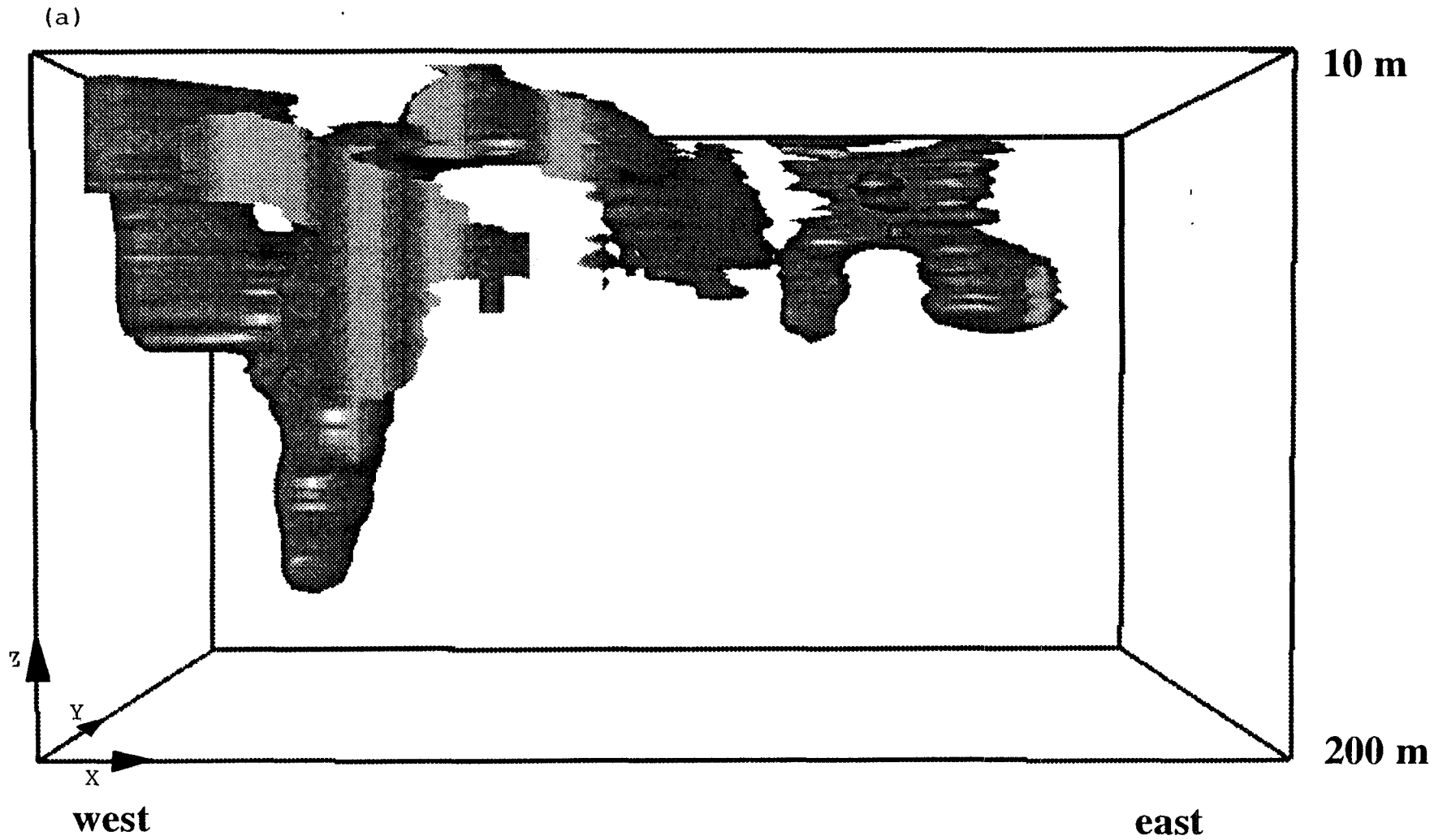


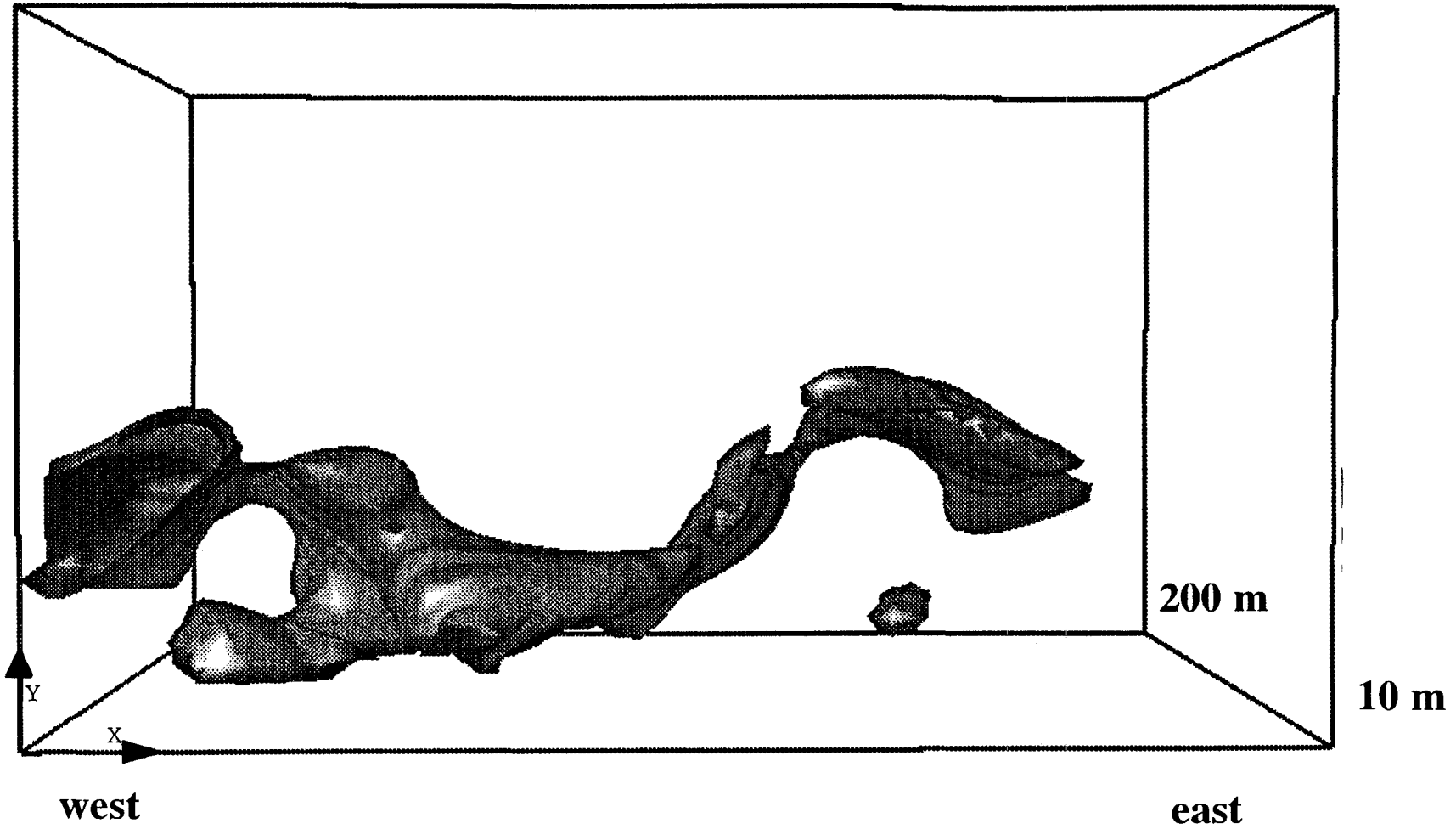
Figure 5



Isosurface 36.45 psu

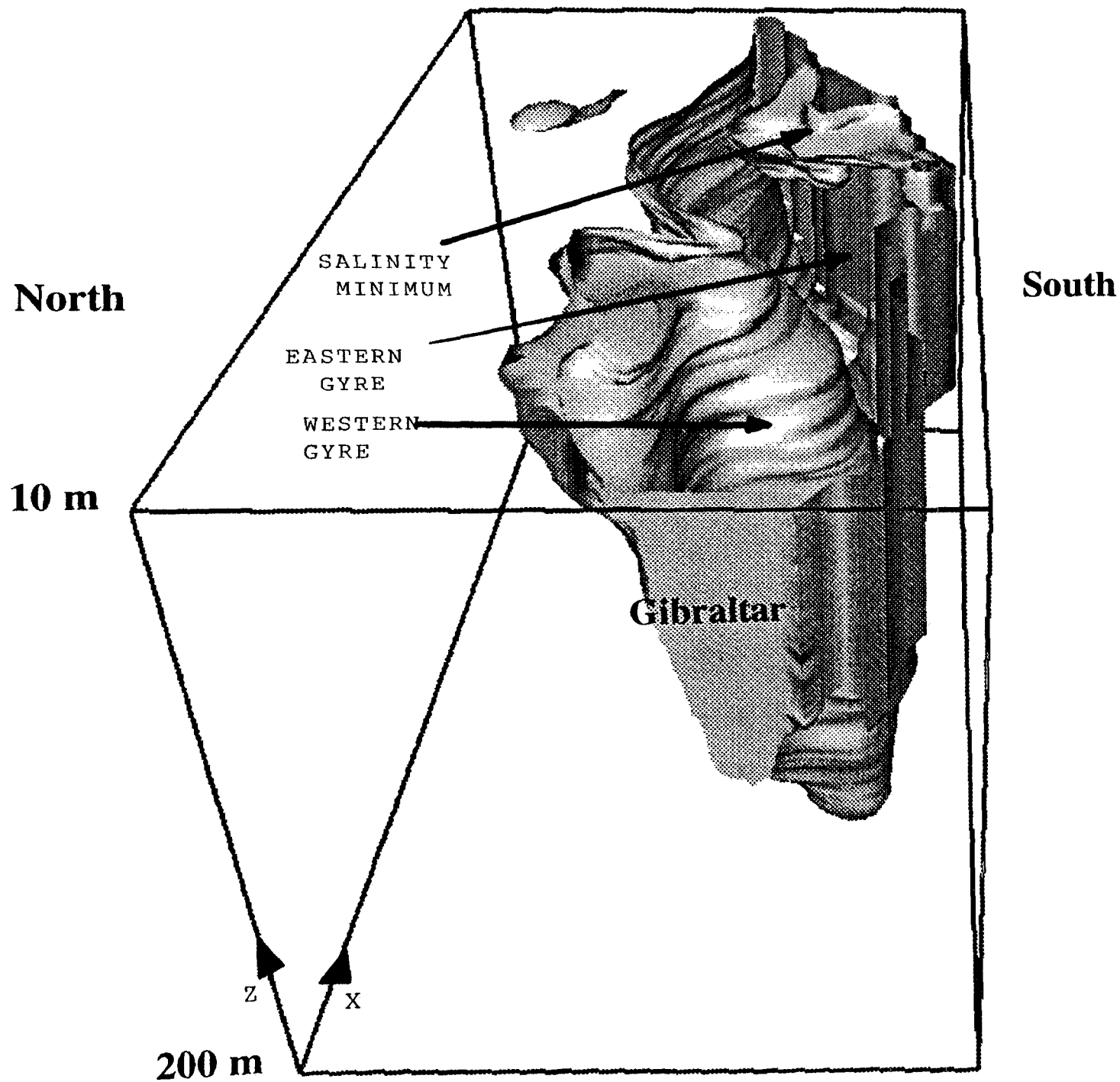
Figure 6a

(b)



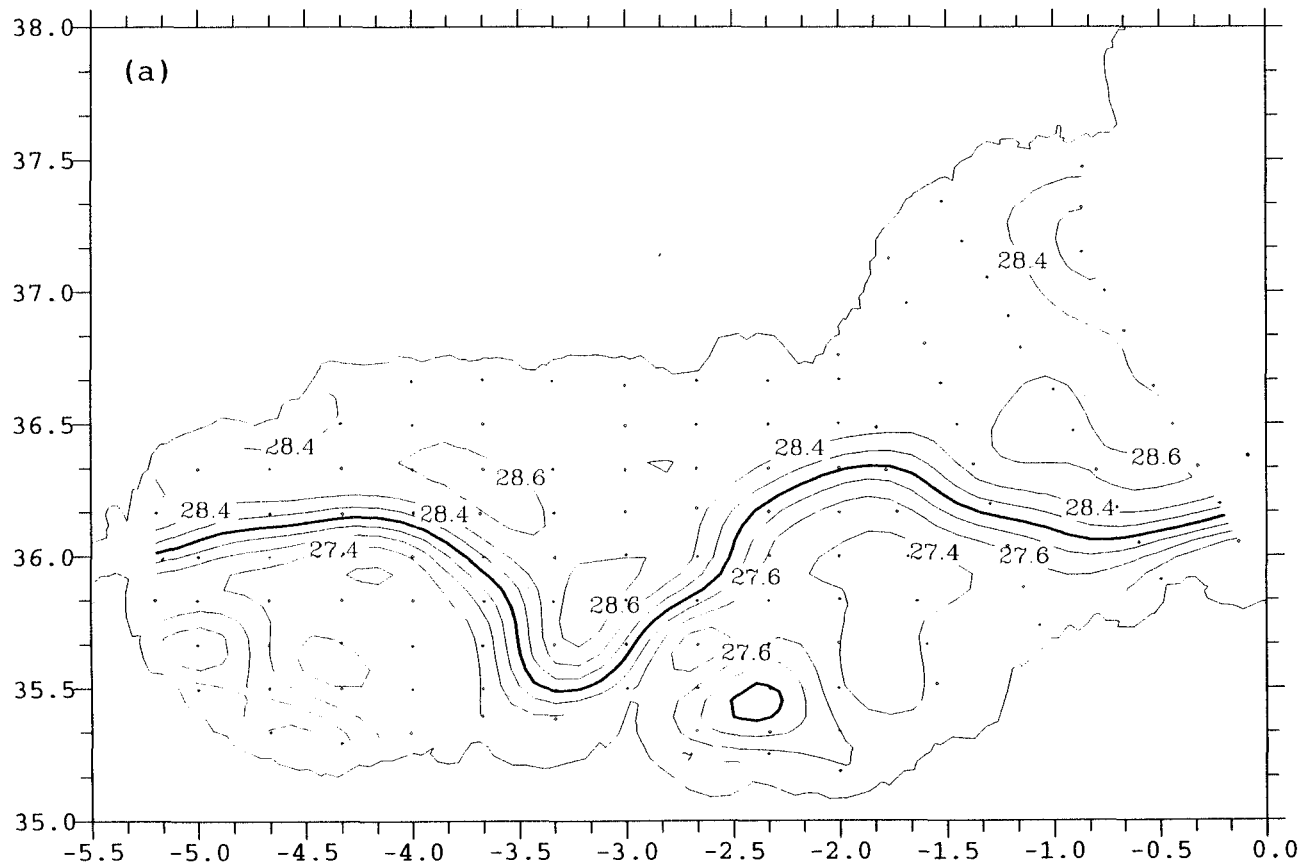
Isosurface 36.45 psu

Figure 6b



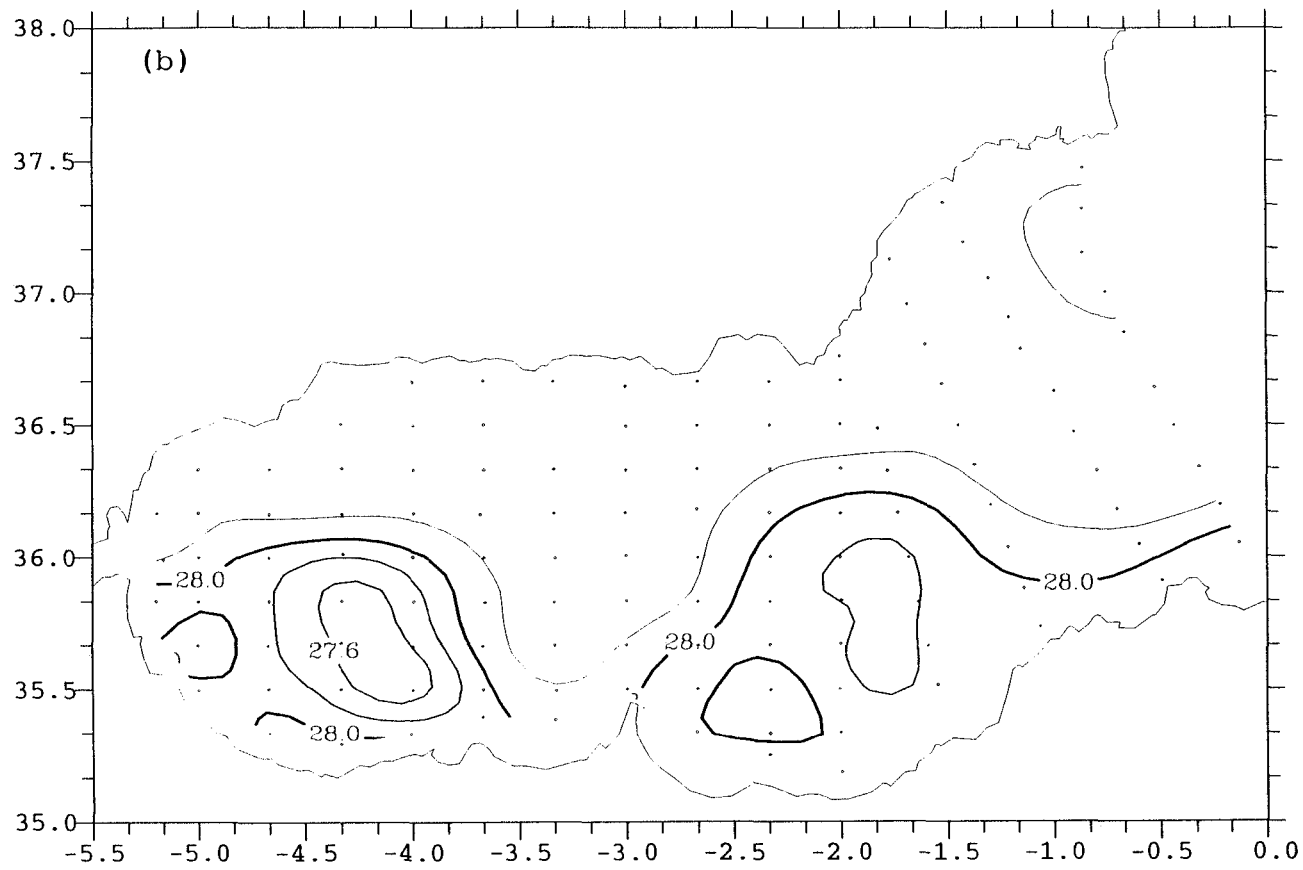
Isosurface 36.7 psu

Figure 7



SIGMA^2 (100 m) for $\langle T \rangle = 14.2$ C

Figure 8a



SIGMAT (100 m) for $\langle S \rangle = 37.6$ psu

Figure 8b

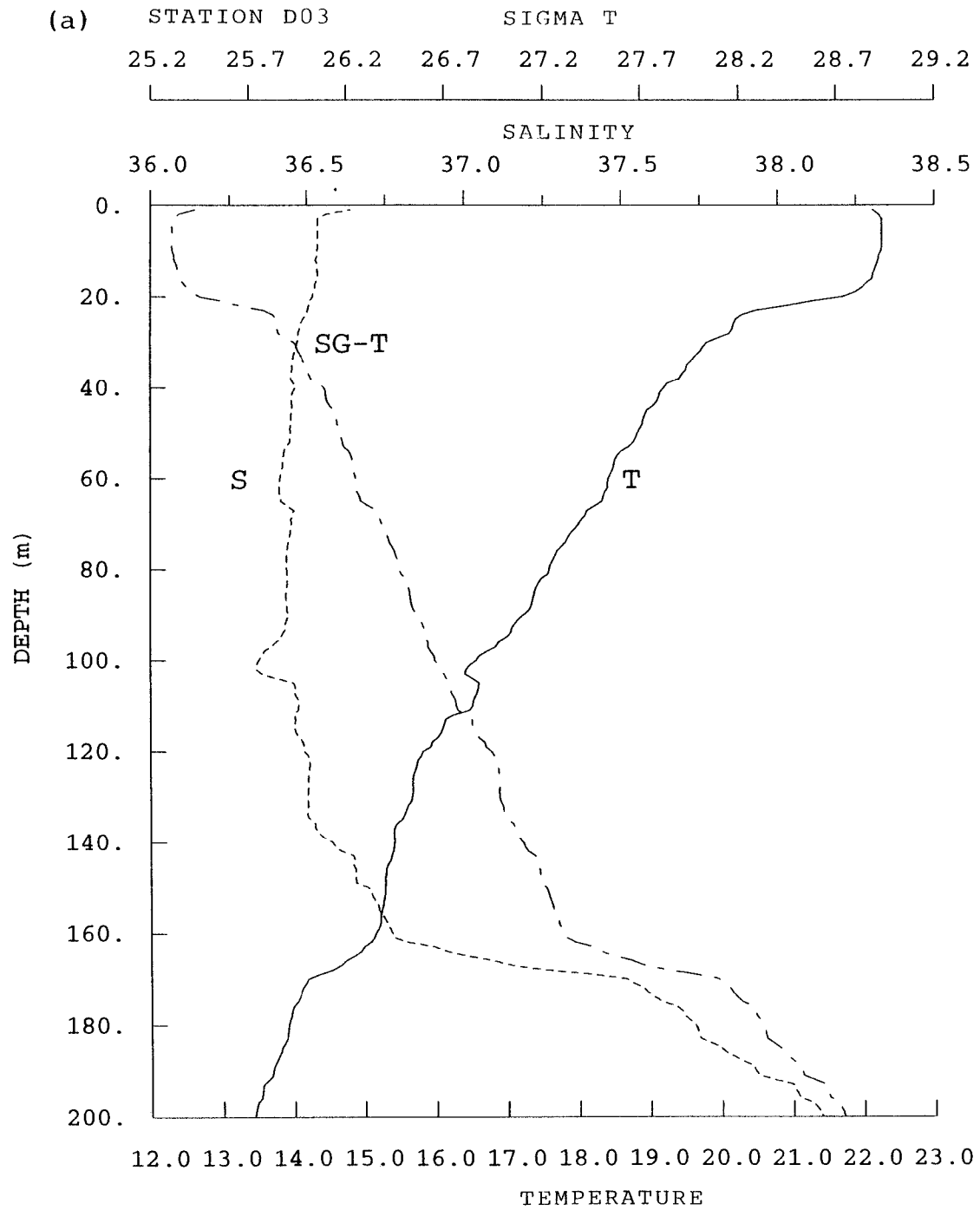


Figure 9a

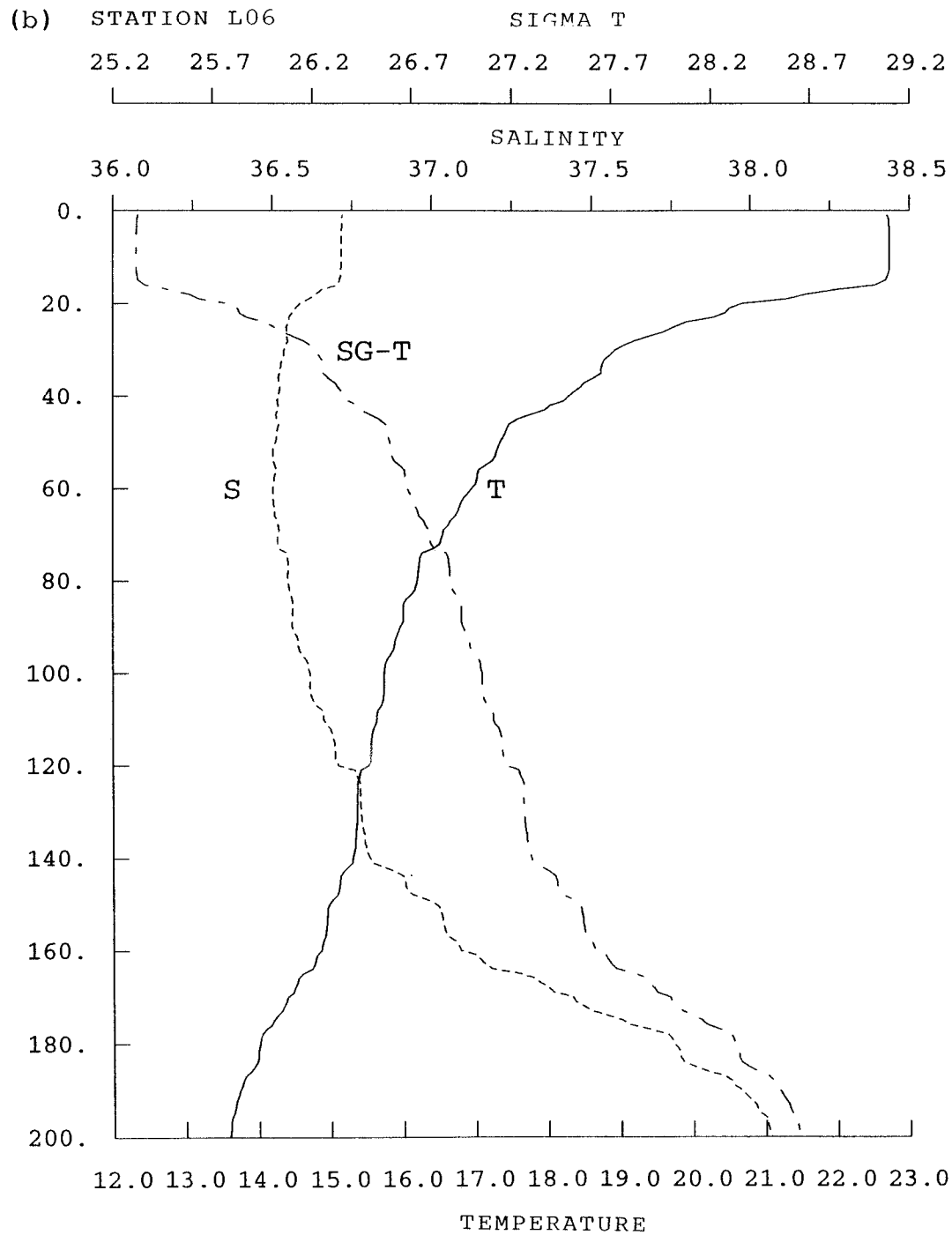


Figure 9b

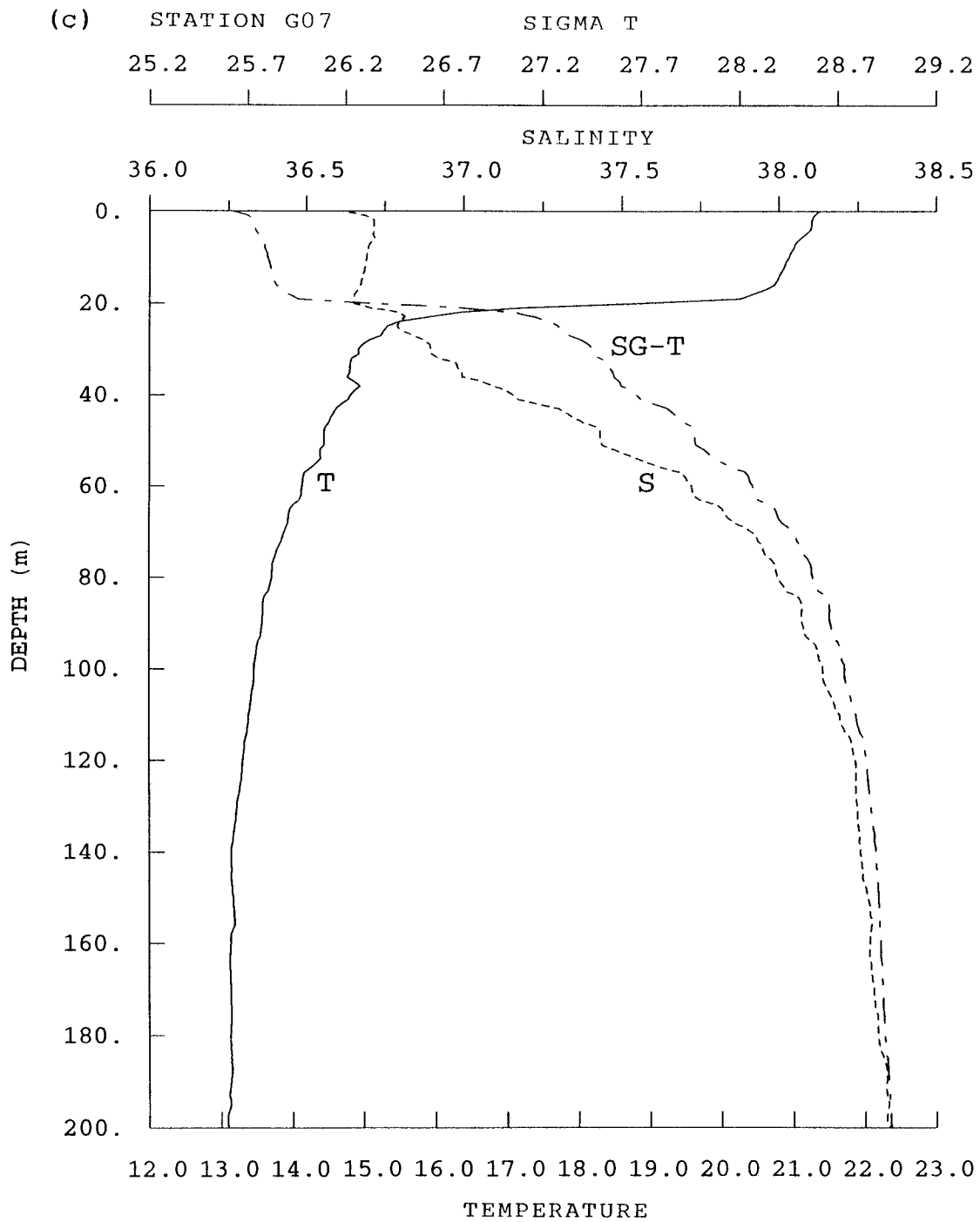
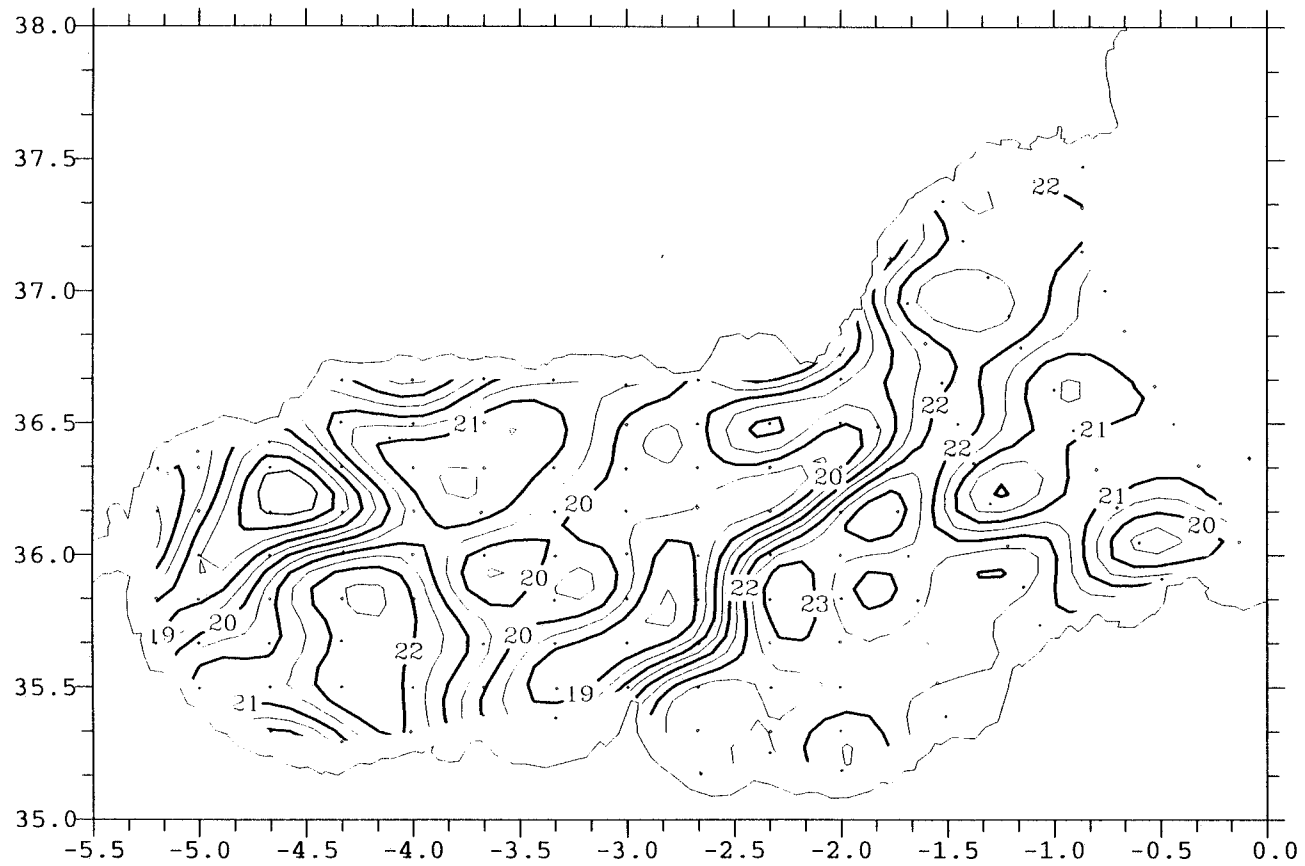


Figure 9c

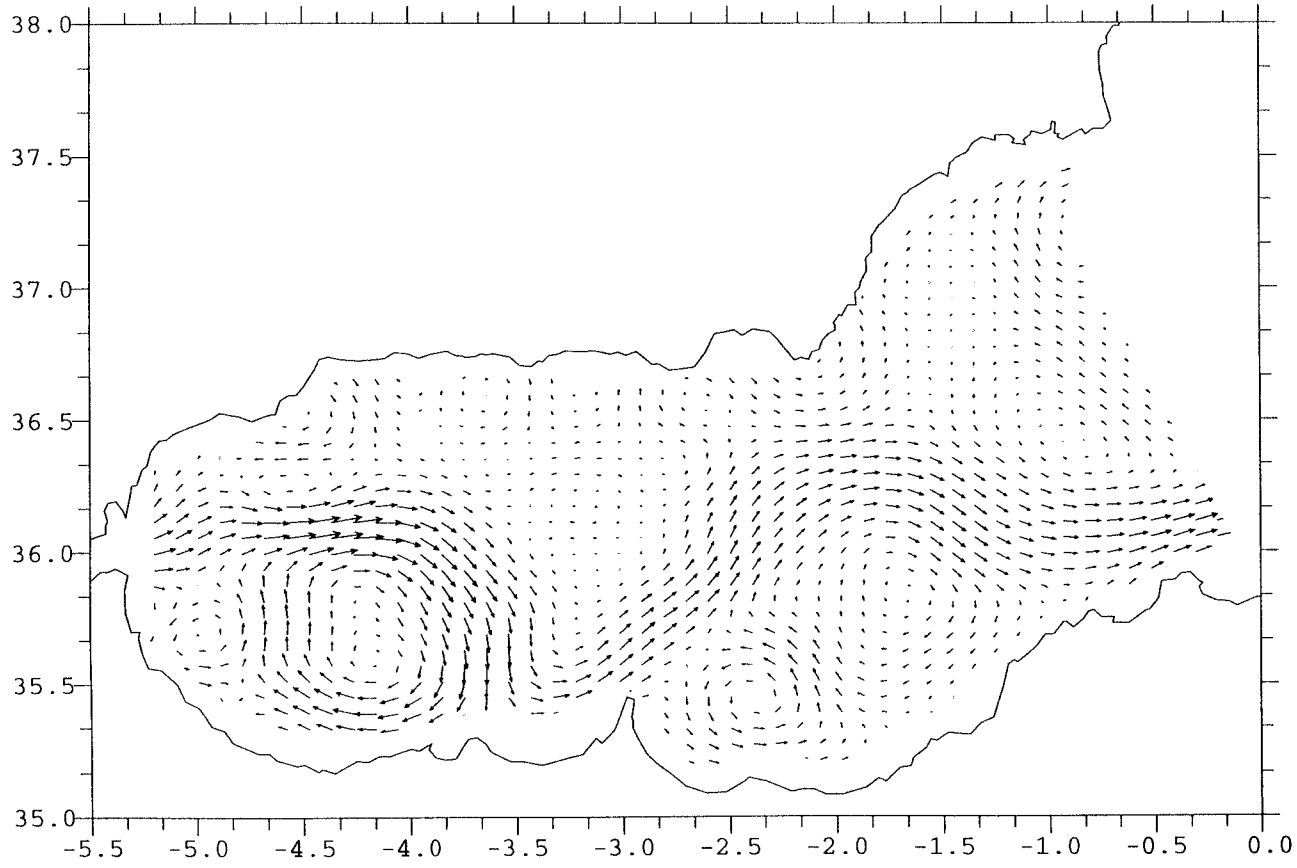


TEMPERATURE AT 10 m

Figure 10



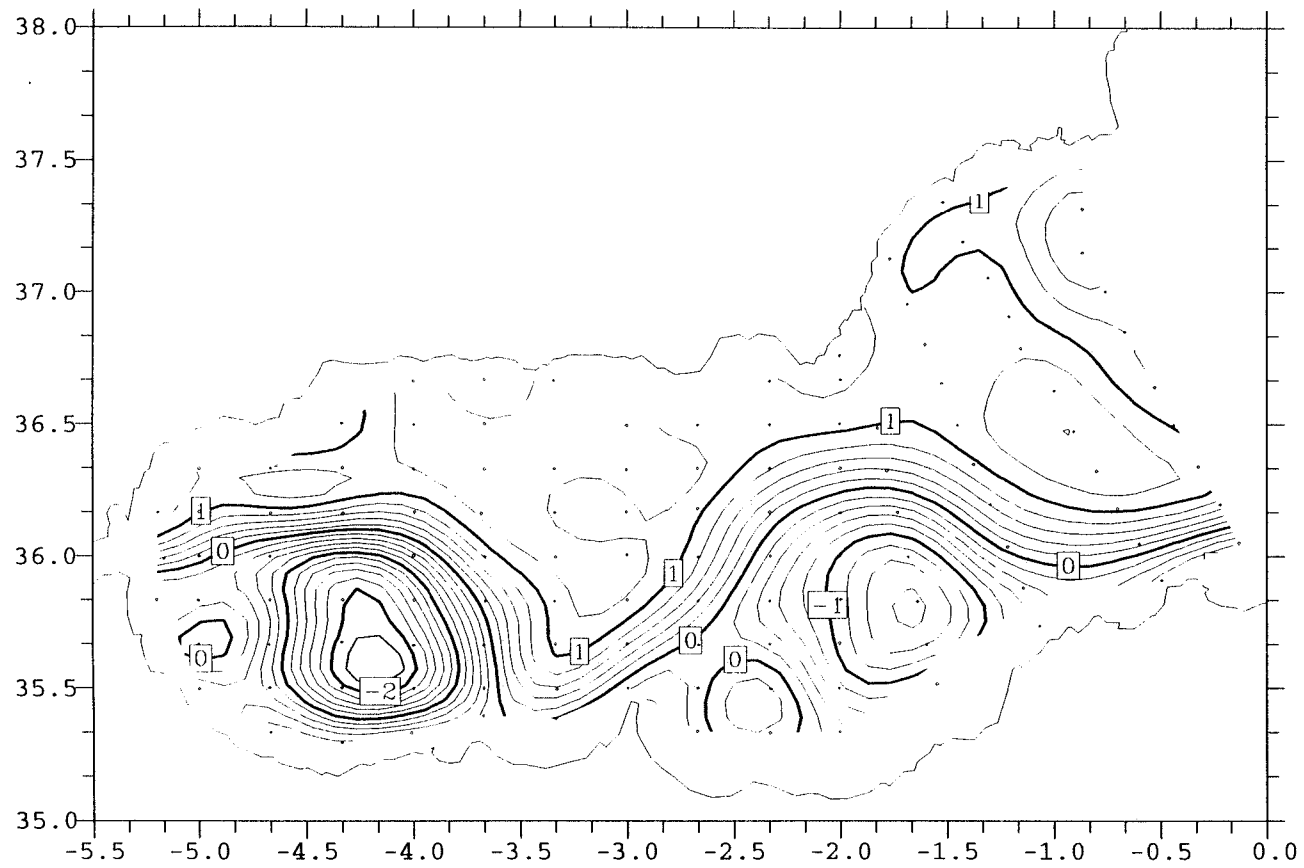
Figure 11



GEOSTROPHIC VELOCITY AT 10 m. REFERENCE LEVEL 200 m.

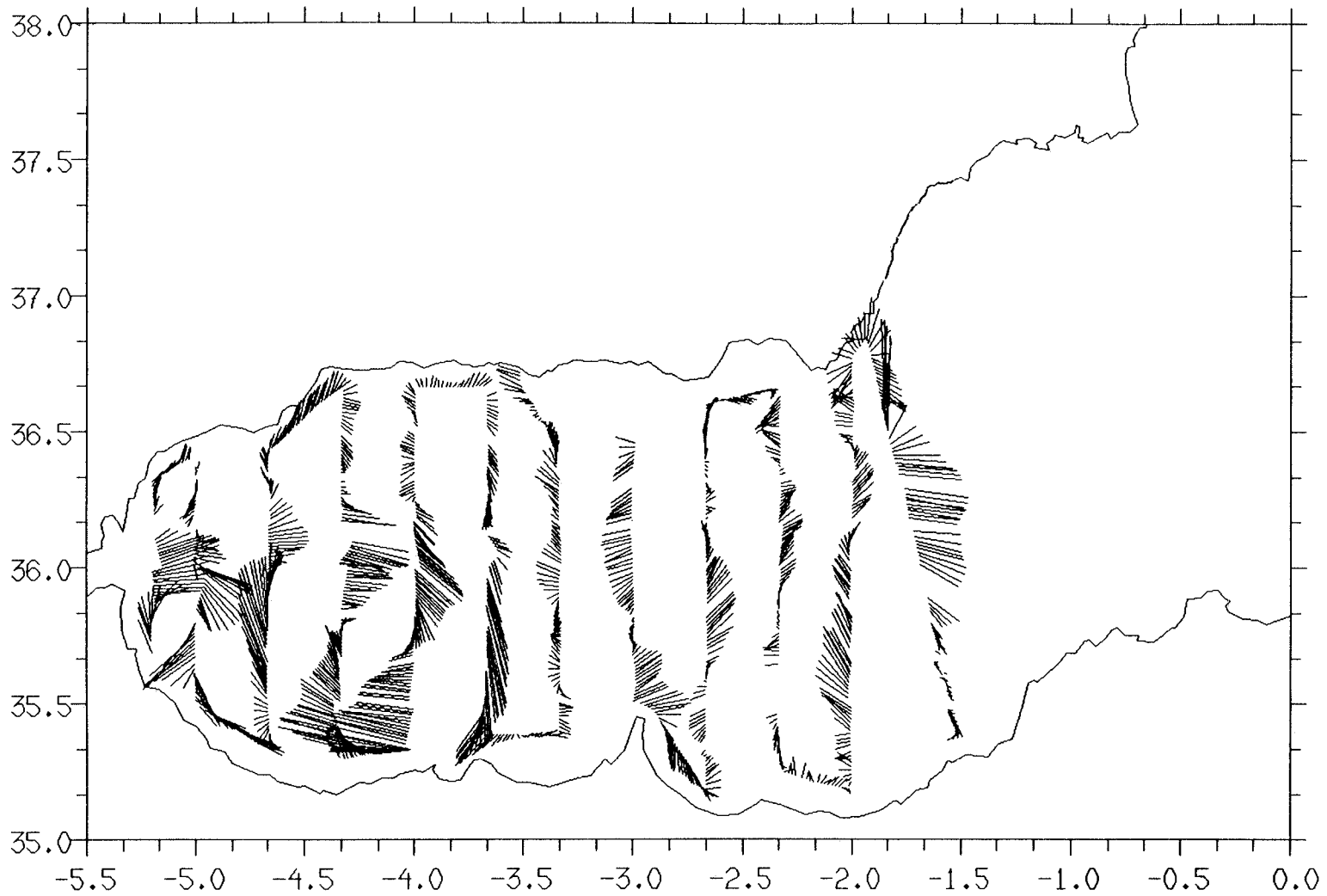
0.150E+03
→
MAXIMUM VECTOR

Figure 12



TRANSPORT FUNCTION (Sv) AT 10 m. REFERENCE LEVEL 200 m. 50x40

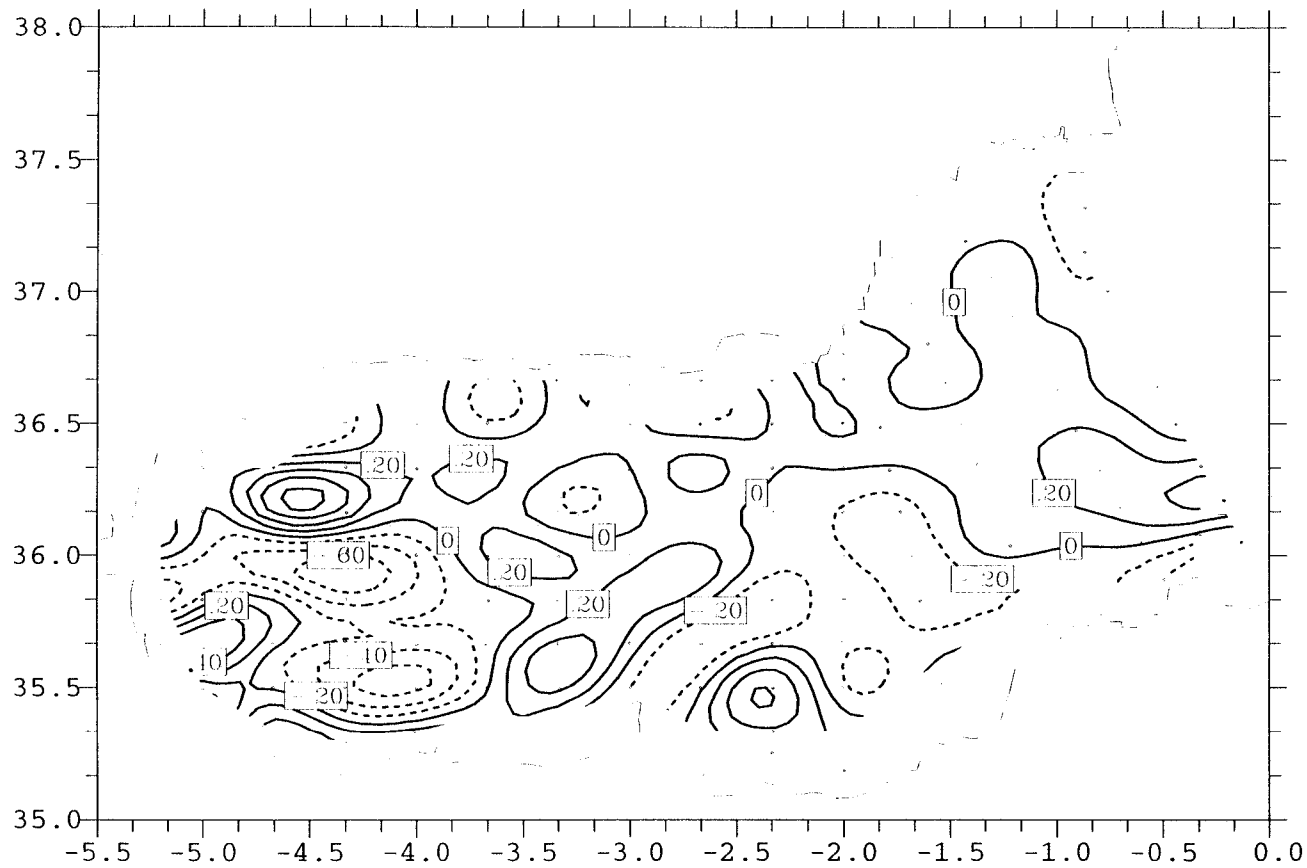
Figure 13



100.00

40

Figure 14



Rel. Vorticity f at 10 m

Figure 15

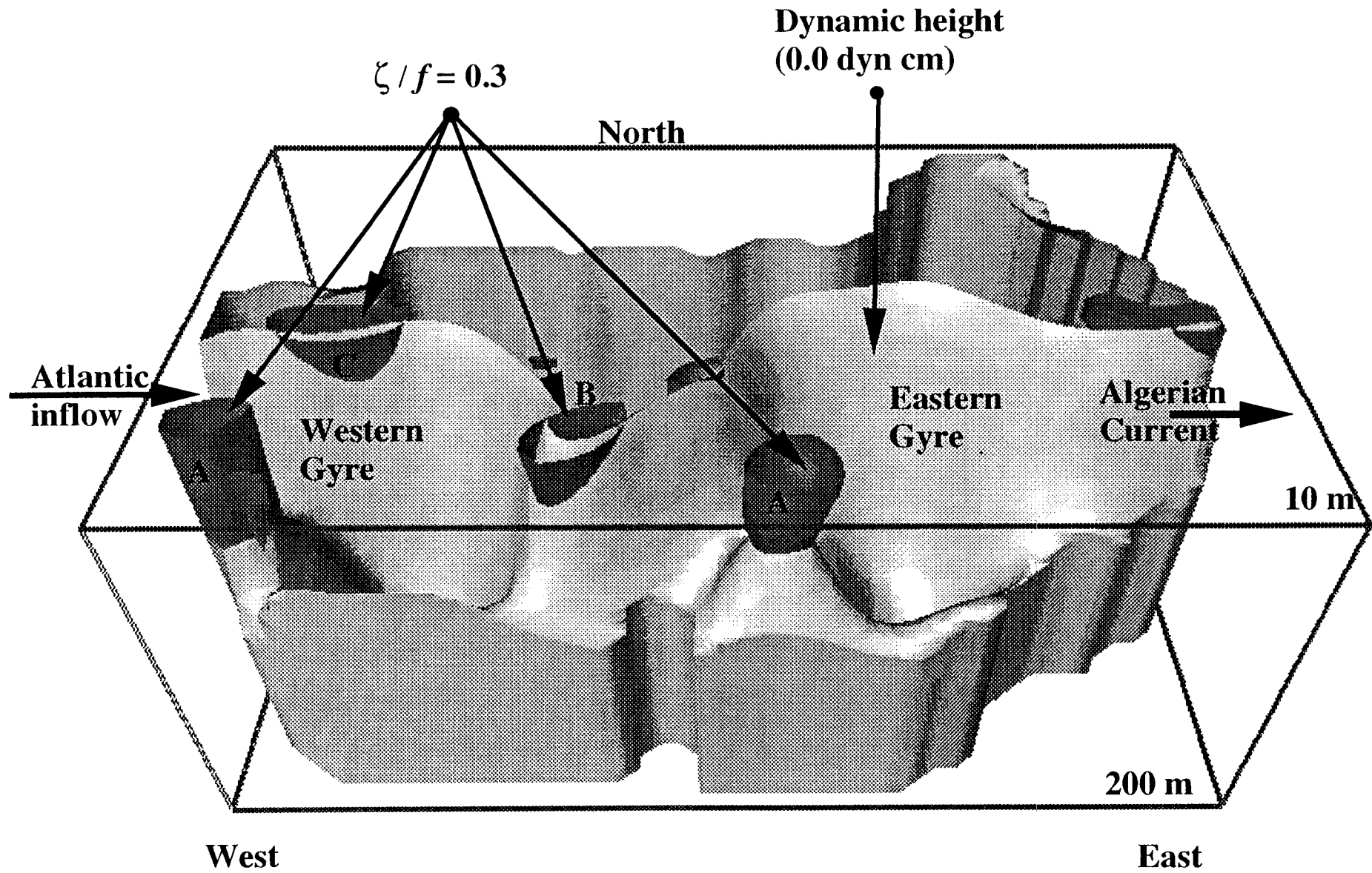
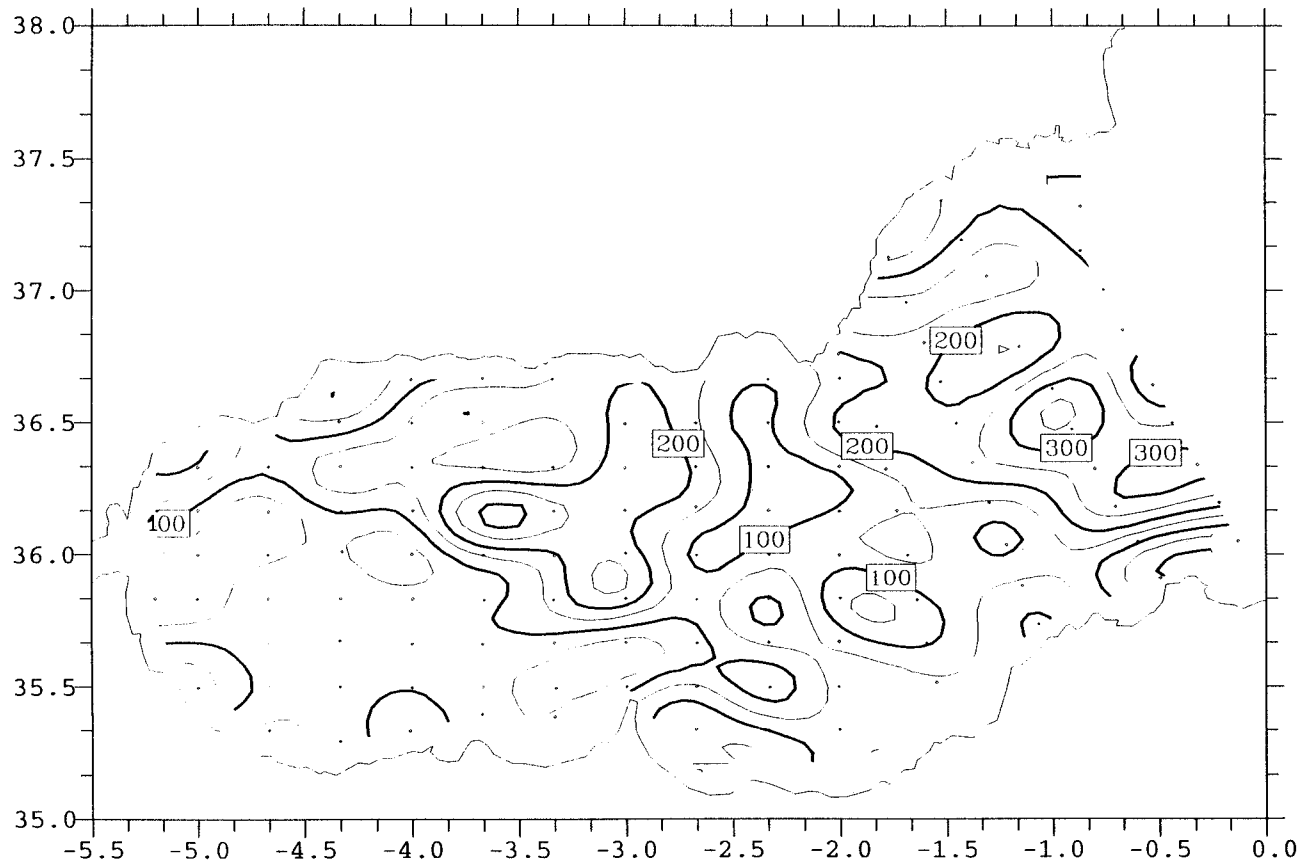
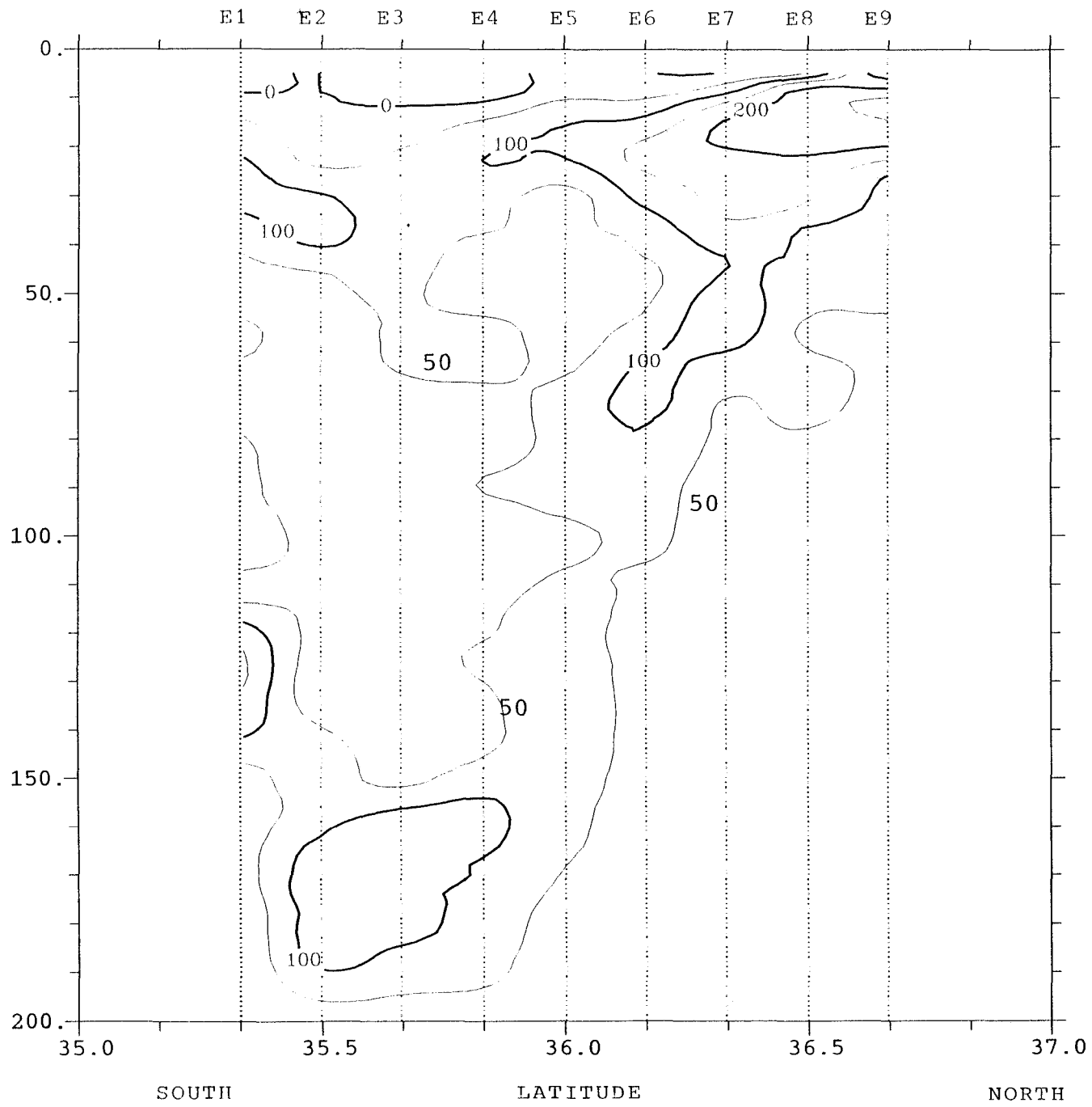


Figure 16



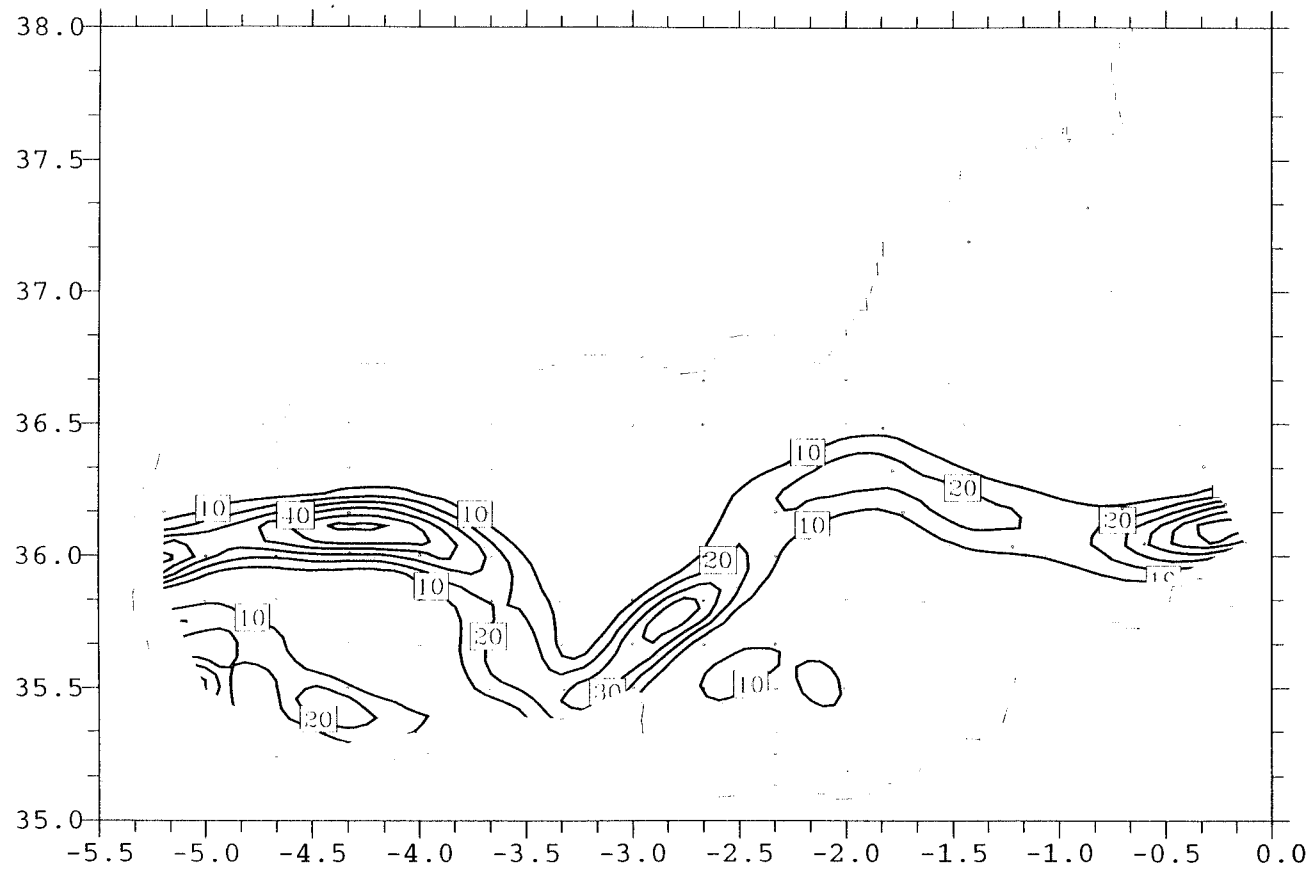
SQUARED BRUNT-VAISALA FREQUENCY N^2 (cph²) at 30 m

Figure 17



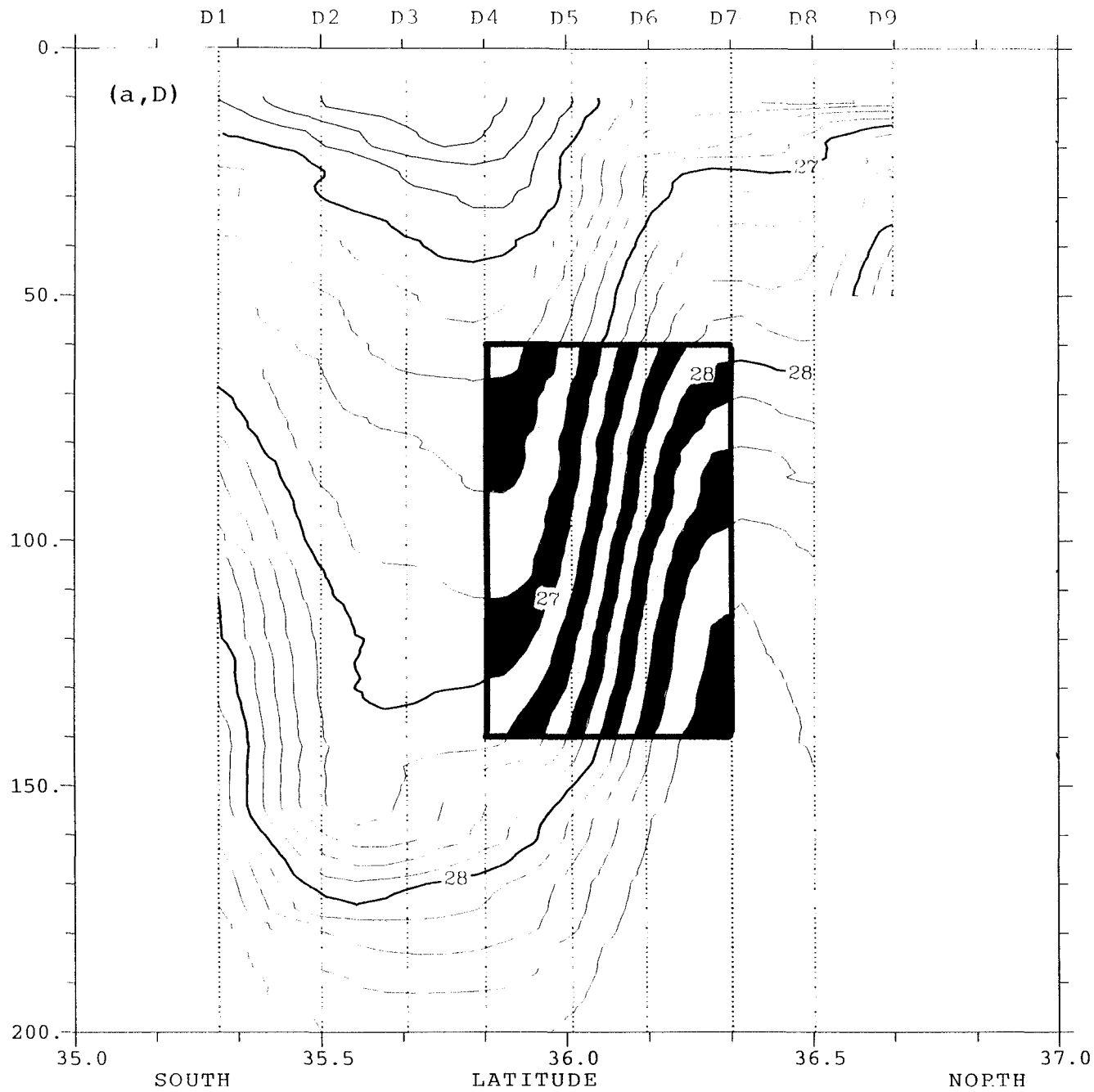
SQUARED BRUNT-VAISALA FREQUENCY N2 (cph2). SECTION E

Figure 18



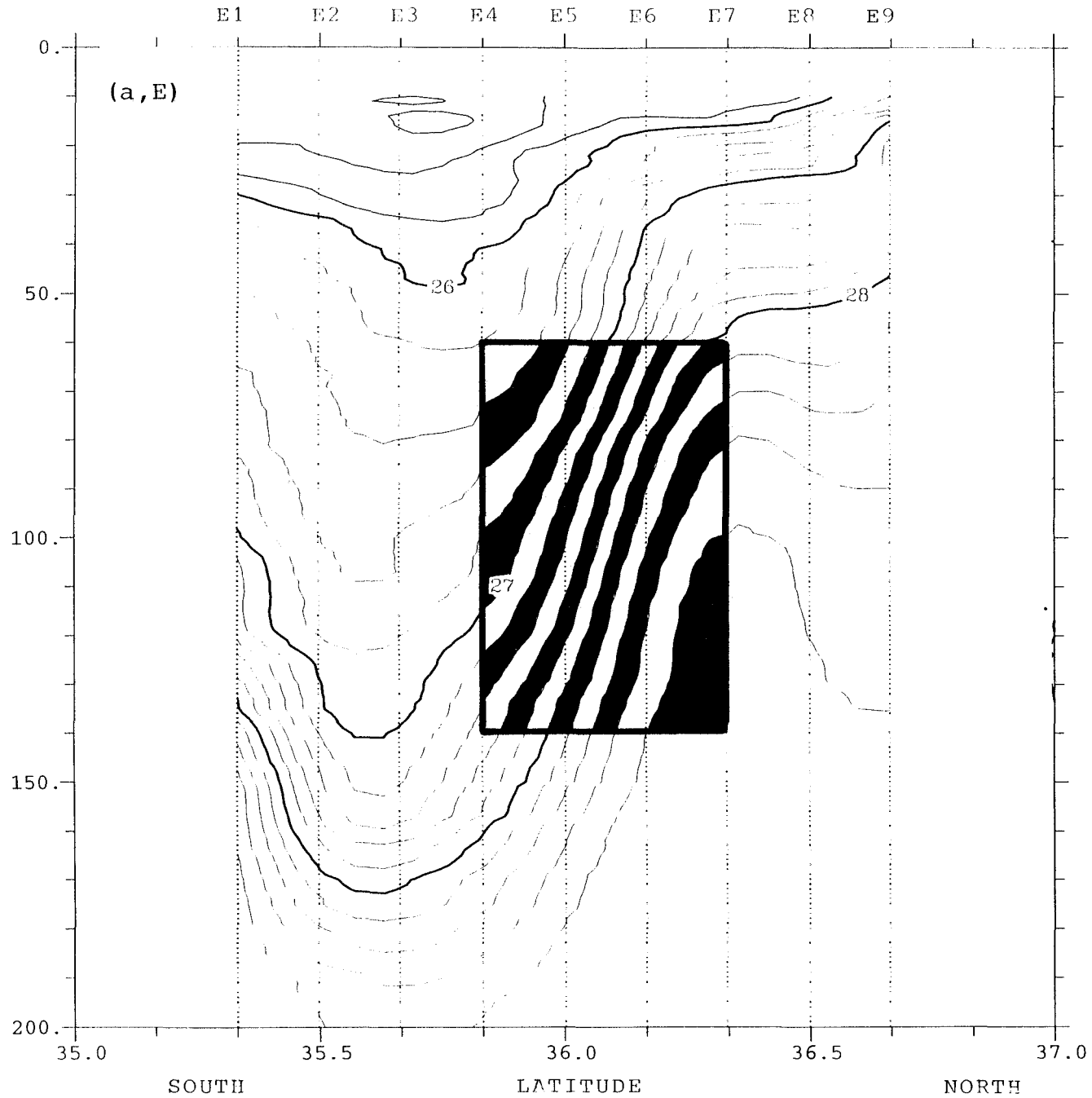
$[(U_z'^2 + V_z'^2) / 10E(6)] \text{ s}^2 \text{ at } 100 \text{ m}$

Figure 19



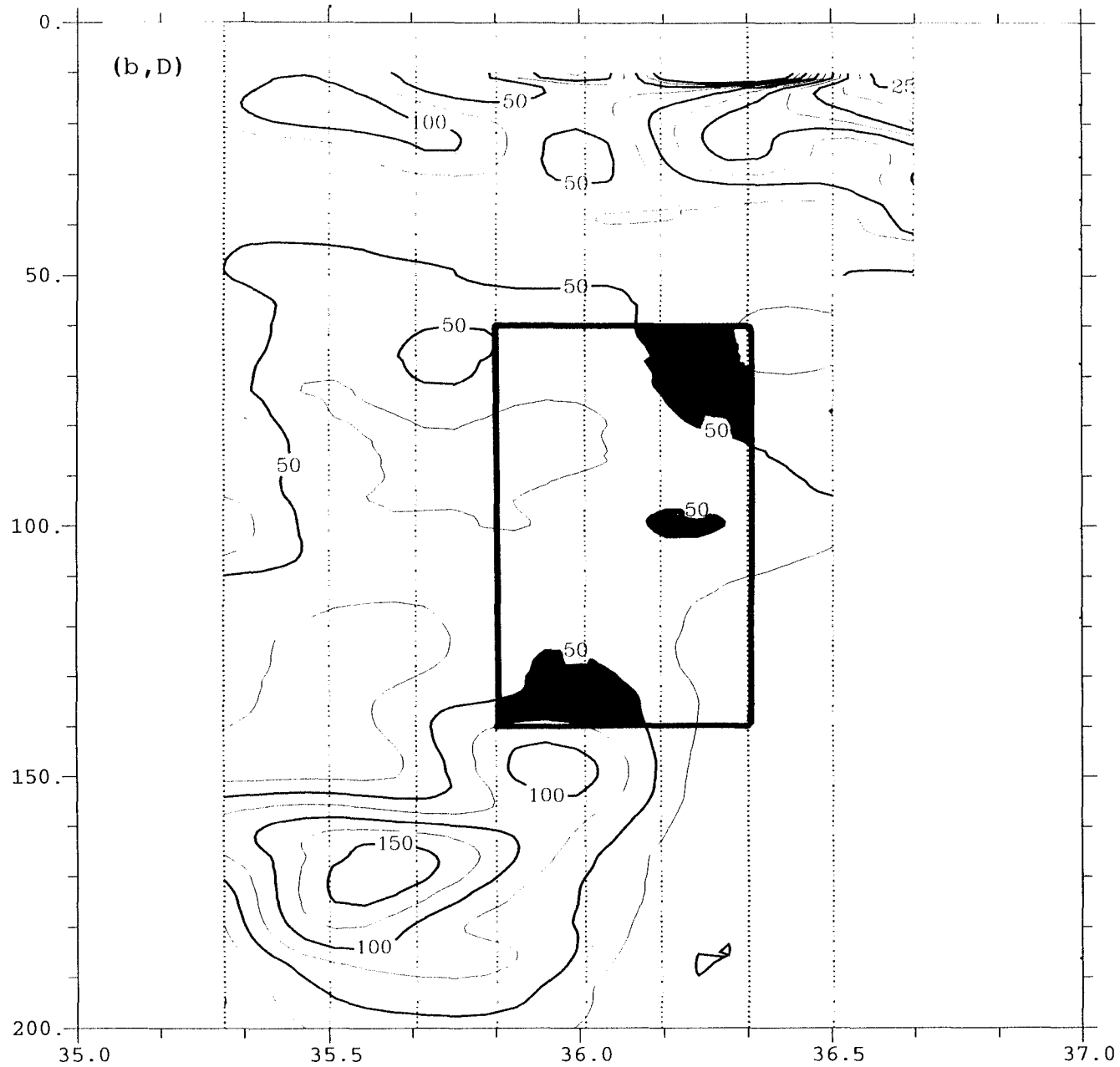
SIGMA-T SECTION D (3D).

Figure 20a(D)



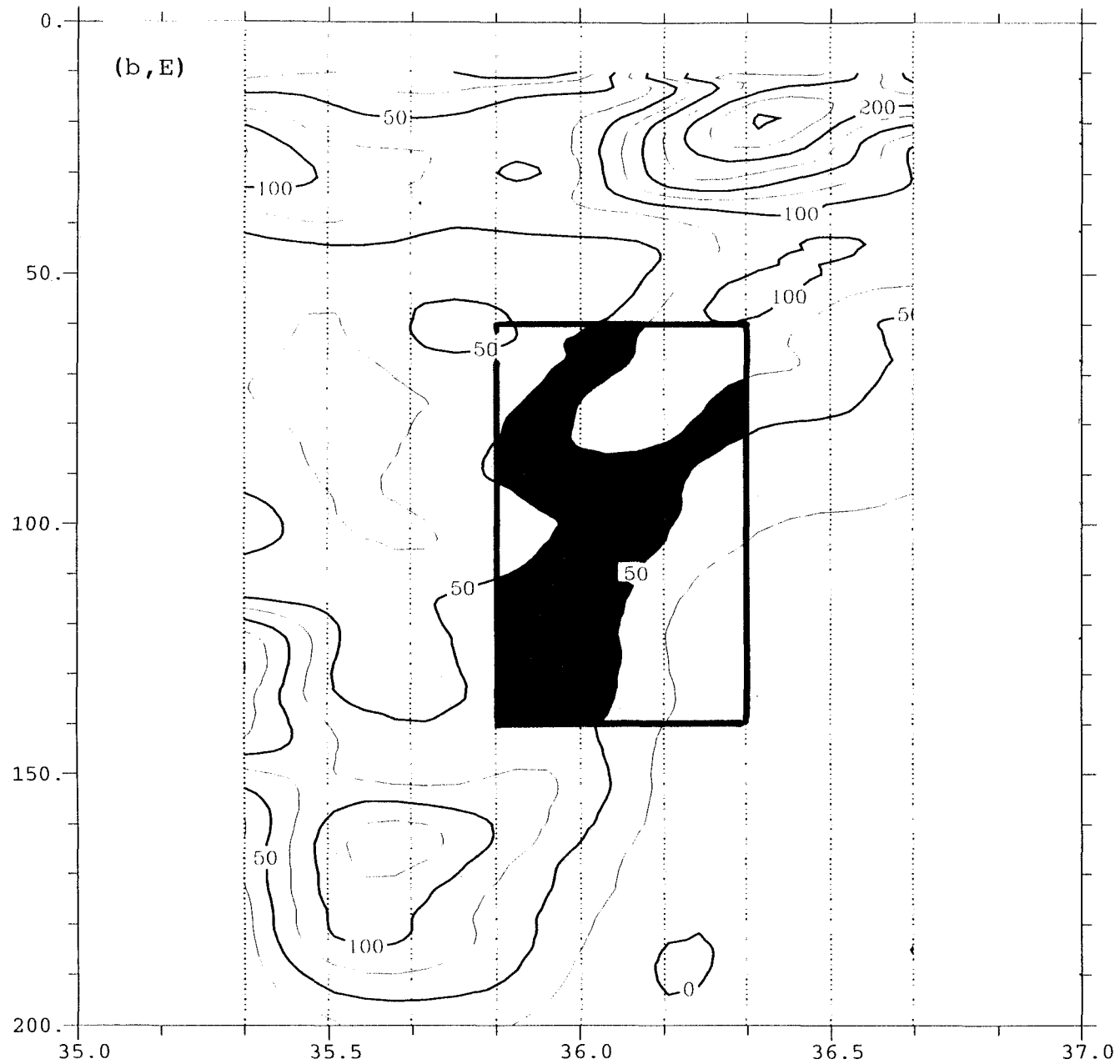
SIGMA-T SECTION E (3D)

Figure 20a(E)



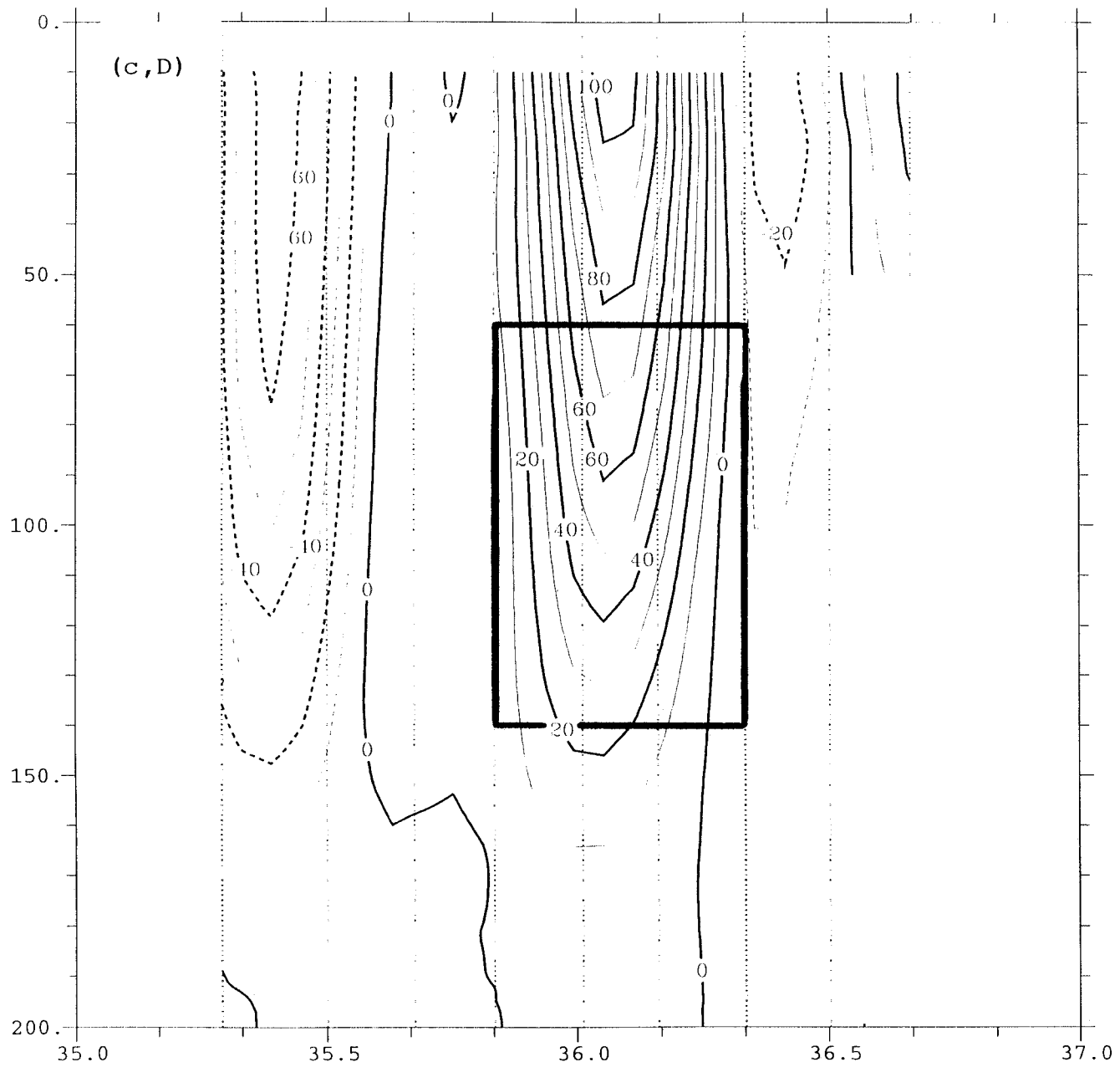
Squared Brunt-Vaisala frequency (cph^2). SECTION D (3D).

Figure 20b(D)



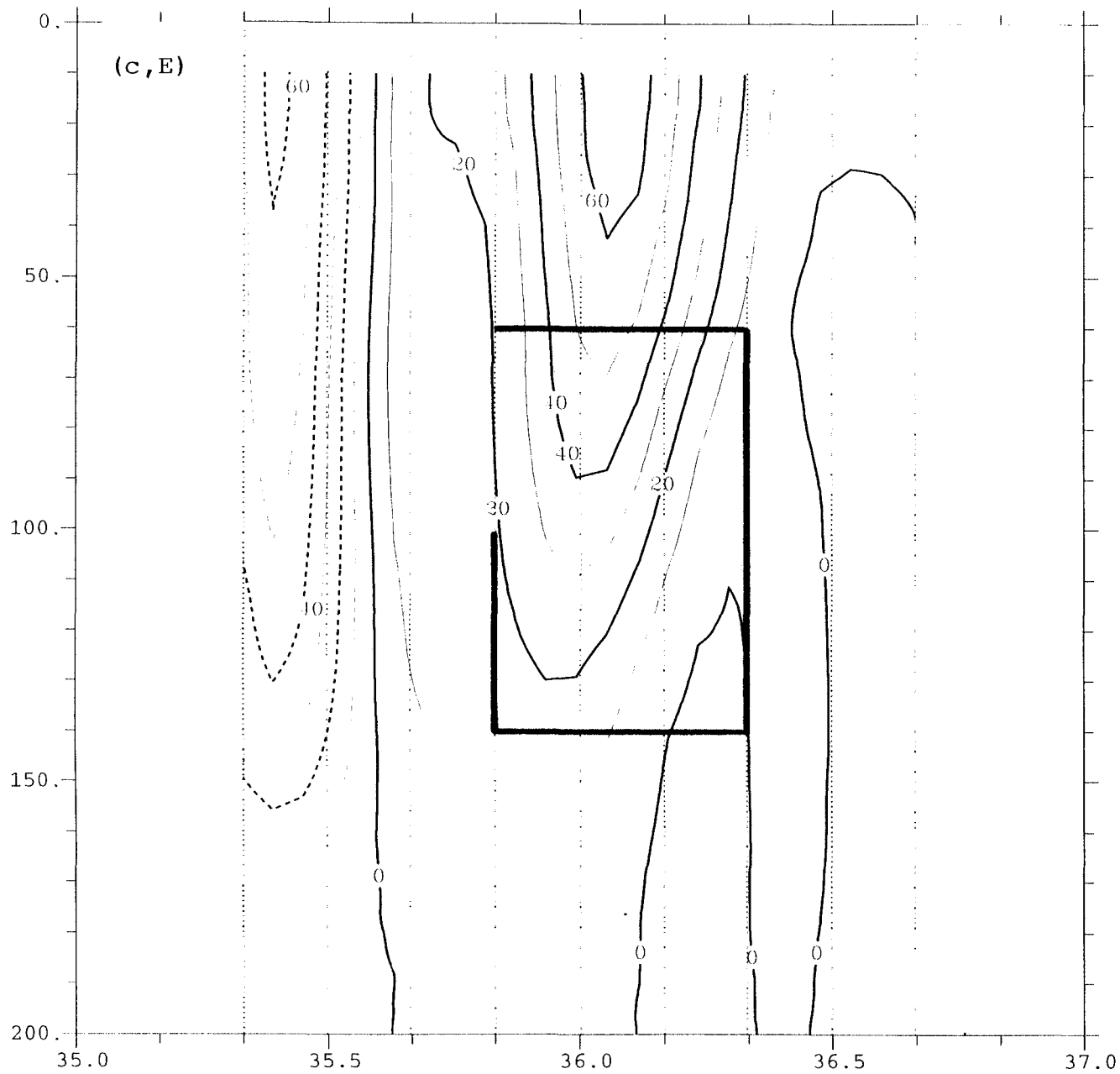
Squared Brunt-Vaisala frequency (cph^2). SECTION E (3D).

Figure 20b(E)



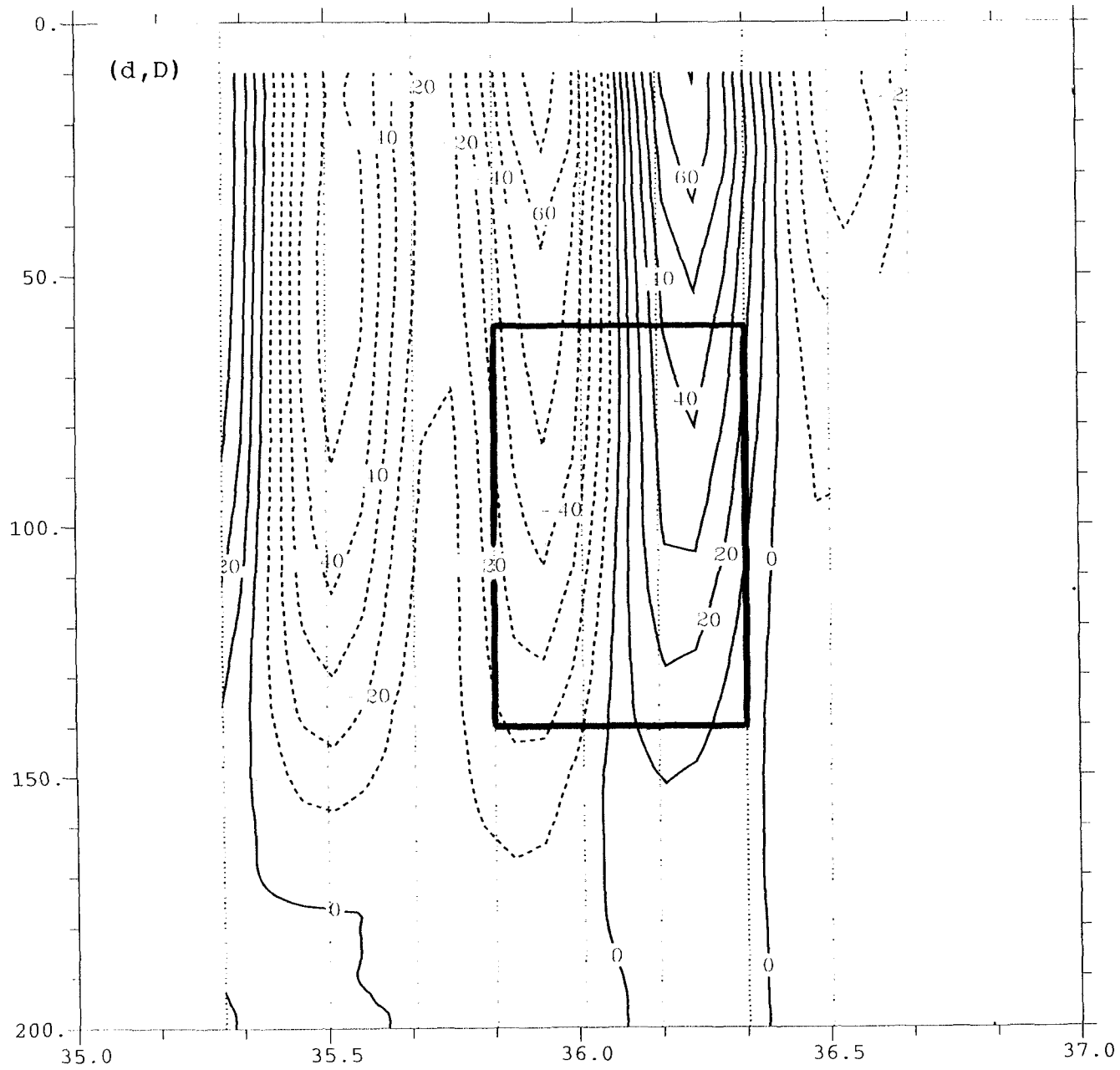
EAST WEST VELOCITY (cm s). SECTION D (3D).

Figure 20c(D)



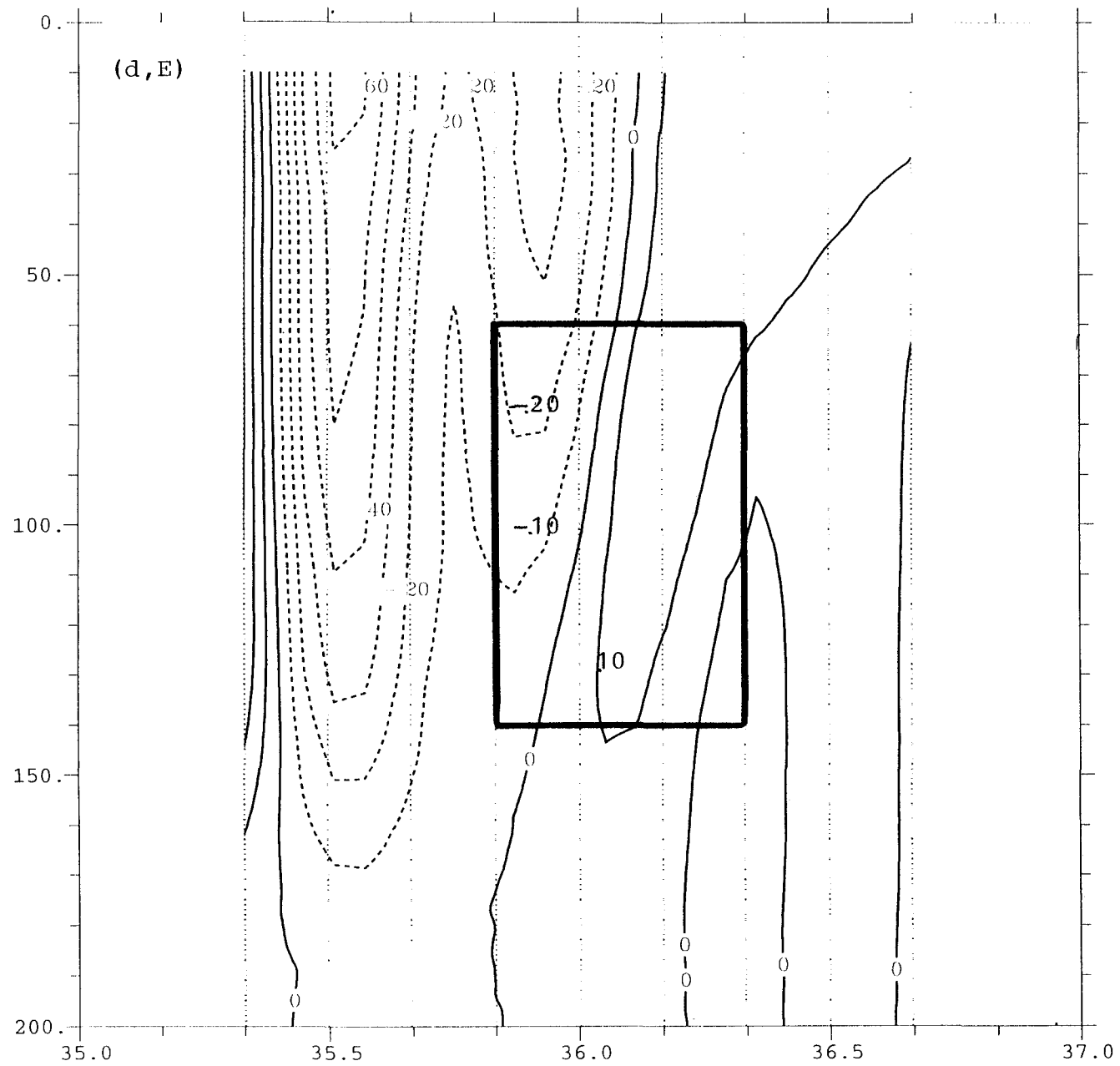
EAST WEST VELOCITY (cm/s) SECTION E (3D)

Figure 20c(E)



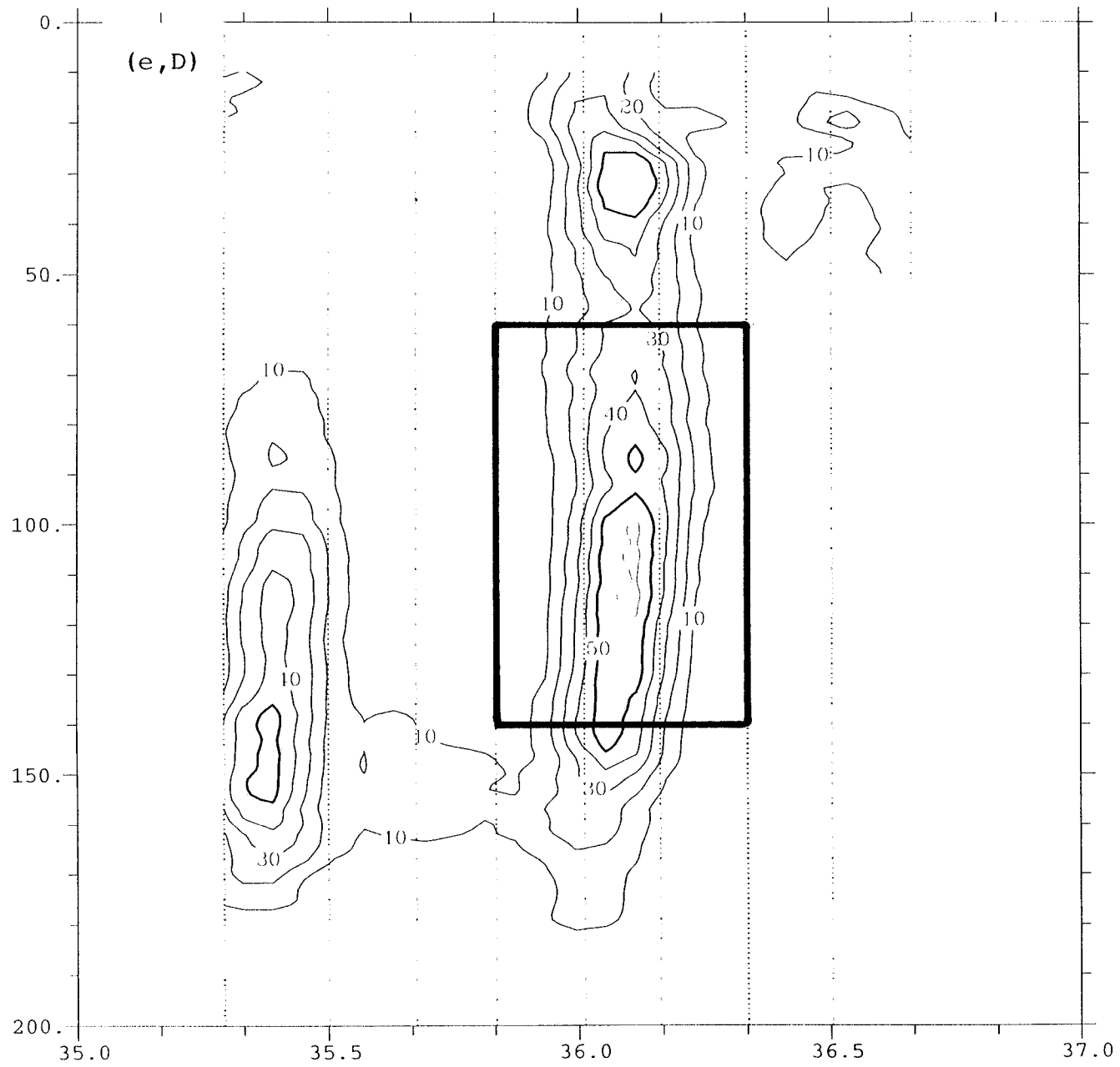
RELATIVE VORTICITY PLANETARY VORTICITY SECTION D (3D)

Figure 20d(D)



RELATIVE VORTICITY PLANETARY VORTICITY SECTION E (3D)

Figure 20d(E)



$\sqrt{U_z'^2 + V_z'^2}$ (10E(6)). SECTION D (3D)

Figure 20e(D)

Figure 20e(E)

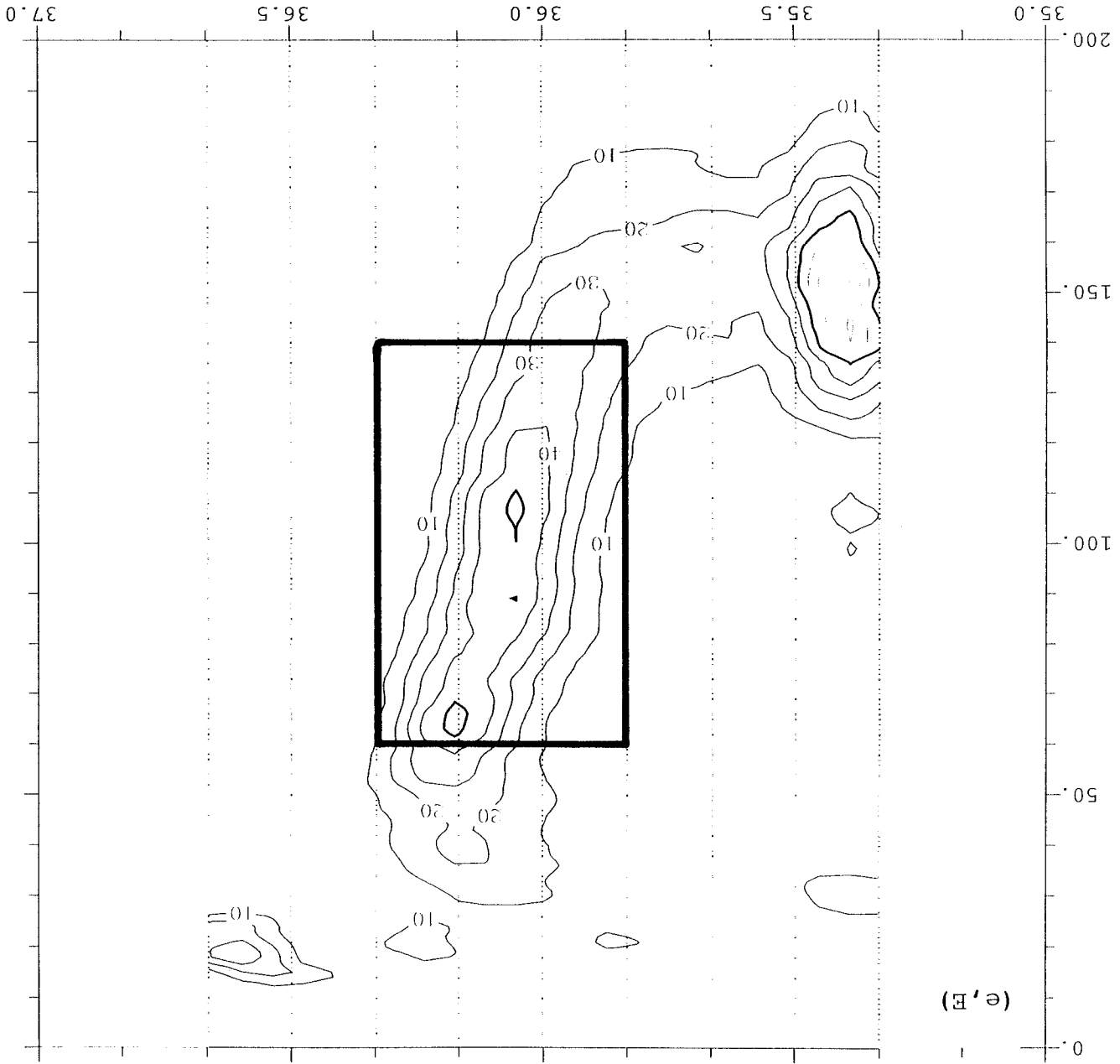
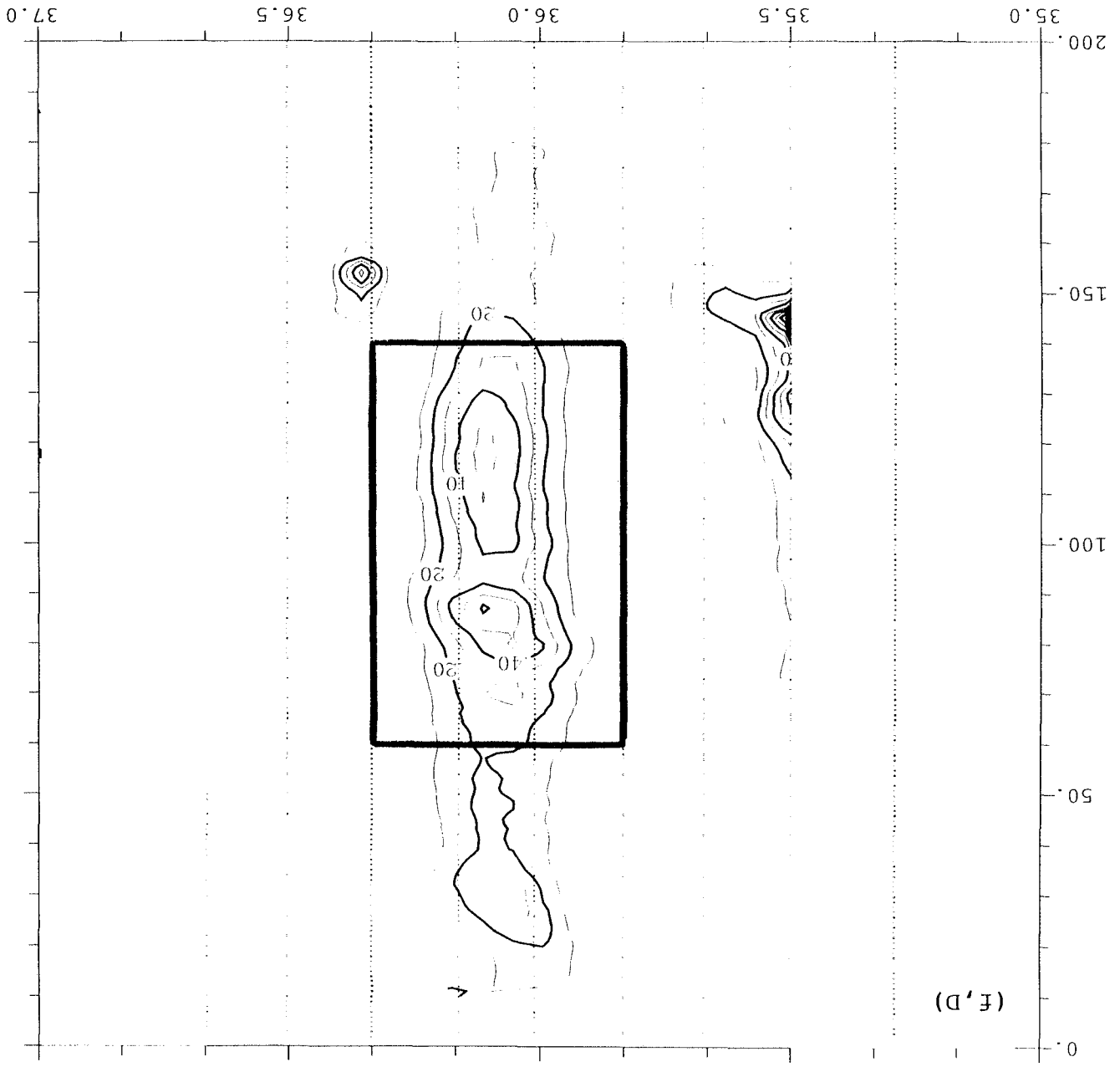


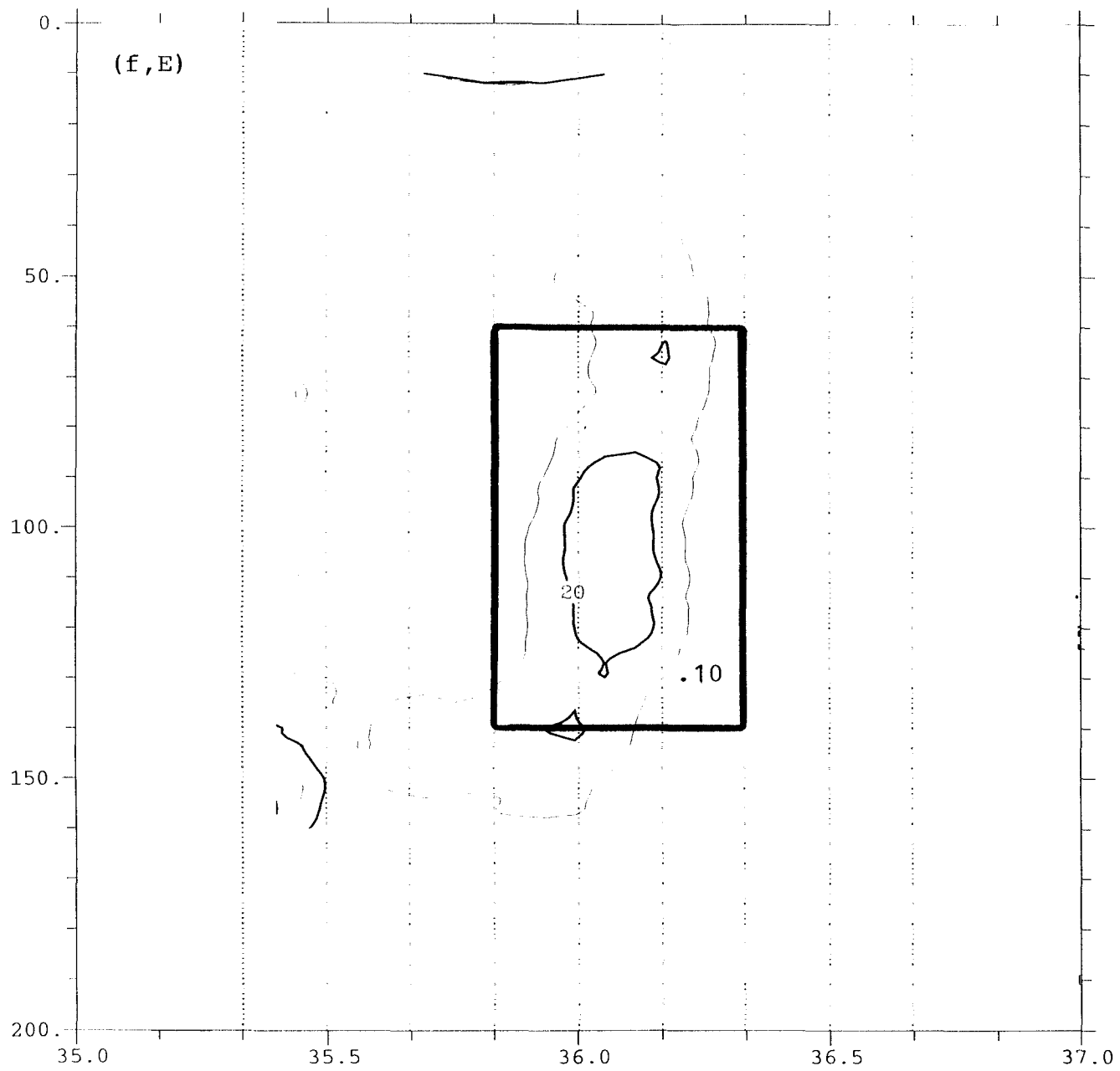
Figure 20e(E) (10E) (6) SECTION E (3D)

(F, D)



[PROFILE NUMBER, SECTION D (3D)]

Figure 20(F,D)



FROUDE NUMBER, SECTION E (3D)

Figure 20f(E)

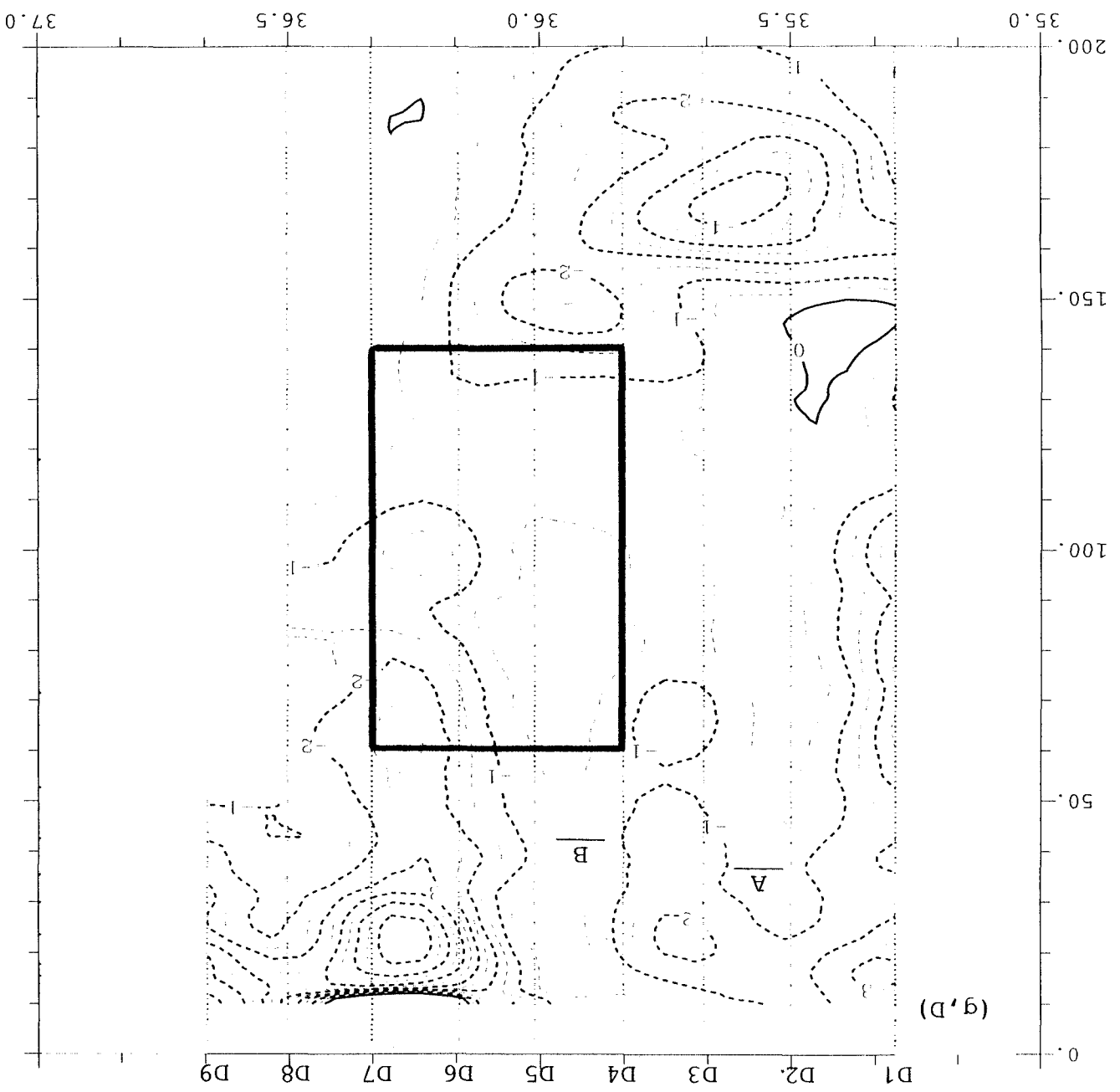
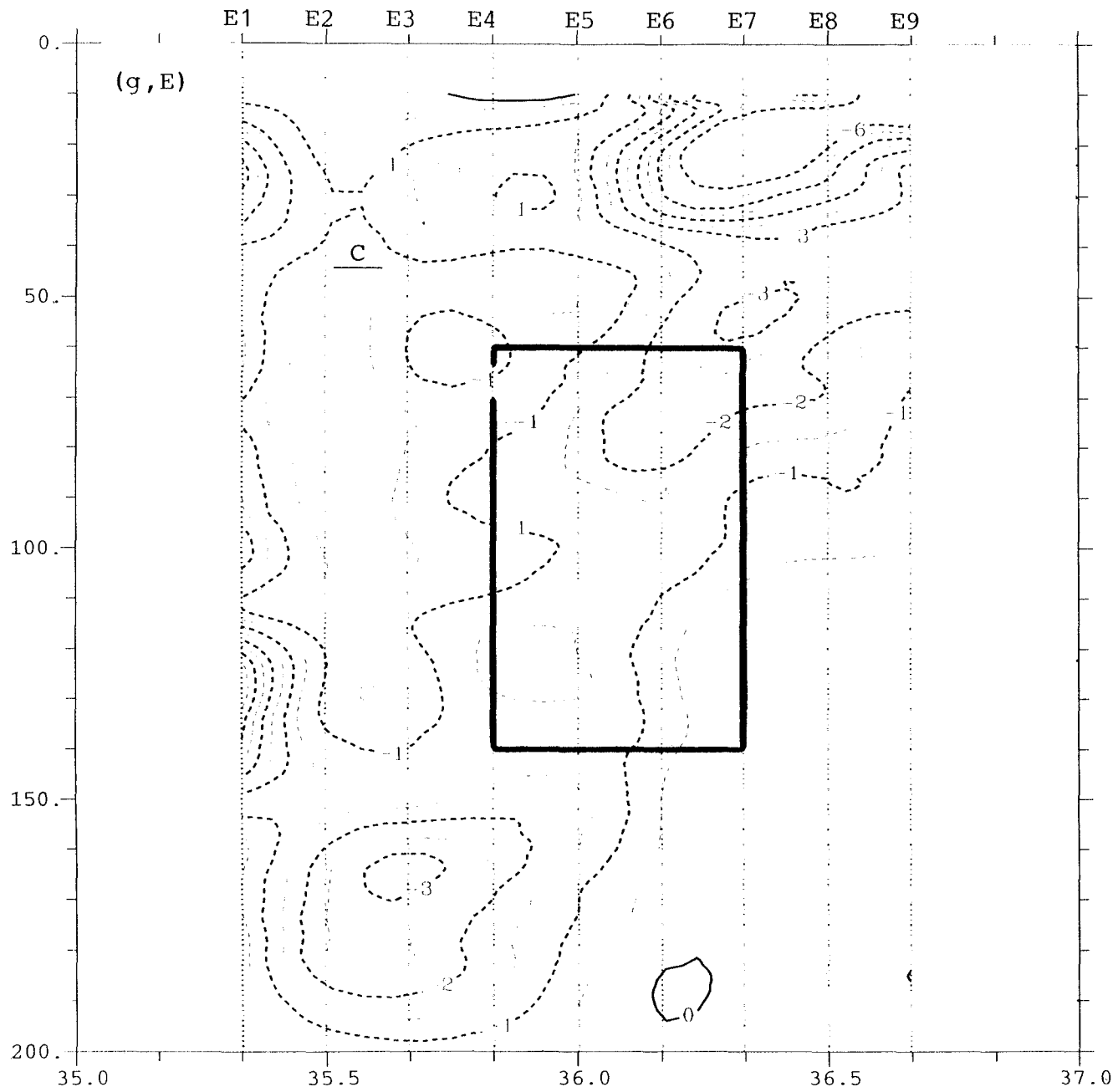
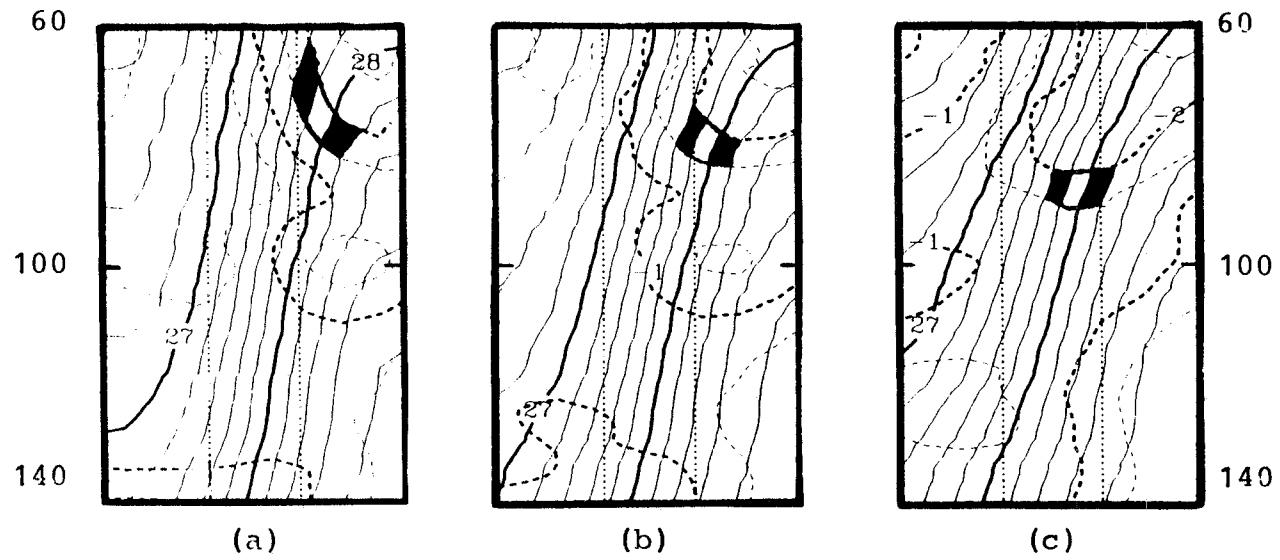


Figure 20g(D)



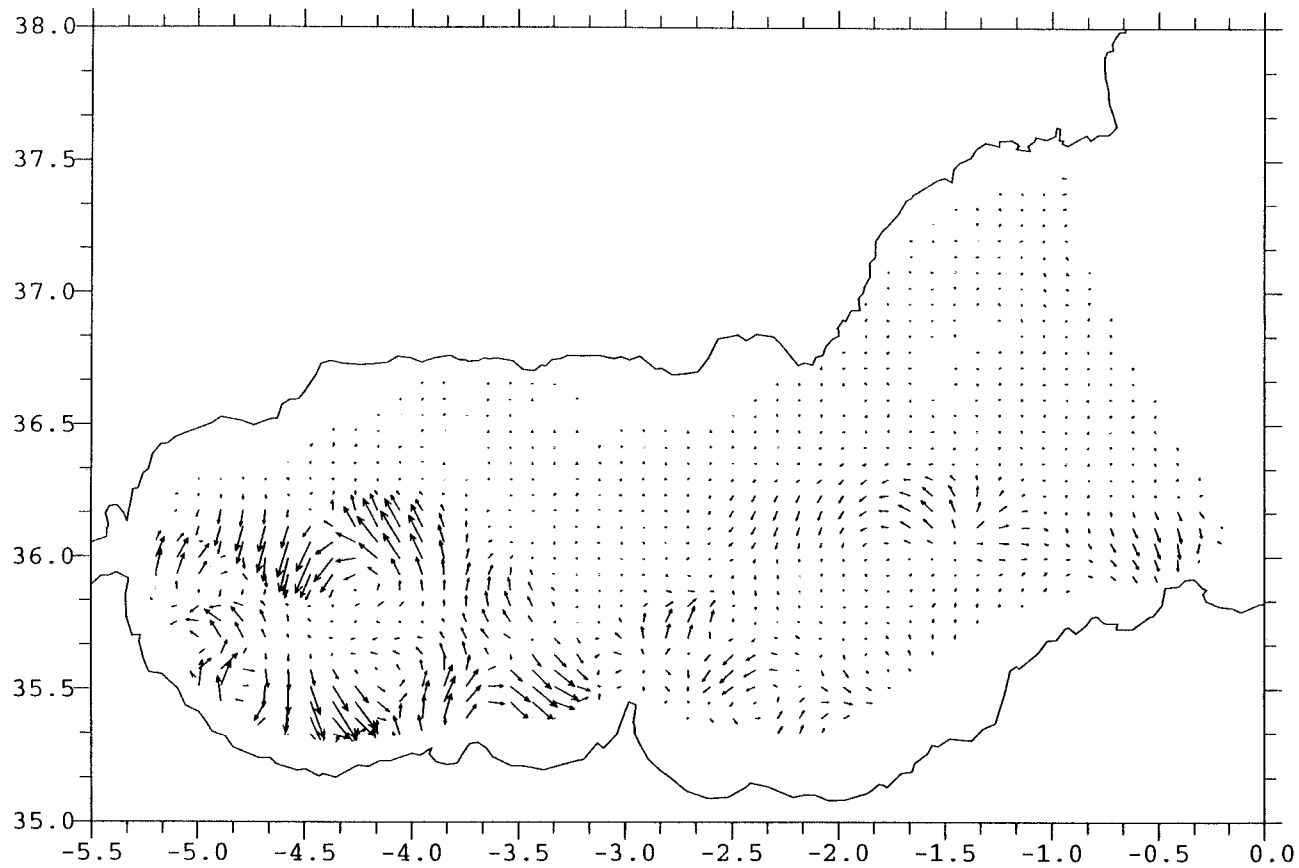
[POTENTIAL VORTICITY (PVU), SECTION E (3D)]

Figure 20g(E)



ABC

Figure 2



VECTOR Q ($10^{(-13)}$ $1/s^{(-3)}$) AT 100 m. REFERENCE LEVEL 200 m.

0.200E+03
 \rightarrow
 MAXIMUM VECTOR

Figure 22

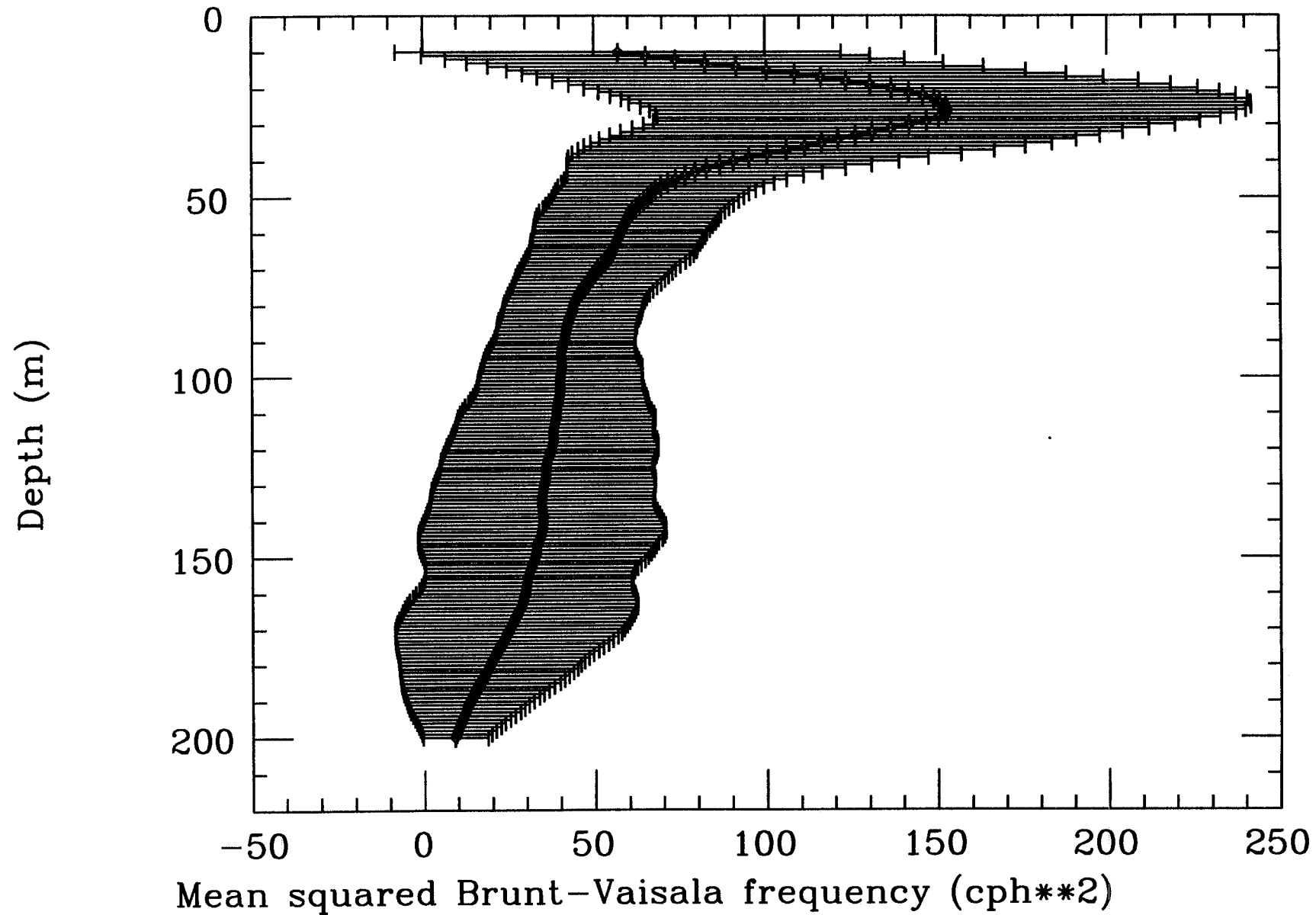
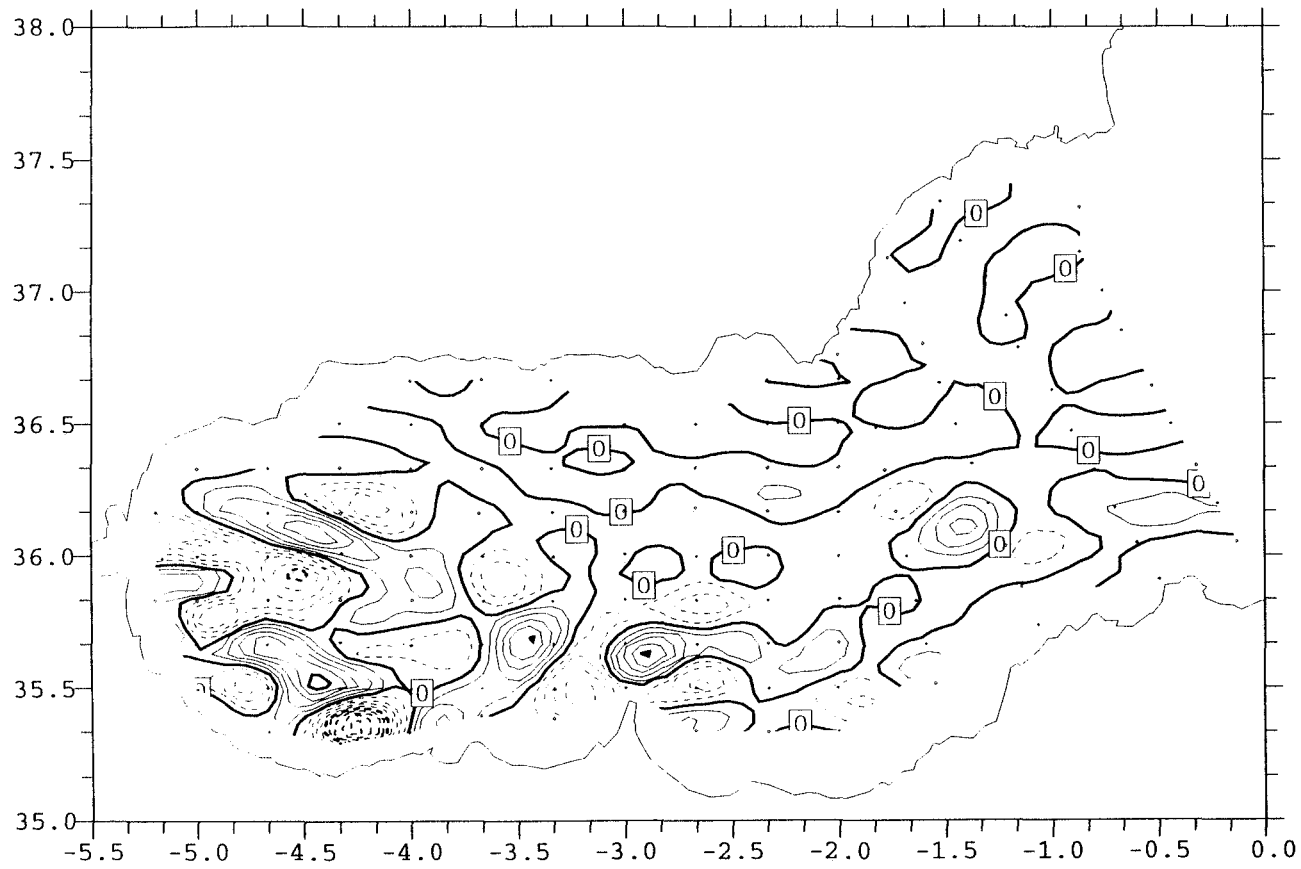
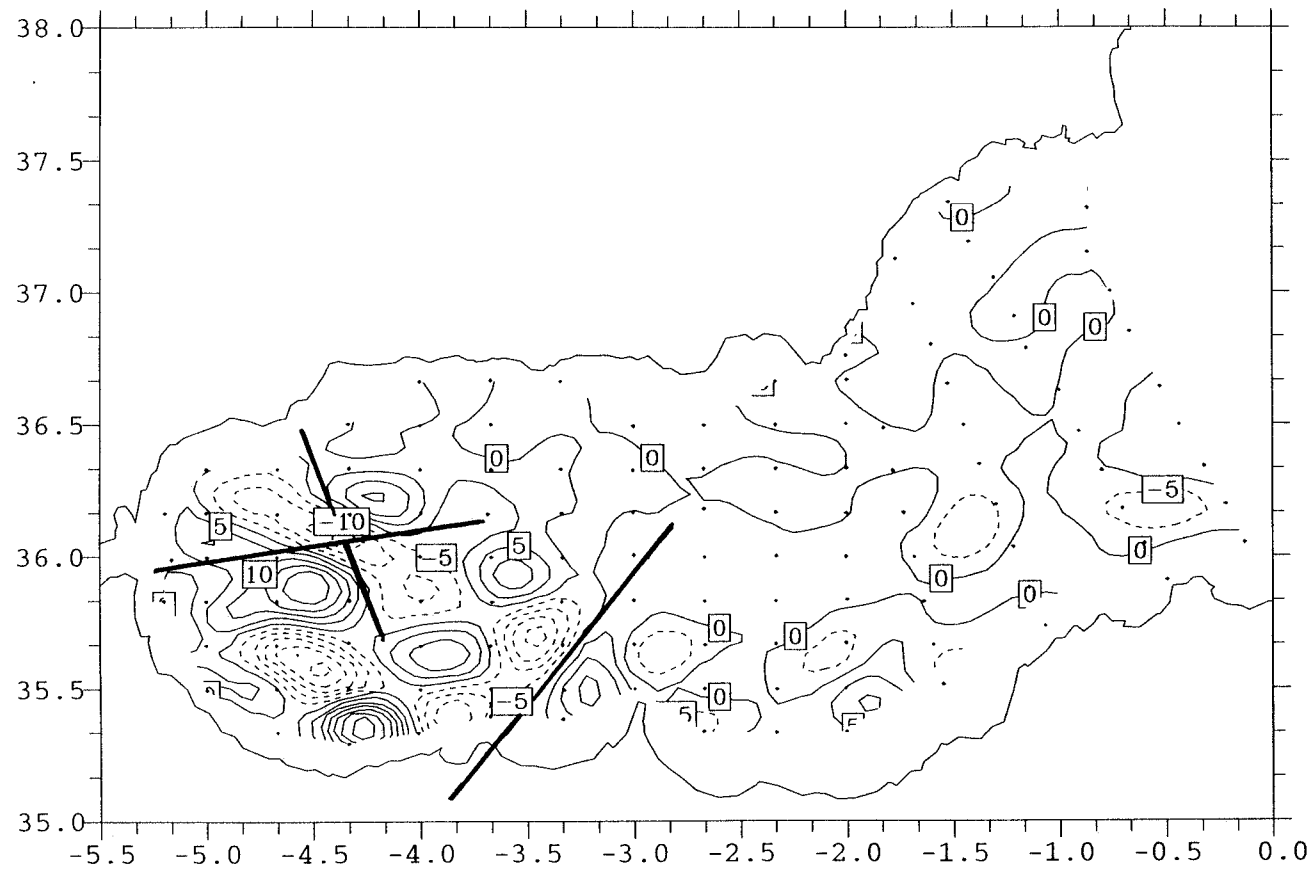


Figure 23



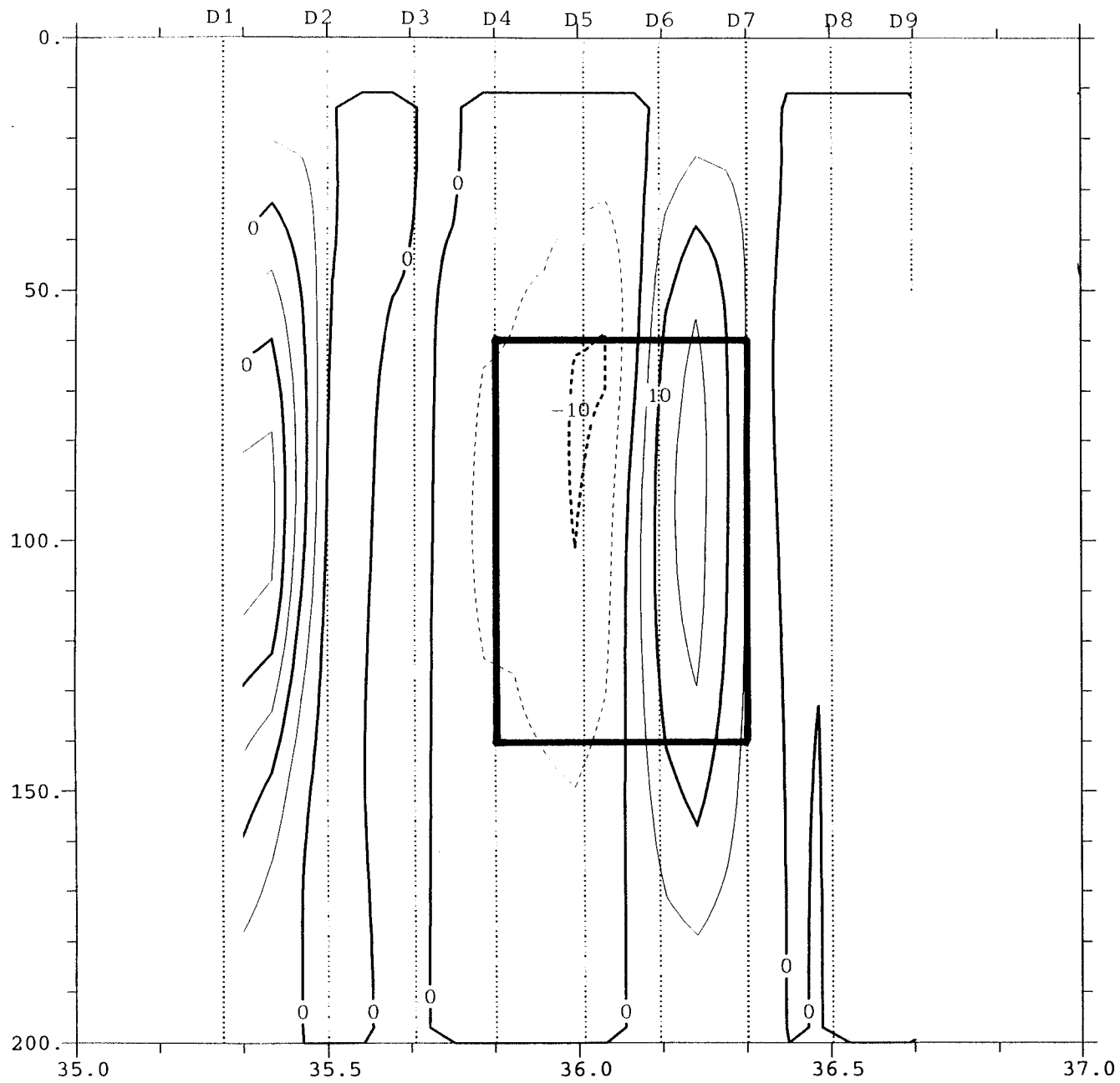
DIVERGENCE OF Q ($10^{(-17)} \text{ 1/(s}^3 \text{ m)}$) AT 100 m. REFERENCE LEVEL 200 m.

Figure 24



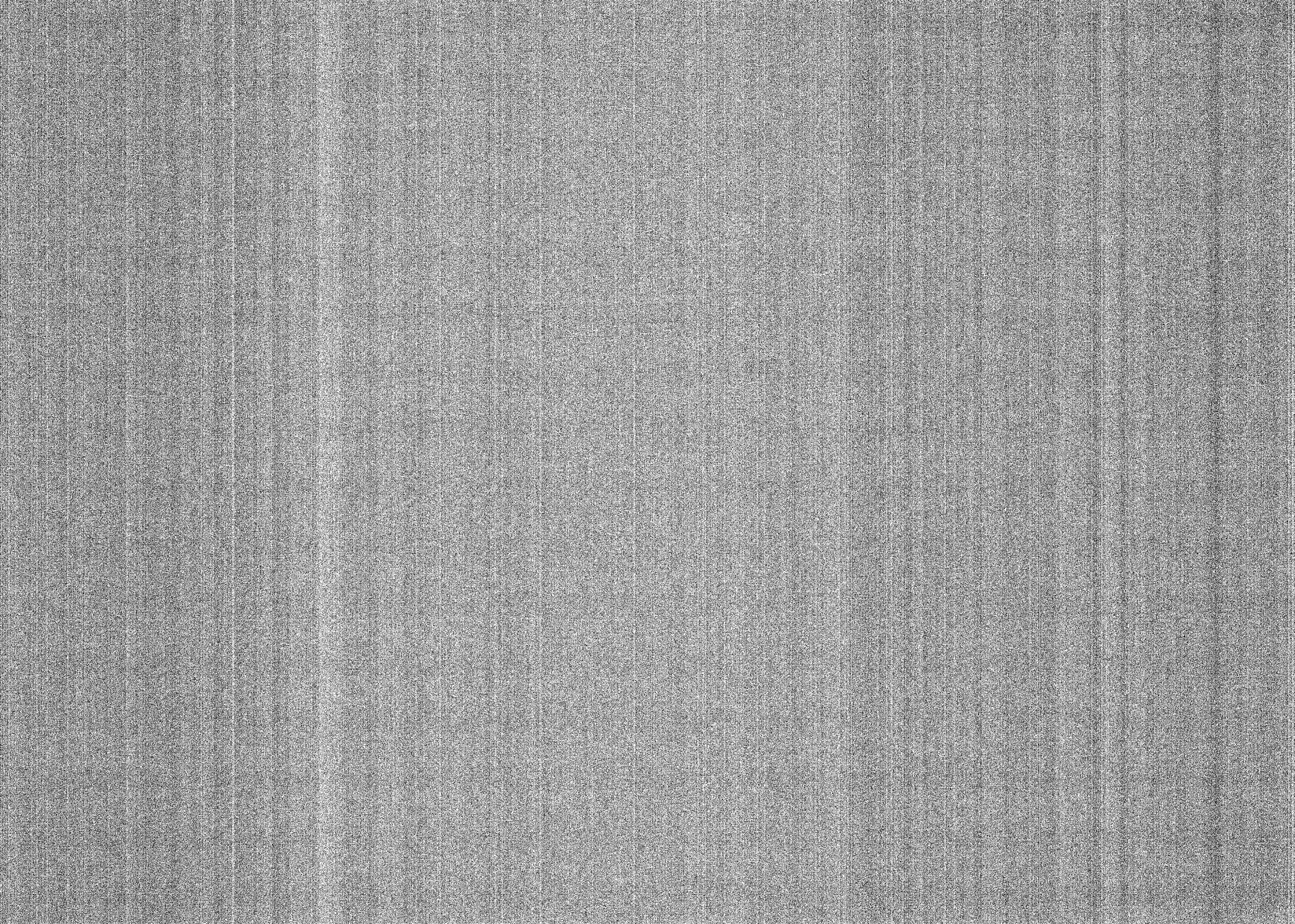
VERTICAL VELOCITY (10^{*-5} m/s) AT 102 m (N2ijk, cohe)

Figure 25



VERTICAL VELOCITY ($10^{**}(-5)$ m/s). SECTION DE. (3D-3Z-N2ijk).

Figure 26



Capítulo 5

Diagnosis of Mesoscale Ageostrophic Motion through Density Dynamical Assimilation: Application to the Alboran Sea

Álvaro Viúdez¹
Robert L. Haney²
Joaquín Tintoré¹

J. Phys. Oceanogr. (Submitted).

¹Departament de Física, Universitat de les Illes Balears, Palma de Mallorca, Spain.

²Department of Meteorology, Naval Postgraduate School, Monterey, CA.

LIST OF FIGURES

1. The Alboran Sea (bottom topography in m). The different vertical CTD sections are referenced. The box represents the model domain.
2. Geostrophic transport function at 10 m without the boundary condition of no normal geostrophic flow ($\Delta = 0.2$ Sv).
3. Quasigeostrophic (ω -equation) vertical velocity distribution w_{qg} at 100 m ($\Delta = 5 \times 10^{-5}$ m s⁻¹).
4. (a) Measured vertical density distribution along the northern coastal boundary and mean vertical profile which imposed the no normal geostrophic flow condition, (b) the same as (a), but for the southern coastal boundary ($\Delta = 0.2 \sigma_t$, Y-axis represents relative distance in km).
5. Geostrophic transport function at 10 m computed with the boundary condition of no normal geostrophic flow ($\Delta = 0.2$ Sv). The small rectangle represent the Northern Western Alboran Gyre (NWAG) area.
6. Isosurface of 28.0 σ corresponding to the initial density field assimilated by the PE model.
7. Absolute vertical velocity averaged over the NWAG volume, $\langle W \rangle$, as function of the integration time t_n .
8. Advection of water parcels at 100 m in the NWAG area (located at $t = 0$ on a squared black and white grid) after (a) 6 and (b) 24 hours of forward integration. The water advection is less than one distance between consecutive grid points in the first 6 h, and as a result forward and backward (not shown) integrations produce very similar locations of black and white water parcels. The large advection after 24 h produce significant different patterns for the forward and backward (not shown) integrations.
9. Initial horizontal velocity vectors $\mathbf{v}(t = 0)$, and 24-hour hodographs of the horizontal velocity deviation from the initial state, $\mathbf{v}(t_n) - \mathbf{v}(t = 0)$, at each grid point at 100 m in the NWAG area for (a) the forward, (b) the backward and (c) the mean between the forward and backward integrations. The hodographs at each time-step were plotted as points, but the density of points due to the small time interval (7.5 minutes) makes the hodographs appear as

continuous lines. Note that the two scales (one for the initial vector and another for the hodographs) differ by one order of magnitude, and that each hodograph begins from a zero value (*i.e.* from each grid point location).

10. Time series (from 0 to 24 hours) of vertical velocity at each grid point at 100 m in the NWAG area for (a) the forward, (b) the backward and (c) the mean between the forward and backward integrations. The distance between consecutive grid points in the Y-axis is equivalent to $100 \times 10^{-5} \text{ m s}^{-1}$. Labels S and A represent areas of symmetric and antisymmetric (in relation to the vertical velocity) grid points. The vertical velocity at each time-step was plotted as points, but the density of points due to the small time interval (7.5 minutes) makes the points appear as continuous lines.
11. The Lynch and Huang (1992) filter (*c*) and the weight function used here (*h*) to compute the final state from the model output.
12. The vertical velocity distribution at 100 m computed as the mean $\hat{w}(t_M) \equiv \frac{1}{2}[w(-t_M) + w(+t_M)]$ between the vertical velocity field at $\pm t_M = \pm 6 \text{ h}$ of forward/backward integrations $\Delta = 5 \times 10^{-5} \text{ m s}^{-1}$.
13. Weighted vertical velocity distribution $\tilde{w} \equiv \sum_{n=-2M}^{2M} w_n h_n$ at 100 m ($\Delta = 5 \times 10^{-5} \text{ m s}^{-1}$).
14. Streamlines of the 3D current in the wave-like jet: (a) top view, (b) western view, and (c) southern view. The “initial” vertical separation [(on the right side of the box] is one grid point (4 m). Vertical displacements of $\sim 20 \text{ m}$ occur along the jet in the trough between the WAG and EAG.

ALBORAN SEA

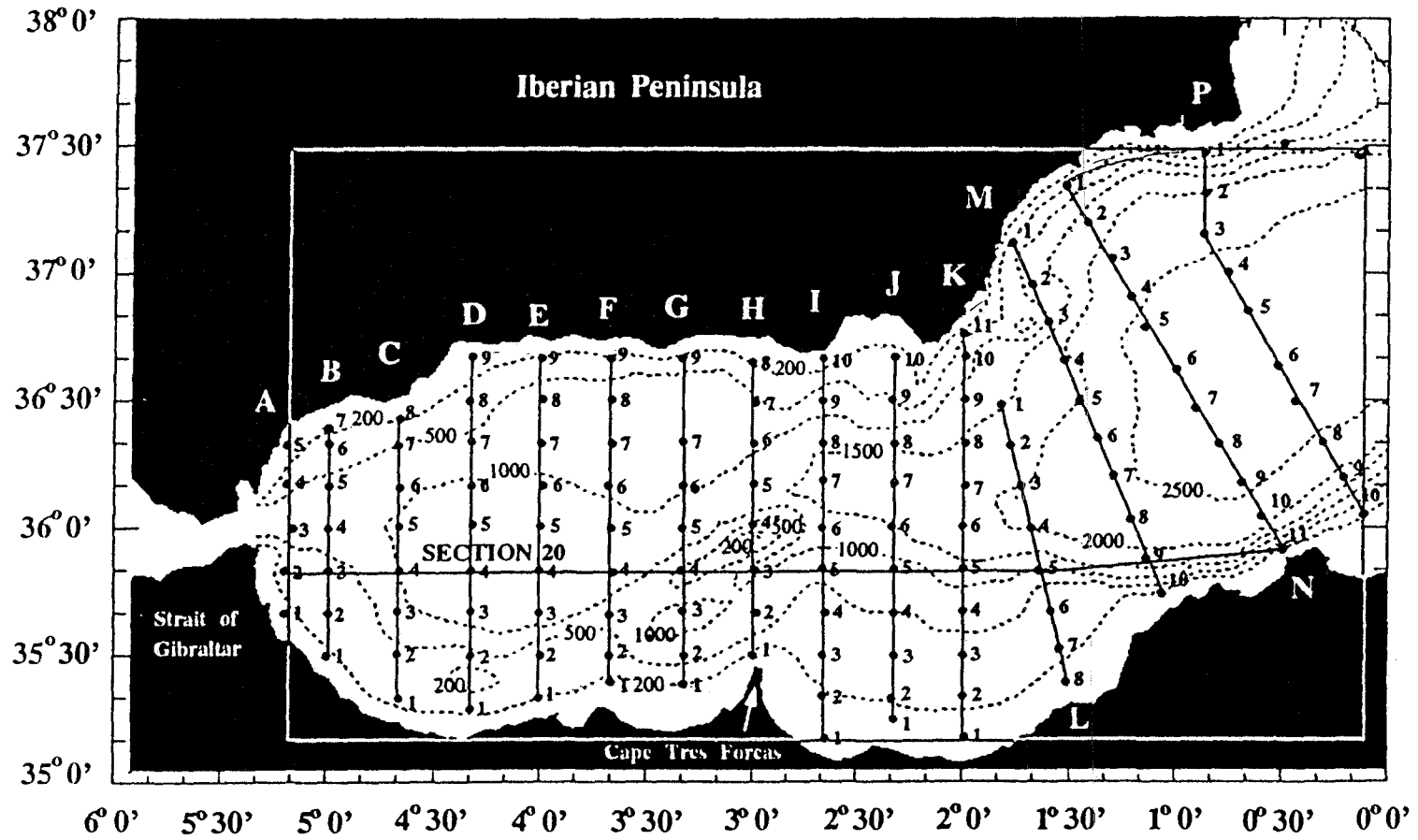
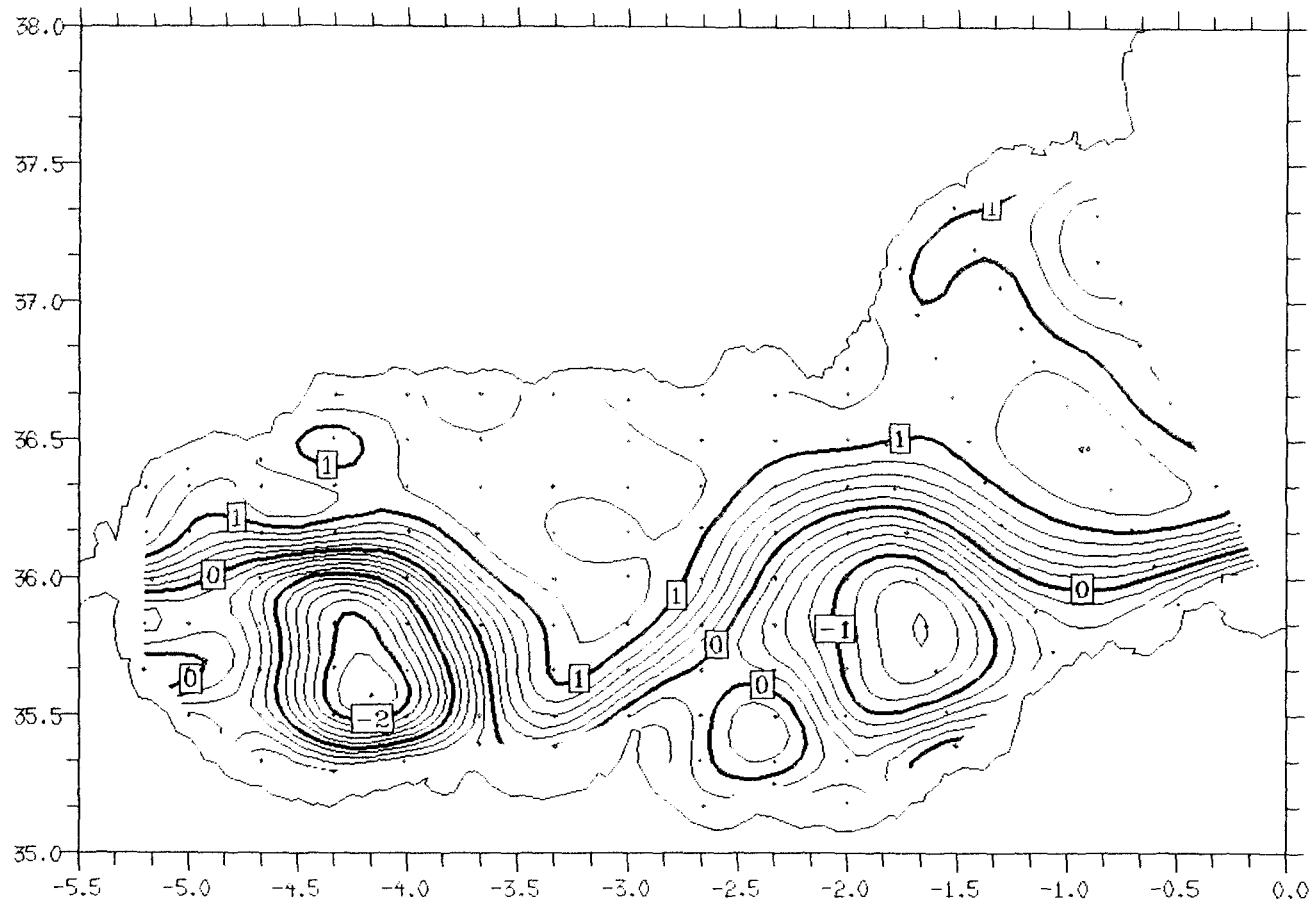


Figure 1



GESTROPHIC TRANSPORT FUNCTION at 010 m (Sv) (reference level 200 m).

Figure 2

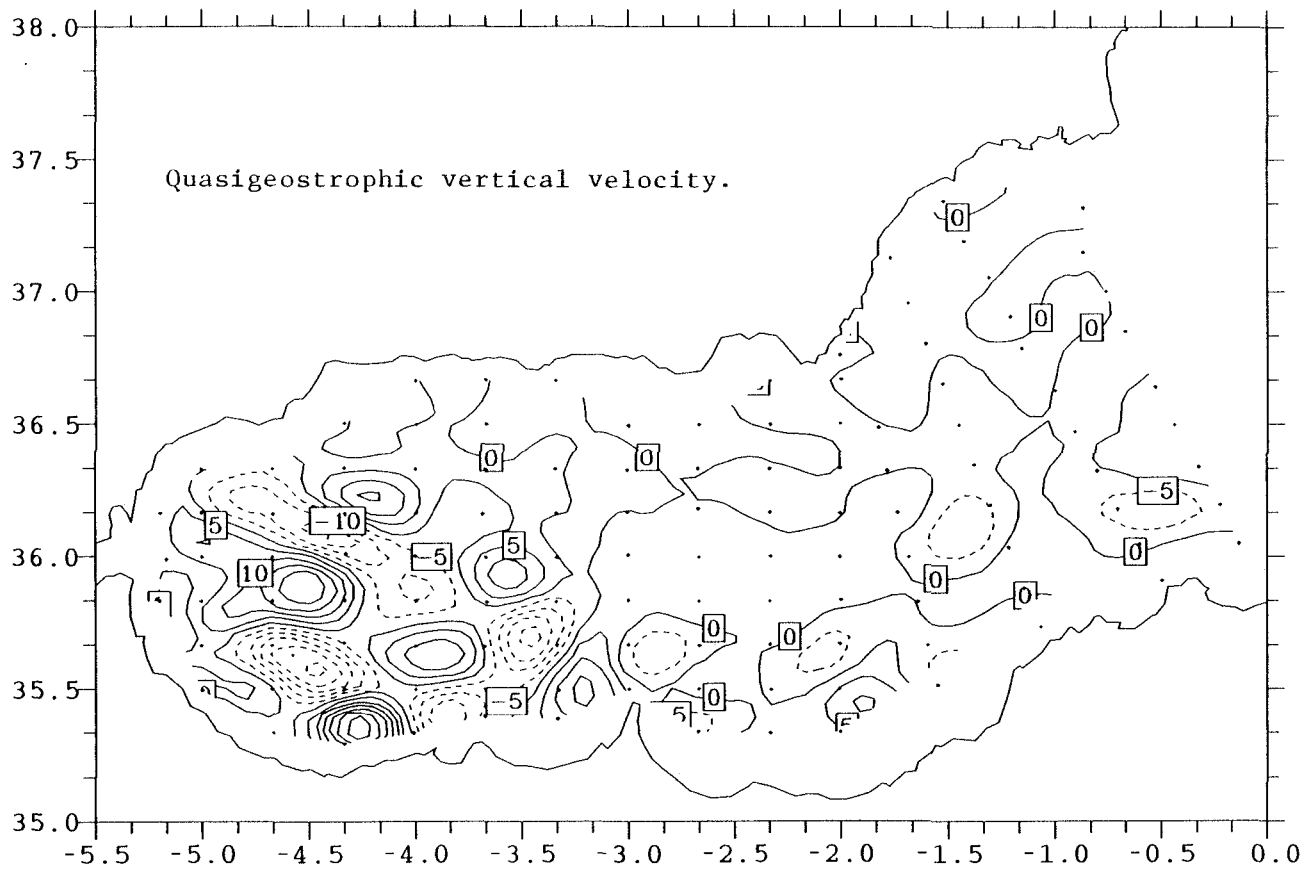


Figure 3

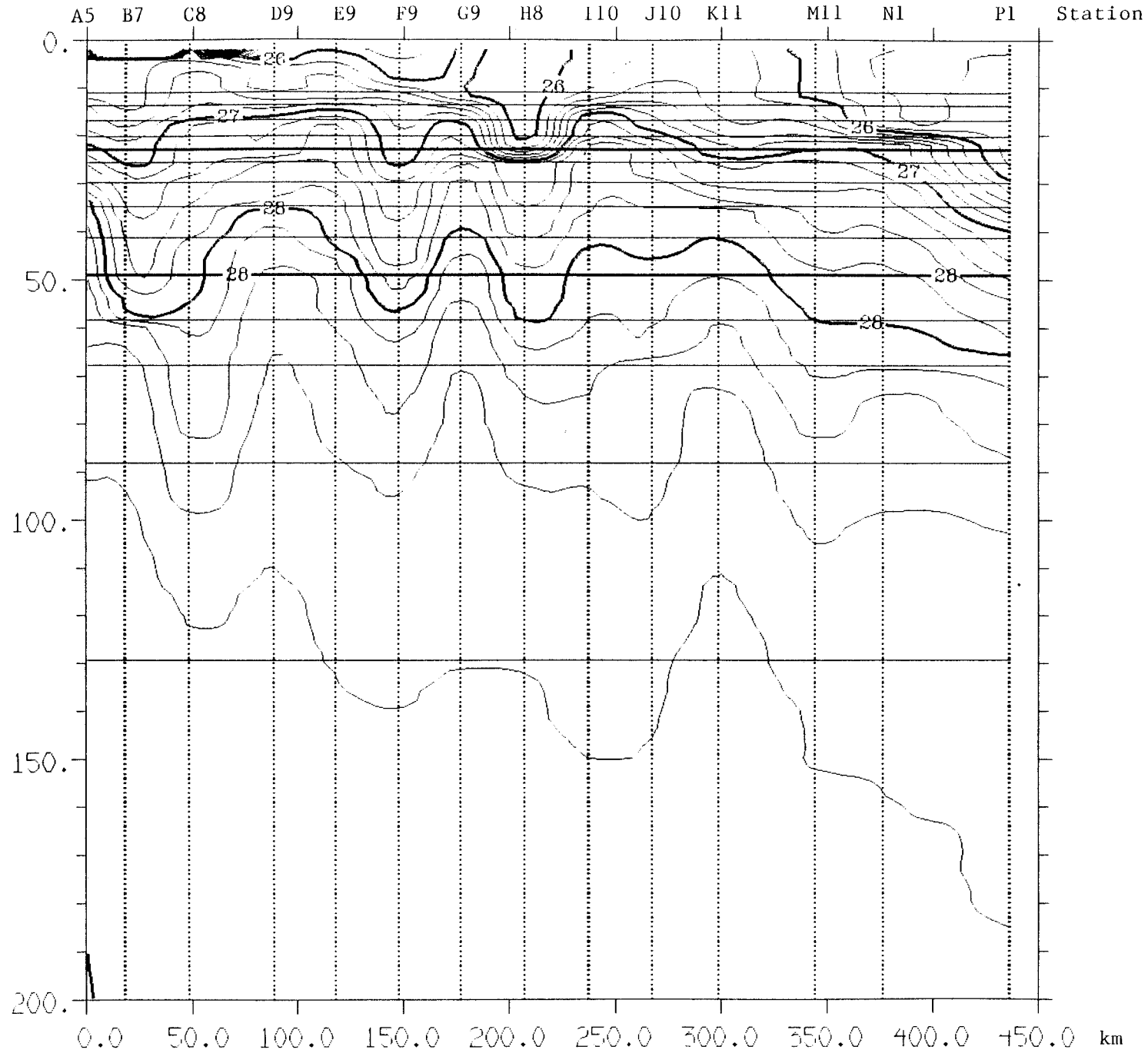


Figure 4a

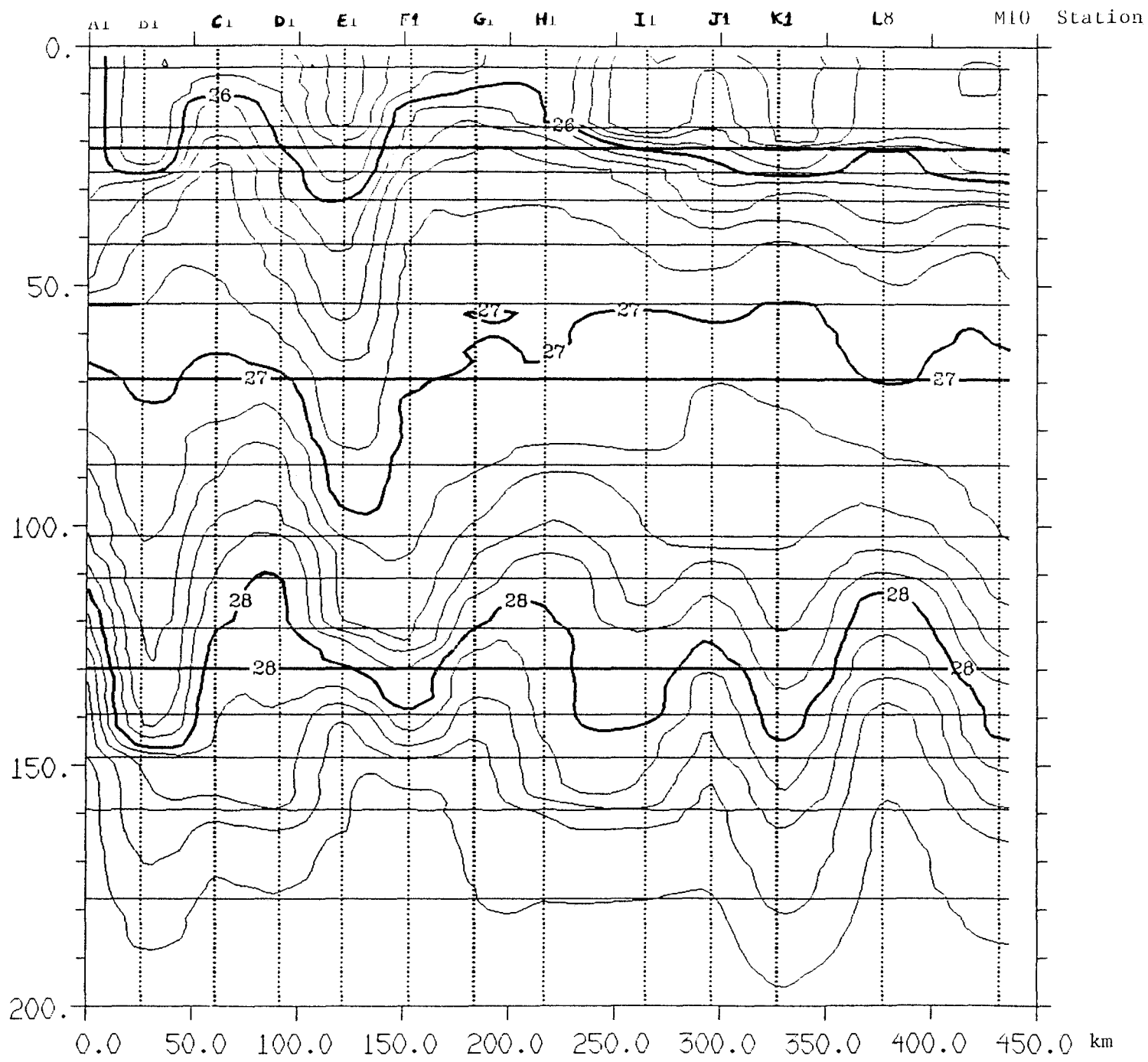
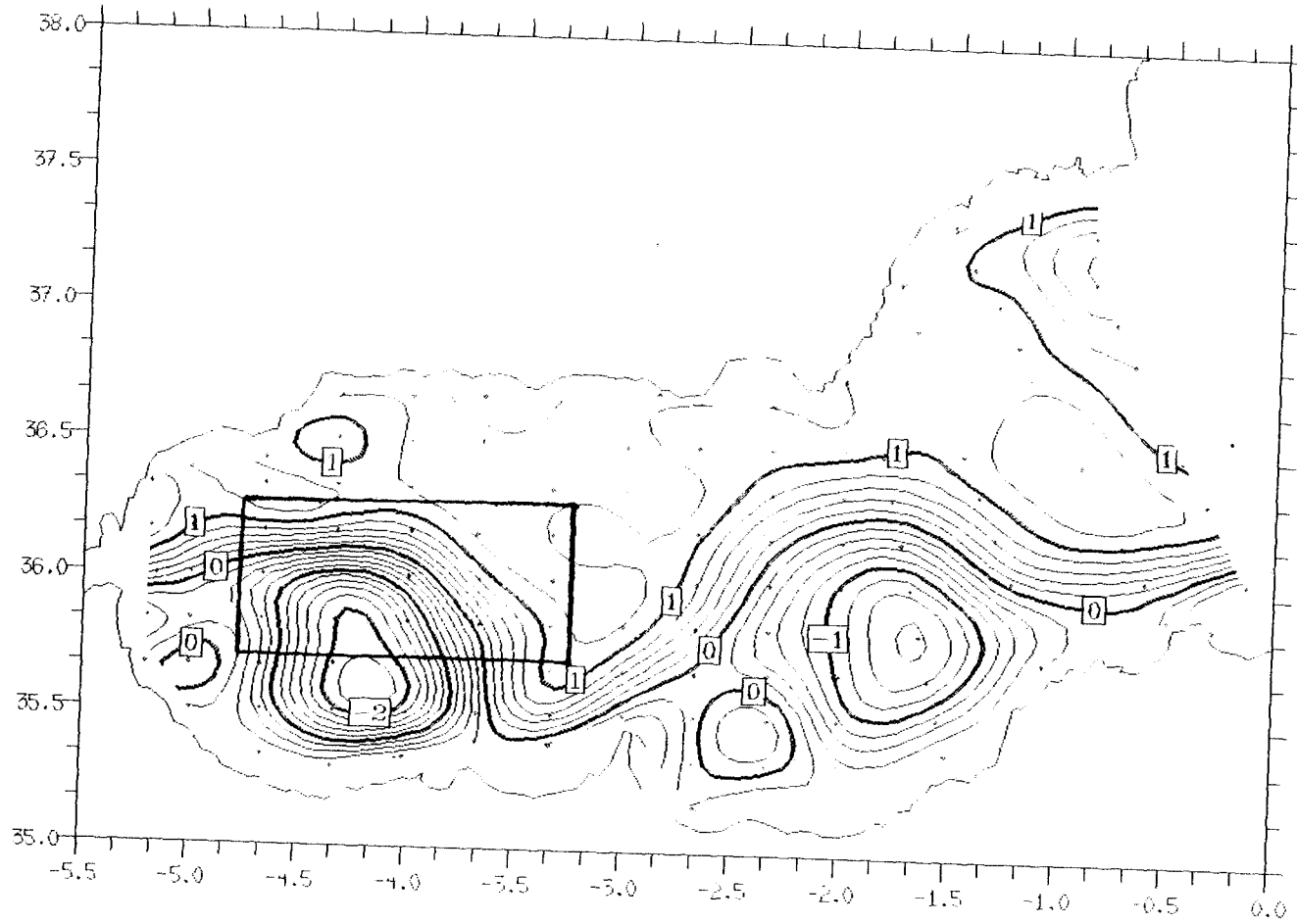
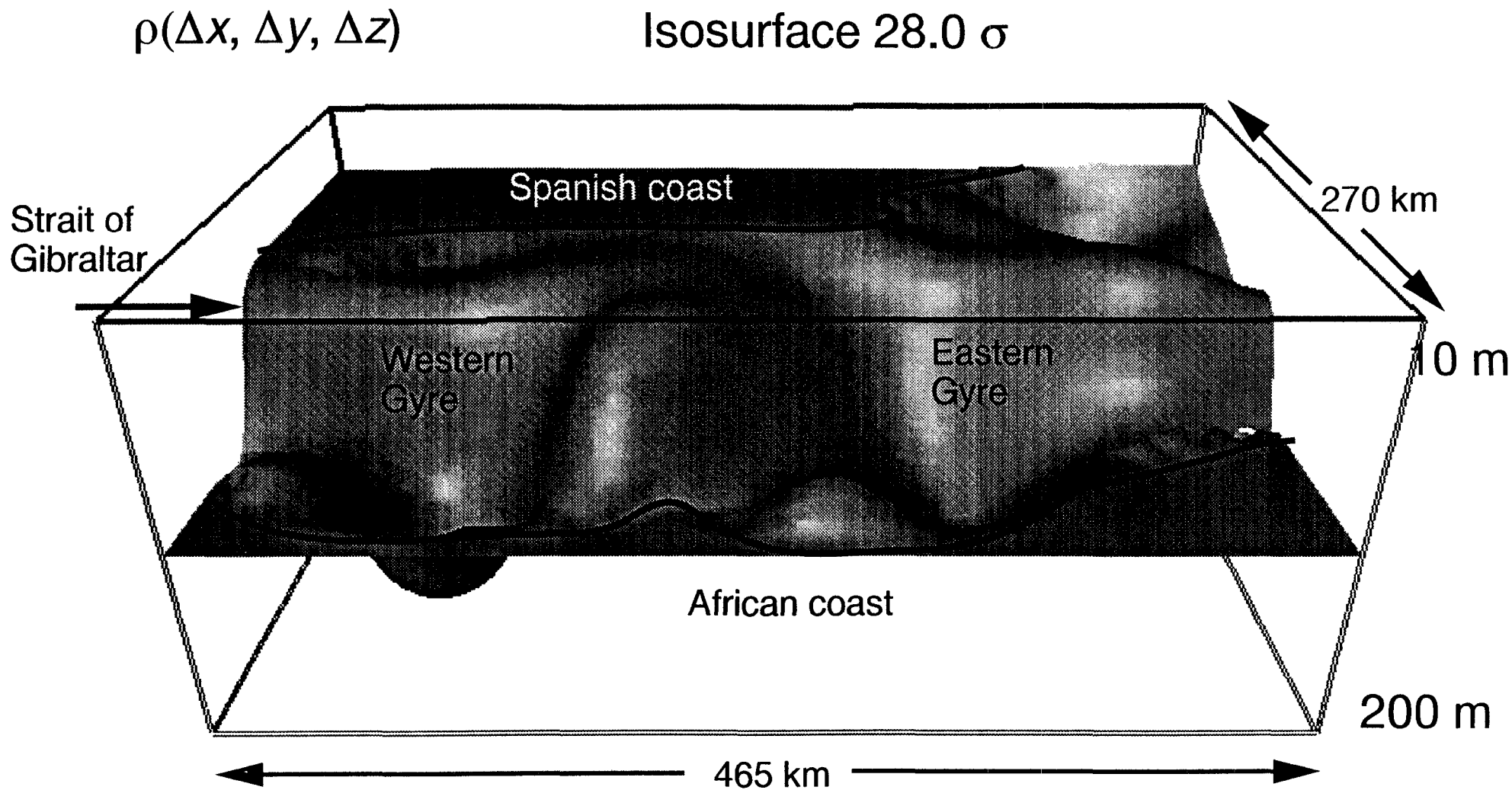


Figure 4b



GEOSTROPHIC TRANSPORT FUNCTION at 010 m (Sv) (reference level 200 m)

Figure 5



$(\Delta x, \Delta y, \Delta z) = (9.3 \text{ km}, 6.7 \text{ km}, 4 \text{ m})$
 matrix dimensions = (50, 40, 48)

Figure 6

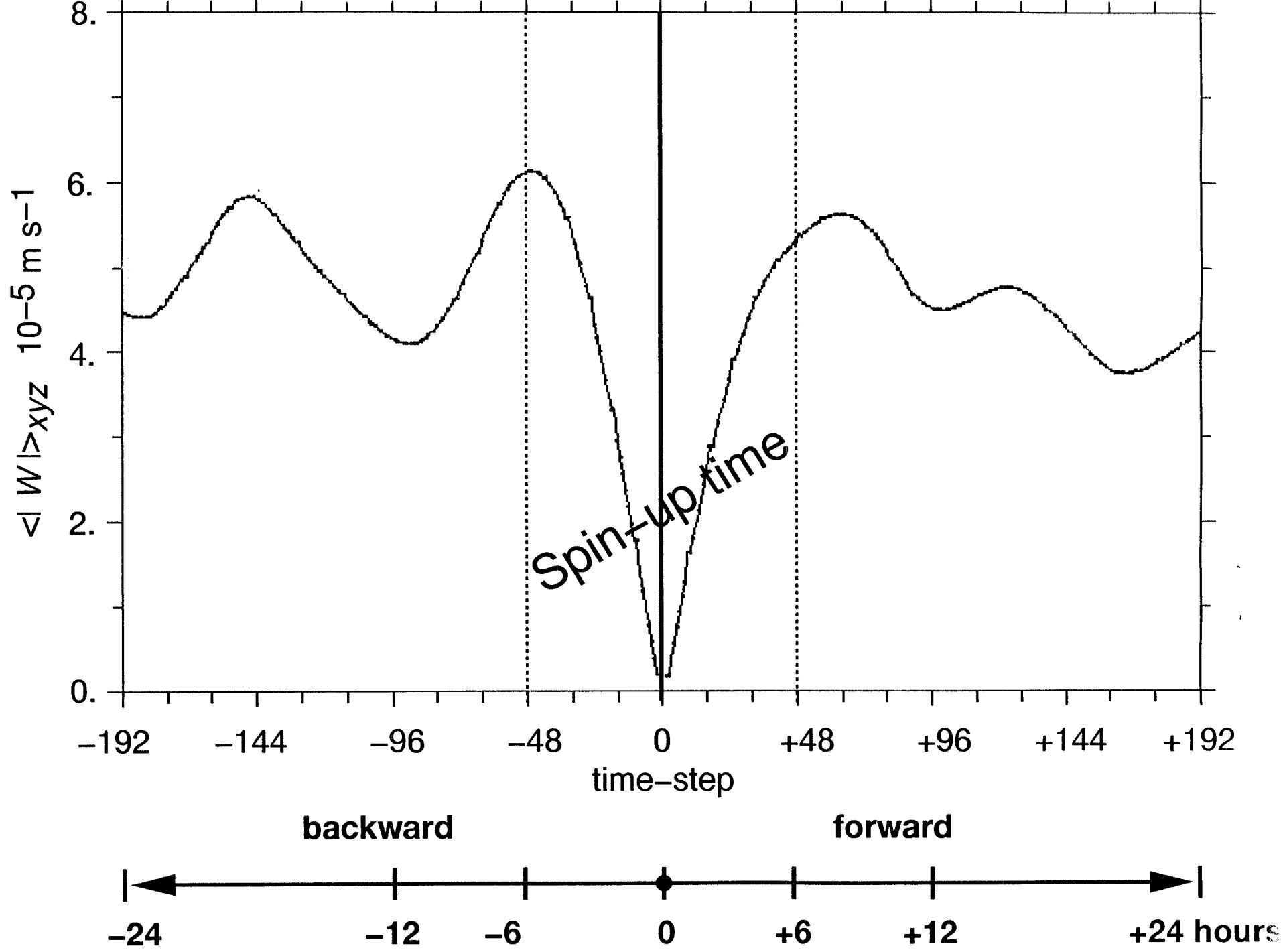


Figure 7

(a)

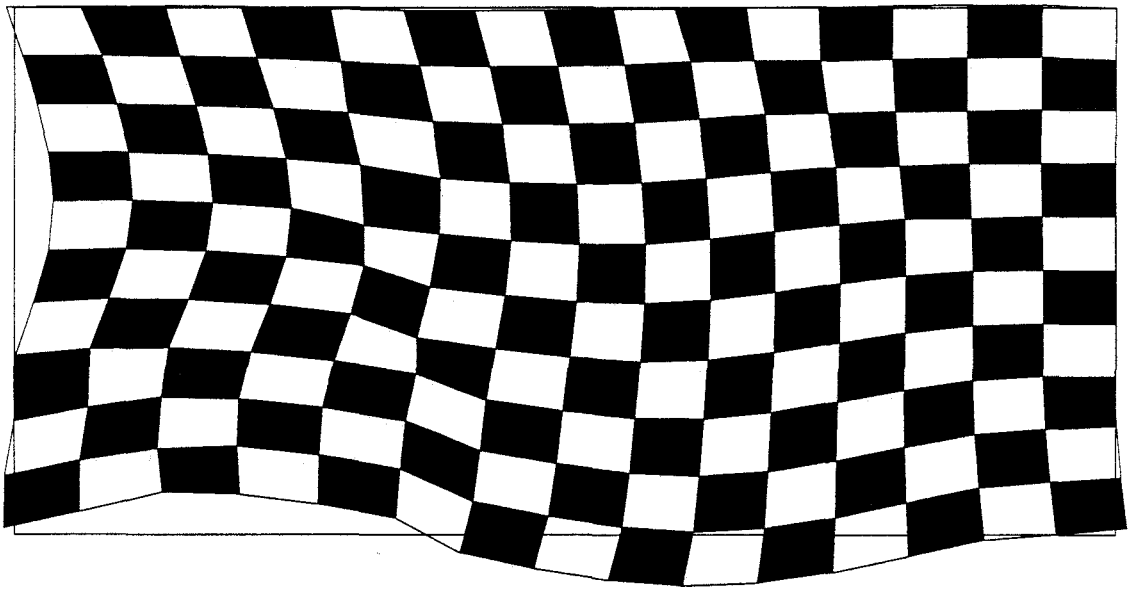


Figure 8a

(b)

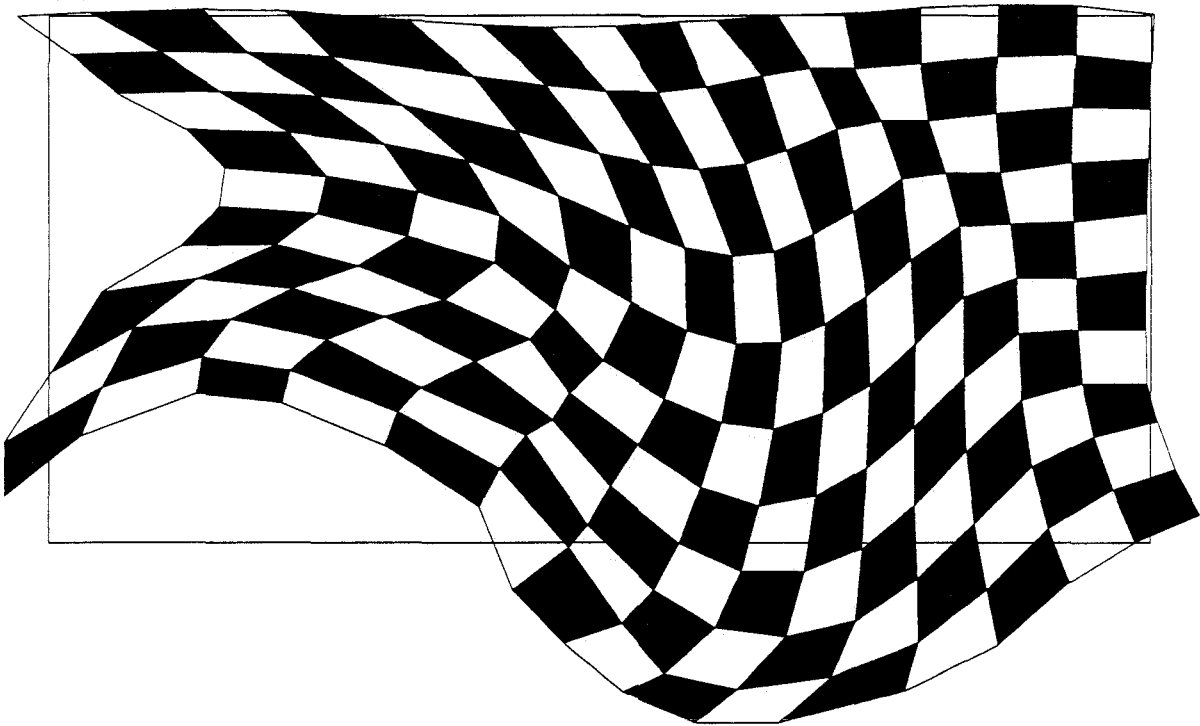
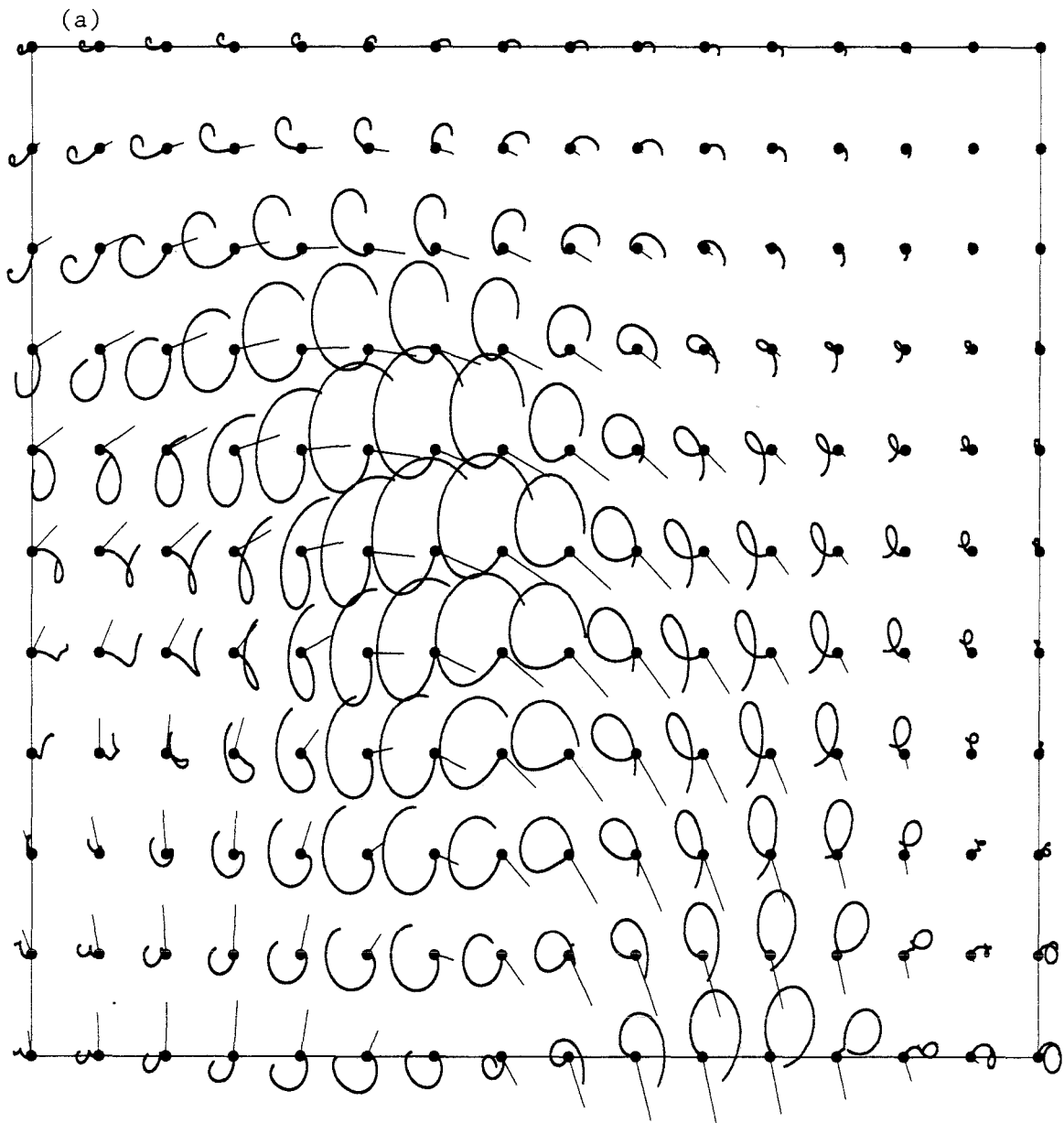


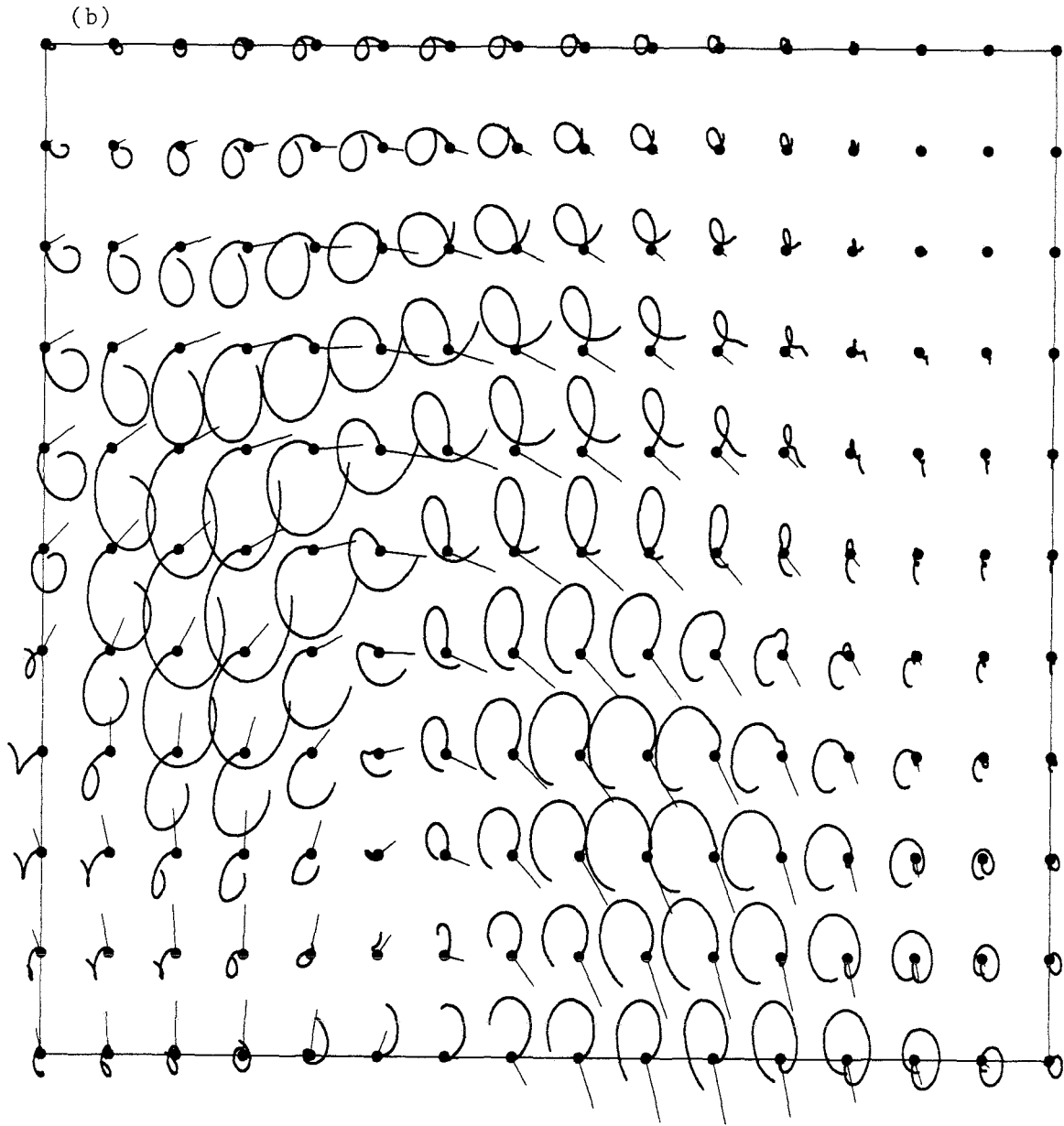
Figure 8b



vector scale: 50 cm/s

Hod. esc. 5 cm/s

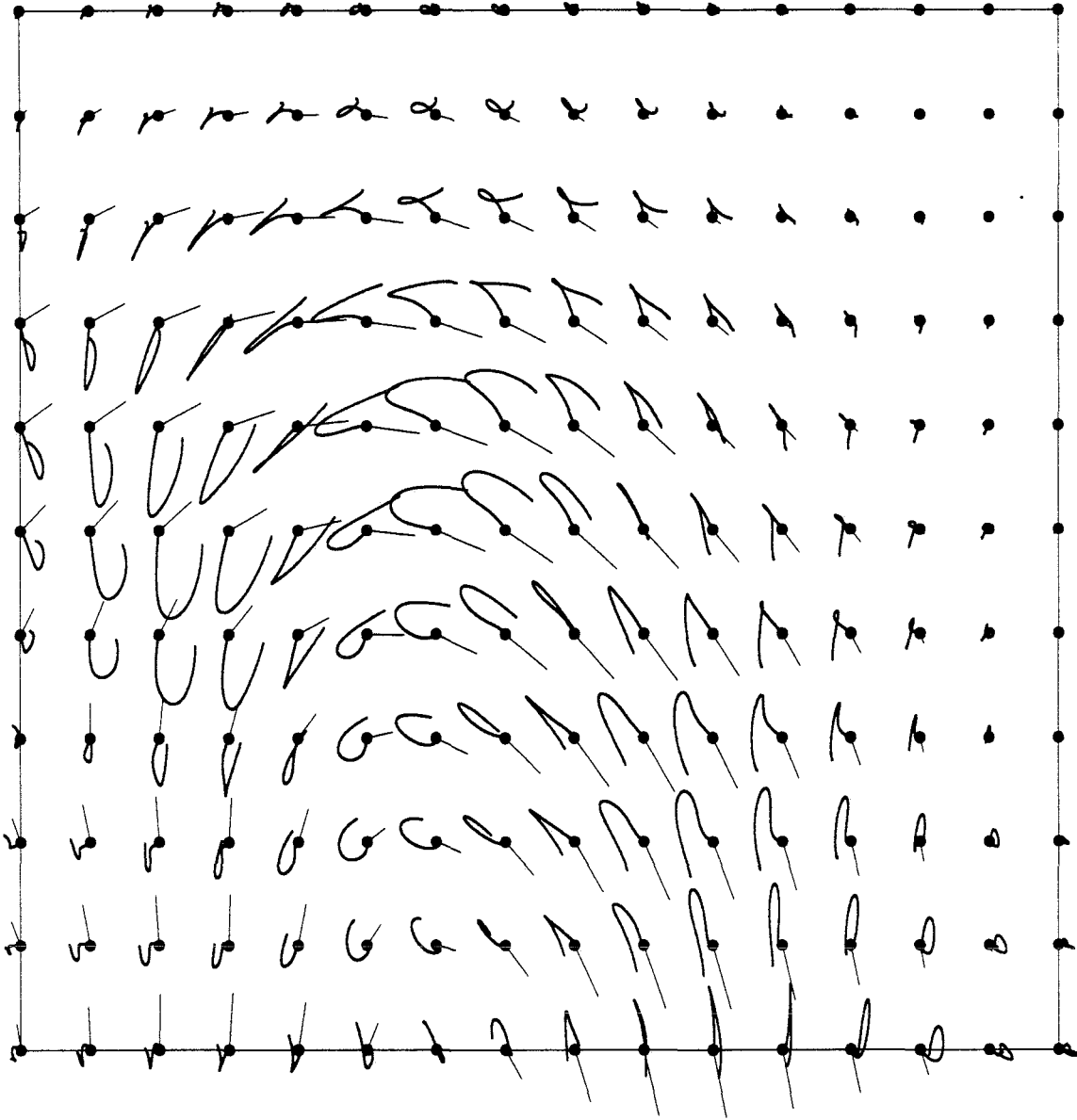
Figure 9a



vector scale: 50 cm/s hod. esc. 5 cm/s

Figure 9b

(c)



Vector scale: 50 cm/s

Hod. esc. 5 cm/s

Figure 9c

(a)

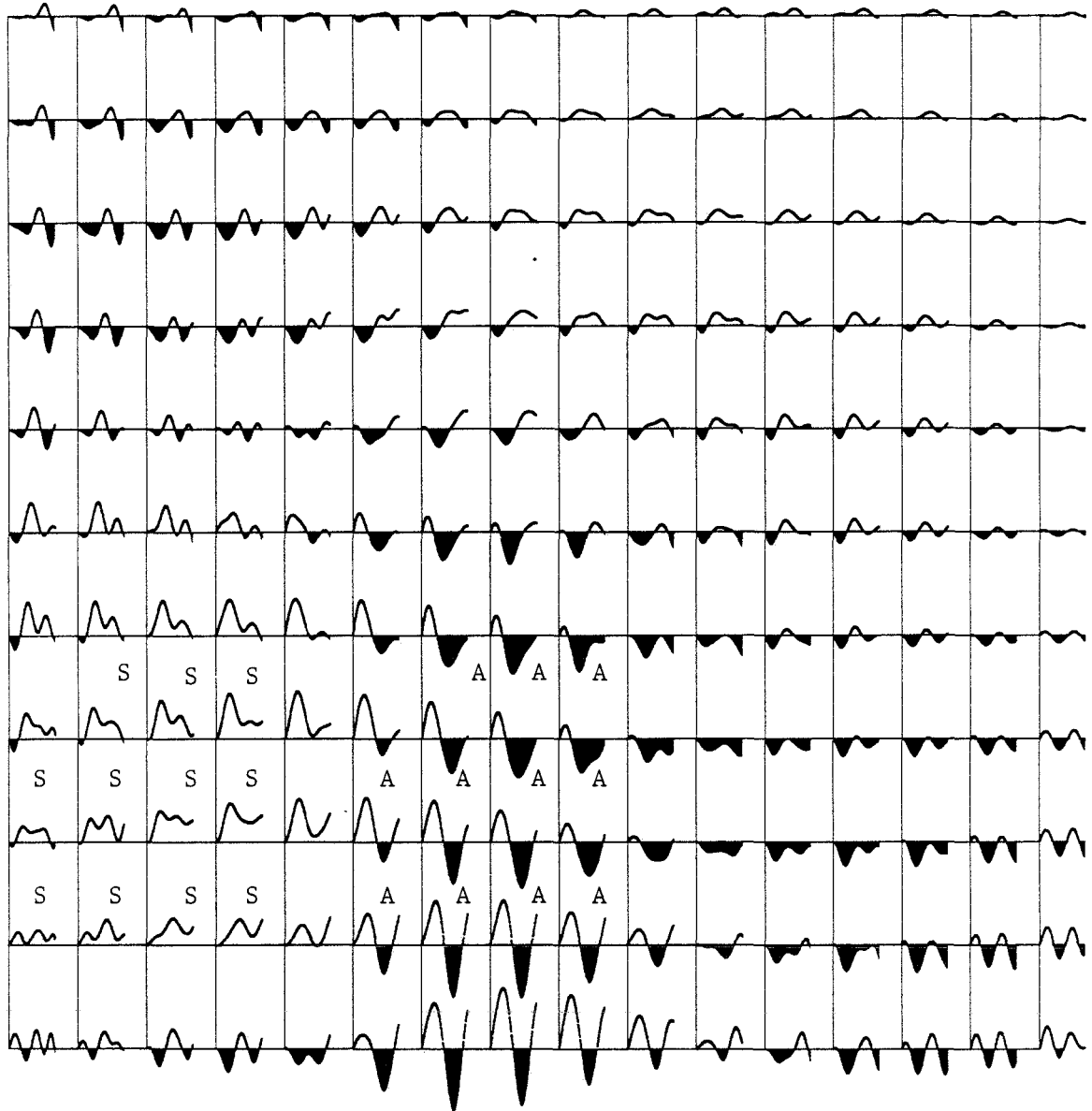


Figure 10a

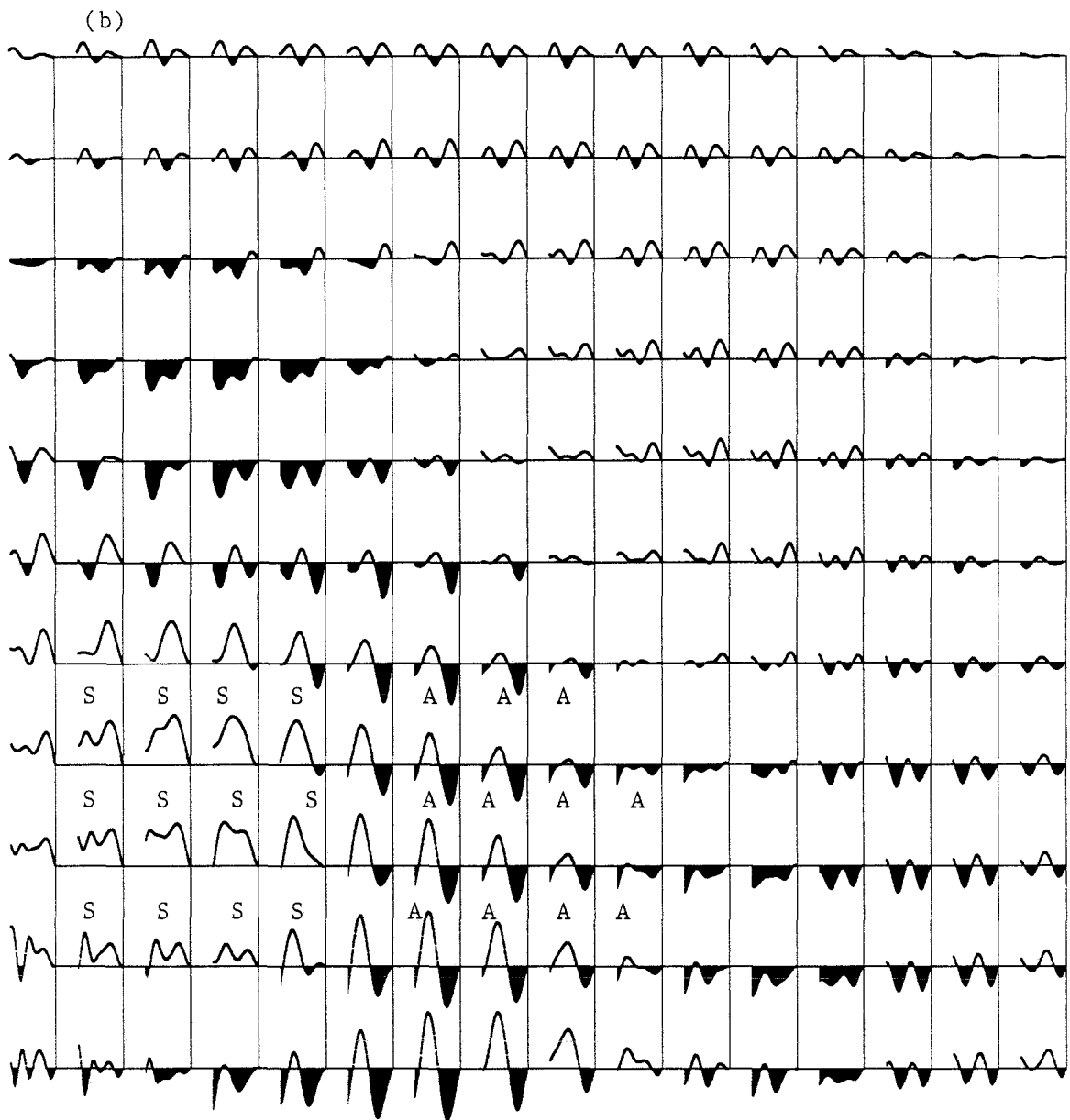


Figure 10b

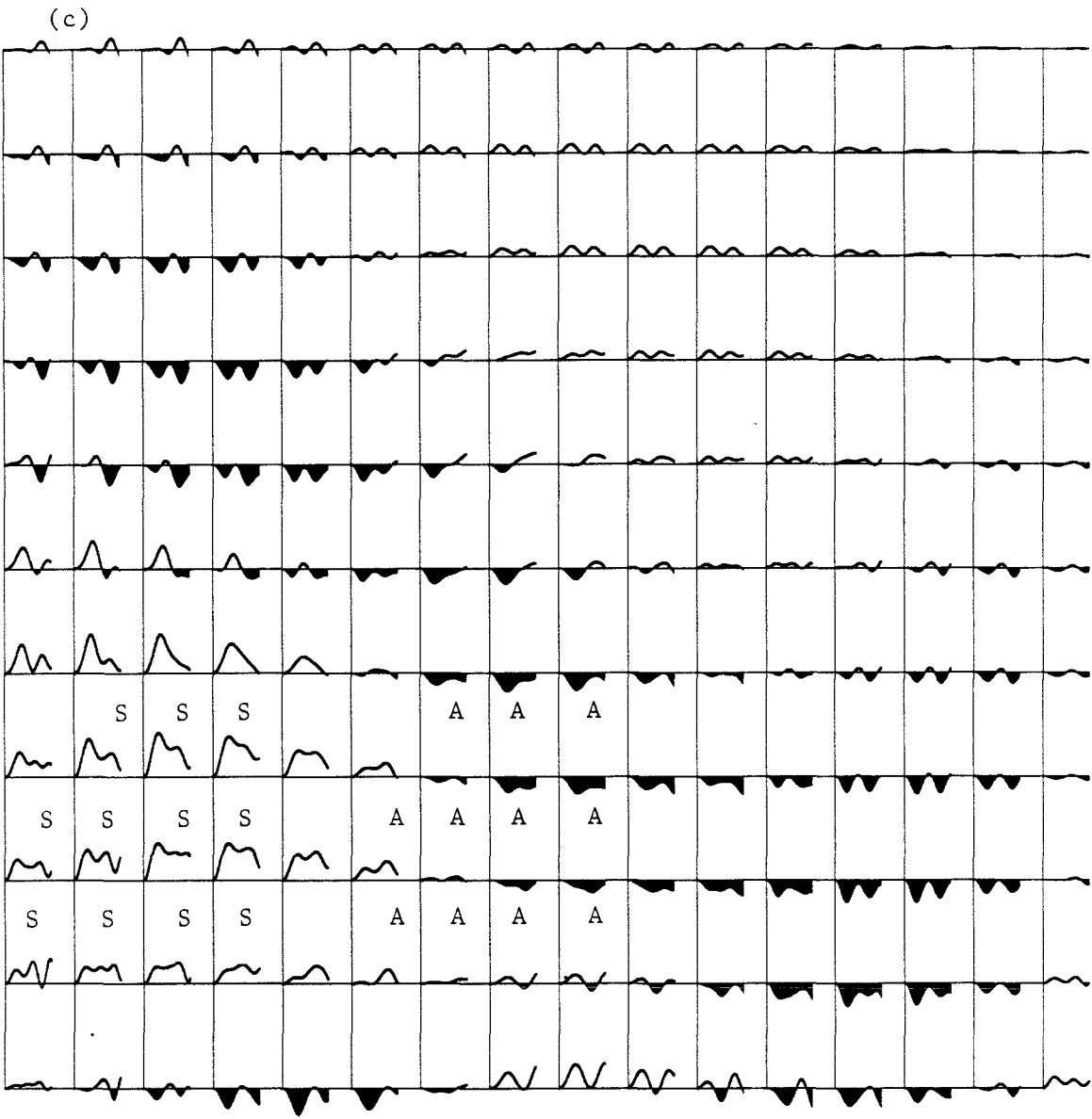


Figure 10c

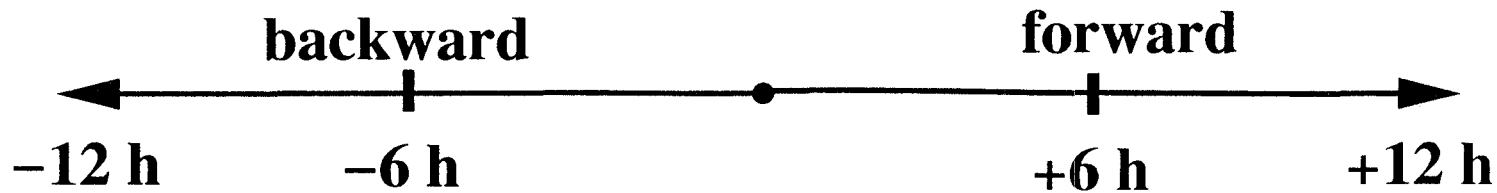
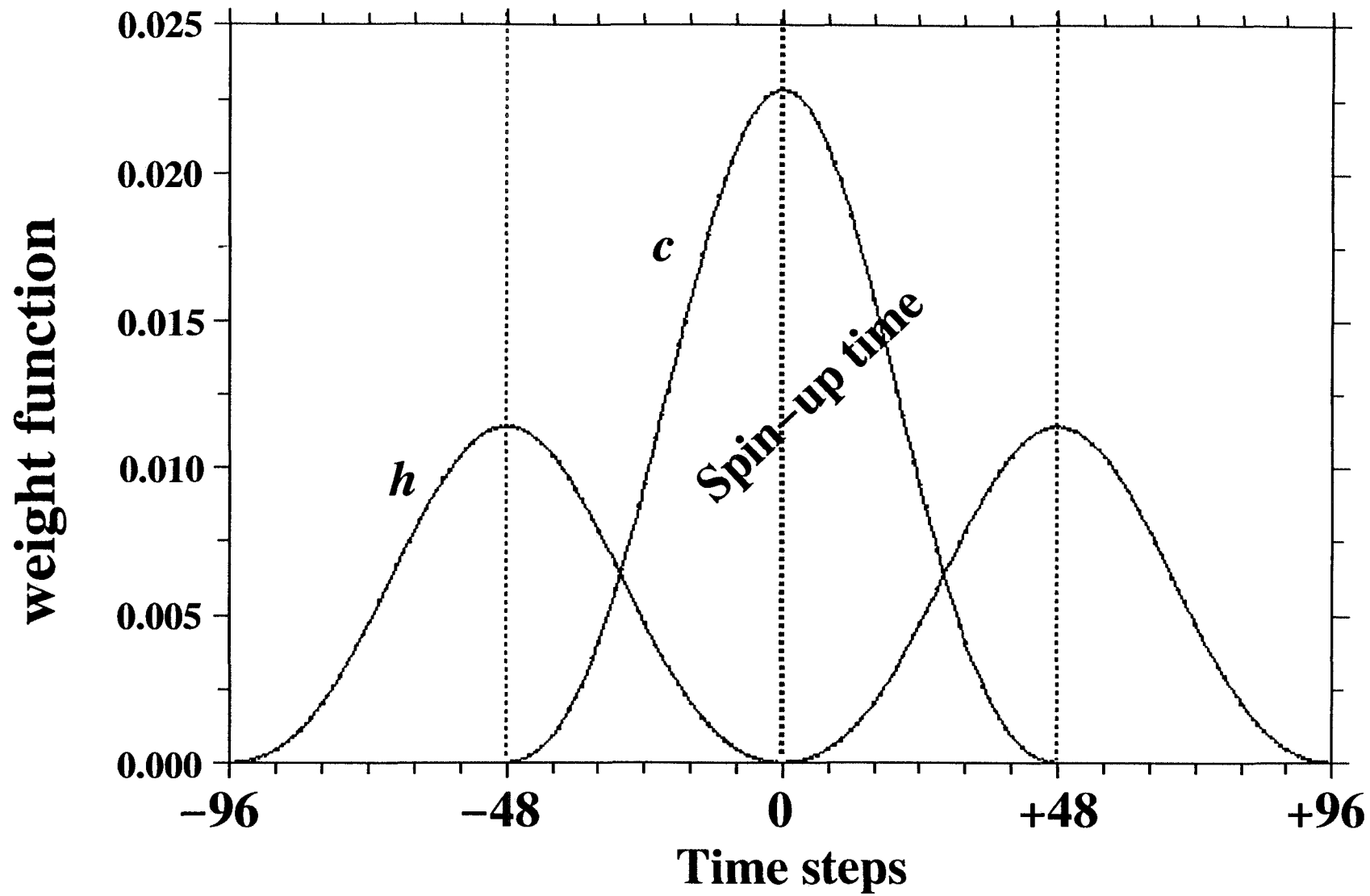


Figure 11

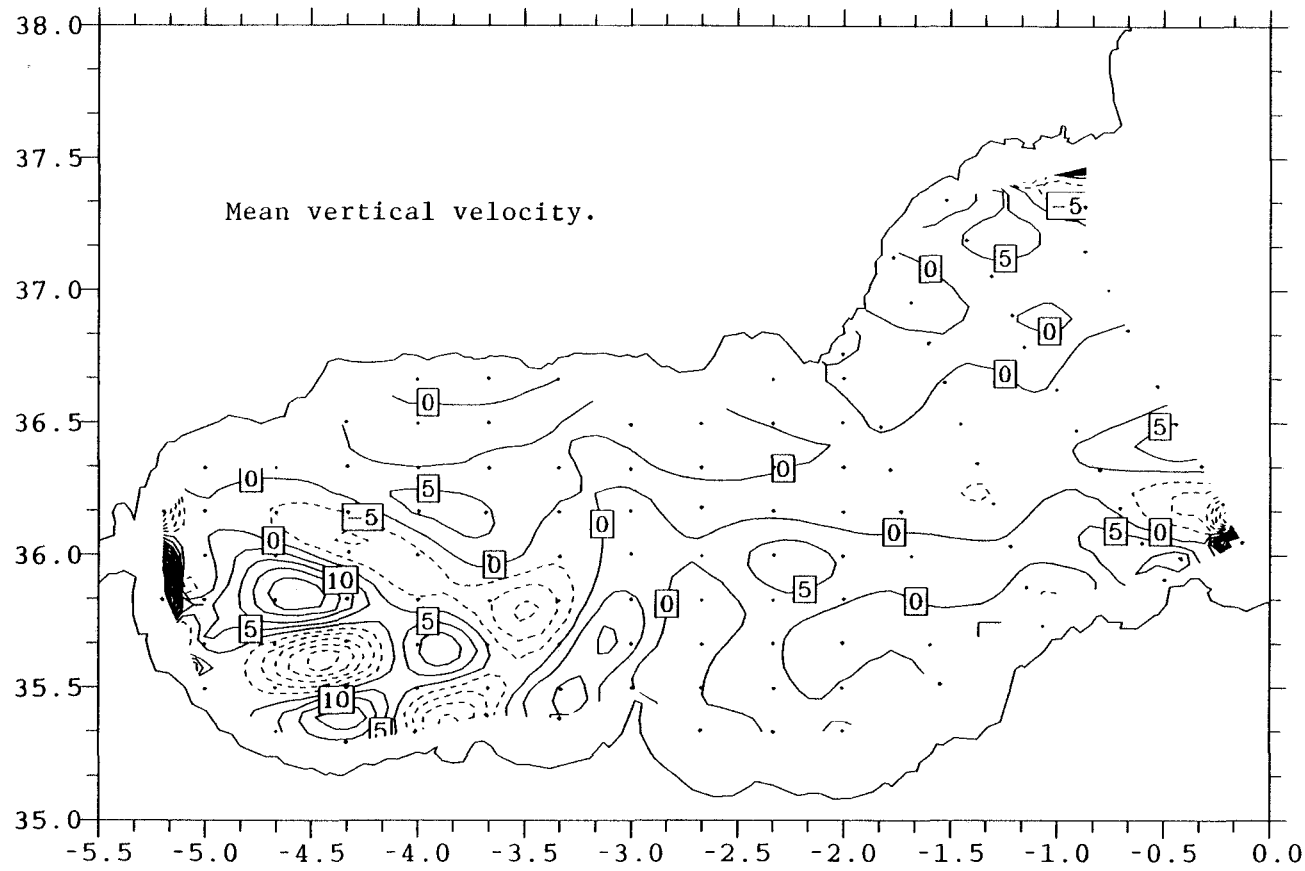


Figure 12

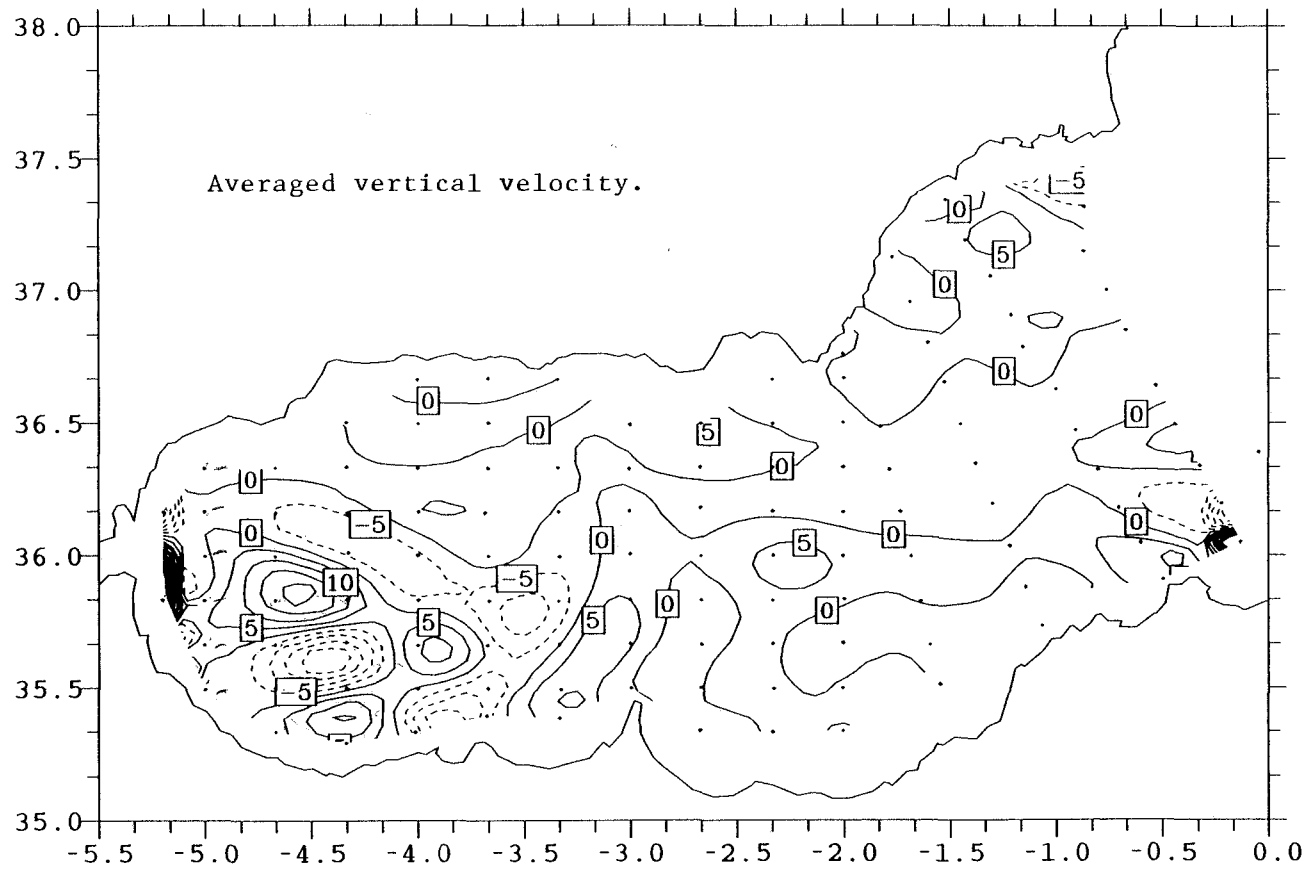


Figure 13

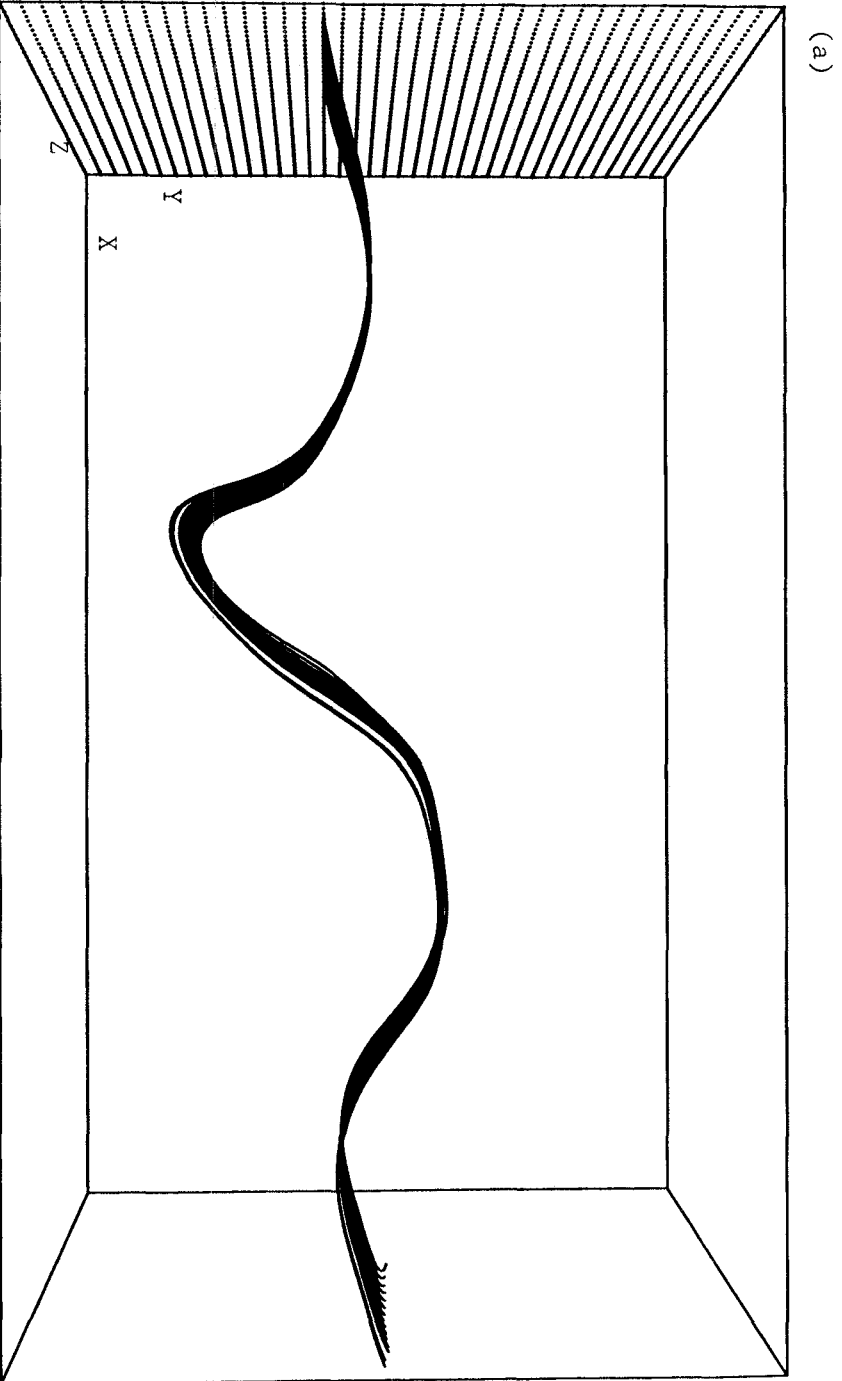


Figure 14a

(b)

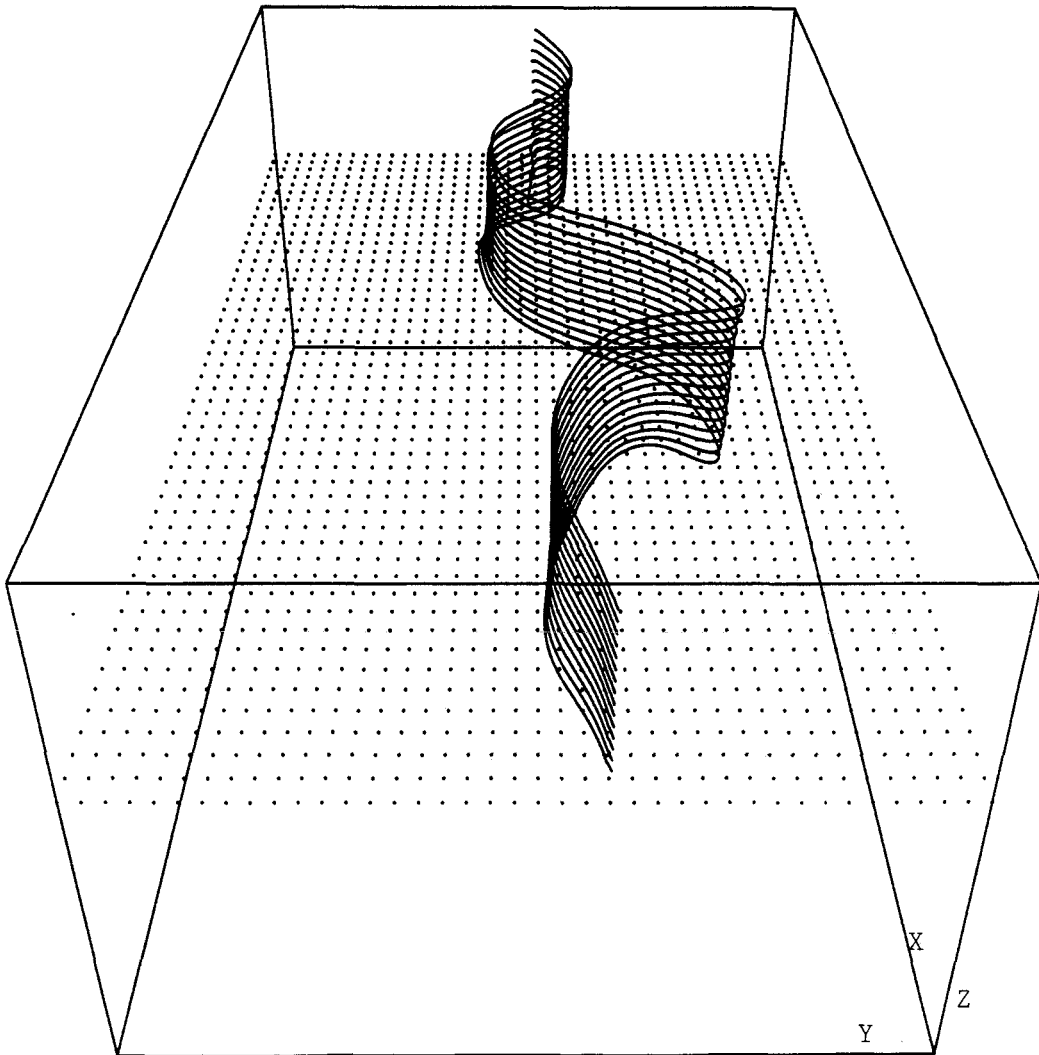


Figure 14b

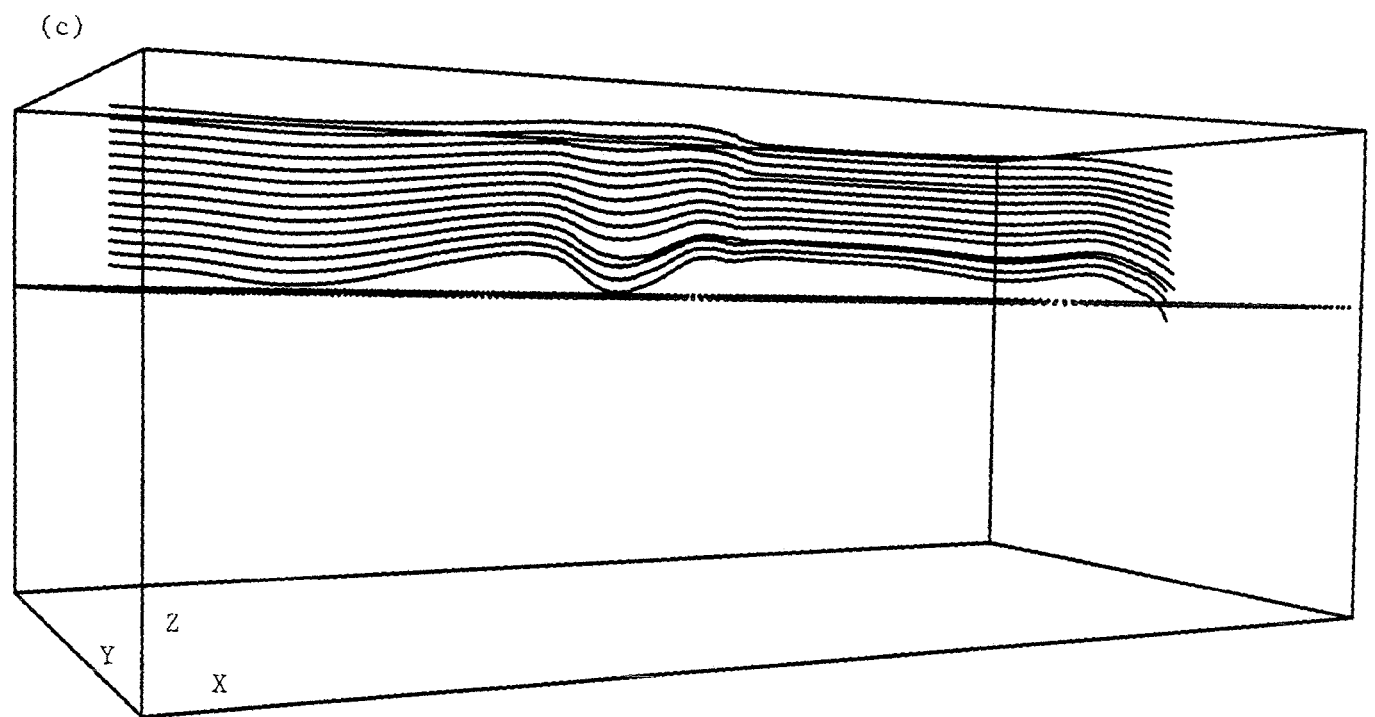
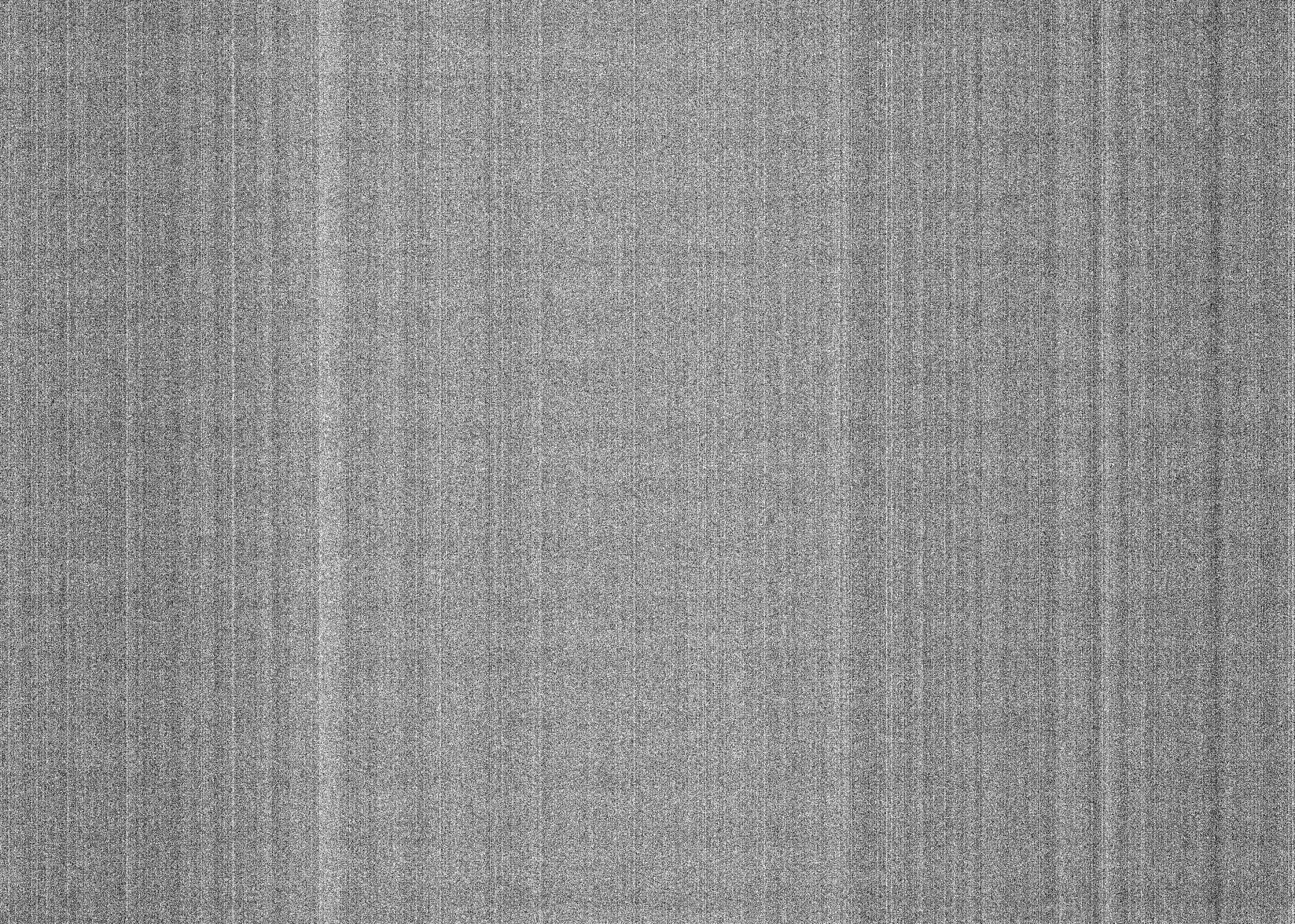


Figure 14c



Capítulo 6

About the Nature of the Generalized Omega Equation

Álvaro Viúdez¹
Joaquín Tintoré¹

J. Phys. Oceanogr. (Submitted).

¹Departament de Física, Universitat de les Illes Balears, Palma de Mallorca, Spain

TABLE 1. List of symbols.

$\nabla \equiv (\partial_x, \partial_y, \partial_z)$	gradient operator
$\nabla_H \equiv (\partial_x, \partial_y)$	horizontal gradient operator
$\mathbf{v} \equiv (u, v, w)$	velocity vector
$\mathbf{v}_H \equiv (u, v)$	horizontal velocity vector
$\mathbf{V} \equiv (U, V)$	horizontal geostrophic velocity
$\mathbf{v}' \equiv (u', v', w)$	ageostrophic velocity
$\mathbf{v}'_H \equiv (u', v')$	horizontal ageostrophic velocity
$\zeta_3 \equiv \nabla \times \mathbf{v}$	relative vorticity
$\zeta \equiv v_x - u_y$	vertical component of ζ_3
$\zeta_g \equiv V_x - U_y$	geostrophic part of ζ
$\zeta' \equiv v'_x - u'_y$	ageostrophic part of ζ
f	Coriolis parameter (constant)
g	acceleration of gravity
$\rho(x, y, z)$	potential density field
ρ_0	mean constant density value
$b \equiv g(f\rho_0)^{-1}\rho$	buoyancy divided by f
$N^2(x, y, z) \equiv -g\rho_0^{-1}\rho_z$	Brunt-Väisälä frequency
$\zeta_P \equiv (-v_z, u_z, \zeta)$	relative pseudovorticity
$\zeta_{PH} \equiv (-v_z, u_z)$	horizontal relative pseudovorticity
$\zeta'_{PH} \equiv (-v'_z, u'_z)$	ageostrophic part of ζ_{PH}
$\mathbf{G} \equiv \partial v_i / \partial x_j, \text{ for } i, j \in \{1, 2, 3\}$	three-dimensional velocity gradient tensor
$\mathbf{G}_H \equiv \partial v_m / \partial x_n, \text{ for } m, n \in \{1, 2\}$	horizontal velocity gradient tensor